NASA-TM-82578 19840017677

NASA Technical Memorandum 82578

Space Processing Applications Rocket Project

SPAR VIII Final Report

LIBRARY COPY

JUN 4 - 1984

LANGLEY RESEARCH CENTER
LIBRARY, NASA
HAMPTON, VIRGINIA

JUNE 1984

NASA

NASA Technical Memorandum 82578

Space Processing Applications Rocket Project

SPAR VIII Final Report

Roger P. Chassay, *Editor*
George C. Marshall Space Flight Center
Marshall Space Flight Center, Alabama

National Aeronautics
and Space Administration

**Scientific and Technical
Information Branch**

1984

TABLE OF CONTENTS

CHAPTER I

SPACE PROCESSING APPLICATIONS ROCKET (SPAR) PROJECT

SPAR VIII- FINAL REPORT

INTRODUCTION

The unique low-g environment of space affords an opportunity for exploring and developing techniques for processing a variety of materials without the constraining gravitational influences as evidenced with the processing of liquid phase materials or melts on Earth. The Materials Processing in Space (MPS) program is directed toward the stimulation and development of the associated science and technology required to pursue these investigations. This NASA activity is undertaken in cooperation with the scientific community and includes follow-on studies of specific areas of scientific research emphasizing those selected investigations of materials and processes which best demonstrate potential benefit from the enhanced sensitivity of the controlled processing in a low-g environment. Examples of interest in the program are the reduction and/or elimination of adverse thermal effects such as convection, sedimentation of heavy particles, buoyancy rise and positioning aspects of bubbles in liquids or melts, and the stratification effects of particulates of variable densities in solution. These and similar studies are considered to be the means to expand the limiting frontier in the development of new materials and processes which are envisioned ultimately to be of benefit to mankind. As complementary to the research and technological nature of the investigations, the evolving emphasis is being directed, with the advent of the Shuttle and increased payload potential, toward the development of self-sustaining programs yielding direct product benefit.

The initial precursory zero-g demonstrations and investigations asociated with this family of scientific experiments were proposed and developed for the Apollo flights beginning in the late 1960's and continued with Skylab and Apollo-Soyuz flights through the mid-1970's. During the period between the close of that era and the orbital space flights on the Space Shuttle in the 1980's, the Space Processing Applications Rocket (SPAR) project has provided the only viable flight opportunity for low-g scientific investigations for experimenters, and has served in a precursory role for planned and approved Shuttle investigations.

The SPAR project is part of the MPS program of the Office of Space and Terrestrial Applications (OSTA) which is responsible for directing research into the scientific effects of materials processing in the unique environment of space. This effort involves participation and interaction from various disciplines of the scientific community, government-supported laboratories, universities, and industrial organizations, in addition to foreign participation.

The Black Brant VC (BBVC) sounding rocket series, which is currently the carrier vehicle for the scientific payloads, with a Nike-boosted configuration available for heavier payloads, provides the opportunity to process materials in a low-g environment for periods up to five minutes in duration during a sub-orbital flight.

The rocket flights, which are conducted at White Sands Missile Range (WSMR) in New Mexico, afford experimenters and apparatus developers a flight opportunity for a proof-of-concept verification and/or refinement of equipment operation and procedures prior to the longer duration, more sophisticated Shuttle flights.

This SPAR flight, the eighth in a planned series of rocket flights, occurred on November 18, 1980 and carried three experiments. The investigations for the experiments comprising the payload manifest were managed and coordinated by the MPS Projects Office of the Marshall Space Flight Center (MSFC). Two of these experiments were proposed and devised by industrial firms and one by a government-supported laboratory.

Previous experiments flown on the SPAR flights include the measurement of liquid mixing due to spacecraft motion; the dispersion of normally immiscible materials in the area of fluid dynamics; solidification experiments involving the gravitational effects on dendritic growth, epitaxial growth, and solidification of eutectic materials with widely differing densities have flown previously, in addition to solidification studies of interactions between second-phase particles and an advancing crystal-liquid interface and gravity-induced convection on cast microstructures. In the area of multiphase particle interaction, various experiments were conducted on the migration and coalescence of bubbles and particles, closed-cell metal foam, and the dispersion strengthening of composites.

The SPAR project has been increasingly active in supporting research in the promising area of containerless processing with previous flights, including experiments on cast beryllium and the processing of amorphous ferro-magnetic materials in an electromagnetic field, and control of liquid droplets by an acoustic field in the furtherance of the state-of-the-art of acoustic containerless processing technology.

The SPAR flights have, through an evolutionary program, addressed experiments of increasing complexity and refinement and have afforded additional flight opportunities consistent with the maturity of each investigation. The payloads selected for this SPAR VIII flight manifest were based on the advanced state-of-the-preparedness of their ground-based research activity.

The following experiments are included in this SPAR VIII report:

- Glass Formation Experiment, SPAR Experiment 74-42/1R
- Glass Fining Experiment in Low-Gravity, SPAR Experiment 77-13/1
- Dynamics of Liquid Bubbles, SPAR Experiment 77-18/2

The post-flight results and analyses of each experiment flown on SPAR VIII as prepared by the respective flight investigators, in addition to an engineering report on the performance of the SPAR VIII Science Payload, are contained in separate sections of this technical memorandum. With the successful completion of this flight and subsequent data analysis, much useful data and information were accumulated for directing and developing experimental techniques and investigations toward an expanding, beneficial program of materials processing in the Shuttle era.

SPACE PROCESSING APPLICATIONS ROCKET PROJECT

SPAR VIII

ENGINEERING REPORT

APRIL 1984

Prepared by:

Roger P. Chassay
and
Eli G. Osburn
of the
Marshall Space Flight Center

TABLE OF CONTENTS

CHAPTER II

1.0 SUMMARY

The SPAR VIII (R-19) Nike-Black Brant VC rocket was launched from White Sands Missile Range (WSMR), New Mexico, at 5:40 p.m. MST on November 18, 1980. The 435 kg (959 lbs.) gross payload achieved an apogee of approximately 198 km (123 statute miles); and a low-g period of 331 seconds. The launch and mission were very successful, but the payload encountered significant damage upon range impact.

2.0 SPAR VIII (R-19) PAYLOAD CONFIGURATION

The SPAR VIII (R-19) science payload consisted of three materials experiments, as well as the Experiment Support Module (ESM) and the Abbreviated Measurement Module (AMM). The SPAR VIII experiments are:

74-42/1R, Containerless Processing of Glass
77-13/1 Glass Fining in Low-Gravity
77-18/2 Dynamics of Liquid Bubbles

The orientation of the science payload to the rocket systems is shown in Figure 1 and the experiments orientation within the SPAR VIII rocket vehicle is shown in Figure 2.

3.0 ROCKET PERFORMANCE

3.1 Flight Sequence

The SPAR VIII flight profile is shown in Figure 3. The actual sequence of events are shown as a function of flight time.

3.2 Low Gravity

The low-g (10^{-4} or less) period was 331 seconds. The minimum low-g period required by experiments was 260 seconds. The gross payload weight was 435 kg (959 lbs.).

SPAR PROJECT
NIKE BLACK BRANT VC
CONFIGURATION

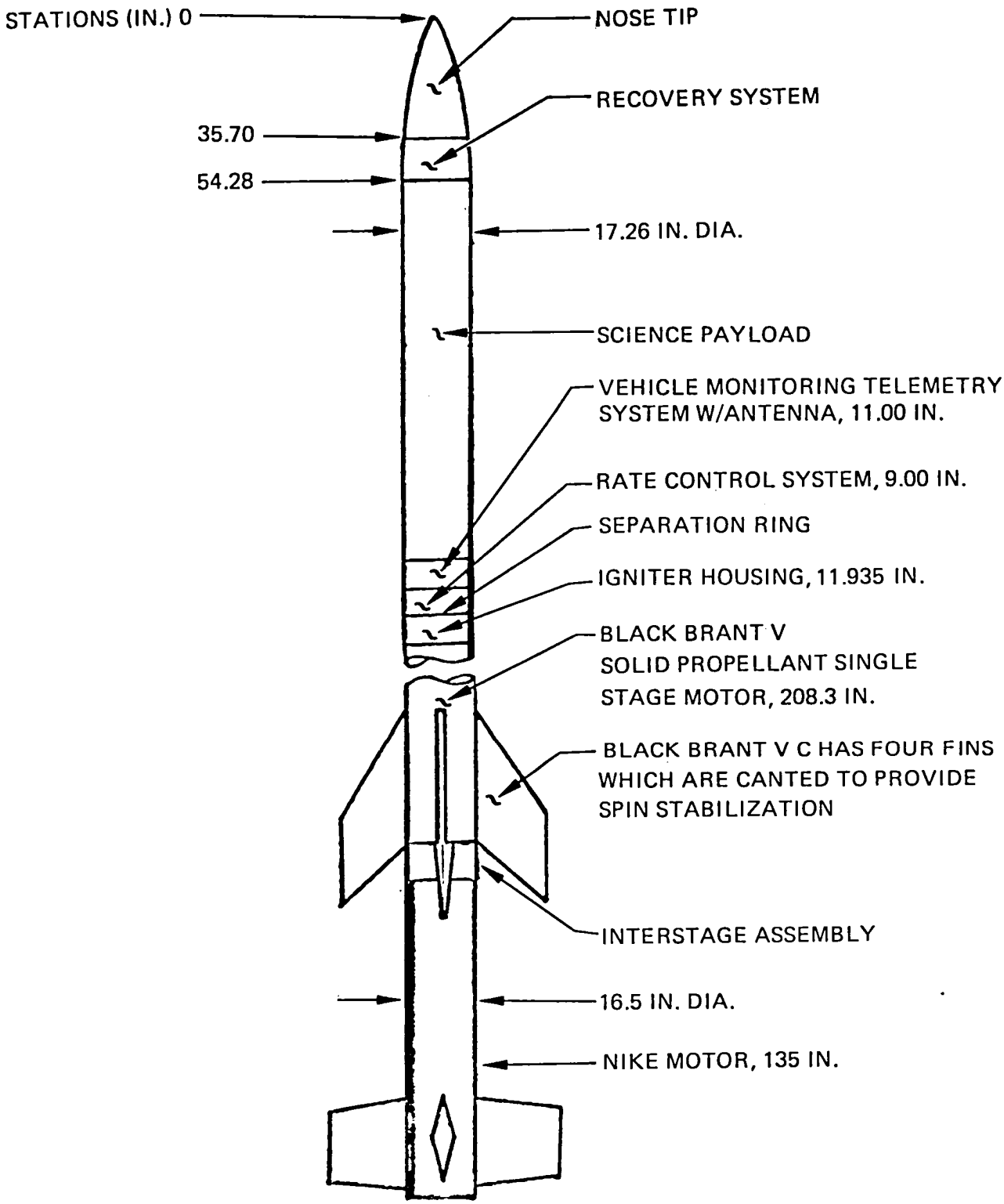

FIGURE 1

SPAR R-19
SCIENCE PAYLOAD
FLIGHT CONFIGURATION

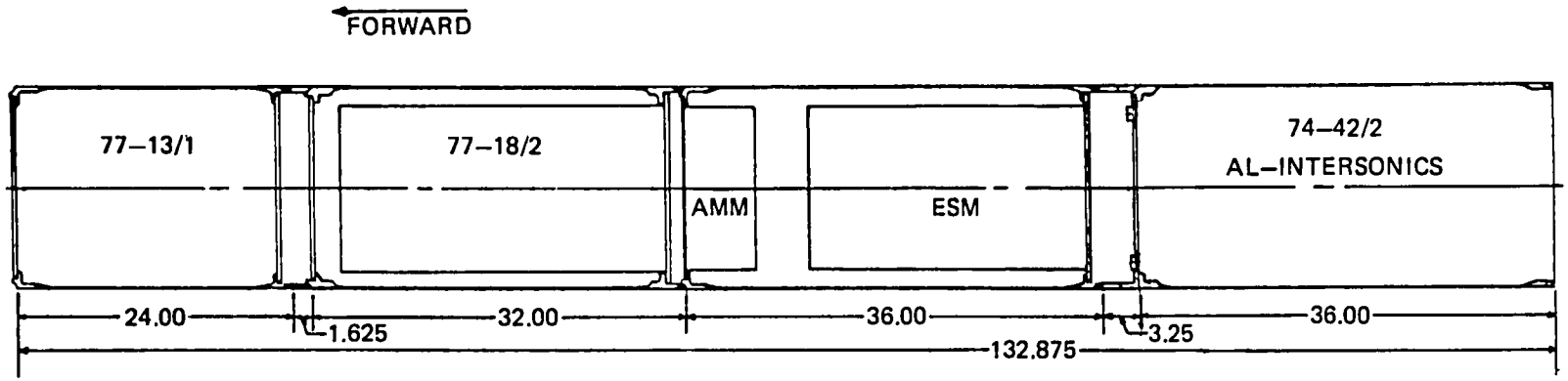

FIGURE 2, EXPERIMENT ARRANGEMENT WITHIN THE PAYLOAD

SPAR PROJECT
NIKE – BLACK BRANT VC ROCKET 27.019
MISSION PROFILE, EVENTS AND CONDITIONS

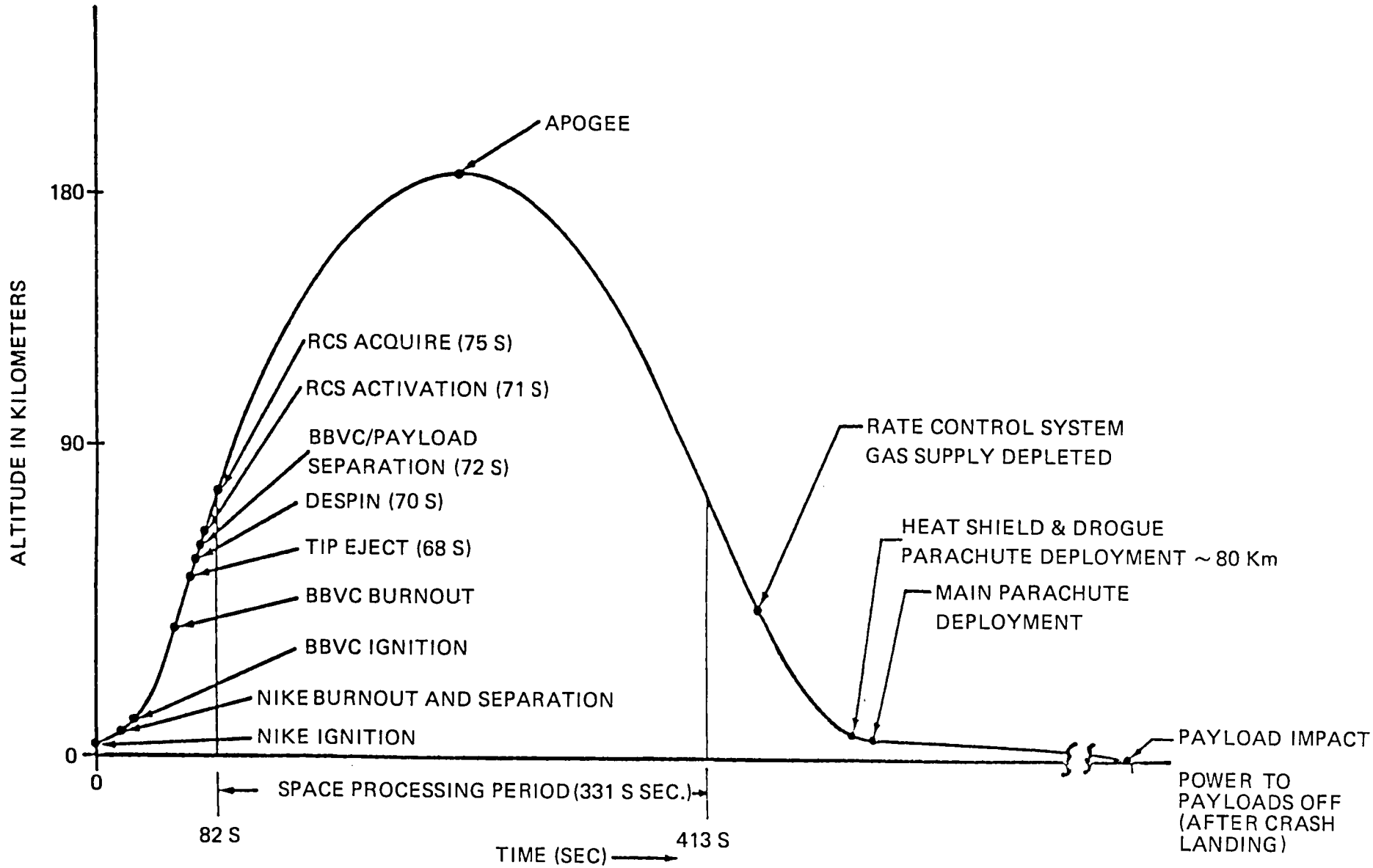

FIGURE 3. FLIGHT PROFILE AND EVENTS

4.0 PAYLOAD SUPPORT

4.1 Payload Sequence of Events

Experiment 74-42 required preheat power prior to launch which was supplied by ground power, beginning at T-45 minutes. At T-0, a lift-off signal was given which activated a timer within all experiments for control of events during the flight. All payload events sequenced as planned, except deactivation (reference paragraph 4.2 below).

4.2 Payload Power

Transfer of electrical power from ground support equipment to the flight battery was accomplished at three minutes prior to launch. The science payload battery, located in the Experiment Service Module (ESM), suppplied power to all experiments. Battery voltage measurement (MOOl-SM) indicates that the battery voltage was approximately 32 volts at lift-off. The bus voltage remained within allowable limits throughout the flight. Both voltage and amperages were as planned in the flight timelines.

The flight data indicated that the planned deactivation of the lDl bus at T+728s and T+738s (KO77-SM), the planned deactivation of the 2Dl bus at T+728s and T+738s (K105-SM) and the planned deactivation of the Measurement Module at T+804s (K107-SM) did not occur. This was attributed to the crash and damage to the payload prior to the times these commands were to have been issued.

5.0 EXPERIMENT INSTRUMENTATION

5.1 Experiment 74-42/IR: Containerless Processing of Glass

This experiment utilized the Intersonics, Inc. Single Axis Acoustic Levitator (SAAL) for providing the containerless processing of the glass sample. The objectives of the experiment are:

a. Determine the characteristics of low-gravity-prepared glass samples.

b. Gain experience with the performance of a low-gravity flight experiment.

c. Gain insight into the degree of equipment complexity required to prepare glasses in low-gravity.

d. Attain a position that will permit the determination of accurate optical properties of the new glass.

The data for experiment 74-42 indicated that the cooling shroud gate (G002-42), sound source gate (G003-42), sample gate (G001-42), and camera window gate (G004-42) opened and closed in the proper sequence during the mission.

Pressure measurement (D014-42) indicated that experiment 74-42 maintained its internal pressure during the flight. The sample temperature measurements (C160-42 and C159-42) indicate that the sample temperature profile was per requirements defined by the Principal Investigator.

The acoustic sound source measurements (M114-42, M115-42, M116-42, and M117-42) indicated that the sound system operated properly. However, post-flight analysis determined that levitation of the experiment sample was prematurely terminated at 82s instead of the planned 240 s. Extensive post-flight testing in a laboratory system duplicated this anomaly which was caused by excessive humidity in the acoustic field, which in turn results in significant sound reduction and loss of stable positioning of the specimen. Dessication of the extremely porous material used for the specimen injector as well as dessication of the entire levitator is planned for future flights.

The SAAL was completely destroyed when the R-19 payload crash landed. The experiment sample could not be found after the crash.

5.2 EXPERIMENT 77-13/1: Glass Fining in Low-Gravity)

It is the objective of this experiment to record the motion of bubbles of known size in a known temperature gradient under low-gravity conditions in a sodium borate glass. This record will be needed to determine the rate of motion of bubbles due to the temperature gradient as a function of bubble size. This data will be compared to a theoretical model of this motion that is being developed at Clarkson College. It is necessary to eliminate buoyant forces that are generated in a gravitation field in order to be able to accurately measure the motion of a bubble in a molten glass in the presence of a temperature gradient. The SPAR rocket flight provides the appropriate environment to make the above motion measurements.

The flight telemetry data for experiment 77-13 indicated that the experiment functioned as designed during the flight. The four temperature measurements (C180-13, C181-13, C182-13, C183-13) on the sample indicated that the sample attained the proper temperature profile defined by the PI. The camera current measurement (MI12-13) indicated that the experiment camera functioned as required.

The experiment apparatus was significantly damaged by the crash-landing of payload R-19.

5.3 Experiment 77-18/2: Dynamics of Liquid Bubbles

The objectives of this experiment are to:

a. Determine the sphericity of a positioned liquid bubble.

b. Study the natural resonant frequencies and damping mechanism of bubble oscillation.

c. Study the adiabatic expansion of a liquid bubble.

The experiment 77-18 data indicated that it functioned as designed during the flight. The measurements that monitored the fluid and air syringe positions (M090-18, M096-18) and the injector in/out positions (PF2-17-C03, PF2-17-CO4) indicated that the sequencing was proper. The measurements monitoring the various internal DC voltage sources in the experiment (measurements M091-18, M098-18, M102-18, M099-18, M103-18, M100-18, M104-18, M101-18) indicated that all internal voltages were within required tolerances during the mission. Measurement D015-18 indicates that the experiment 77-18 depressurized at approximately T+293 seconds as required. The sound source data measurements (M092-18, M093-18, M094-18, M105-18, M106-18, M107-18, M095-18) were compared to the baseline data and indicated that the 3AAL functioned properly during the mission.

Some damage occurred to the experiment apparatus due to the crash landing of payload R-19.

6.0 SCIENCE PAYLOAD INSTRUMENTATION

6.1 Low-G Accelerations

The low-g data indicates that a low-g environment considerably less than 1×10^{-4}g was achieved in all three axes. (Reference Figures 4, 5, and 6.) The X-axis Linear Acceleration Measurement (AO2-MM) indicates that low-g entry in that axis was at about T+82 seconds and exit at about T+413 seconds with the g-levels during this period as shown in Figure 4. The Y-axis (AO3-MM) had low-g entry at T+79 seconds and exit at T+415 seconds as shown in Figure 5. The Z-axis Linear Acceleration Measurement (A04-MM) indicates the low-g entry in that axis as 82 seconds and exit at 431 seconds as shown in Figure 6. These values indicate a total low gravity period (less than 1×10^{-4}g's in all axis) of 331 seconds.

6.2 ENGINEERING TEMPERATURES

The engineering temperature measurements which monitor the R-19 payload structure at various points throughout the payload (CO39-MM, CO28-MM, C184-13, C177-42, C178-18, and C179-18) indicated normal and expected temperature levels.

SPAR R–19

BOOK NO.1 PLOT NO. 1
DATE OF RUN 12/10/80
FILE CREATED 12/8/80

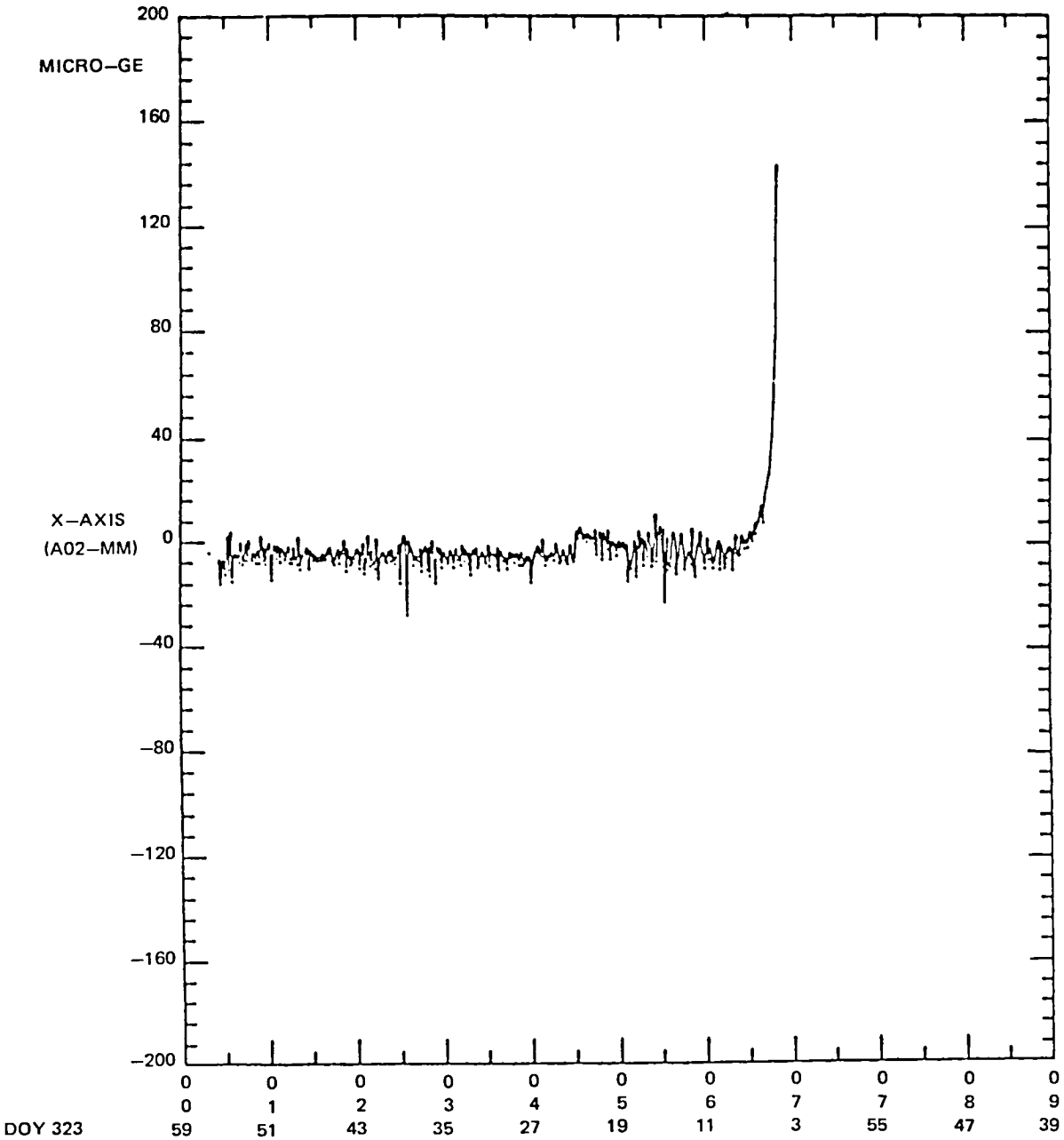

FIGURE 4

BOOK NO. 1 PLOT NO. 2
DATE OF RUN 12/10/80
FILE CREATED 12/8/80

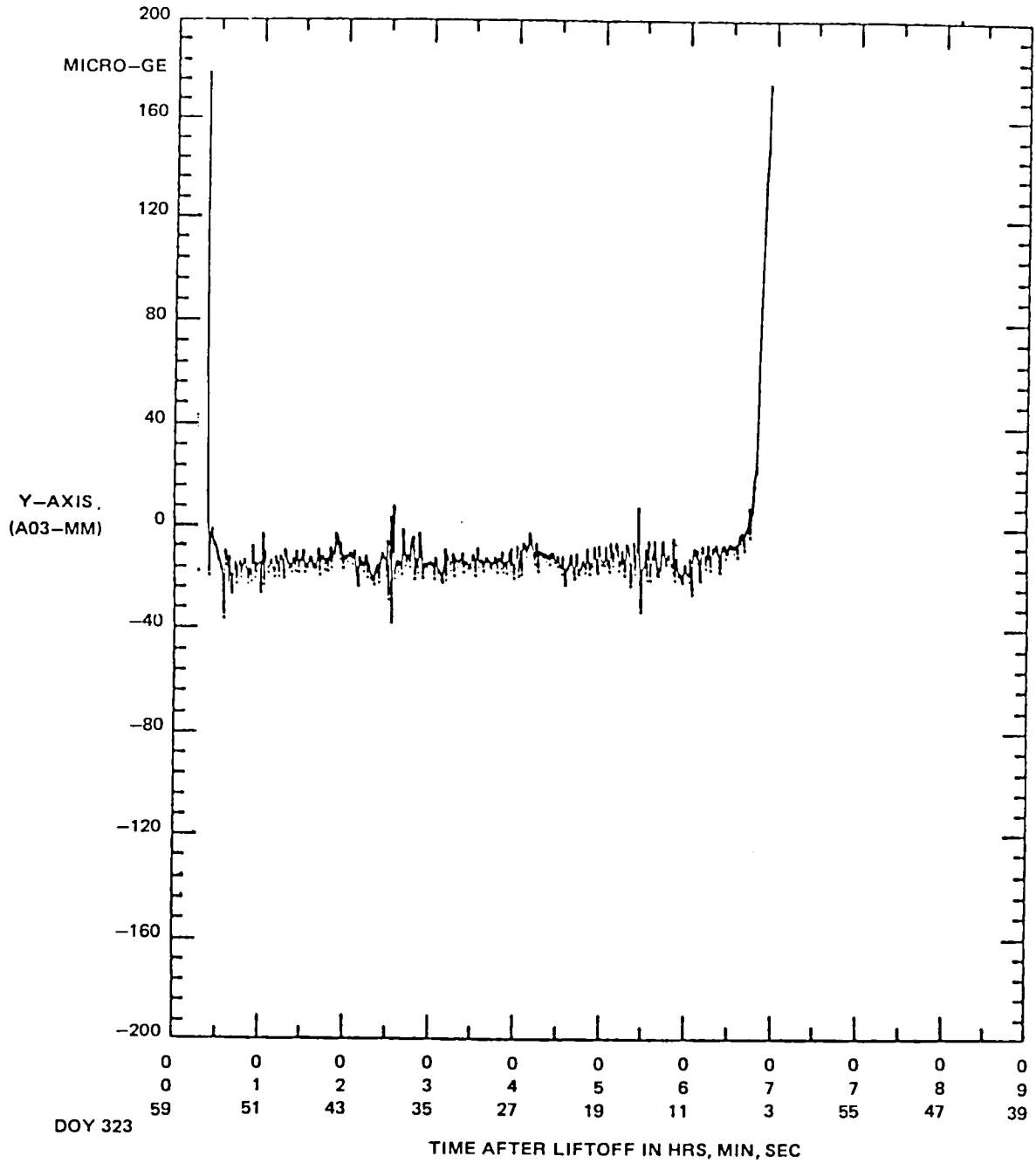

FIGURE 5

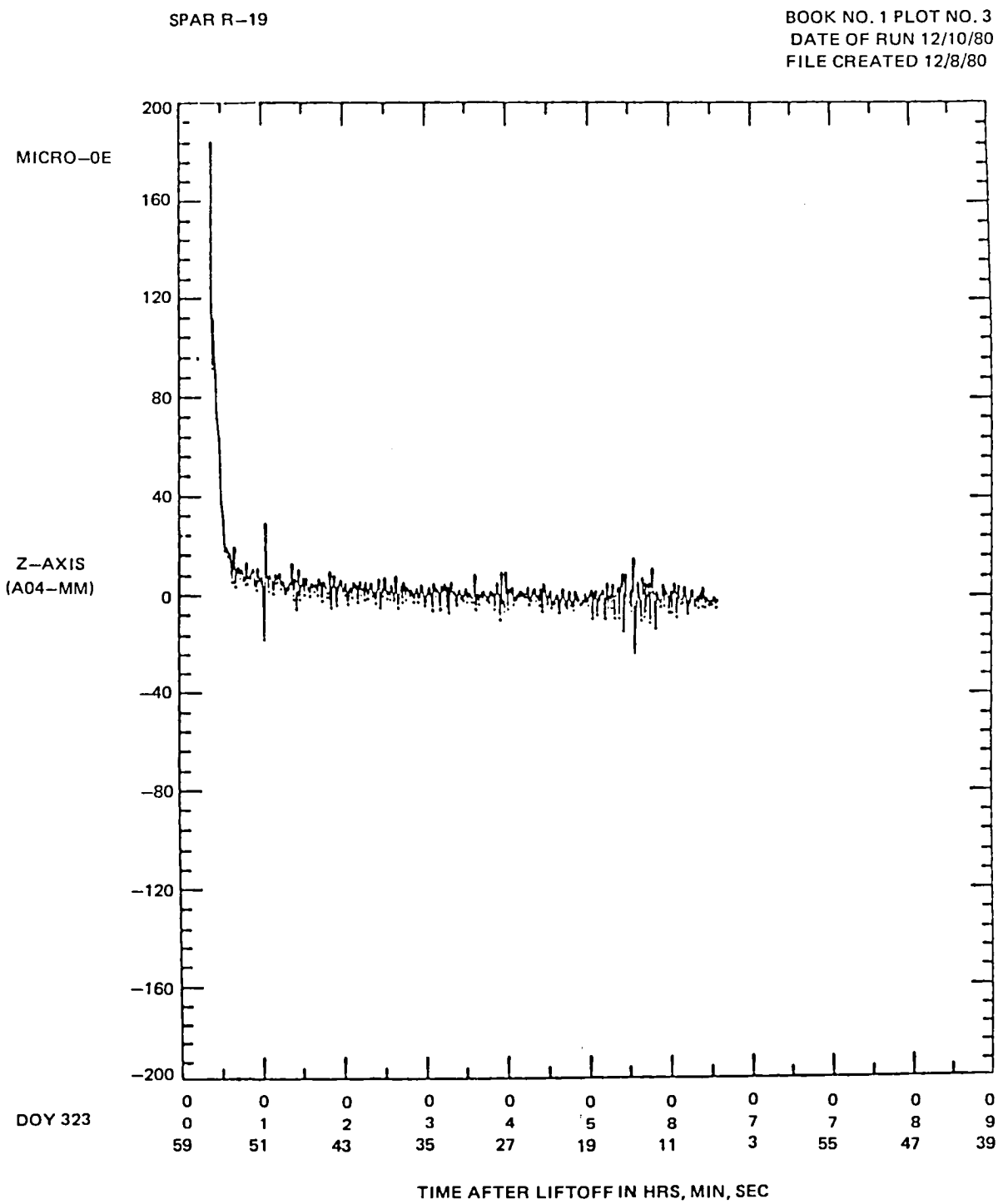
SPAR R–19
BOOK NO. 1 PLOT NO. 3
DATE OF RUN 12/10/80
FILE CREATED 12/8/80
MICRO–0E
Z–AXIS
(A04–MM)
200
160
120
80
40
0
–40
–80
–120
–160
–200
DOY 323
0 0 0 0 0 0 0 0 0 0 0
0 1 2 3 4 5 8 7 7 8 9
59 51 43 35 27 19 11 3 55 47 39
TIME AFTER LIFTOFF IN HRS, MIN, SEC

FIGURE 6

7.0 PAYLOAD RECOVERY/POST-RECOVERY OPERATIONS

Due to the premature deployment of the recovery parachute during atmospheric re-entry at about 80 km altitude (instead of the normal 30 km) and the resultant crash of the payload, the normal recovery procedure was not performed. The following is a description of the recovery.

Upon arrival at the crash scene, it was found that the recovery chute had deployed but was entangled in what looked like a huge knot. However, the payload impacted with the ground tail first which is normal. The payload impacted with the ground with such force as to completely smash the aft experiment (Experiment 74-42) and shear it from the rest of the payload which was about twenty feet from the impact point. A search was made around the ESM battery area to determine if the battery had ruptured on impact and lost its acid. Indications were found that the battery was ruptured. The battery fluid was pointed out to personnel on recovery to assure that no one touched it. The ESM battery door was then removed and the battery disconnected. The ESM was disconnected from the remainder of the payload. The area was searched for any pieces of the payload. All of the pieces found were placed in the bed of a pickup truck for transporting to the Vehicle Assembly Building (VAB). At the VAB the experiments were further inspected for damage. Experiments 77-13 and 77-18, which still had their access doors intact, were taken into a dark room to remove the access doors and then the film. The film was removed in complete darkness. The film was out of the film magazines but was put into black bags while in darkness. After the film recovery, the lights were turned on and the flight sample from Experiment 77-13 was removed and turned over to the PI. The PI on Experiment 74-42 searched through the remains of his experiment apparatus for the flight sample and film, but neither was found. On November 20, 1980, the PI with the aid of some Navy personnel returned to the crash site and found the Experiment 74-42 flight film embedded in the ground at the initial impact point. The flight sample was never recovered, although five searches of the impact area were made between November 19, 1980 and February 24, 1981.

CONTAINERLESS PROCESSING TECHNOLOGY EXPERIMENT

DYNAMICS OF LIQUID BUBBLES

REPORT

SPAR VIII EXPERIMENT 77-18 FLIGHT 2

Nov. 18, 1980

A. P. Croonquist, W.-K. Rhim, D. D. Elleman and T. G. Wang

submitted February 1983

ACKNOWLEDGMENTS

The authors wish to thank L. Robinson, K. Tarver, D. Kerrisk, and H. Press of JPL for their valuable assistance in all phases of this experiment. Dr. Wang wishes to thank R. Chassay, D. Schaeffer, and R. Fallon of MSFC for their patience in handling this experiment. For their pertinent comments and insights, A. Croonquist wishes to thank Drs. Barmatz, Jacobi and Kendall. We also appreciate the assistance of M. Swass in taking data from the cine film and of H. J. Brown in developing software to plot that data.

This paper presents the results of one phase of research carried out at the Jet Propulsion Laboratory, California Institute of Technology, under Contract No. NAS 7-100, sponsored by the National Aeronautics and Space Administration

CONTENTS

CHAPTER III

SECTION 1

INTRODUCTION

This report describes one phase of an experimental research program designed to contribute to the understanding of containerless processing of microballoons in space. Study of the stability and manipulability of liquid shells at room temperature is a useful and cost effective intermediate step in the development of a better understanding of the fluid physics pertinent to the production of rigid spherical shells and the capability to fabricate metallic or glass shells and fusion targets in a zero-G environment.

The primary goal of the experiment is to study three aspects which will be very important in the containerless processing of rigid shells in space: drop sphericity, bubble centering and adiabatic bubble expansion.

Drop sphericity studies will help to determine the magnitude of the distortion on a thin shell due to the acoustic forces required to overcome anticipated levels of G-jitter, thus impacting the orbital requirements on the spacecraft.

Bubble centering studies will enable us to determine the centering capabilities of various techniques such as rotation, forced oscillation, and expansion, thus impacting the design requirements of the facility for the containerless processing of microballoons and shells in space.

Adiabatic bubble expansion studies will allow us to better understand the phenomena observed as the bubble expands: fluid in the thicker regions of the shell flowing to the thinner regions. In addition, adiabatic expansion will allow us to increase the range of microballoons available by varying size and wall thickness in a controlled manner, thus impacting the versatility of containerless processing of microballoons and fusion targets in space.

The practical knowledge obtained in these studies will aid in the design of a high-temperature system for the generation and containerless processing of rigid shells in space. The study takes advantage of the laboratory work and zero-G aircraft tests under way at JPL, KMS, and LLL as part of the overall Office of Applications Space Processing Program.

This experiment was performed in an acoustic levitation chamber configured for use in the SPAR rocket which has been described in AO:OA-76-02. This report describes the results of the second of two scheduled flights, 77-18 SPAR VIII. The first experiment was conducted on SPAR VII.

CHAPTER III

SECTION 2

OBJECTIVES

The primary objectives of the flight were to:

1) Determine the sphericity of a positioned liquid shell. The equilibrium shape of a positioned liquid shell is the result of the balance of acoustic forces and surface tension. The sphericity of the liquid bubble will be determined from the film record.

2) Study acoustic techniques for centering a large bubble. The centering forces generated by the acoustic oscillation and rotation of the liquid shell will be determined. The acoustic fields will be configured to first impart a torque to the shell and then to excite selected normal modes of oscillation. The centering due to oscillation will be compared with theoretical models developed at JPL. The centering force upon the bubble as the shell is rotated acoustically will be determined and, in addition, any centering along the rotation axis due to secondary effects will be sought.

3) Determine the perturbation on bubble centering by G-jitter. As the rocket experiences G-jitter, the chamber moves back and forth arround the shell. The bubble experiences a non-symmetrical modulating force, thus perturbing its shape and position within the shell. This can produce unwanted coupling between rotation and oscillation of the drop.

4) Study the resonant frequencies and damping mechanism of bubble oscillation. The resonant frequencies of the liquid shell have been calculated. This experiment allows comparison of observed and calculated values. It provides data for determining the functional form of the damping coefficient.

5) Adiabatic expansion of a liquid bubble. The liquid bubble's size and wall thickness are determined by the pressure difference and surface tension across the two water/air interfaces. As the exterior pressure decreases, the bubble expands in size while its wall thickness decreases. Analysis of the flight film will provide information on any surface instabilities and also on the velocities and accelerations of flows within the liquid.

CHAPTER III

SECTION 3

APPARATUS

The experimental package used for this SPAR flight was the acoustic levitation rocket instrument which had flown on SPAR VII 77-18/1 on May 14, 1980. The instrument was designed to allow the injection of air into the drop to form a liquid shell. For this flight the dimensions of the chamber and the signals to the drivers were modified to enable the shell to be rotated. This flight was the second of two flights studying liquid shell behavior.

A. General Description

Figure 1 shows the SPAR VIII rocket payload 77-18 with the payload shell removed. The instrument consists of a triaxial acoustic resonance levitation chamber which has been used to position and control liquid drops and shells in low-G environments.[1-11] This particular chamber is nearly cubical with two equal dimensions to generate interference effects which could be used to rotate the shell. The chamber's inside dimensions are 11.42 x 11.42 x 12.70 cm along the x, y, and z axes respectively. Acoustic drivers are fixed rigidly to the centers of three mutually perpendicular faces of the chamber. The walls opposite to the drivers are made of glass to allow illumination and observation of the shell.

During operation of the system, each driver excites the lowest-order standing wave along the direction in which it faces. In a resonant system, the pressure is maximum at the nodes of the velocity wave and minimum at the antinodes; for this geometry the velocity nodes occur at the walls and the antinodes at the center of the chamber. There is a tendency for introduced objects (if their density is greater than that of air) to be driven toward the antinodes, where they collect and remain until the acoustic excitation is turned off. Because this is a three-dimensional system with independent control on each dimension, it has a great deal of versatility. It can position a drop acoustically and then manipulate it - also acoustically - by inducing either drop oscillation or rotation.

The primary source of data for this experiment was the cine film record showing three views of the shell obtained by the 16 mm camera. The camera is directed along the z axis; two mirrors give nearly orthogonal views along the x and y axes. Figure 2 shows the positions of the chamber, camera and mirrors. In addition the sound intensity at each wall, the deployment system, camera and lighting status, the frequency of the z axis signal and the ambient pressure were monitored and recorded. In addition to this telemetered data, accelerometer data was supplied by MSFC to aid in the data analysis. The x, y, and z axes of the accelerometer are parallel to the x, y, and z axes of the acoustic chamber; the view of the camera for each of the axes is from the positive axis to the negative axis of the accelerometer.

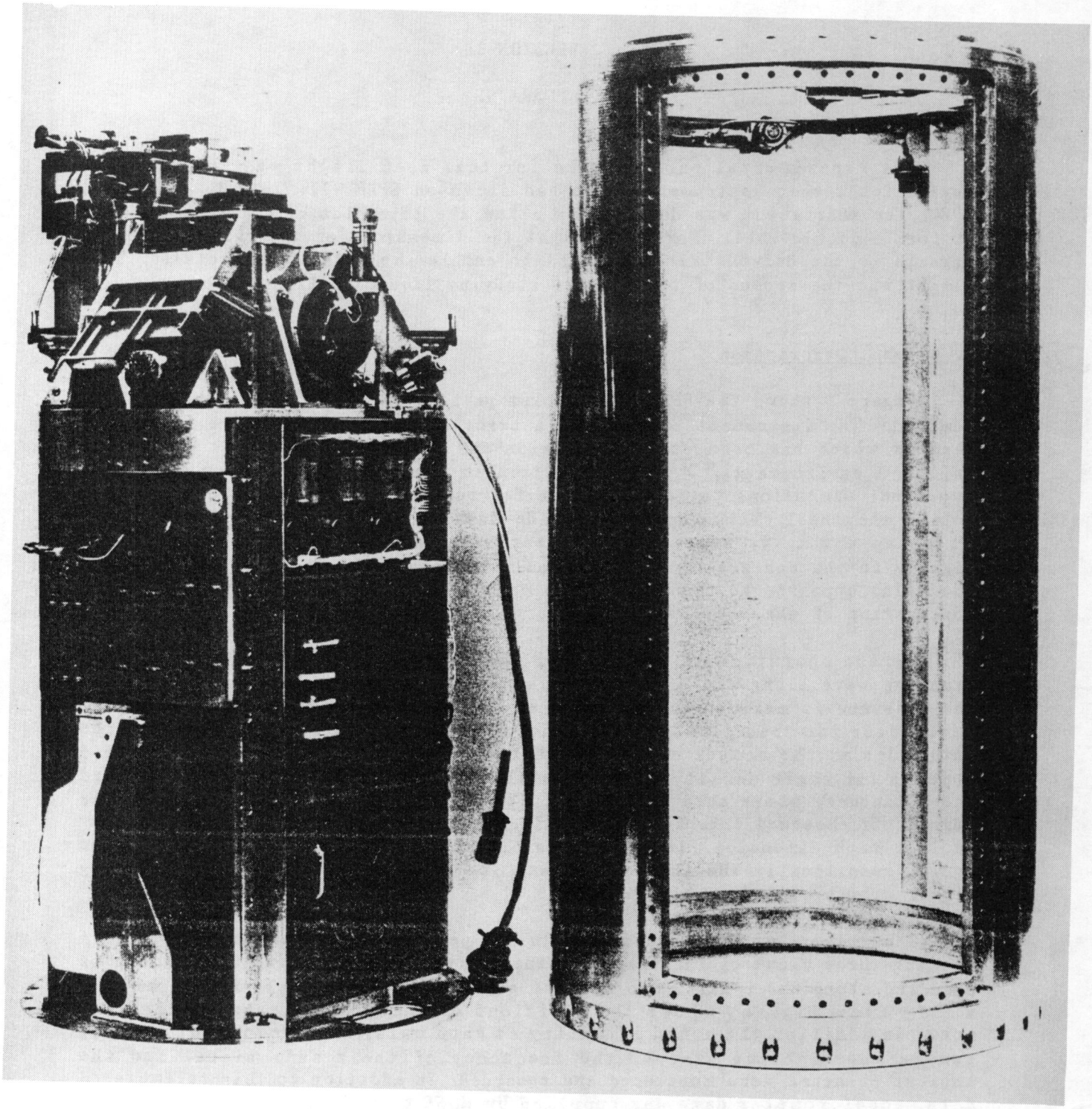

Figure 1. The SPAR Experiment 77-18 payload and its housing.

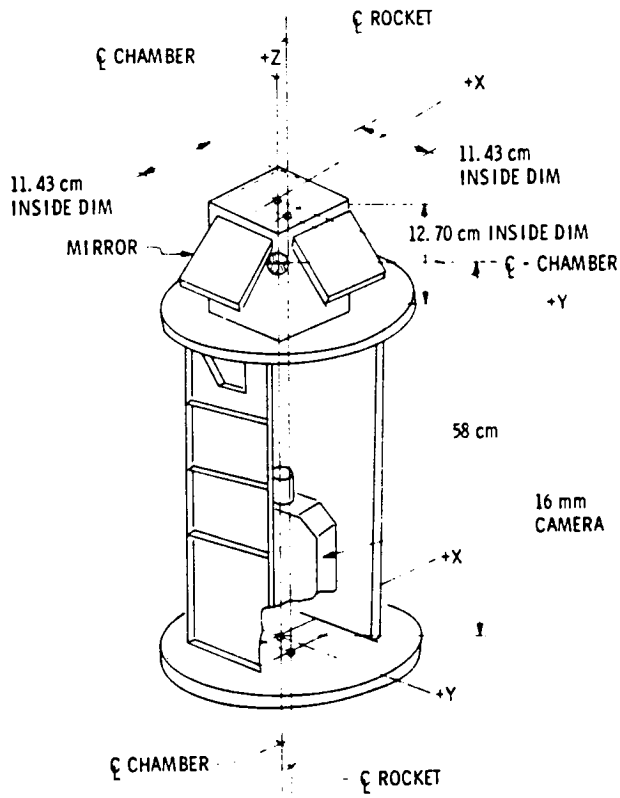

Figure 2. Sketch of the SPAR experiment payload showing the relation of the acoustic chamber, camera and mirrors.

B. Sequence of Operations

This section gives the operating characteristics of the acoustic chamber required to deploy a shell as well as oscillating, rotating, and expanding it adiabatically.

(1) Deployment and Initial Positioning The liquid used in this experiment was distilled water to which a small quantity of red dye had been added to provide optimum contrast in the cine film. The water had been left under vacuum for 24 hours to minimize the dissolved air in it. The surface tension of the dyed water sample was measured before the flight and was found to be 71.0 ± 2.0 dynes/cm.

Before the liquid was injected into the chamber the acoustic drivers were turned on and allowed to warm up. The water was deployed into the center of the chamber through both syringes. The 5.77 cc of water was deployed in 15 sec. Five seconds after the end of the water injection, 4.21 cc of air was injected over 15 seconds through lines that were concentric within the water

syringes. The slow injection of the air was critical to minimize unwanted flows within the shell and to generate a single large bubble. To increase the odds of a successful deployment the outside of the injectors were coated with Fluorad FC-721, an antiwetting agent produced by 3M, to inhibit the flow of liquid away from the tips of the probes. This was performed immediately before the payload was sealed at WSTR.

Because two of the dimensions of the chamber were identical - a condition required by the rotation sequence of the experiment - the signals used to center the drop along those axes had to be modified. The interference resulting from signals of the same frequency would greatly distort the acoustic potential well causing the shell to be distorted or even shattered. To prevent these undesirable results caused by the interference, the signals were alternately turned on and off at a relatively low frequency and at a correspondingly higher intensity to provide the centering force used to position the shell in the center of the chamber. This technique has been called complementary modulation. Some of the pertinent mathematical expressions are presented and discussed in Section 4.

(2) Rotation The desirable result from the interference caused by driving two of the signals at the same frequency is the ability to generate a torque on the shell about the z-axis. The centripetal forces on the bubble created by any rotation insure that the bubble boundary and the outer boundary will become concentric - at least when viewed along the axis of rotation. The interference effects between two signals provide a net torque when the relative phase between the dynamical variables of the two signals is sustained; this requires that the frequencies be the same. For a phase difference of 90 degrees the torque will be maximum. The torque is applied for 15 seconds and an equal period is provided for studying its spin down.

(3) Forced Oscillations With the bubble centered in the x-y plane by the rotation, the acoustic signal in the z direction was amplitude modulated at a frequency which was swept through four of the shell's calculated resonances. The oscillation of shells in response to a force applied near one of their resonances has been observed to center compound drops in laboratory experiments performed using a neutral buoyancy tank.

(4) Adiabatic Expansion The chamber was connected through two valves to an overboard vent. The first valve was opened at 293 seconds and closed at 323 seconds while the second system was used between 327 and 366 seconds. This chamber depressurization provided controlled expansion of the liquid bubble. The volume of the shell system was expected to increase by a factor of 250%.

C. Instrument Calibration

(1) Acoustic Calibration The determination of the acoustic intensity inside the chamber is difficult to accomplish without a calibrated microphone in the chamber. Because the primary interest was in the balancing of the positioning forces produced by the acoustic standing waves along the three directions, the amplitude of the signals to the acoustic drivers were cal-

ibrated by measuring the acoustic positioning force itself in each of the directions. This force measurement was made by suspending a low density (styrofoam) sphere (1.25 cm in radius and weighing 0.229 g) 3.175 cm from the center of the chamber on a thin string 5.08 cm long (see Figure 3). The signal to each speaker was adjusted so that the acoustic force deflected the sphere 0.115 in. (0.292 cm) toward the center of the chamber. This corresponded to a force of 12.9 dynes.

The signal levels to the speakers were preset so that the acoustic centering force would be 25.0 dynes during this flight. During the rotation sequence the signal levels to the x and y drivers were reduced so that the centering forces would be the same as those during the periods of complementary modulation.

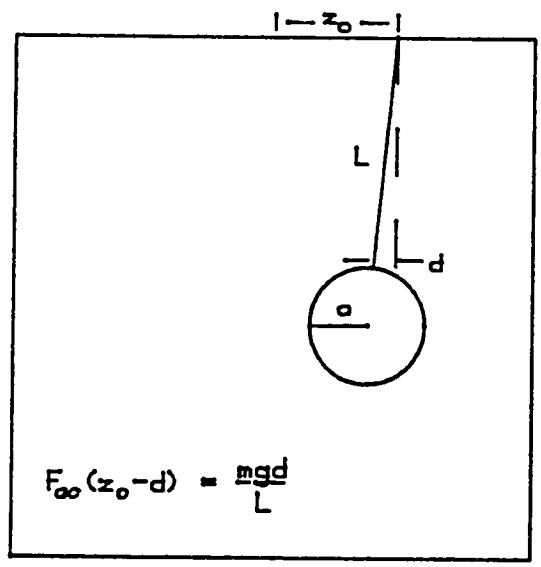

Figure 3. Arrangement used to balance the acoustic forces during calibration.

(2) Liquid and Gas Volumetric Calibration The liquid and gas deployment systems were tested before the flight by taking repeated volumetric measurements of the deployed liquid and gas. There was a variability of several percent in these measurements caused by backlash in the gears that drove the syringe system. Typical measured volumes were 5.77 $\pm$ 0.1 cc water and 4.21 $\pm$ 0.1 cc air.

(3) Sequence and Time Line Calibration The control program for this experiment had been run through the flight sequence over 100 times in preflight tests. No deviation from the programmed sequence was observed in

these tests.

(4) Cine Camera and Lighting Calibration Camera, lighting and film tests were run before the flight. A liquid drop was simulated, placed in the chamber and photographed with the flight camera to test light levels and camera alignment. In addition, twenty reference points (in the form of 1/4 in. bull's eyes) were carefully located on the paper surface covering the walls opposite the windows to aid in the data analysis of the cine record. A typical frame from the cine film is shown in Figure 1 of Section 5. The quality of the images was confirmed by the PI and CoI to be acceptable for data analysis.

D. On-Site Activity (Nov 18, 1980)

(1) Pre-flight Preparation Pre-launch testing of the 77-18/2 instrument flown on SPAR VIII indicated all systems were functioning and ready for flight. The day before the probes had been cleaned, the anti-wetting solution applied and the injectors had been positioned in the payload. The dyed water was transferred to the experiment's reservoirs.

For this flight it was decided to not use the stabilization system, i.e. not fire the small control jets, and hope that the rocket did not tumble or rotate too fast. This was decided on the basis of experience from previous flights.

(2) Telemetry Analysis Initial study of the telemetry data from the experiment indicated that the experiment functioned according to the pre-launch timeline that had been programmed into the instrument. All subsystems on the instrument operated as commanded by the programs.

CHAPTER III

SECTION 4

THEORETICAL BACKGROUND

This section contains a review of the theoretical considerations used in the design of this experiment as well as the models used in the analysis of the data. Acoustic positioning in one dimension is described mathematically. The interference effects generated by the acoustic field in a chamber with two equal dimensions are described and complementary modulation, the method used to minimize the undesirable interference, is presented. The results of a theoretical model of compound drop behavior are used to predict the natural oscillation frequencies and estimates of the damping coefficients for the liquid shell produced in this experiment. Short descriptions of the acoustic torque and a review of theory of rotating liquids are presented. Several comments are included on stimulated oscillation and the adiabatic expansion of a liquid shell.

A. Acoustic Positioning

The use of acoustic standing waves in a rectangular resonance chamber to position and manipulate samples is an established technique.[1-3,7-11] Experimental measurements have been made on the centering force for various configurations of the resonant chamber. Parallel theoretical descriptions have been developed which characterize the force fields and the underlying processes involved.[14,15,16] A short review of the theory of acoustic levitation is presented in this section.

The frequency of the sound used for positioning is picked so that the chamber becomes a resonator which stores the acoustic energy injected by the loudspeaker driver(s). To generate the constructive interference inside a rectangular chamber it is necessary that the sound from each of the drivers be in phase at any position within the chamber with all previous waves from that driver which have been reflected: the time it takes for the wave to cross the chamber and return to the wall should be the period of the wave: $T = 2L_z/c$. Or its frequency is $\omega = 2\pi c/2L_z$. In fact since the resonance condition requires only that the incident and any re-reflected waves be in phase, many frequencies are possible: $\omega_n = n\pi c/L_z$ where n can be any integer. For the fundemental mode, n=1, there will be a single plane located midway between the walls (corresponding to the antinode of the velocity potential) to which particles will be forced by the acoustic field.

The centering force generated by a standing wave in the z direction can be related to the various parameters of the system: the acoustic field can be described by either the acoustic pressure, p, or the particle velocity, u; the atmosphere by two of the three parameters - density, ρ, the speed of sound, c, or the temperature of the gas, T; and the geometry of the chamber is completely defined by its length along the direction of propagation, which

will be L_z when the source of the sound is the driver located on the z axis.

The microscopic parameters of the acoustic field, the pressure and the particle velocity, can be expressed as simple functions of a velocity potential, q: $u_i = \partial q/\partial x_i$ and $p_i = -\rho \partial q_i/\partial t$. Because the sound is reflected the acoustic fields are standing waves in which the nodes and antinodes of the pressure and velocity waves are stationary. The velocity potential of a one-dimensional standing wave in an empty rectangular chamber and the corresponding pressure and component of the particle velocity are

$$q(\underset{\sim}{r},t) = (p_{z0}/i\omega_z\rho)\cos(k_z z)e^{i\omega_z t} \tag{1a}$$

$$p(\underset{\sim}{r},t) = p_{z0}\sin(k_z z)\sin(\omega_z t) \tag{1b}$$

$$\text{and } u_z(\underset{\sim}{r},t) = -(p_{z0}/\rho c)\cos(k_z z)\cos(\omega_z t) \tag{1c}$$

where p_{z0} is the amplitude of the acoustic pressure at the wall, k is the wave number defined by $k_z = \omega_z/c$, and z=0 at the center of the chamber.

The quality of the chamber as a resonator is embodied in Q_n, the quality factor for each of the modes,

$$Q_n = \frac{f_n}{\Delta f_n} = \frac{nc/L_z}{\Delta f_n}$$

where Δf_n is the full width at half maximum of the resonance curve (i.e. the acoustic intensity versus frequency curve). It reflects the precision of the chamber's construction: the parallelness of its walls, the size of any disruptions in the walls, and the success of the coupling and transmission of sound from the drivers to the chamber. Typical values for SPAR-size chambers range from 25 to 75. The energy injected into the acoustic chamber when at the correct frequency for resonance, f_n, will persist for 25 to 75 periods of oscillation. As a result a finite time is required both for the build-up and dissipation of the acoustic energy - times on the order of Q/f_n.

Calculation of the acoustic forces on a liquid drop or shell is simplified by the fact that there is a large impedance mismatch between the liquid and the air and complicated by the fact that the surface of the drop is neither rigid nor static. The characteristic impedance of the liquid, $\rho_s c_s$, is very much greater than that of the gas, ρc: $\rho_s c_s/\rho c \sim 10^5$ cgs/40 cgs $\sim 10^3$ where ρ_s and ρ are the densities of the liquid and gas, respectively, and c_s and c are the respective sound velocities. Because of this mismatch, the acoustic power transmitted into the drop is three orders of magnitude smaller than that in the gas and can be neglected. Because the mathematics of determining the forces of a deformed sphere are complex, most calculations have been for rigid spheres or for shapes which have been slightly perturbed from spherical.

The acoustic radiation pressure is the change in the ambient pressure due to the presence of the acoustic wave. It results from considering nonlinear effects due to the distortion of real acoustic waves and is defined by

$$\langle \Delta P \rangle = \overline{(p^2/2\rho c^2)} - (1/2)\rho \overline{\underset{\sim}{u} \cdot \underset{\sim}{u}} \tag{2}$$

The bars indicate the averages over time of the dynamic variables, p^2 and u^2. Thus from time-varying acoustic quantities a time-invariant pressure is obtained but only when the former are large enough so that their behavior cannot be described by linear equations of motion. When the standing wave expressions of (1) are used, the radiation pressure can be written as

$$\langle \Delta P \rangle = - \frac{k_z^2 p_z^2}{2\rho c^2} \cos(2k_z z) \tag{3}$$

where p_z is the rms value of the acoustic pressure. This change in the static pressure has been verified experimentally to behave sinusoidally in space and to be proportional to the intensity.[15] The centering force can be found by integrating this time-invariant pressure over the surface of the object which is to be positioned (assuming for the present that the presence of the object does not affect the the acoustic field):

$$\underset{\sim}{F} = - \iint \langle \Delta P \rangle \, \underset{\sim}{n} \, dS \tag{4}$$

where $\underset{\sim}{n}=(\sin\theta\cos\phi, \sin\theta\sin\phi, \cos\theta)$ is an outward-facing vector normal to the surface at the point (a,θ,ϕ), and $dS = a^2 \sin\theta d\theta d\phi$ is an element of area on S, the surface of the sphere. The force resulting from the radiation pressure of Equation 3 on a sphere of radius a and density ρ_s is

$$\underset{\sim}{F}(z) = -\hat{e}_z \frac{2\pi}{3\rho c^2} p_z^2 \, k_z \, a^3 \sin(2k_z z) \tag{5}$$

This force is maximum at the planes described by $z = \pi/4k_z = \pm L_z/4$ and is zero at $z = 0$, $L_z/2$ (the center of the chamber and the two walls). Because the force is positive when $z < 0$, the object will feel a force towards the right (or center). Similarly on the right the force will be negative and toward the center (or left). In a zero-gravity environment the object will be positioned with its center at $z = 0$.

An object positioned by the acoustic field also affects the field: to correct for the effects of the scattering of the sound by a finite sample the force in Equation 5 should be increased by a factor of 1.25. To more accurately describe the scattering from a finite sphere, the function $f(2ka)$ which is due to King must be incorporated.[13]

$$F_z = \frac{5\pi}{6\rho c^2} p_z^2 \, k_z \, a^3 \, f(2k_z a) \sin(2k_z z) \tag{6}$$

$$= F_{max} \sin(2k_z z)$$

where $f(\alpha) \equiv 3\alpha^{-3}\{\sin\alpha - \alpha\cos\alpha\}$

$$\sim 1 - \alpha^2/8.$$

If consideration is limited to the case in which the object stays close to the center, i.e. $(2k_z z) << 1$, Eq. 6 becomes

$$F_z \sim \frac{5\pi\, p_z^{\,2}\, k_z^{\,2}\, a^3\, f(2k_z a)}{3\rho c^2}\, z \qquad (7)$$

$$\sim (\text{constant})\ z$$

which has the same form as the restoring force for a simple harmonic oscillator. If the argument of the sine function, $2k_z z$, is not too large, the object in the acoustic well will move with a well-defined frequency when displaced from its equilibrium position

$$\Omega_z^2 = \frac{5k^2{}_z p^2{}_z}{4\rho_s \rho c^2}\, f(2k_z a) \qquad (8)$$

in which ρ_s is the density of the sample. Using this formula and the frequency of the oscillations of the drop about its equilibrium position in the acoustic resonance chamber the sound pressure level can be determined. For the SPAR experiments the frequencies of oscillation in the potential well of the simple water drops have been roughly 0.15 Hz. Because the density of the shell is less, its frequency of oscillation in the potential well will be higher: roughly 0.18 Hz.

If there is an acceleration acting on the entire system, the system will move and the sphere will become displaced from its equilibrium position because the object is loosely coupled to the chamber and the outside world by the small acoustic forces. If the perturbing acceleration, a_{pert}, is in the z direction and constant in time the equilibrium position will be displaced by $\Delta z_{pert} = -(m\, a_{pert})/\{2k\, F_{max}\}$ from its initial location. When the object's response as a function of time is considered, account must be taken of the slight resistance to the sphere's motion through the air for it is the force which determines how quickly the oscillations die out. This resistance is characterized by the drag coefficient, δ.

When an acceleration is applied to the system the object will respond by moving toward the new equilibrium position, pass through it, and oscillate about it for times on the order of $1/\delta$, if the perturbing acceleration remains constant. When the sample is displaced the time required to reach the equilibrium value is $(4\Omega_z/2\pi)^{-1}$ where Ω_z is the frequency at which the object will continue to oscillate as it passes through the new equilibrium value. Because the duration of the non-zero accelerations in experimental situations will generally be much smaller than $1/\delta$ (~100sec.), the object will have insufficient time to reach the equilibrium position initially much less to oscillate about the new point. Whenever the acceleration changes, the positioned object will move towards the new equilibrium point. The center of the oscillations will be the center of the chamber unless the average acceleration over a sufficient period of time is not zero. Oscillation in the potential well results only when the perturbation has a certain size and duration.

To determine the minimum acoustic pressure required for stable positioning for a given sample, the acoustic force (Eq. 7) is equated to the product of the object's mass, the maximum anticipated acceleration and a safety factor, S. The result can be expressed as the amplitude of the acoustic pressure or as a sound pressure level (in decibels relative to the reference pressure, $p_o \sim 0.0002$ dynes/cm^2) which describes the intensity of the

sound:

$$SPL = 20 \log(p_{rms}/p_o)$$

$$= A + R + \gamma \tag{9}$$

where $A = 10 \log\{S(a_{max}/1\mu g)\}$

$$R = 10 \log\left(\frac{8}{5} \frac{\rho c^2 (ws)}{p_o^2} \frac{\rho_s}{k_i \int(2k_i a)} 1\mu g\right)$$

and $\gamma = \begin{cases} 0.0\text{dB at WSMR} \\ 1.9\text{dB at JPL} \end{cases}$

A is composed of the maximum anticipated acceleration, a_{max}, and a safety factor S to guarantee that F_{max} will be sufficient to keep accelerations less than a_{max}. R contains information about the positioned sample - its density and size and aboust the size of the chamber, while γ compensates for the difference in ambient pressures between JPL (near sea level, $\rho c^2 \sim 1.4 \times 10^6$ dynes/cm^2) and the White Sands Missile Range (nearly one mile higher, $\rho c^2 \sim 1.12 \times 10^6$ dynes/cm^2). For this experiment the acoustic forces were balanced so that the sound pressure level would be 145dB for each axis and Sa_{max} would be 1300μg.

Two-Dimensional Acoustic Pressure Well

When standing waves are generated along two nonparallel axes the centering in of the two directions is similar to that described above and the combined result of the two forces is that the equilibrium position is a line - the intersection of the two one-dimensional nodal planes. The two signals and the resulting forces are independent to the extent that they do not interfere. In order for the waves to interfere the frequencies of the signals must be very close. Consider the general velocity potential describing standing waves along the x and y axes (for which L_x anf L_y may or may not be the same)

$$\varphi = \varphi_x \sin(k_x x) e^{i\omega_x t} + \varphi_y \sin(k_y y) e^{i(\omega_y t + \xi)} \tag{9}$$

where $p = -\rho \partial \varphi / \partial t$ and $u_i = \partial \varphi / \partial x_i$ and ξ is the relative phase between the the x and y signals at t=0. The resulting pressure before time-averaging is

$$\Delta P = \frac{1}{2\rho c^2} \{ p_x^2(1-\cos^2 k_x x - \cos^2 \omega_x t)$$

$$+ p_y^2(1-\cos^2 k_y y - \cos^2 \omega_y t) \tag{10}$$

$$+ p_x p_y (\sin k_x x \sin k_y y) [\cos\xi(\cos\omega_- t - \cos\omega_+ t)$$

$$+ \sin\xi(\sin\omega_+ t + \sin\omega_- t)] \}$$

where $\omega_\pm \equiv \omega_x \pm \omega_y$. The largest distortion occurs at the locations in the chamber where the force is maximum (at a distance $d = L_x/4$ or $d = L_y/4$ from

the center).

When ω_x and ω_y are sufficiently seperated, the effects of interference can be neglected and the resulting radiation pressure is the sum of two single-axis pressures. In this experiment the x and y dimensions of the chamber are different than that in the z direction: 11.43cm and 12.70cm, respectively. The seperation is sufficient that when the amplitudes of each component (p_x, p_y, p_z) are chosen correctly the isobars are circular near the center of the chamber providing balanced and symmetric forces near the center. The time-average of Equation 10 is

$$\langle \Delta P \rangle = - \frac{1}{4\rho c^2} \{ p_x^2 \cos 2k_x x + p_y^2 \cos 2k_y y \}. \tag{11}$$

When the two dimensions are equal the interference term becomes important and the resulting acoustic radiation pressure is

$$\langle \Delta P \rangle = - \frac{1}{2\rho c^2} \{ p_x^2 \cos 2k_x x + p_y^2 \cos 2k_y y + 2p_x p_y \cos\xi \sin k_x x \sin k_y y \} \tag{12}$$

The interference will distort the lines of constant pressure from circularity near the center of the chamber - except when ξ is near $\pm\pi/2$. The x and y dimensions of the chamber are the same: 11.43cm. Unless the signals are modified or have a 90^o seperation between their phase, the radiation pressure, the force field and also the shell will be distorted.

When $\xi = \pm\pi/2$, the fact that the two waves interfere does not affect the positioning force and it is the same as the that given in Equation 11 with $k = k_x = k_y$. A fact which has not been mentioned in this section is that when the relative phase is neither 0^o nor 180^o, there is a torque about a line through the center and perpendicular to the square cross-section. This torque is maximum for $\xi = \pm\pi/2$. So although the centering force is not distorted for this phase separation, the object will feel a torque. It is this condition which has been used to generate rotation in both laboratory and SPAR experiments.

Complementary Modulation

To take advantage of the acoustic torque capability provided by a chamber with two equal dimensions required some signal modification in order to provide a balanced acoustic centering force when the torque was not desired. The technique which has been used in both SPAR and KC-135 experimennts is complementary modulation.

In this mode the x and y signals are alternately switched on and off at the frequency, f_{cm} (Figure 1a illustrates the waveforms). f_{cm} was chosen to lie well above the highest frequency to which the liquid might respond and well below the frequency used for the centering force: $f_{4,-} \sim 6$ Hz $<<$ $f_{cm} \sim$ 30 Hz $<<$ $f \sim 1000$ Hz, where $f = f_x = f_y$. A finite time is required both for the buildup and decay of the acoustic intensity in the chamber every time the speakers are switched on or off: $t \sim Q/f$. The resulting amplitude of the

acoustic pressure will look more like those shown in Figure 1b than those of 1a. The only times the signals are both present and able to interfere are just after switching and its effects diminish as the decreasing amplitude vanishes. In this manner the signals are not allowed to interfere with the drop's behavior.

To lowest order the appropriate velocity potential for complementary modulation can be written

$$\varphi(x,y) = \frac{1}{2\rho\omega} \{ p_x \sin kx \sin\omega t \ (1+\sin\omega_{cm}t) + p_y \sin ky \sin\omega t \ (1-\sin\omega_{cm}t)\}. \tag{13}$$

When the time-averaging of the dynamic quantities is taken over times short compared to the complementary modulation switching time, the acoustic radiation pressure is

$$\langle \Delta P \rangle = - \frac{1}{8\rho c^2} \{p_x^2 \cos 2kx \ (1+\sin\omega_{cm}t)^2 + p_y^2 \cos 2ky \ (1-\sin\omega_{cm}t)^2\} \tag{14a}$$

When the time scale used is on the order of a period of the drop's oscillation, the radiation pressure is

$$\langle \Delta P \rangle = - \frac{3}{16\rho c^2} \{p_x^2 \cos 2kx + p_y^2 \cos 2ky \} \tag{14b}$$

Equation 14a shows that the field is oscillating at Ω_{cm} while 14b demonstrates that this oscillation of the centering force will not perturb the drop.

The on/off character of the complementary modulation means that both the radiation pressure and the effective force for each axis are reduced because each signal is at full strength for only half of the time. They are reduced by a factor of 3/4 and the corresponding frequency of oscillation in the well will be reduced by a factor of 0.87.

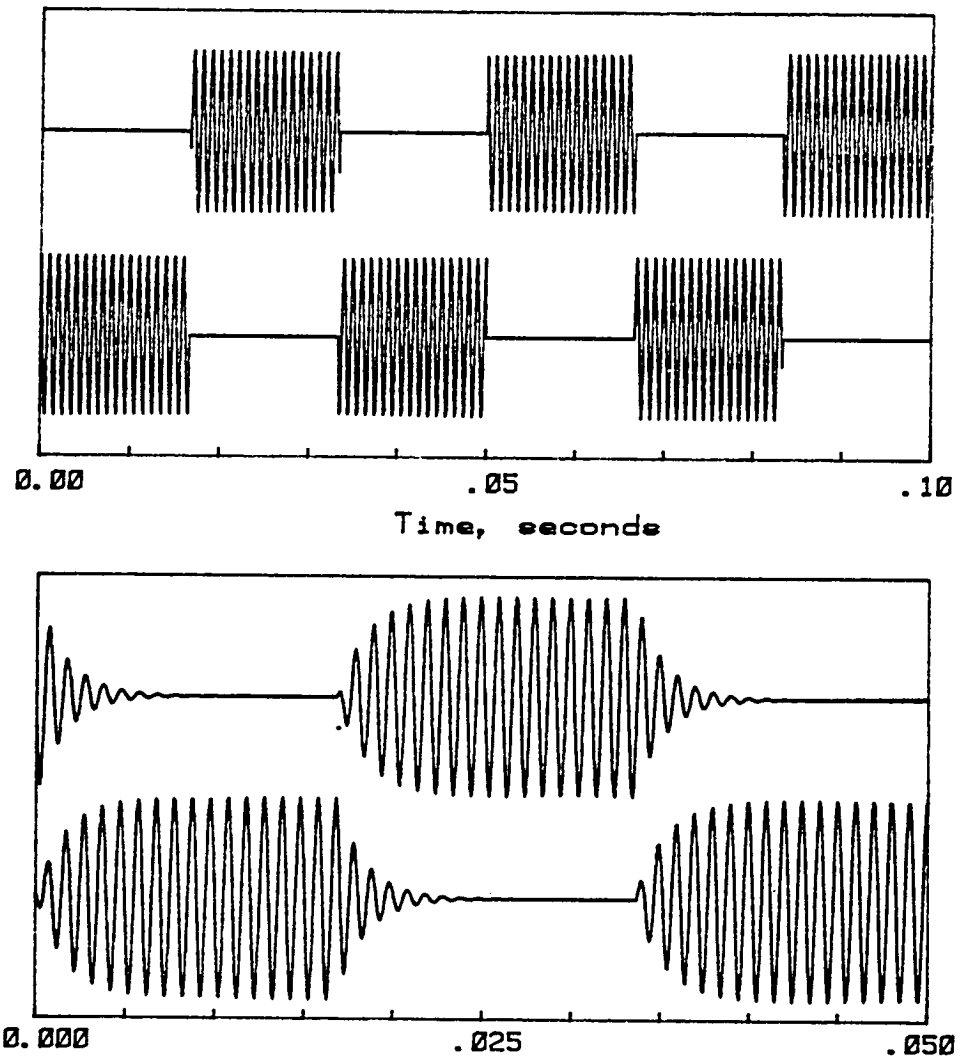

Figure 1. (a) The signals sent to the x and y drivers during complementary modulation. The switching frequency is roughly 30 Hz and the positioning frequency is 1300 Hz.
(b) The x and y signals as seen in the throats of the respective loudspeakers. The finite time required for buildup and decay is related to Q/f.

B. Natural Oscillations

A theoretical treatment of the normal modes of oscillation for compound drops has been formulated by Saffren, Elleman and Rhim.[17,18] It includes observations of compound drops in a neutral buoyancy system which corroborate the basic features of the theory. Assuming that the boundaries of the resting compound drop are concentric and the fluids are inviscid and incompressible, the theory predicts shape oscillations similar to those for a simple drop. They can be described by a 'principal' mode parameter, n, where n=2 corresponds to oblate/prolate oscillations and n=3 to a series of triangular shapes (see Figure 1). In addition there are two sub-modes corresponding to each principal mode for compound drops: for the higher frequency branch, the + mode, the inner and outer surfaces of the shell oscillate in phase, whereas for the - mode, the two surfaces move with a relative phase of 180° and at a lower oscillation frequency (see Figure 2). The existence of these modes has been demonstrated in a neutral buoyancy system and the frequencies and amplitudes of the oscillations have been found to agree with the predictions of the theory.[17,18] All of the shapes obtained from the normal mode solution are symmetric about a vertical line passing through their centers (which for the plots in Figures 1 and 2 would be in the plane of the paper).

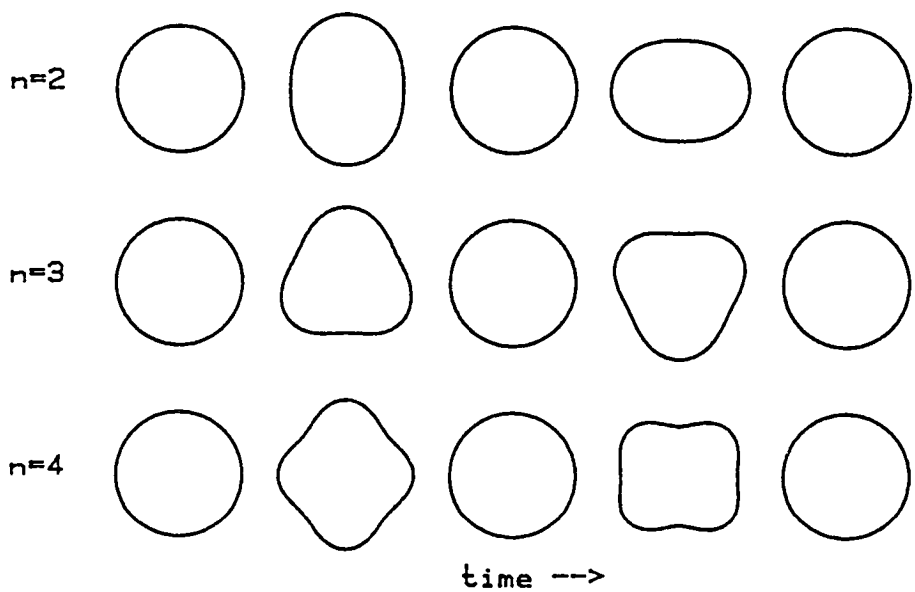

Figure 1. Normal mode oscillation shapes for a simple drop. The increment of time between shapes is $1/(4f_n)$.

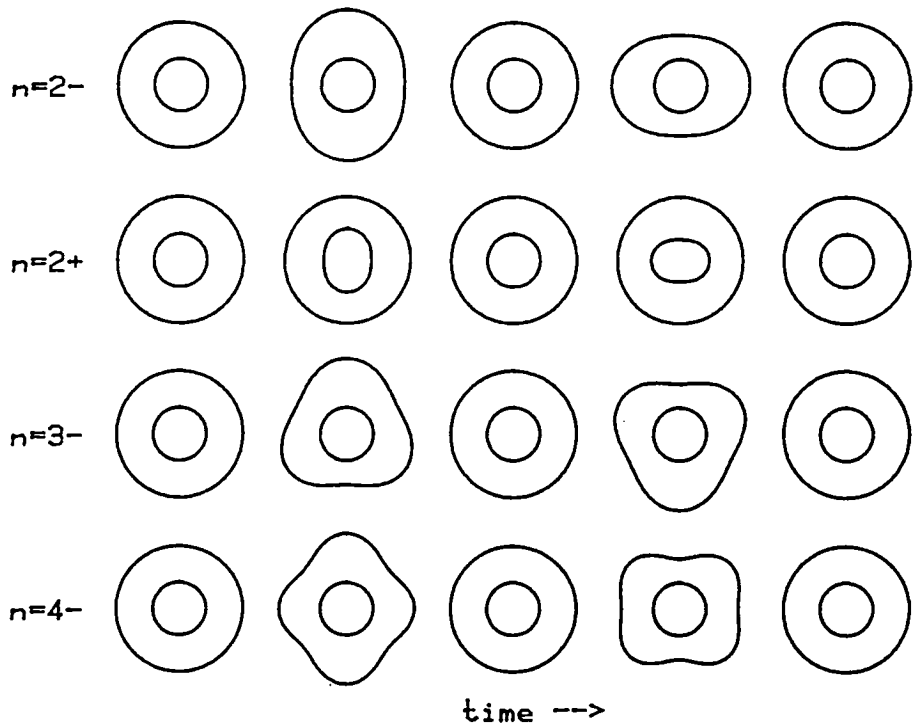

Figure 2. Normal mode oscillation shapes for a compound drop. The time increment between adjacent shapes is $1/(4f_n)$.

The two sub-modes are also called the sloshing mode and the bubble mode because of the characteristics which the compound drops displayed in the neutral buoyancy experiments. In the - (or sloshing) sub-mode the fluid seems to rush from the poles to the equator and then back again and in the bubble (or +) sub-mode the shape of the outer surface mirrors the oscillations of the bubble.

The theory describes the boundaries by a pair of equations of the form

$$R(\theta,\varphi,t) = \bar{R} + \Delta R(\theta,\varphi,t) \tag{1}$$

where R is the radius of the inner or outer boundary at rest and ΔR represents the deviation from sphericity. A normal mode solution for the boundary oscillations is used

$$R(\theta,\varphi,t) = \bar{R} + \sum_{n,m} \delta R(n)\ Y_{nm}(\theta,\varphi)\ e^{i\omega_n t} \tag{2}$$

in which the boundary is represented by the superposition of spherical har-

monics, Y_{nm}, which oscillate with an amplitude $\delta R(n)$ at the frequency ω_n. The frequencies of the natural oscillations are predicted to be

$$\omega_{n,\pm}^2 = \frac{-\beta \pm \sqrt{\beta^2-4\alpha\gamma}}{2\alpha} \tag{3}$$

$$\text{where } \alpha = n\{\bar{\rho}_i\bar{\rho}_o - \Delta\rho_i\Delta\rho_o\varepsilon^{-2n-1}\}/\rho^2, \tag{4a}$$

$$\beta = -\omega_n^2\varepsilon^3\{(\bar{\rho}_o+\bar{\rho}_i\varepsilon^{-3}+\Delta\rho_o\varepsilon^{-2n-1}+\Delta\rho_i\varepsilon^{-2n-4})\}/\rho\sigma, \tag{4b}$$

$$\gamma = \omega_n^4\,\varepsilon^3\,\{1-\varepsilon^{-2n-1}\}/\sigma^2, \tag{4c}$$

$$\text{and } \omega_n^2 = n(n-1)(n+2)\sigma_o/(\rho\bar{R}_o^3). \tag{5}$$

ω_n are the frequencies of the normal modes of oscillation for a simple drop with the same radius as the shell, R_o. ε is the aspect ratio, the ratio of the equilibrium outer and inner radii of the shell, $\varepsilon = R_o/R_i$. $\sigma \equiv \sqrt{\sigma_o/\sigma_i}$ in which σ_i and σ_o are the surface tensions across the inner and outer surfaces of the shell. ρ, ρ_i and ρ_o are the densities of the shell, the inner and outer (or core and host) fluids with $\Delta\rho_i \equiv (\rho-\rho_i)/n$, $\Delta\rho_o \equiv (\rho-\rho_o)/(n+1)$, $\bar{\rho}_i \equiv \rho_i/n + \rho/(n+1)$, and $\bar{\rho}_o \equiv \rho_o/(n+1) + \rho/n$.

In this experiment the inner and outer fluids were air and the shell was dyed water. It has been assumed that the surface tension across the inner and outer surfaces was the same. For an air/water/air system the parameters of Equations 4 can be rewritten as

$$\alpha = -\,n\,\varepsilon^{-3}\,(1-\varepsilon^{-2n-1}), \tag{6a}$$

$$\beta = \omega_n^2\,\{(n+1)(1+\varepsilon^{-2n-4}) + n(\varepsilon^{-3}+\varepsilon^{-2n-1})\} \tag{6b}$$

$$\text{and } \gamma = -\,(n+1)\,\omega_n^4\,\{1-\varepsilon^{-2n-1}\}. \tag{6c}$$

Using these equations a set of curves describing the natural frequencies of oscillation for the various modes was constructed. Figure 3 contains a set of universal curves for a shell (i.e. an air/liquid/air compound drop) of constant total volume which give normalized frequencies for each of the two submodes for n = 2, 3, and 4 as functions of the relative bubble size. For the programmed volumes of 5.77 cm^3 water and 4.21 cm^3 air (for a relative bubble volume of 0.42 or ε = 2.37) the frequencies corresponding to the sloshing sub-mode are 1.80 Hz (n=2-), 3.90 Hz (n=3-) and 6.51 Hz (n=4-) while the lowest frequency of the bubble mode family would be 6.32 Hz (n=2+). The programmed volume ratio is indicated by the arrow and the scale on the right side of the graph is the frequency in Hertz for a system with a total volume of 9.98 cm^3. To find the frequencies (in Hertz) of the normal modes for a liquid shell of any size determine N for the desired mode and sub-mode from the left scale of Figure 3 and use the relation

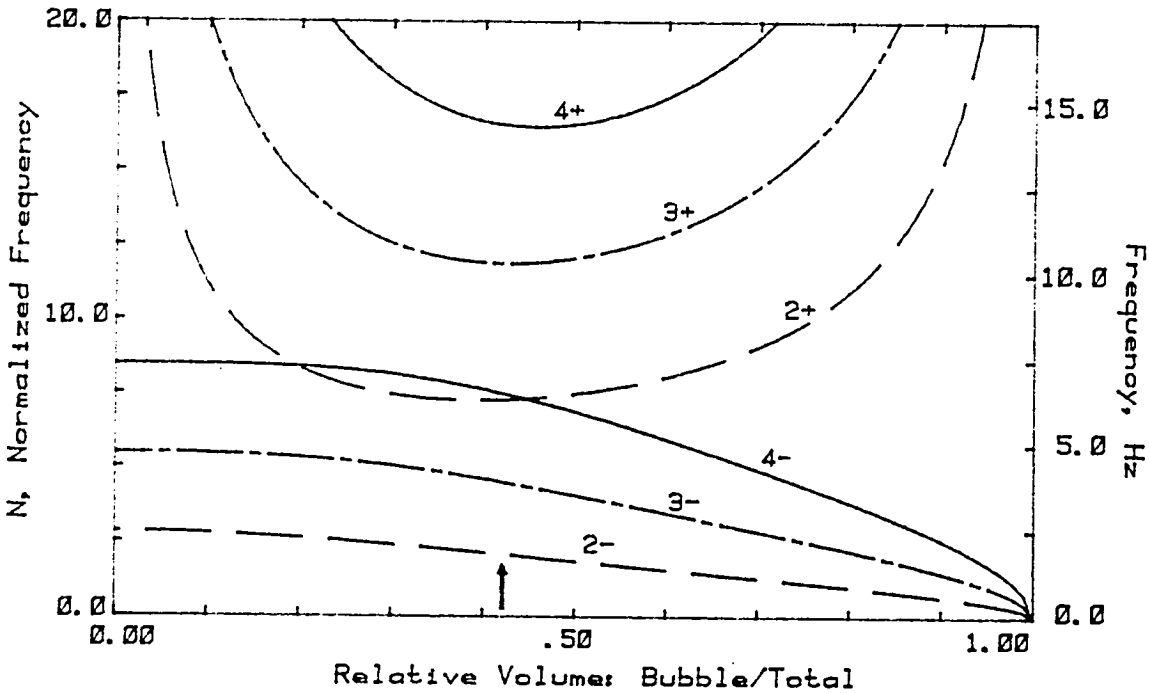

Figure 3. Theoretical curves of the normalized frequencies of oscillation for a liquid shell in air as a function of the relative volume of the bubble for constant total volume.[18] The frequency scale on the right is for a water shell with $V_{tot} = 9.98$.

$$f\ (\mathrm{Hz}) = \frac{N}{2\pi}\sqrt{\frac{\sigma_o}{\rho R_o^3}}. \tag{7}$$

The theoretical treatment does not give the amplitude of the inner and outer boundaries' displacements, $\delta R_i(n)$ and $\delta R_o(n)$, but their ratio

$$\left(\frac{\delta R_o}{\delta R_i}\right)_{\pm} = \frac{1}{d \pm \sqrt{d^2+1}} \tag{8a}$$

$$\text{where } d = \frac{(n+1)\ \varepsilon^{2n+4}}{2(2n+1)\sigma^2}\ G \tag{8b}$$

$$\text{and } G = \{1+\frac{n\varepsilon^{-4n-2}}{(n+1)}\}\{1-\sigma^2\varepsilon^{-6}\frac{n+(n+1)\varepsilon^{-4n-2}}{(n+1)+n\varepsilon^{-4n-2}}\} \tag{8c}$$

$$\approx 1 \text{ for } \varepsilon > 1.1\ .$$

The amplitudes of the displacements of the two submodes for the same principal mode number, n, are related by

$$\left(\frac{\delta R_o(n)}{\delta R_i(n)}\right)_+ = \frac{-1}{\sigma^2}\left(\frac{\delta R_i(n)}{\delta R_o(n)}\right)_- \tag{9}$$

The right side of Equation 9 will be positive because the two boundaries always move out of phase in the sloshing mode. For the expected shell the ratios of the outer to inner displacements are predicted to be -597. for n=(2-), 0.002 for n=(2+), -3205. for n=(3-), 0.0003 for n=(3+), -18726. for n=(4-), and 0.0005 for n=(4+). These numbers indicate that the motions of the two surfaces are relatively uncoupled according to the inviscid model. The shapes shown in Figure 2 reflect these ratios. Only when the shell becomes very thin ($\varepsilon \lesssim 1.1$) does the predicted coupling increase significantly.

The theoretical characterization of the damping processes within a compound drop (or a liquid shell) has not been performed. Assuming that the oscillations of the two surfaces are not coupled, the damping coefficients for the normal modes of a simple drop can be used as an estimate for the damping coefficient of the sloshing sub-mode for which the oscillations of the outer boundary have much greater amplitude,[19]

$$\beta_n = (n-1)(2n+1)\ \nu/\bar{R}_o^2, \tag{10}$$

where ν is the kinematic viscosity of the liquid. The damping coefficients for the expected shell are $\beta_2 \sim 0.028\ \text{sec}^{-1}$, $\beta_3 \sim 0.078\ \text{sec}^{-1}$ and $\beta_4 \sim 0.151\ \text{sec}^{-1}$. In an analogous manner using the formula for the damping coefficient for bubble oscillations inside an infinite viscous host,[20]

$$b_n = (n+1)(2n+1)\ \nu/\bar{R}_i^2, \tag{11}$$

which for the anticipated bubble size, gives $b_2 \sim 0.149\ \text{sec}^{-1}$, $b_3 \sim 0.279\ \text{sec}^{-1}$ and $b_4 \sim 0.448\ \text{sec}^{-1}$. These values indicate that the lowest sloshing modes should persist for roughly 40 seconds while the bubble mode oscillations will continue for times on the order of 6 seconds.

It is not clear how to combine Equations 10 and 11 to obtain meaningful estimates of the damping for each of the two sub-modes. The theoretical framework developed to obtain the frequencies of oscillation for compound drops is not appropriate to finding damping coefficients since the viscosity of the shell has been ignored. A phenomenological treatment of the damping in compound drops may be performed using oscillation experiments carried out in the neutral buoyancy tank.

C. Acoustic Torque and Rotation of Liquids

A brief theoretical description of the torque generated by the interference of two orthogonal acoustic waves of the same frequency is presented. A formula for the acoustic torque acting upon a rigid sphere is given as well as a simple model for its spin-up and spin-down. A summary of the theoretical work on the rotation of simple drops is also presented.

Nearly one hundred years ago Lord Rayleigh reported that an acoustic torque was produced on a disk when the direction in which the sound was propagating differed from the axis of symmetry.[21] It was the result of an imbalance in the Bernoulli pressures on the two faces. The acoustic torque used in this and other SPAR experiments as well as laboratory investigations is fundamentally different from that involved in the Rayleigh disk.[22,23] Two more speakers are driven at the same frequency and the interference of the acoustic standing waves causes the air molecules to move along small elliptical paths. When the frequencies differ the axes of the ellipses preccess and the motions of the particles are not coherent. When the frequencies are the same the phase relation between the waves and the individual molecules remains constant and the axes of the ellipses are fixed in space. These microscopic motions are coupled to the macroscopic rotation of a large object in the field by viscosity. The magnitude of the torque is proportional to the product of the amplitudes of the acoustic pressure for the two signals and the surface area of the object and is greatest when the relative phase between the two signals is $\pm\pi/2$.[24]

Model of the Acoustic Torque. A mathematical model of this acoustic torque due to viscosity has been developed by Busse and Wang.[24] They study the effects upon an axisymmetric object of the motions of air molecules induced by a given acoustic pressure field. Formulae for the torques on disks, spheres and cylinders are derived for two orthogonal standing waves of the same frequency. This section provides an outline of the analysis which they performed.

To examine the torque produced acoustically upon a rigid axisymmetric object, they analysed the particle velocity, $\underset{\sim}{u}$, which results from the acoustic pressure

$$p(\underset{\sim}{r},t) = p_o(\underset{\sim}{r})e^{-i\omega t} \tag{1}$$

in which $p_o(\underset{\sim}{r})$ is chosen so that the boundary conditions

$$\underset{\sim}{n} \cdot \underset{\sim}{u} = 0 \quad \text{and} \quad \underset{\sim}{n} \times \underset{\sim}{u} = 0 \tag{2}$$

are met on the surface of the rigid body, S. n is the unit vector normal to the surface. The velocity field which satisfies Equations 2 at the surface is split into a viscous component and an inviscid one:

$$\underset{\sim}{u} = \underset{\sim}{u}_v + \underset{\sim}{u}_i. \tag{3}$$

Each component is determined by appropriate equations of motion and the total must satisfy Equations 2. The velocity field, $\underset{\sim}{u}_i$, is given by the linearized inviscid equation of motion

$$i\omega \underset{\sim}{u}_i = \nabla \frac{p_o}{\rho} \tag{4}$$

where ρ is the mean density of the homogeneous fluid outside the surface S.

u_v is constructed to be infinitesmal beyond a few lengths from the surface. The boundary layer in which the viscous solution is important has a thickness which is scaled by $L_v = \sqrt{2\nu_a/\omega}$. ν_a is the kinematic viscosity of the outside medium and ω is the frequency of the acoustic wave. This viscous length, L_v, is assumed to be small compared to the wavelength, $\lambda = 2\pi/k$, of the acoustic waves as well as the radius of curvature of S. $\underset{\sim}{u}_v$ must satisfy

$$\nabla \cdot \underset{\sim}{u}_v = 0 \tag{5a}$$

$$(\underset{\sim}{n}\cdot\nabla)^2 \underset{\sim}{u}_v = -i\omega \underset{\sim}{u}_v \tag{5b}$$

and decay exponentially away from S. The two problems are coupled through the requirement that the total field satisfy Equations 2.

Using Equation 4 to define $\underset{\sim}{u}_i$ as a function of the pressure field, a solution of (5) can be expressed as

$$\underset{\sim}{n} \times \underset{\sim}{u}_v = -\underset{\sim}{n} \times \nabla \left(\frac{p_o}{i\omega\rho} \right) \Bigg|_{\xi=0} \exp\{-\frac{(1-i)}{2}\xi\} \tag{6}$$

The boundary layer coordinate, ξ, is defined by

$$\xi = \underset{\sim}{n} \cdot (\underset{\sim}{r} - \underset{\sim}{r}_s)\sqrt{\omega/\nu_a} \tag{7}$$

where r_s denotes the position vector of a point at the surface S. While solution (7) satisfies the boundary condition, $\underset{\sim}{n} \times \underset{\sim}{u} = 0$, it does not satisfy the continuity equation, $\nabla \cdot \underset{\sim}{u}_v = 0$. Using Equations 6 and 5a, a higher order correction to $\underset{\sim}{u}_v$ is found to be

$$\underset{\sim}{n} \cdot \underset{\sim}{u}_v' = -(\underset{\sim}{n} \times \nabla)^2 \left(\frac{p_o}{\rho\omega k} \right) \Bigg|_{\xi=0} \left(\frac{1-i}{2} \right) \exp\{-(1-i)\xi\} \tag{8}$$

which decays towards the exterior. In order to satisfy the boundary condition, $\underset{\sim}{u} \cdot \underset{\sim}{n} = 0$, a perturbation of the inviscid velocity field, $\underset{\sim}{u}_i$, is required. That change is

$$\underset{\sim}{n}\cdot\underset{\sim}{u}_i' = (\underset{\sim}{n}\times\nabla)^2\left(\frac{p_o}{\rho\omega k}\right)\left(\frac{1-i}{2}\right)\Bigg|_{\xi=0} \tag{9}$$

A torque on the body can only be generated by viscous stresses exerted on the surface S acting over a sufficient length of time. A nonzero contribution to the time average of the velocity field can only be generated by the nonlinear terms of the equations of motion. Since the potential flow of the exterior, u_i, does not generate a time-independent component of the total velocity field, the mean flow must arise in the boundary layer, i.e., $\underset{\sim}{u}_v$. Using the unit vector a in the direction of the axis, the magnitude of the torque required to produce the velocity at the surface for which all the boundary conditions are satisfied is

$$T = \oiint dS\ \rho v\ \underset{\sim}{a}\times\underset{\sim}{r}\cdot(\underset{\sim}{n}\cdot\nabla\bar{\underset{\sim}{u}})\Big|_{\underset{\sim}{r}=\underset{\sim}{r}_s} \tag{10}$$

where $\bar{\underset{\sim}{u}}$ is the time average of $\underset{\sim}{u}$, the total velocity field,

$$\underset{\sim}{u} = \underset{\sim}{u}_i + \underset{\sim}{u}_i' + \underset{\sim}{u}_v + \underset{\sim}{u}_v' \tag{11}$$

Acoustic Torque on a Rigid Sphere. Restricting attention to the limit $|kr_s| \ll 1$, the pressure field generated by two standing waves of the same frequency propagating in orthogonal directions is

$$\begin{aligned} p_o(\underset{\sim}{r}) &= p_x \sin(kr\sin\theta\cos\phi)e^{-i\omega t} \\ &\quad + p_y \sin(kr\sin\theta\sin\phi)e^{-i\omega(t-t_o)} + p_{os} \\ &= 3[j_1(kr)+\delta_1 y_1(kr)]\{p_x \sin\theta\cos\phi e^{-i\omega t} \\ &\quad + p_y \sin\theta\sin\phi e^{-i\omega(t-t_o)}\} \end{aligned} \tag{12}$$

where r, θ, and ϕ are the spherical coordinates of a point in the pressure field, $j_1(kr)$ and $y_1(kr)$ are the spherical Bessel functions of order 1, δ_1 is a phase angle due to scattering effects, and ωt_o is the phase angle between the two signals. This pressure field gives rise to a torque about the polar axis whose magnitude is

$$\tau = \frac{3p_x p_y}{4\rho c^2} A L_v \sin(\omega t_o) \tag{13}$$

where A is the surface area of the sphere and $L_v = \sqrt{2\nu_a/\omega}$ is the thickness of the boundary layer. For the SPAR acoustic chamber, $L_v \sim 0.015$ cm. For a water shell with inner and outer radii of 1.00 and 1.34 cm and a phase shift of 90° between the x and y signals, the torque resulting from an acoustic pressure

of $p_x = p_y = 3\times10^3$ dynes/cm^2 is 1.971 dyne-cm.

Mathematical Model of Spin-down and Spin-up. The principal force which acts upon a rigid sphere rotating in air is the drag due to the air. In the absence of other forces, the angular velocity, Ω, and its rate of change, $\dot{\Omega}$, are related by

$$\dot{\Omega} = -\delta\Omega^{3/2} \tag{14}$$

where the drag coefficient, δ, is a function of the viscosity of the air in the chamber, ν_a, the densities of the sphere and host atmosphere, ρ_s and ρ_a, and the radius of the sphere, a. Its form is agreed to be

$$\delta = \frac{15\sqrt{\nu_a\rho}}{8\ a\rho_s}\ C, \tag{15}$$

however values of the constant C are not. For convenience C is taken to be 1.0. For a 'rigid' water shell which has the same density as the anticipated liquid shell, the drag coefficient is 6.8×10^{-4} sec$^{-1/2}$. The solution of Equation 14 gives the rotation rate as a function of time

$$\Omega(t) = \frac{\Omega_o}{\{1+(1/2)\delta\sqrt{\Omega_o}(t-t_o)\}^2} = \frac{\Omega_o}{\{1+(t-t_o)/t_{sd}\}^2} \tag{16}$$

$$\text{with } t_{sd} = \frac{1}{2\delta\sqrt{\Omega_o}},$$

the time characterising spin-down, and Ω_o, the angular velocity at time t_o.

When there is a torque acting upon the sphere, the governing equation is

$$\dot{\Omega} = \tau/I - \delta\Omega^{3/2} \tag{17}$$

where τ is the magnitude of the applied torque and I is the moment of inertia of the sphere. While this equation can be integrated, the resulting rotation rate cannot be expressed as an explicit function of time.[34] Its implicit form is

$$\frac{t-t_o}{t_{su}} = \ln\{\frac{1+y+y^2}{(1-y)^2}\} - 2\sqrt{3}\tan^{-1}\{\frac{1+2y}{3}\} \tag{18}$$

$$\text{with } y^2 \equiv \frac{\Omega}{\{\tau/(\delta I)\}^{2/3}} = \frac{\Omega}{\Omega_{max}}, \tag{19a}$$

$$\text{and } t_{su} \equiv \frac{1}{3}\left\{\frac{I}{\delta^2\tau}\right\}^{1/3} = \frac{\Omega_{max}}{3\tau/I}. \tag{19b}$$

Ω_{max} is the steady state rotation rate, t_{su} is a time characteristic of a sphere's spin-up under a constant torque and $t_o = \pi/\sqrt{3}$ so that the rotation

rate at t=0.0 is zero. For a 'rigid' and concentric water shell with $V_{bub} = 4.21 cm^3$ and $V_{liq} = 5.77\ cm^3$, one obtains $I = 5.42\ g\text{-}cm^2$ and $\delta = 6.8 \times 10^{-4}$ $sec^{-1/2}$. The torque predicted for the acoustic levels which had been specified for the experiment and verified during calibration was 1.971 dyne-cm. Using these values an expected spin-up curve was generated: it is the solid line in Figure 1. The steady state value of the rotation rate was $\Omega_{max} = 65.85\ sec^{-1}$ and the characteristic spin-up time, $t_{su} = 60.4$ sec. A graph of the results from a Runga-Kutta solution of (17) was identical to that produced by the analytic expression, (18).

Table 1 shows the times required to achieve a given fraction of the steady state rotation rate. The relative time, t/t_{su}, is valid for the spin-up of any sphere using Equation 19b to evaluate the characteristic time. The times in the third column were calculated for the parameters of this experiment.

In this experiment the acoustic torque was applied for 32 seconds allowing only the early part of the curve to be studied. Because τ/I is greater than $\delta\Omega^{3/2}$ during spin-up for this experiment, it will dominate the shell's response and estimates of the ratio can be determined from the rate of increase of the speed.

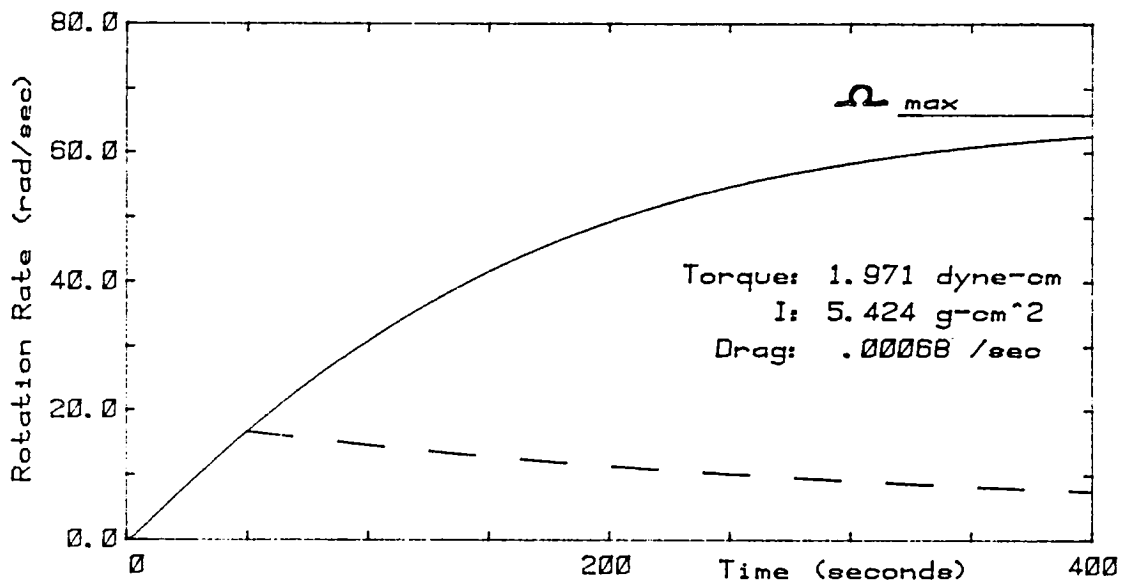

Figure 1. Theoretical spin-up and spin-down curves (solutions of Eqs. 14 and 17) using the values of torque, moment of inertia and drag shown on the graph.

Also shown in Figure 1 is a spin-down curve which was generated using the same value of the drag parameter, δ, and $t_o = 50$ seconds in Equation 16. The scaling factor for the time is $t_{sd} = 230$ sec. The theory indicates that the appropriate time scale for spin-down will be hundreds of seconds ($t_{sd} \sim$ 450 sec.). In the absence of any braking torque, the shell can be expected to rotate for the remainder of the experiment (~ 200 seconds).

Table 1. Spin-up Times for a Sphere

Ω/Ω_{max}	t/t_{su}	t(sec.)
0.309	1.00	60.4
0.50	1.78	107.3
0.90	5.23	315.6
0.99	9.88	596.6

Rotation of a Simple Water Drop. The theoretical study of the shapes of rotating liquids held together by surface tension for the most part has focused on the case of solid body rotation.[25,26,27] In this experiment it is the dynamic behavior as the rotation rate increases relatively quickly from zero to a peak value and then decreases slowly when the torque is removed which is of interest. More accurately, the interest lies in inferring the shell's behavior from its shape.

Chandrasekhar, Ross, and Brown have calculated the equilibrium shapes of a free liquid undergoing rotation as a solid body.[25,26,27] Their model is equally valid for an uncharged nucleus, a free drop of silicone oil, and a star. Because the surfaces are not rigid they deform in such a way that the forces due to surface tension balance the pressures created by the centrifugal forces. For a simple drop with density ρ, resting radius a, and angular velocity Ω, this balance is expressed in the Young-Laplace equation

$$p^{(out)} = p^{(in)} - (1/2)\sigma(\nabla \cdot \underset{\sim}{n}) \qquad (20)$$

$$\text{with } p^{(in)} = p_o^{(in)} + (1/2)\Delta\rho r^2\Omega^2$$

that is, the pressure jump at a point is proportional to the local mean curvature, $(-1/2)\nabla \cdot \underset{\sim}{n}$. $p^{(in)}$ is the pressure on the inside of the surface and is the sum of the pressure at the axis of rotation, $p_o^{(in)}$, and a pressure due to centrifugal forces for which $\Delta\rho = \rho_{in} - \rho_{out}$, and r is the distance between a point on the surface and the axis of rotation. (20) is often expressed in dimensionless form,

$$Ha = \Delta P = K + 2\sum(r/a)^2, \qquad (21)$$

in which the dimensionless parameters $\sum$ and K relate the rotational and

static pressures to those due to surface tension:

$$\sum \equiv \frac{\rho a^3}{8\sigma}\,\Omega^2 = \left(\frac{\Omega}{\omega_2}\right)^2 \tag{22a}$$

$$K = \frac{\{p_o^{(in)} - p_o^{(out)}\}a}{2\sigma} \tag{22b}$$

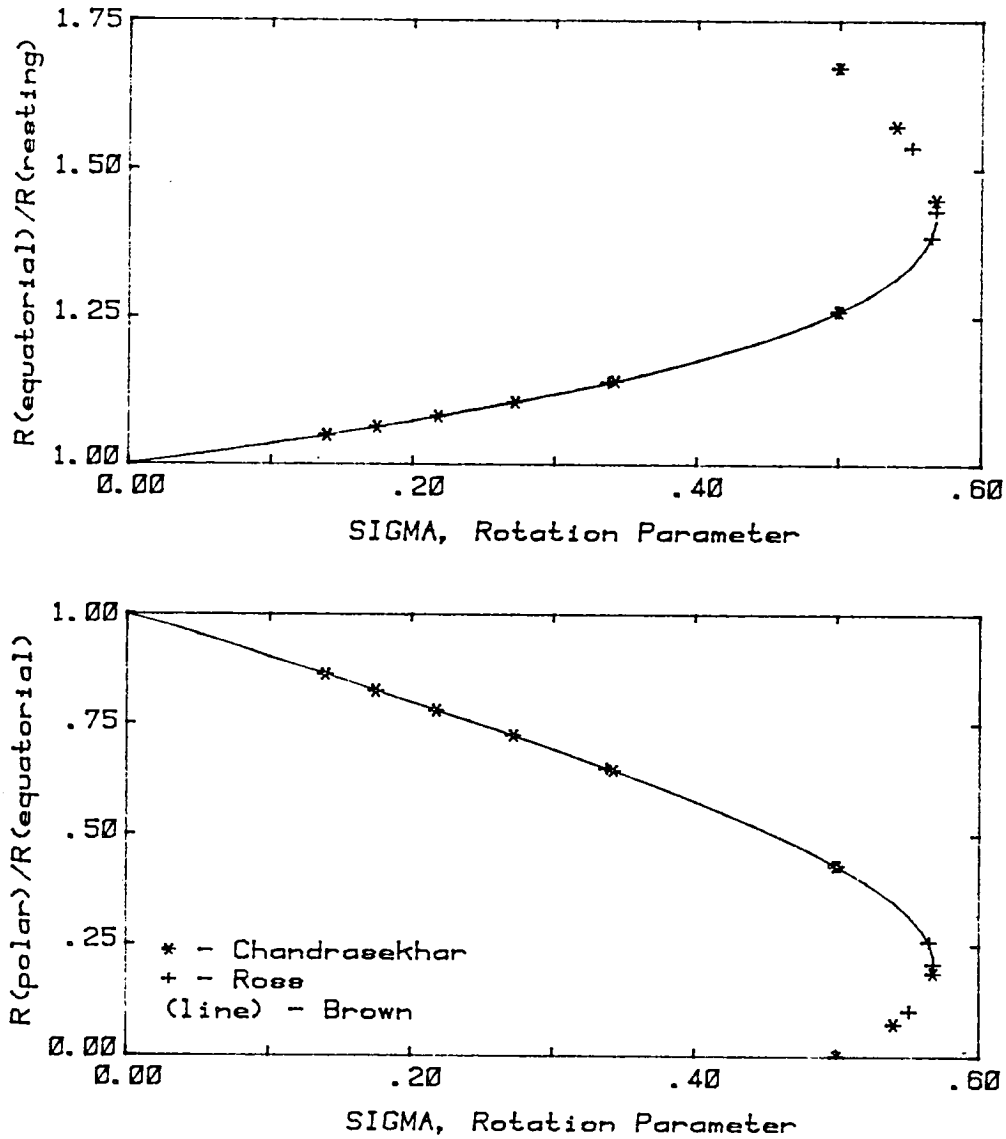

Figure 2. The theoretical relation of drop size to rotation rate: (a) The equatorial radius divided by the non-rotating radius, and (b) the ratio of the drop's polar and equatorial thicknesses as functions of $\sum$, the rotation parameter.

Figure 2a shows the relation of Σ, the dimensionless rotation parameter, to the liquid's equatorial radius which is normalized by its nonrotating radius. Figure 2b shows the ratio of the thickness along the rotation axis to the equatorial diameter as a function of Σ. There is a theoretical bound on Σ of 0.568 which corresponds to a rotation rate of $\Omega_{max} = 0.75\omega_2$.

In a free rotating liquid the ways to confirm rotation are to observe trace particles within the drop or to observe a change in the equatorial or polar dimensions. If the drop is in solid body rotation, the graphs may be used to determine the rotation rate from data describing the change of its shape. When the angular velocity differs from point to point within the drop, the shape and the graphs can still be used to obtain an approximate value of the rotation rate.

In a study of spin-up behavior in a neutral buoyancy experiment in which a simple liquid drop was rotated in a liquid host of the same density, limited confirmation of the theory was obtained.[28,29] The data from the repetition of Plateau's experiment was for low velocities in which the drop was rotated by a disk and shaft assembly.

A further comparison of experimental data and theory was performed with the information from the rotation sequence of the SPAR VI Experiment: 76-20.[9,10] In it a simple drop was rotated acoustically and the changes in its shape were taken from the cine record. Because there were no trace particles there was no way to independently determine the rate. However, using the ratio of polar to equatorial size to determine and the relative equatorial radius, the data was used to show the consistency of the theory (see Figure 3).

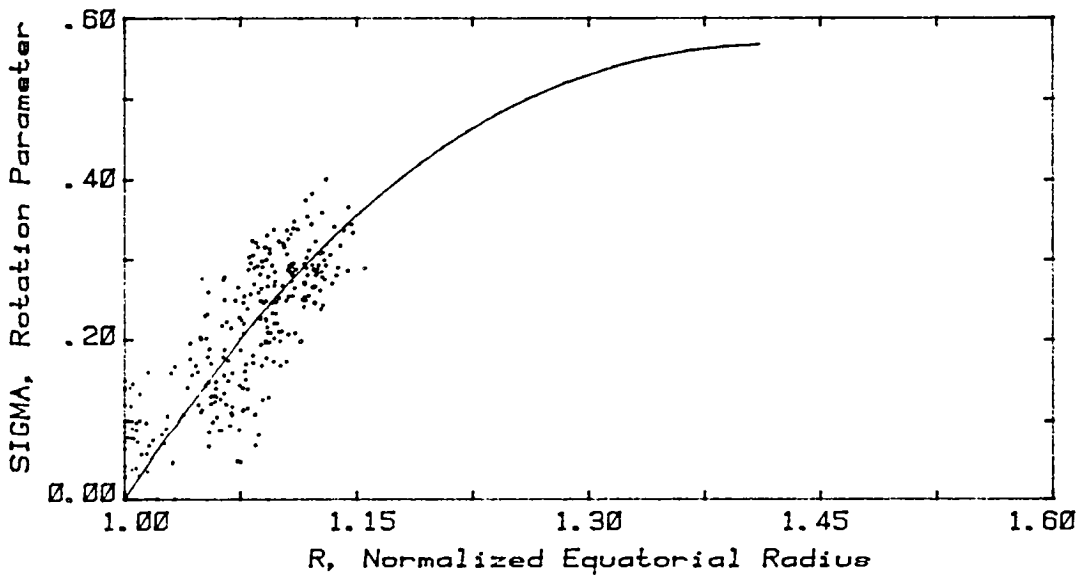

Figure 3. Experimental Results from the SPAR VI Experiment 76-20 which demonstrate the consistency of the rotation data when viewed within the theortetical framework for a simple drop.

D. Stimulated Oscillation

To generate the characteristic shape oscillations of a liquid drop corresponding to one of its normal modes it is necessary to excite the drop surface at a frequency slightly less than the free oscillation frequency. The simplest way to stimulate drop oscillations in a rectangular chamber is to modulate the amplitude of the acoustic pressure at a low frequency. Assuming that the drop's position as well as its stimulation and response are symmetric about an axis, it is convenient to look at the axisymmetric surface deformations: for the n-th mode,

$$\delta r_n(t) = \alpha_n(t) P_n(\cos\theta), \tag{1}$$

with P_n the Legendre polynominal of order n, which defines the shape of the boundary for the nth mode, and $\alpha_n(t)$ which describes the time variation of that mode's contribution. The surface of the axisymmetric drop - whose undistorted radius is a - is the sum of the distortions due to each mode

$$r(\theta,t) = a + \sum_n \alpha_n(t) P_n(\cos\theta) \tag{2}$$

The amplitudes of the normal-mode oscillations, $\alpha_n(t)$, are the solutions of the Navier-Stokes and continuity equations for each mode.

In the potential flow approximation the effects of viscosity are ignored and the particle velocity, $\underset{\sim}{u}$, is described by a scalar field ϕ: $\underset{\sim}{u} = \phi$. The governing equations are

$$\frac{\partial \phi}{\partial t} + \frac{1}{2}(\nabla\phi)^2 + \frac{p}{\rho} = 0$$

$$\nabla^2 \phi = 0 \tag{3}$$

The solution of Laplace's equation in the interior, ϕ_{int}, which is constrained to be finite at the center, is

$$\phi_{int}(\theta,t) = \sum_n g_n r^n P_n(\cos\theta) \tag{4}$$

where g_n can be expressed in terms of $\alpha_n(t)$. This relation is found by studying the velocity of the boundary which is, on one hand, the time rate of change of $r(\theta,t)$,

$$\dot{r} = \sum_n \dot{\alpha}_n(t) P_n(\cos\theta) \tag{5a}$$

and, on the other hand, u_r, the radial rate of change of ϕ_{int},

$$u_r = \frac{\partial \phi}{\partial r}_{int} = \sum_n n r^{n-1} g_n P_n(\cos\theta) \tag{5b}$$

From these it follows that

$$g_n = \frac{\dot{\alpha}_n}{n a^{n-1}}$$

$$\text{and } \frac{\partial \phi}{\partial t} = \sum_n \frac{\ddot{\alpha}_n}{n a^{n-1}} r^n P_n(\cos\theta). \tag{6}$$

Using Equation 3 the pressure in the interior of the drop is, to the lowest order of approximation,

$$p_{int} = -\rho \frac{\partial \phi}{\partial t} = -\rho \sum_n \frac{\ddot{\alpha}_n}{n a^{n-1}} r^n P_n(\cos\theta) \tag{7}$$

The external pressure field which will generate the driving force is the acoustic radiation pressure, $\langle \Delta P \rangle$,

$$\begin{aligned} p_{ext} &= \langle \Delta P \rangle \\ &= -\frac{1}{4\rho c^2} p_z^2 \cos 2k_z z \{1 + a_m(1+\cos 2\Omega_m t)/2\} \end{aligned} \tag{8}$$

This static pressure is the result of modulating the amplitude of the z-axis positioning force at the frequency, Ω_m, with index of modulation, a_m. The modulated acoustic pressure is

$$p = p_z \sin k_z z \sin \omega_z t \, (1 + a_m \sin \Omega_m t). \tag{9}$$

Note that while the acoustic pressure is modulated at Ω_m, the radiation pressure and the acoustic force,

$$F_z = \frac{5\pi k_z p_z^2 a^3}{6 \rho c^2} \sin 2k_z z \{1 + a_m(1+\cos 2\Omega_m t)/2\}, \tag{10}$$

to which the drop responds, are modulated at $2\Omega_m$. The effective external pressure field can also be decomposed into the sum of Legendre polynomials

$$p_{ext} = \langle \Delta P \rangle = e^{i2\Omega_m t} \sum_n q_n P_n(\cos\theta). \tag{11}$$

The pressure difference across the interface is related to the shape of the surface by the Young-Laplace equation

$$H\sigma = p_{int} - p_{ext} \tag{12}$$

where σ is the surface tension, and H is the mean curvature. For small surface deformations the curvature can be expressed as

$$H = \frac{2}{R} + \frac{1}{R^2} \sum_n (n-1)(n+2) \, \alpha_n(t) \, P_n(\cos\theta). \tag{13}$$

When this expression and Equations 7 and 8, are substituted into Equation 12, we obtain the equation of motion for the boundary deformation coefficients

$$\ddot{\alpha}_n + \omega_n^2 \alpha_n = \frac{n q_n}{a\rho} e^{i2\Omega_m t} \tag{14}$$

where ω_n is the frequency of oscillation for the drop's nth normal mode. This is the equation of a forced harmonic oscillator. Including the effects of viscosity gives the equation describing forced and damped oscillation

$$\ddot{a}_n + 2\beta_n \dot{a}_n + \omega_n^2 a_n = \frac{nq_n}{a\rho} e^{i2\Omega_m t} \tag{15}$$

where β_n is the damping coefficient,[19]

$$\beta_n \cong (n-1)(2n+1)\nu/a^2 \tag{16}$$

in which $\nu = \eta/\rho$ is the kinematic viscosity of the liquid. Since the sample is being driven at $2\Omega_m$, a solution of the form $a_n(t) = A_n \exp(2i\Omega_m t)$ is assumed and substituted into (15). The magnitude of the coefficients is

$$|A_n| = \frac{nq_n}{a\rho\sqrt{(\omega_n^2 - 4\Omega_m^2)^2 + 16\beta_n^2\Omega_m^2}} \tag{17}$$

The amplitude of the n-th mode is not maximum when the sample is driven at the frequencies of the normal mode resonances, $2\Omega_m = \omega_n$, but at $2\Omega_m = \omega_n\sqrt{1 - 2(\beta_n/\omega_n)^2}$. At the latter frequency the amplitude is

$$|A_n|_{max} = \frac{nq_n}{2a\rho\{\beta_n + \sqrt{\omega_n^2 - \beta_n^2}\}} \tag{18}$$

To evaluate $|A_n|_{max}$ we must know the magnitude of the driving force for each of the modes, the q_n's,

$$q_n = \frac{2n+1}{2}\frac{p_z^2}{4\rho c^2}\{1+\frac{a_m}{2}(1+\cos 2\Omega_m t)\}\int_{-1}^{1} d\mu \cos(2ka\mu)P_n(\mu). \tag{19}$$

The integral will be 0 for all odd modes. This means that one cannot excite the odd modes acoustically. This is a consequence of the fact that the pressure profile $\langle\Delta p\rangle$ is a symmetric function of the coordinate z. Odd modes can only be stimulated as a result of asymmetries in the pressure field felt by the drop.

Stimulated Oscillation of Compound Drops

The existence and strength of the acoustic radiation pressure depends upon the impedance mismatch between the liquid and the surrounding atmosphere. The much greater acoustic impedance of the liquid, $\rho_s c_s$, means that the acoustic intensity in the drop will be much less than in the air outside it. In fact the amount of sound power transmitted through the surface is

$$\alpha_t = \frac{4R}{\{1+R\}^2} \quad \text{where } R \cong \frac{\rho_s c_s}{\rho c} \tag{20}$$

which is the ratio of the intensities on either side of the surface and is independent of whether the sound is travelling from air into water or vice versa. α_t will be small unless $R \approx 1$.

Because the intensity of the sound in the liquid is very small the magnitude of the acoustic forces stimulating oscillations on the inner surface will be very small. Because the amplitude of the inner surface oscillations is greater than that of the outer surface for the bubble sub-modes, it

will be very difficult to stimulate bubble mode oscillations acoustically. This effect is aggravated by the thickness of the shell which causes the ratio of the amplitudes to be even greater.

The strength of the coupling is indicated by the ratio of the amplitudes of oscillation of the outer and inner surfaces. The ratio of the outer to inner amplitude is

$$S_{n,\pm} = \pm \left\{ \frac{2n+1}{n+1} \varepsilon^{-2n-4} \right\}^{\pm 1} \tag{21}$$

where $\varepsilon = R_{out}/R_{bub}$. Only as the shell gets thinner and ε approaches 1, does the coupling between the oscillations of the two surfaces increase. However as the shell becomes very thin the sound will be transmitted through the shell

$$\alpha_t \cong \frac{4}{R^2 \sin^2 k_s \delta} \tag{22}$$

If the thickness of the shell were $\delta \sim 0.01$cm, the sound transmission coefficient would be 44%. For the fully expanded bubble, if it were concentric, the thickness of the shell would be 0.15cm. For this value $\alpha_t < 0.1\%$. However if the shell were not concentric the acoustic forces would be lessened at the thinner region because of sound transmitted into the shell. But it would be any easier to stimulate the inner boundary directly because the sound would be transmitted across that surface also.

E. Adiabatic Expansion of a Liquid Shell

This section touches on three theoretical aspects pertinent to the expansion of the bubble as the outside pressure drops. In the absence of buoyant forces the fluid between the two surfaces should flow toward regions where the shell is thin insuring that the bubble will not burst as it grows. The acoustic force will change due to changes in the size and density of the shell and in the ambient pressure of the chamber. As the shell gets thinner the frequencies of its normal mode oscillations will decrease. If one of them is the same as the frequency at which the complementary modulation is operating shape oscillations may be stimulated.

Stability during Shell Growth. As the external pressure decreases and the shell grows, the fluid between the boundaries flows into regions where the shell is thinnest. Because of this condition the bubble is not expected to burst free of the liquid and, in fact, is expected to become more centered as the shell expands - if it was not so originally.

Acoustic Forces and the Motion in the Potential Well. As the pressure decreases and the shell grows, the centering force changes as a function of two terms: ρc^2, which is proportional to the ambient pressure, and $a^3 f(2ka)$, which depends upon the size of the shell (Equation 6 in section 4A).

To the extent that the air in the chamber is an ideal gas, the dynamic pressure can be given in terms of $P_{ext}(t)$, the ambient pressure, by

$$\rho c^2 = \left(\frac{c_o^2}{RT_o}\right) P_{ext} = (\rho_o c_o^2)\, P_{ext}(t)/P_{ext}(o) \qquad (1)$$

where ρ_o and c_o are its density and speed of sound at $T_o = 273^oK$ and R is the gas constant. $P_{ext}(0)$ is the pressure inside the chamber at 280 seconds ALO (after liftoff). If the pressure change is adiabatic inside the shell,

$$R_{bub}(t) = R_{bub}(0)\left\{\frac{P_{in}(0)}{P_{in}(t)}\right\}^{1/\gamma} \qquad (2)$$

with R_{bub} the radius of the bubble and γ the ratio of specific heats. The relation between the inside and outside pressures is found by combining the Young-Laplace equations describing the jump in pressure at each surface:

$$P_{in} = P_{ext} + \frac{2\sigma}{R_{bub}} + \frac{2\sigma}{R_{out}} \qquad (3)$$

in which σ is the surface tension and R_{out} (or a) is the radius of the shell. Because the volume of liquid does not change the sizes of the bubble and the total shell can be related

$$R_{bub}(t) = a(0)\left\{\left(\frac{a(t)}{a(0)}\right)^3 - \frac{V_{liq}}{V_{tot}(0)}\right\}^{1/3} \tag{4}$$

This leads to an expression for the outer radius as a function of ambient pressure in which the fact that the first term on the right of Equation 3 is much larger than the other two has been used:

$$a(P_{ext}(t)) = a(0)\left\{\frac{V_{liq}}{V_{tot}(0)} + \left(\frac{R_{bub}(0)}{a(0)}\right)^3 \left(\frac{P_{ext}(0)}{P_{ext}(t)}\right)^{3/\gamma}\right\}^{1/3} \tag{5}$$

Figure 1 shows the how the size of the shell changes as the ambient pressure decreases.

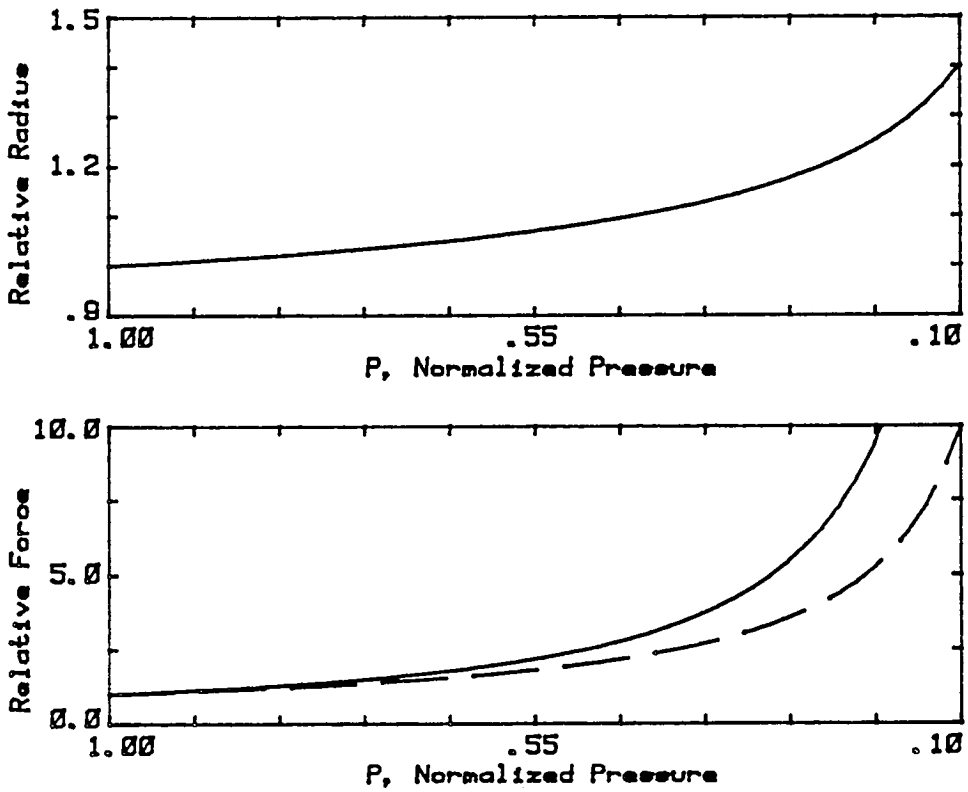

Figure 1. (a) The size of a water shell in air as a function of the ambient pressure.
(b) The acoustic force on both a water shell (the solid line) and a water drop (the dashed line) versus pressure.

The one-dimensional acoustic force is

$$F_{ac} = -\frac{5\pi}{6} p^2 k \left[\frac{a^3 \oint(2ka)}{\rho c^2}\right] \sin(2kx). \qquad (6)$$

The term in the brackets is a function of the pressure - the numerator depends on the shell's size and the denominator is proportional to the atmospheric pressure. The bracketted term's dependence on P_{ext} is shown in Figure 1b. The change in the force on a drop whose density does not change as the pressure does is included (the dashed line) for comparison. The frequency of oscillation in the potential well will change by a factor proportional to the square root of the bracketted term in Equation 6. Because the force increases as the ambient pressure decreases, the acoustic pressure will be decreased as the shell expands to maintain the centering force at a constant level.

Stimulated Oscillation of the Higher Modes. As the shell grows, ε, the ratio of the outer and inner radii, decreases from its unexpanded value of 1.33 and the relative bubble size increases from 0.75. The possibility arises that one of the higher-frequency normal modes of oscillation might be stimulated by the complementry modulation which switches at a frequency of 30Hz. Figure 2 shows the frequencies of natural oscillation as functions of the relative bubble size for several of the shell's even modes which might be stimulated. The double dashed line corresponds to 30Hz for this shell. The left scale is normalized by the frequency of the nth normal mode of oscillation for a simple drop with radius R_{liq}. During this sequence the relative bubble size, η, should increase from roughly 0.75 to 1.66. The only predicted mode that would be stimulated in this range by the 30 Hz signal is the n=6 bubble mode. Any lack of concentricity in the shell is expected to cause the actual frequency to vary from the predicted value.

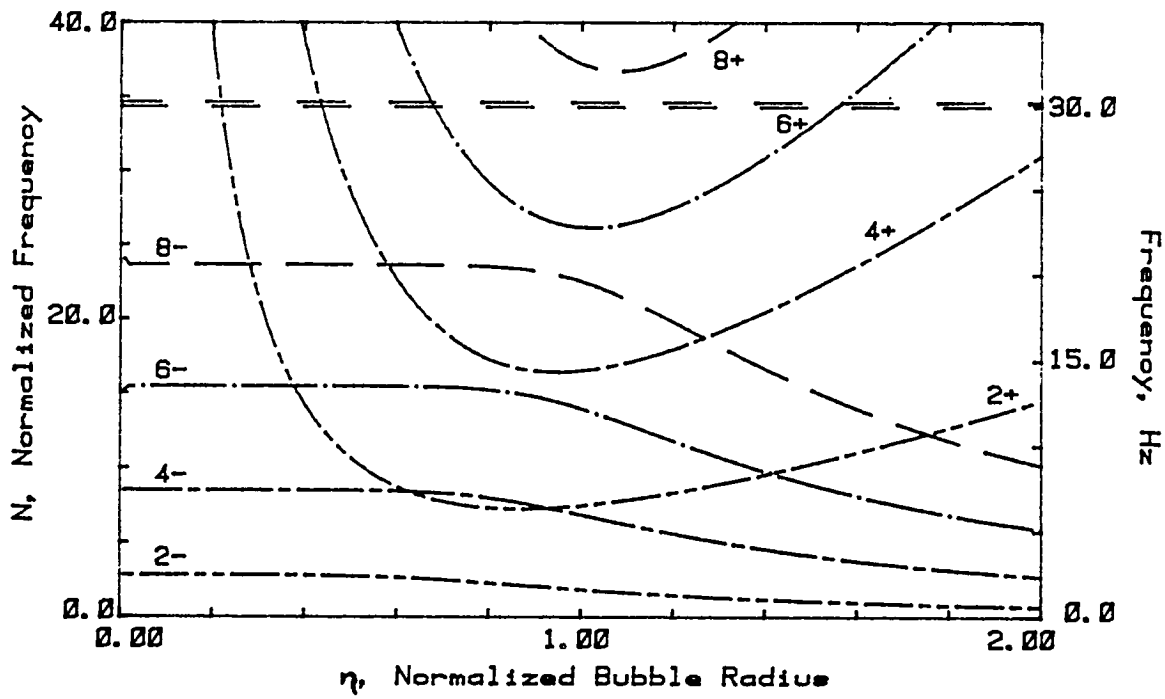

Figure 2. Frequencies of various modes of oscillation for a shell as functions of the shell size. The complementary modulation (at 30Hz) may stimulate oscillations in the shell at the intersections of the dashed line and the curves.

CHAPTER III

SECTION 5

DATA ANALYSIS

A. Introduction

Experiment 77-18/2 was designed to deploy a shell, maintain it in the center of the chamber, rotate it and stimulate several modes of its natural shape oscillations - all acoustically, and then to decompress the acoustic chamber so that the shell would expand. Throughout these sequences a 16mm cine camera was recording the shell behavior through an optical system which provided three nearly orthogonal views. In addition experimental parameters, such as the acoustic pressure for each driver, the ambient pressure and temperature and the voltage levels to the payload were monitored and telemetered.

The guiding philosophy for this analysis has been to search the data provided for anomalous or unexpected features using the most direct and simple methods and then to study more carefully any variant data from as many points of view as possible to provide a supportable explanation for the observation. Data were available in the form of listings from the telemetry signals for the various parameters of the system and from the 16mm cine film record of which single frames could be studied using a Vanguard Motion Analyzer. Figure 1 shows a frame from the adiabatic expansion sequence of the film record. The three views, the retracted probes, the speaker ports, the fiducial marks on the walls and the small and large bubbles are all visible.

The BOX method, which is described in the Appendix, was used for the first step in most of the analyses and in several cases was also the only step. When this method was inappropriate other simple techniques were used so that all the features of the experiment were accessible to some form of simple analysis. The benefits from a full digitization of all or part of the boundaries were felt to be too small to be practical because the volume of data would have grown very large for a slight increase in information. In addition the available digitization routines were inadaquate for the type of data to be studied and unappropriate for the desired level of analysis. The investment in time and resources to develop software to enhance the images in order to permit meaningful analysis - especially for the inner boundary which was difficult to observe - was felt to be too great. The human hand and eye in conjunction with the Vanguard Motion Analyzer, although slow, provided the most practical method for data generation.

Table 1 shows the programmed timeline for this experiment. All sequences were activated for the proper duration however there was a one second difference between the program and the times indicated on the side of the film: 138.0000 from the edge of the film corresponded to 139 seconds after liftoff in the experiment control program. The telemetry data agreed with the times on the edge of the film when the prescribed correction of 50min 01sec was used. With the exception of an improper signal amplitude to one acoustic driver during the rotation sequence (which lasted for only 15 seconds) all systems performed as desired.

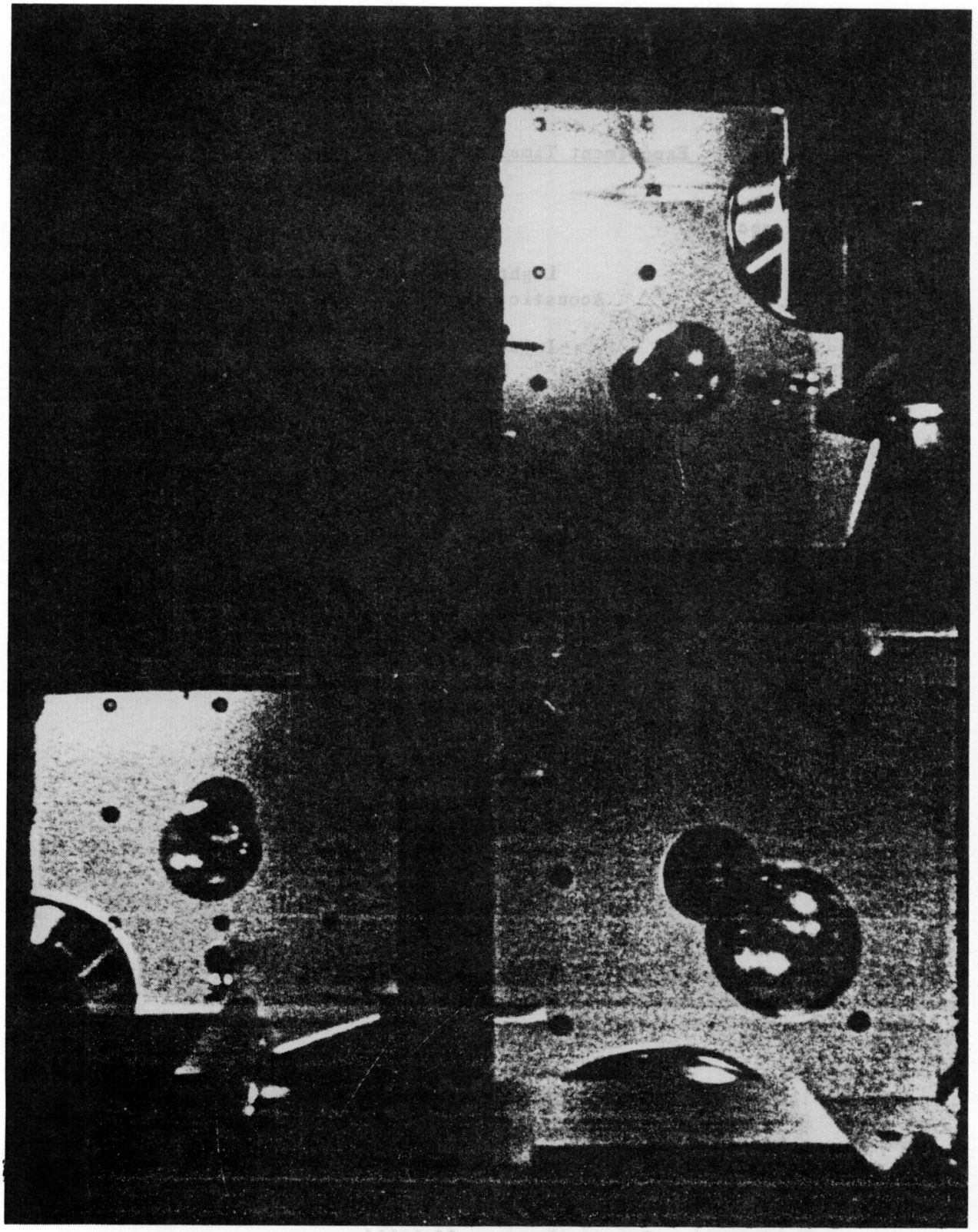

Figure 1. A single frame from the 16mm cine film record which shows the three views of the shell as the bubble expands.

Table 1. Experiment Timeline (Kent Tarver 7/1/80)

Time, sec ALO	Event
88	Lights and camera turn on
95	Acoustics turn on: comp. mod.
103	Injectors insert
105	Liquid injection on
112	Liquid injection off (5.77cm^3)
113	Air injection on
135	Air injection off (4.21cm^3)
139	Injectors retract
142	x and y acoustics change: 90° phase
174	x and y acoustics change: comp. mod.
199	z modulation on: 5.0 to 7.0 Hz
217	z modulation off
232	z modulation on: 1.0 to 2.4 Hz
247	z modulation off
262	z modulation on: 2.5 to 4.0 Hz
277	z modulation off
293	Valve 1 opens
323	Valve 1 closes
327	Valve 2 opens
366	Valve 2 closes (?)
450	Acoustics, lights, camera off

Table 2 lists several significant events which were not scheduled but were important to the outcome of various parts of the experiment.

Table 2. Significant Events

Time, sec ALO	Event
141-173	Error in the amplitude of x axis centering force
316.6	One of three small bubbles pops
338.6	One of two small bubbles pops
419.9	Shell hits the wall

B. Acoustic Positioning

The purpose of the analysis of the motion of the shell in the acoustic potential well is to estalish the limits of the models developed to characterize the acoustic fields and to discern what the physical processes are which could cause deviations. In addition the conditions under which the shell is distorted from sphericity due to acoustic forces are to be identified. The acoustic positioning forces were to be kept constant throughout the experiment with a calibrated strength of 12.5 dynes at a distance of 2.88 cm from the chamber center along each of the three axes.

One of the data combinations available from the BOX analysis is an approximate center of mass of the shell. It is the average value of either the two x or the two y coordinates used to define the box (see Figure 1). In order to use this technique profitably the intersection of the diagonals of the minimum rectangle for the outer surface should be close to the true center of mass and the density of the shell must be uniform or at least symmetric about that point. The former requires that the outer boundary is relatively smooth and the latter requires that the inner boundary is roughly concentric.

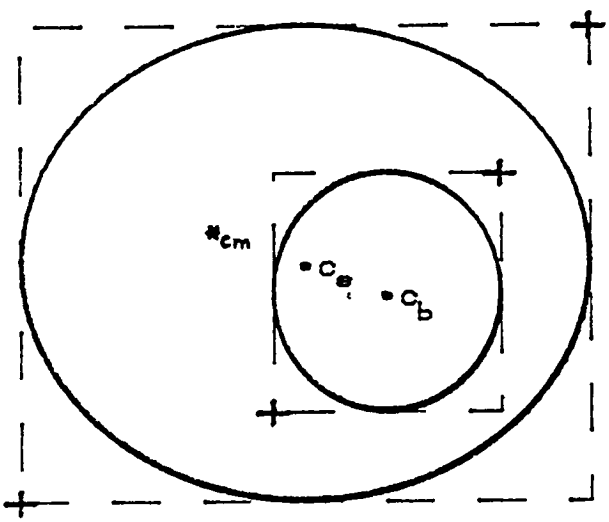

Figure 1. An image of the shell which illustrates the limitations of the data analysis used: to use the center of the large box as the center of mass is invalid if the bubble is large and not concentric. The point c_s is the basis for the graphs of this sub-section.

The outer boundary of the shell was strongly distorted only twice: for a few frames just after the retraction of the injectors and for the last 60 seconds of the experiment due to the presence of a small bubble. The former was not critical since the time scale was short compared to a single oscillation of the shell in the potential well. The latter distortion was significant and coupled with the fact that in the expanded shell the mass distribution was far from concentric, it made the shell's motion appear very erratic when the BOX analysis was used on it. For most of the experiment the bubble center was close to the center of the shell in the x and y directions but not along the z axis. The center of mass data obtained in the former directions reflect the bulk motion of the shell, while along the z axis the data are a combination of the center of mass motion and other factors (eg. oscillation of the shell surface during the stimulated oscillation sequence - 198 to 276 seconds ALO).

Much of the motion in the acoustic potential well is a result of the initial conditions imposed upon the shell during its deployment. A spherical shell (or drop) centered between two probes is in unstable equilibrium if the separation between the probe tips is less than its diameter. If the shell moves slightly off center, that motion will continue until the surface of the liquid near the tips of the injectors is as parallel to the injectors as possible.

At no time during injection did the center of either the drop or the bubble lie on the line between the probe tips. By the time it was possible to call the amount of injected water a drop it was already clearly off center with the liquid wetting the tips just enough so that the water flowed into the interior of the drop. When the bubble appeared its surface was also pinned to the inner injector tubes. The adjacent design shows the relative positions of the probes and the shell in the z=0 cross-section of the chamber at the conclusion of the air injection . The shell's center of mass was positioned very close to the z = 0 plane with x ~ y ~ 0.5a as the probes were retracted. (a is the average radius of the outer surface.)

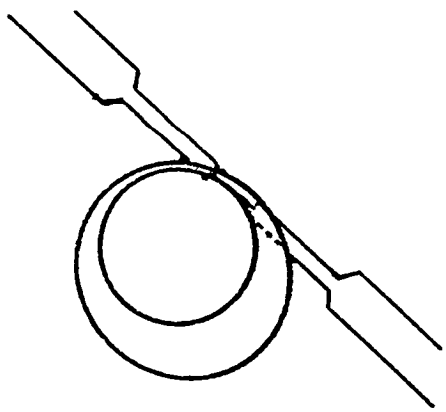

In addition to this initial displacement, the shell was given momentum in the z=0 plane as the probes retracted and the liquid in the shell adherred to the probe tips slinging the shell through the center of the chamber. Because the shell was centered in the z direction before retraction there was almost no component of the velocity in this direction.

Center of Mass Motion: First Half of the Experiment. Figures 2, 3, and 4 show data for the 140 seconds after deployment: the position of the center of the shell's mass (with an estimate of the center of the chamber indicated by

the dashed line), the rocket's accelerometer data for the same time period and the Fourier transform of the time data. The horizontal bars in the time data are used to identify the several sequences of the experiment: the applied torque sequence (I), the three forced oscillation sequences (IIa,b,c), and the period when the chamber was being depressurized (IIIa,IIIb).

The top graphs show the position of the shell for each of the three axes as a function of time normalized by the resting radius of the outer surface. Data was taken every twenty frames (i.e. 0.42 sec) from both the main (z axis) view for the x and y data and from a side (x axis) view for the z axis motion. Note that in the x and y directions the response was primarily sinusoidal - as expected. The amplitude of the motion in the z direction was much smaller and the signal was erratic.

Estimates of the resistance of the air to the motion of the shell through it were obtained from the damping of the oscillations in the acoustic potential well shown in Figures 2 and 3. The sinusoidal behavior of the x axis data decreased at a rate characterized by the damping coefficients: $\beta_{air} \sim 0.019 sec^{-1}$ (between 141 and 173 sec) and $\beta_{air} \sim 0.003 sec^{-1}$ (between 173 and 280 sec). From the y-axis data: $\beta_{air} \sim 0.0123 sec^{-1}$ (between 141 and 173 sec) and $\beta_{air} \sim 0.0117 sec^{-1}$ (between 173 and 280 sec ALO) for an average value of $0.012\ sec^{-1}$. The characteristic decay time for the y-axis data was 80 seconds.

Examination of the accelerometer data (in the middle graphs) showed no large spikes either during deployment or later in the flight. Table 1 at the end of this section lists the average acceleration and the rms deviation for various times during the experiment. There were no changes in amplitude of the oscillations in the potential well which were the result of significant g-events, nor did the smaller g-bumps give rise to observable changes in the motion. Similarly there was little correlation between the time-average accelerations and the displacement of the center of the oscillations from the center of the chamber.

To aid in identifying the frequencies of oscillation of the bulk motion the data in the top graphs were Fourier-transformed. Instead of a single peak at the expected frequency of 0.18 Hz, the x-axis spectra showed a narrow peak at 0.131 Hz and a broad peak at 0.240 Hz. The y axis data show the expected signal at 0.179 Hz and a broader peak at 0.138 Hz. The strong peaks at 0.13 Hz in the x data and at 0.179 in the y data represent the oscillation frequency in the well during complementary modulation. They correspond to a values of F_{max} of 7.1 and 13.3 dynes. The frequency spectra for the z direction shows three small peaks - small because there was little oscillation in this direction and three (at 0.139, 0.179, and 0.220 Hz) because the expected 0.18 Hz signal was prominent for very short periods of time.

The period of higher frequency response in the x axis data between 141 and 173 seconds ALO and lower frequency response in the y data (in Figures 2a and 3a) corresponds to the rotation sequence. The x axis frequencies were 0.240, $.24 \pm 0.05$ Hz and in the y direction 0.139 Hz. These should have been at the planned level of 0.18 Hz. The peak in the x data had side lobes because of the relatively short duration of the rotation sequence.

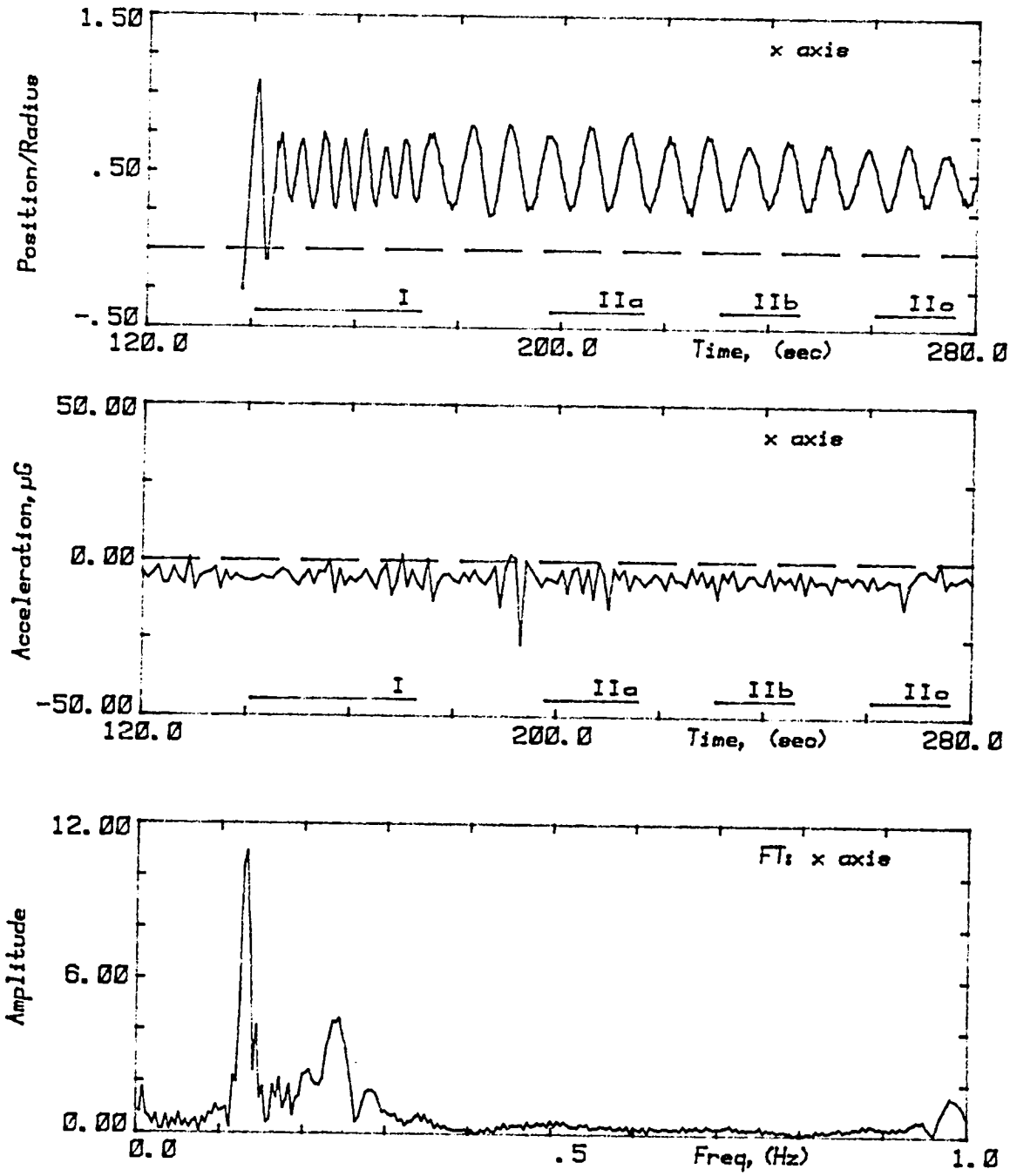

Figure 2. Summary of the motion of the shell's center of mass along the x axis during the first half of the experiment: (a) its relative position in the chamber, (b) the acceleration measured at the rocket's center of gravity, and (c) the Fourier spectra obtained from the data in (a).

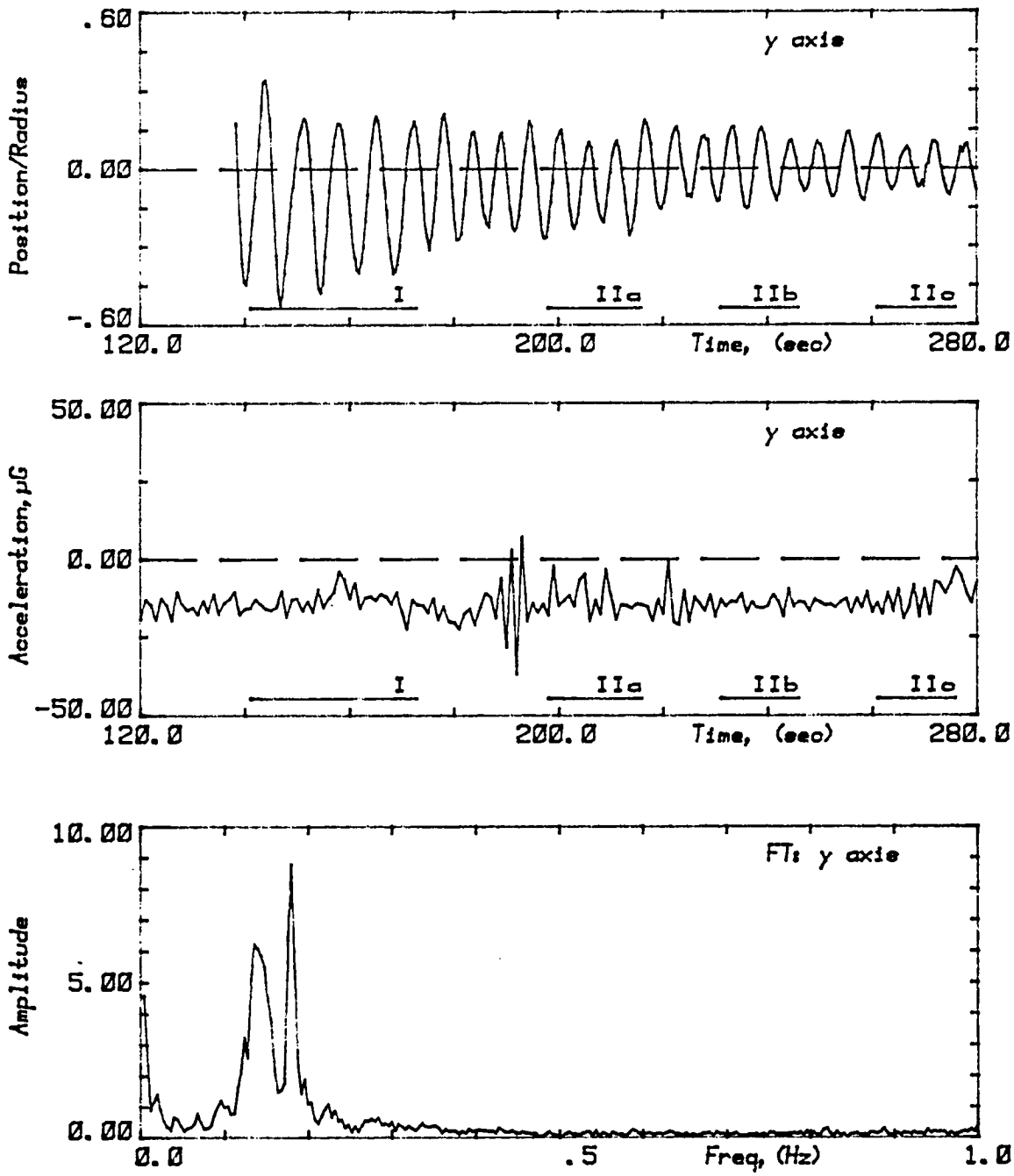

Figure 3. Summary of the motion of the shell's center of mass along the y axis during the first half of the experiment: (a) its relative position in the chamber, (b) the acceleration measured at the rocket's center of gravity, and (c) the Fourier spectra obtained from the data in (a).

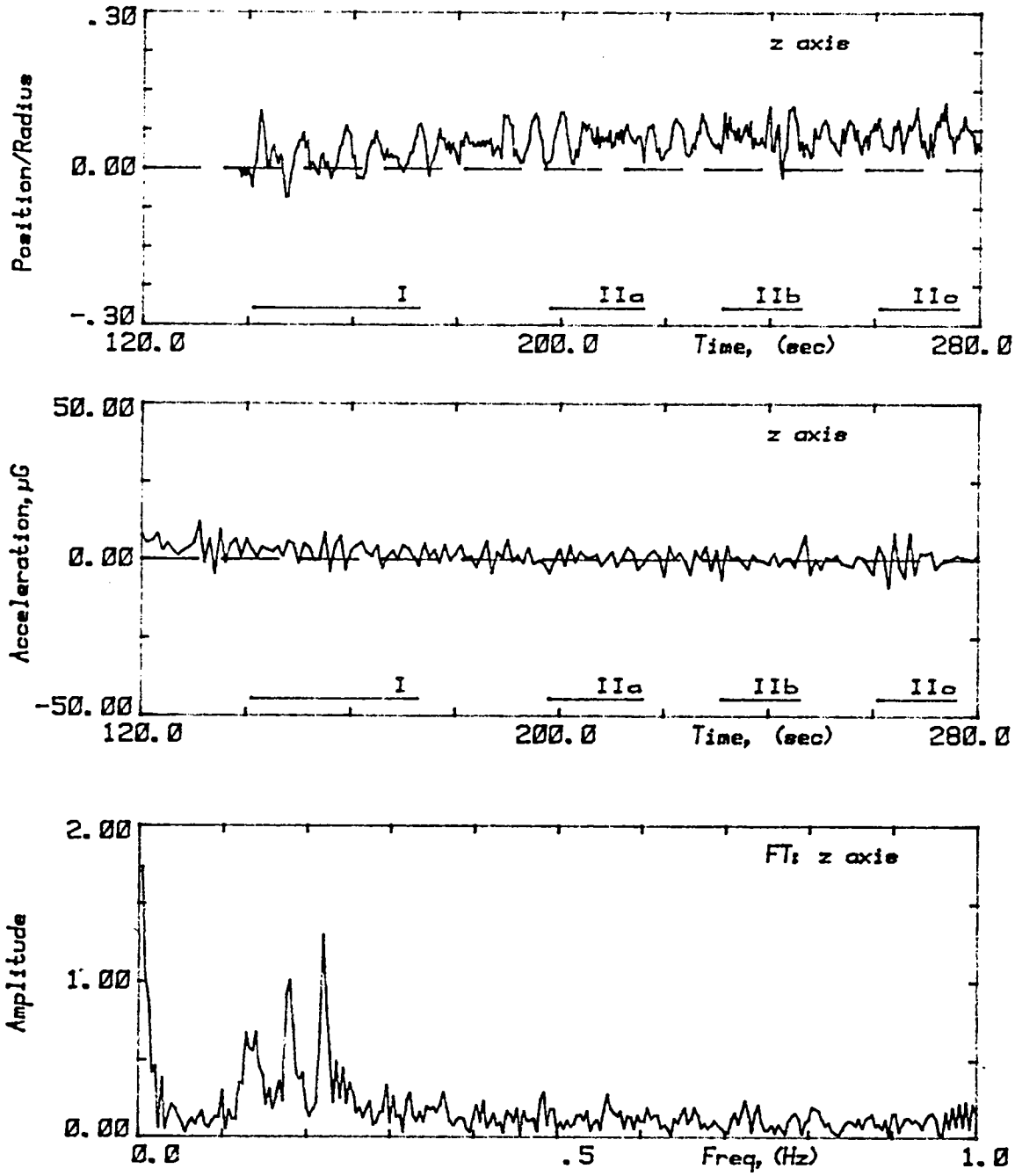

Figure 4. Summary of the motion of the shell's center of mass along the z axis during the first half of the experiment: (a) its relative position in the chamber, (b) the acceleration measured at the rocket's center of gravity, and (c) the Fourier spectra obtained from the data in (a).

During the rotation sequence the complementary modulation was turned off and acoustic torque was applied to the shell by adjusting the x and y signals so that there was a constant 90 degree phase difference between them. Because the amplitudes of the signals entering the chamber for the x and y axes were constant in this mode - not switching between zero and full amplitude as during complementary modulation - the intensity was greater for the same signal levels. To keep the centering forces balanced at the levels used before and after this sequence, the amplitudes of the x and y acoustic pressure were to be reduced to 87% of the level used during complementary modulation. The signal in the z direction was not affected.

An error was made in the x-channel program: the two signal levels were switched so that instead of the amplitude decreasing, it increased. Figure 5 shows the output of microphones in the center of the x and y axis speakers. The y axis data shows the desired drop in amplitude during the 'torque on' sequence. The oscillatory behavior shown in Figure 5 before and after the torque was applied is an artifact of complementary modulation and the sampling rate used for the telemetry data. The levels after the rotation sequence are slightly higher for both signals - this is due to the presence of the shell in the chamber.

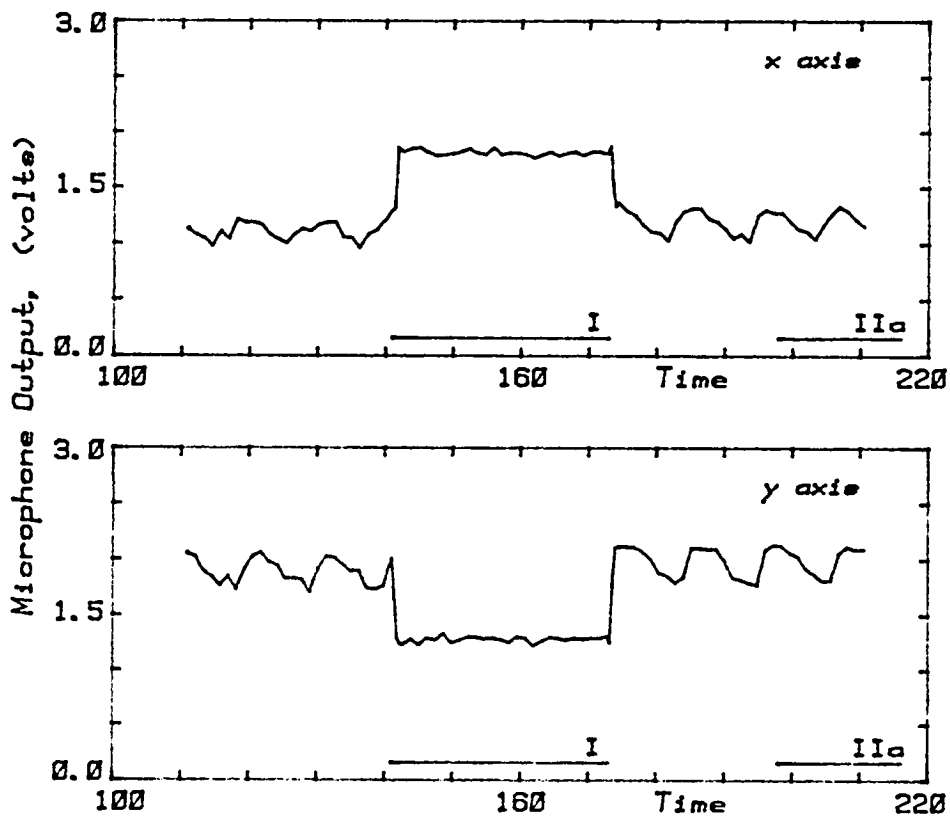

Figure 5. Telemetry data showing the voltage levels of the x and y axis signals used to center the shell. Both should decrease between 141 and 173 seconds ALO (after liftoff).

In the x direction the acoustic pressure increased by a factor of 1.32 and the strength of the centering force by a factor of $(1.32)^2$, while in the y direction the pressure amplitude decreased by 70%. Fourier analysis of the time data showed that the frequencies of oscillation during complementary modulation were 0.131 and 0.179 Hz for the x and y axes, respectively, while those during the rotation sequence were 0.240 and 0.138 Hz. The corresponding values of F_{max} (in dynes) are: 7.1 (x,c.m.), 13.3 (y,c.m.), 23.9 (x,rot.), and 7.9 (y,rot.).

One of the effects of the increase in the centering force of the x direction compared to that of the y direction was the flattening of the shell. Figure 6 shows the difference between the relative cross-sections of the shell along the x and y axes before, during and after the rotation sequence. For a rotating shell the average amplitude of the difference should be zero. In the period between 141 and 173 seconds after liftoff there is evidence of a sustained distortion of the shell on the order of 6% of the shell's resting radius. That this unexpected behavior is due to a decrease in the shell's size along the x axis is supported by the data of Figures 2a and 5a. A summary of information gathered about distortion due to the acoustic forces is located later in this sub-section.

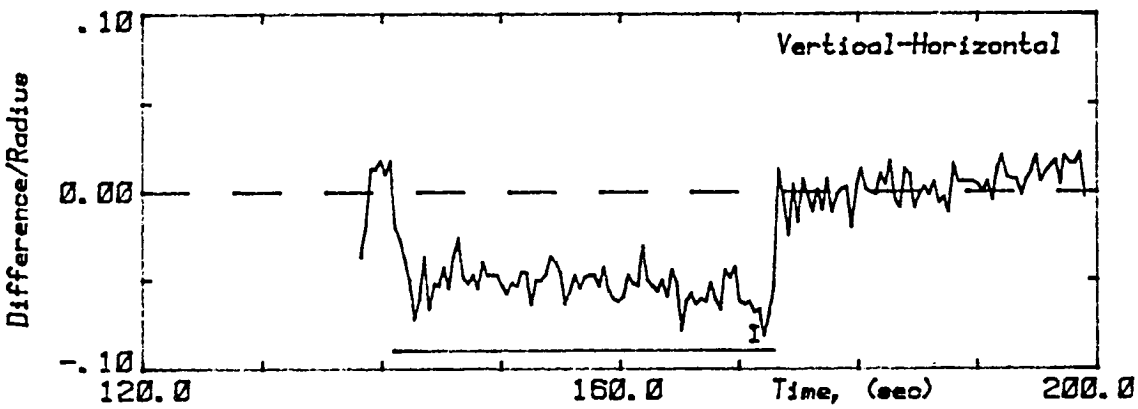

Figure 6. Distortion due to the imbalance in acoustic pressure. The difference between the shell's x and y dimensions should average to zero, especially when rotating about the z axis.

During the stimulated oscillation sequences the bulk motion of the shell in the z direction appeared to respond to the modulated force at the forced oscillation frequency. This was due to the facts that the bubble was not centered along the z axis and that the amplitude of the center of mass motion in this direction was very small. The former meant that the true center of mass was not approximated very well by the BOX method.

Some of the dislocations in the time data of the y axis were due to inconsistencies in the registration of the film image in the Vanguard Motion

Analyzer in the direction that the film travelled. They posed no problem in studying the data, although it created frustration as non-existent g-events were sought to explain the sudden changes.

Center of Mass Motion: Second Half of the Experiment. Figures 7a, 8a, and 9a show the center of mass motion of the shell along the three axes between 280 sec and 420 sec ALO (when it hit the wall). During this period the chamber was depressurized twice: between 292 and 322 seconds and between 326 and 365 seconds. After 276 seconds the only external force which acted on the shell was the acoustic centering force.

The pressure drop while the first valve was open affected the size of the shell but did not seem to change the character of the x and y axis bulk motion. A graph showing the increase in the shell's size is given in sectio 5F - Figure 2. The opening of the second valve, an increase in the level of g-jitter, and the slowing down of the shell's rotation coincided with generally increased amplitudes of the shell's oscillation in the potential well. There were also changes in the frequencies of the motion in the y and z directions.

Along the x axis the motion was not affected by the early growth of the shell. It continued to oscillate at a frequency near 0.13 Hz (0.115 Hz) until 340 seconds at which time there was a flurry of g-activity and the second small bubble popped. After that the character of the center of mass motion changed: after seven seconds of very small amplitude motion the excursions of the shell increased rapidly until at 360 seconds the peak to peak amplitude was almost twice the pre-expansion radius. Throughout this half of the experiment the shell oscillated without any change in its frequency of oscillation in the acoustic well.

The amplitude of the motion along the y-axis began increasing shortly after the second valve opened. The accelerometer data shows some activity arround 340 seconds but no large events which might have have triggered the change in the amplitude of the oscillation. The second small bubble popped at 340 and the shell began to wobble, i.e. to precess as its rotation rate neared zero. The shell slowed down at an increasing rate as it grew in order to conserve angular momentum. After 350 seconds both of the larger surfaces were visibly distorted by the small bubble. More importantly without rotation there was no force to keep the centers of the two bubbles aligned along the z axis. At his point the utility of the BOX method became questionable for the center of mass was not near the intersection of the diagonals of a box containing the outer surface but in the vicinity of where the two bubbles met.

The amplitude of the z-axis motion was much smaller than that of the other two directions when the first valve opened. It began to lose its random behavior after 310 seconds as the the shell size began to increase. As in the y signal the amplitude grew until arround 350 seconds. The change in frequency charcteristic of the rocking of the distorted shell did not occur for another twenty seconds. Again the behavior was the result of rotation and distortion effects as there were no large accelerations.

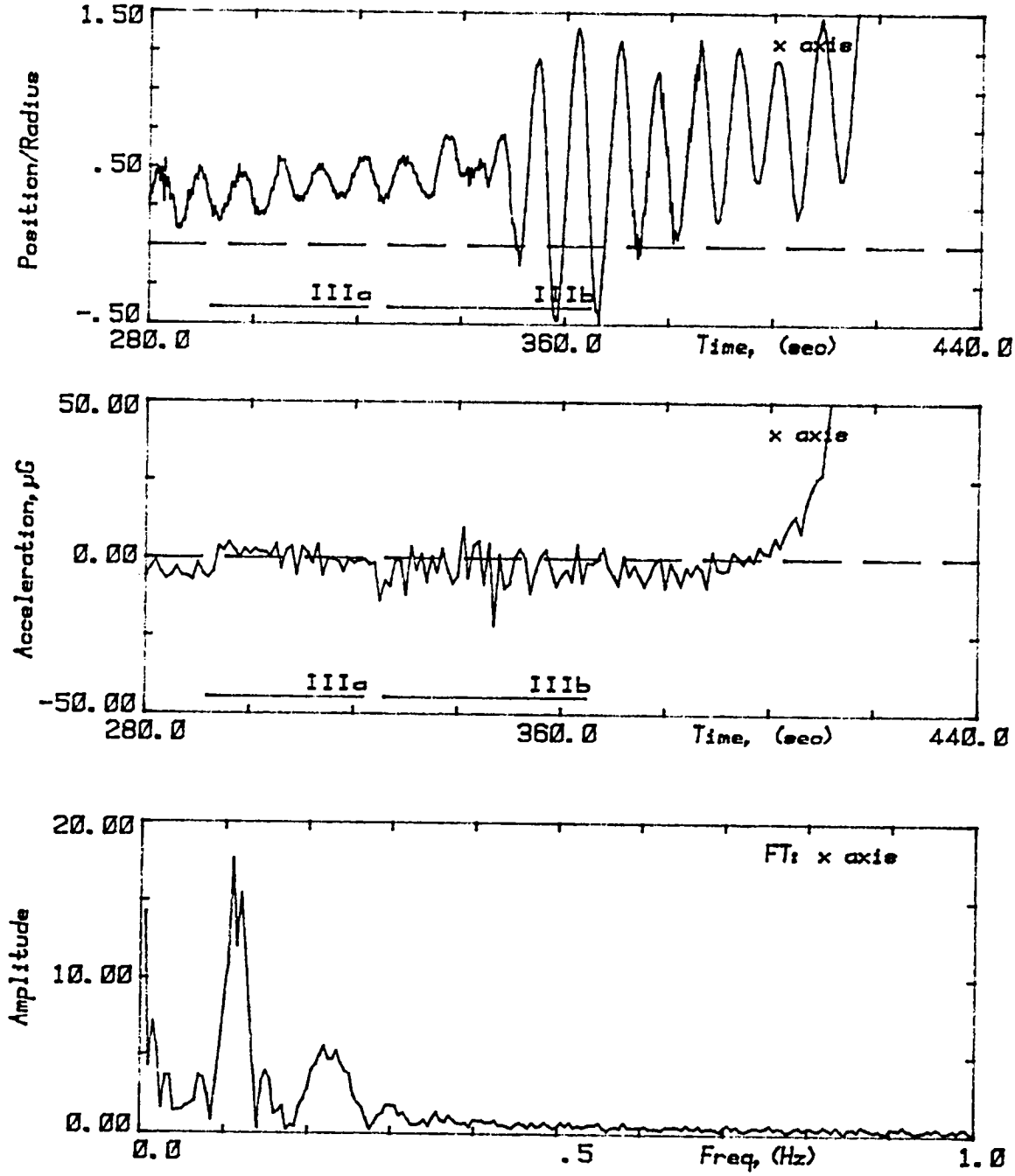

Figure 7. Summary of the motion of the shell's center of mass along the x axis during the second half of the experiment: (a) its relative position in the chamber, (b) the acceleration measured at the rocket's center of gravity, and (c) the Fourier spectra obtained from the data in (a).

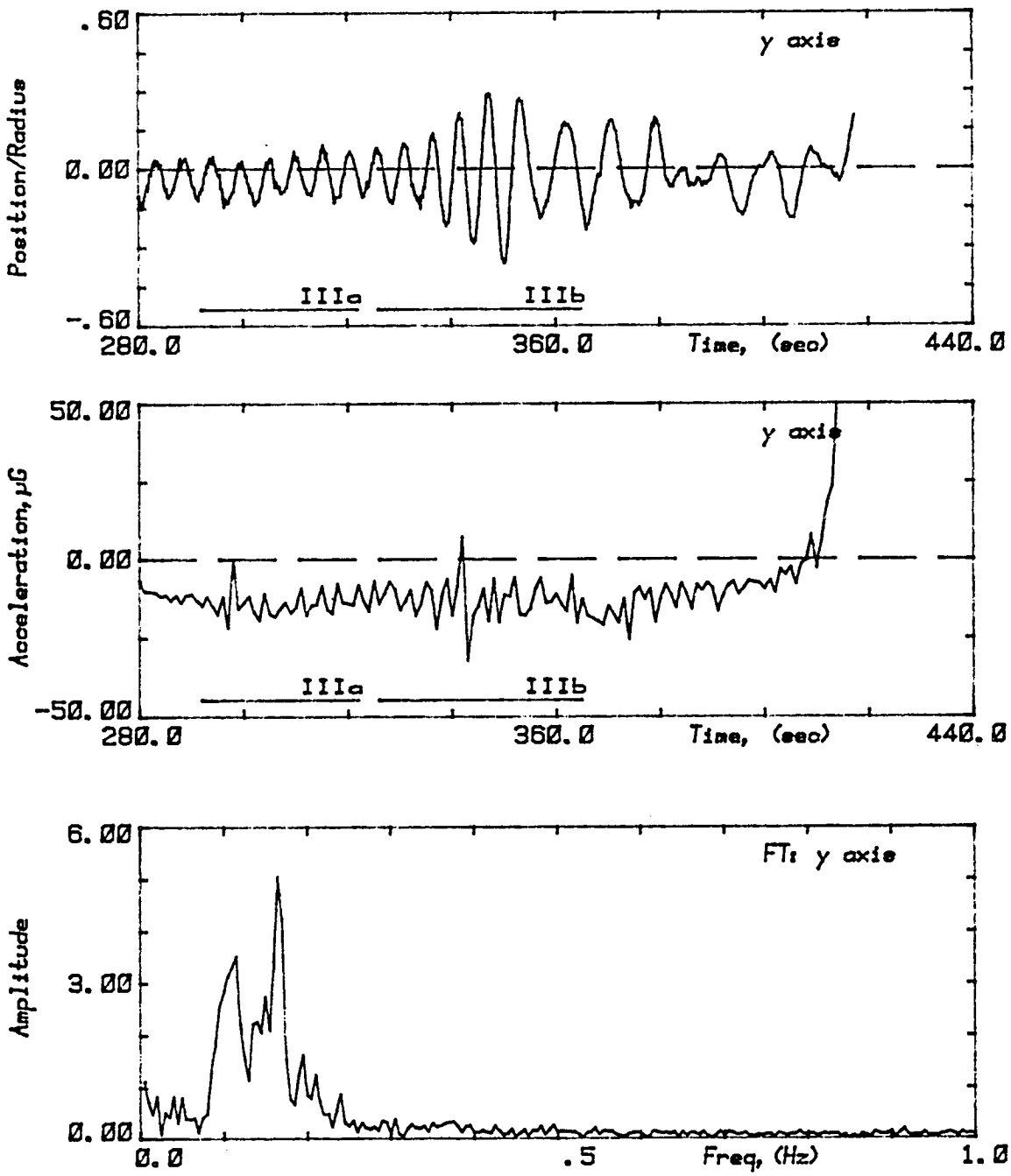

Figure 8. Summary of the motion of the shell's center of mass along the y axis during the second half of the experiment: (a) its relative position in the chamber, (b) the acceleration measured at the rocket's center of gravity, and (c) the Fourier spectra obtained from the data in (a).

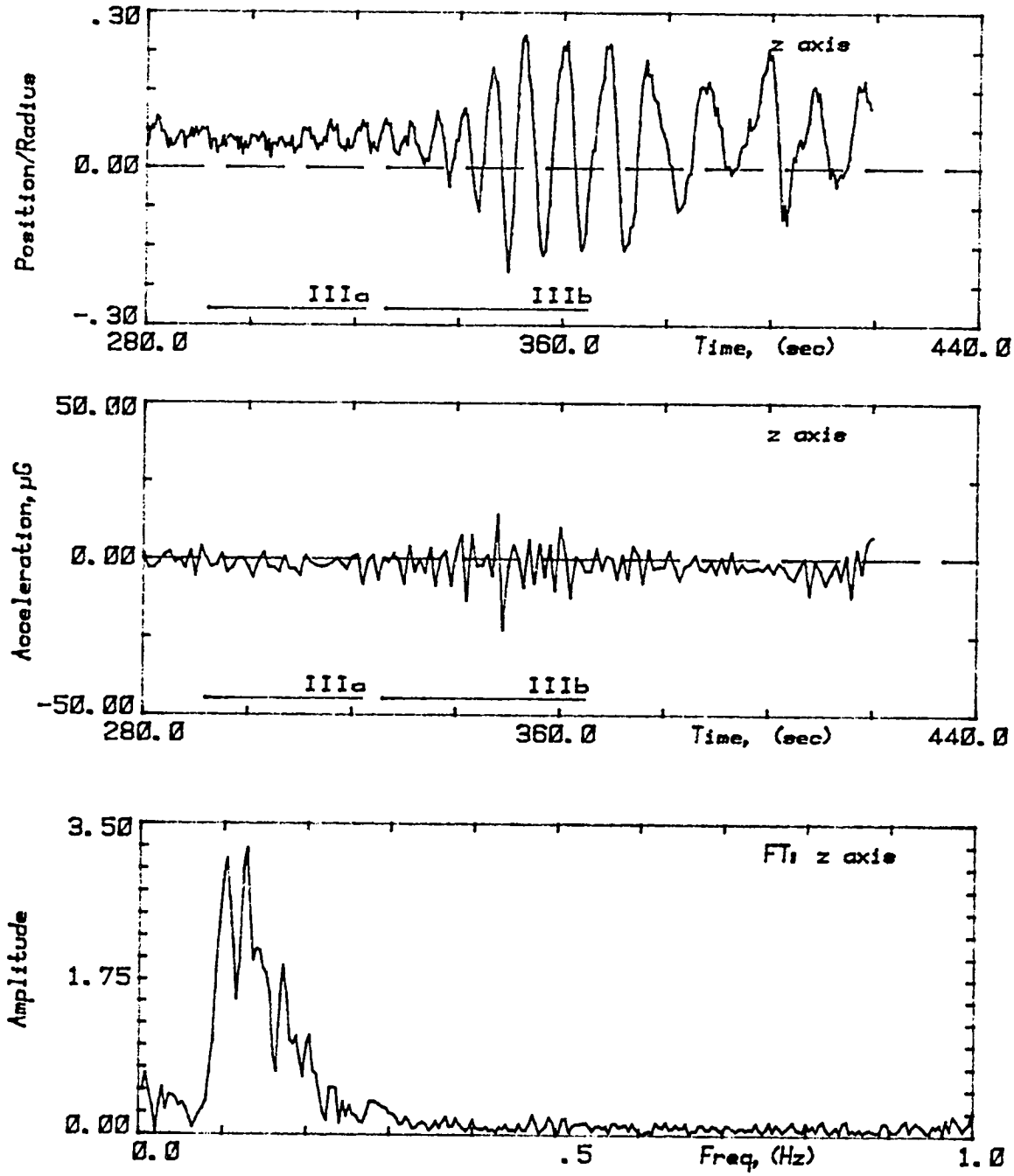

Figure 9. Summary of the motion of the shell's center of mass along the z axis during the second half of the experiment: (a) its relative position in the chamber, (b) the acceleration measured at the rocket's center of gravity, and (c) the Fourier spectra obtained from the data in (a).

The stimulus for most of the activity during this period was the end of the stability maintained by the rotation of the shell: as it slowed the motion in the well caused more and more precession - with the result that energy from the oscillation and from the shell's rotation fueled the increase in amplitude of motion for all three axes. At 350 there was some jostling of the payload: but as mentioned before it is difficult to reconcile the magnitudes of the changes in acceleration and in the amplitudes of the center of mass motions.

Table 1. Acceleration History of the SPAR VIII Rocket
(all values are given in μg's)

time	$\bar{\ddot{x}}$	$\ddot{x}_{rms}$	$\bar{\ddot{y}}$	$\ddot{y}_{rms}$	$\bar{\ddot{z}}$	$\ddot{z}_{rms}$
100 - 138	-4.68	3.33	-15.58	4.06	5.46	6.15
138 - 141	-6.01	0.72	-14.99	2.74	4.33	2.44
141 - 173	-5.33	2.76	-13.32	3.55	2.38	2.99
173 - 198	-5.86	5.69	-15.91	8.36	0.91	2.87
198 - 292	-5.00	2.77	-13.17	4.09	0.14	3.04
292 - 327	-0.74	4.19	-13.74	4.24	-1.33	3.86
327 - 366	-3.02	6.06	-12.90	6.34	-1.46	7.00
366 - 400	-2.58	3.70	-12.62	4.85	-1.71	3.00
400 - 420	128.52	172.46	43.46	67.67	-2.72	4.79

Effects of the Acoustic Forces on Shell Shape

1. Sphericity. The acoustic intensity must be sufficient to position the shell without distorting its shape. To this end the acoustic field must be as symmetric as possible. It is therefore critical that signals be correctly balanced under all conditions of the experiment. Lack of balance may be the cause whenever the average cross-sections of the shell image along two axes differ for the same view. The imbalance was obvious during the rotation sequence as shown in Figure 6 but other sequences of the experiment were examined for smaller deviations. Table 2 lists the results of this comparison at various times.

Table 2 indicates that the x and y forces were balanced to better than a percent for the entire experiment except during the sequence in which the torque was applied. This must be tempered by the observation that one of the effects of rotation about the z axis was to keep the shell symmetric when viewed along that axis. Rotation did not die out until roughly 350 seconds and at that time the shell had expanded to the point where the distortion caused by the presence of the small bubble was much more severe.

Table 2. Sphericity Test Results: BOX Data

Sequence	Time	View	Dir:Dim	Dir:Dim	% Difference
Free Oscillation	138-141	z	x: 0.683	y: 0.675	-0.59
Torque Applied	141-173	z	x: 0.654	y: 0.689	-2.60
	141-142	z	x: 0.667	y: 0.686	-1.40
Relaxation	173-198	z	x: 0.684	y: 0.682	0.15
	173-175	z	x: 0.678	y: 0.674	0.30
bet. Forced Osc.	216-231	z	x: 0.681	y: 0.679	0.15
	246-261	z	x: 0.682	y: 0.674	0.59
	276-292	z	x: 0.689	y: 0.685	0.29
Adiabatic Exp.	292-322	z	x: 0.721	y: 0.717	0.28
	322-326	z	x: 0.758	y: 0.753	0.33
	326-379	z	x: 0.867	y: 0.857	0.58
	379-408	z	x: 0.936	y: 0.922	0.75

Because complementatry modulation was required to remove the undesirable interference during the non-rotation sequences, distortions peculiar to it - although none were expected - would have been symmetric about the $y = \pm x$ planes. Although the frequency of the modulation was too high to measure its dynamic effects from the film, a check was made for any static deformation. None were apparent to the eye nor detectable by the data from the BOX analysis. To check more thoroughly for possible distortion, for several frames sets of points along the outer boundary of the main view image were taken using the Vanguard Analyser, concentrating on points near the diagonals. These sets were then fitted to ellipses from which the eccentricity and angle of orientation of the major axis relative to the x axis were obtained. These results are listed in Table 3.

Table 3. Sphericity Test Results: Complementary Modulation

Sequence	Time	N(pts)	ε	Angle
Rotation: T on	170.01	43	0.007	88.9
T off	180.02	42	0.005	-88.0
betw. Forced Osc	225.01	45	0.015	-38.4
	255.02	44	0.003	16.0
	285.00	46	0.007	-15.6
Expansion	315.01	45	0.004	28.7
	345.02	50	0.005	1.9
	375.02	53	0.004	18.3

The data in Table 3 indicate that any static distortion due to the complementary modulation or the acoustics in general were less than 1% which was felt to be close to the limit of the technique used to digitize the surface.

2. Concentricity. The other aspect of shell shape of concern in this experiment was the concentricity of the two air/water boundaries. The torque applied a few seconds after deployment quickly moved the bubble to the center of the shell and it remained there until the middle of the expansion experiment. There was no success in centering the bubble along the z axis. Rotation and the stimulated oscillation were not able to move the bubble into a more centered position. The effect of the presence of the three small bubbles was to inhibit the bubble's centering. Even though they appeared small enough to move freely between the two larger surfaces, the fact that they did not leave the plane in which they were rotating - despite the centripetal forces toward the center - indicated that there was no freedom of movement between the bubble and the shell near the small bubbles. Just as the small bubbles were constrained, so was the large one.

C. Natural Oscillation

The experiment was designed to provide several opportunities for observing the frequencies and damping characteristics of the natural oscillations of the liquid shell and to compare the former with the predictions of compound drop theory. The retraction of the injectors was expected to excite oscillations in both boundaries. When the amplitude-modulated driving forces were removed at the end of the three stimulated oscillation sequences, the frequencies and decay times of the oscillations which occurred were characteristic of the shell's free oscillations.

After deployment the shell oscillated freely for three seconds before the acoustic torque was applied. The oscillations after each of the three forced oscillation sequences damped out relatively quickly but some frequency and damping information was available. During the expansion sequence two of the three unexpected small bubbles popped causing ripples which were visible to the eye when the film was reviewed at slow speed but were not accessible to quantitative analysis. In addition because of an imbalance in the acoustic forces during the rotation sequence which deformed the shell, there were slight oscillations in the outer boundary at 173 seconds ALO (after lift-off) when the forces were brought back into balance.

The BOX method was used to describe the boundaries and various combinations of this data were used to identify which modes of oscillation were present. For each mode that was observed an oscillation frequency, f_n, and whenever possible, a damping coefficient, β_n, were determined.

Because the inner and outer surfaces of the shell adherred to the coaxial air/water injectors, they both were deformed when the probes retracted. The surfaces moved with the probes until the adhesive forces were no longer able to balance the surface tension forces and the surfaces broke free of the metal tips. The extra surface energy gained in the 0.04 seconds (~ 138.0674-138.0267sec) that it took for the shell to break free from the retracting injectors was sufficient to generate surface tension-driven oscillations whose amplitudes were 5 and 10% of the outer radius for the outer and inner surfaces, respectively. Because the injectors were in contact with both the inner and outer surfaces and because both surfaces were 'plucked' at the same time, the lowest order bubble mode, f(2+) ~ 6.3Hz, was expected to be prominent. The n=2,+ sub-mode is the lowest frequency mode in which the two surfaces move in phase. However since the shell was not centered between the probes and hence the stimulation was not symmetric, it was not clear to what degree this mode would be present.

Because the bubble was not centered, the existing theoretical development did not apply exactly. However it was felt that the frequencies of the free oscillation would be close to those for a concentric shell, especially since the theory predicted that the oscillations of the two surfaces would not be coupled very strongly (even if concentric) for such a thick shell. The

three small bubbles which were injected before the air flowing from each injector coalesced into what became the large bubble have been ignored in the calculation of the oscillation frequencies because they occupied only 0.3% of the volume of the total shell.

Data Analysis

A. Outer Boundary - after deployment. At no time was it possible to visually identify a particular mode directly from the film record. Because the inner boundary was difficult to define, the outer boundary alone was used for the initial study. It was felt that the response of the outer boundary would be adaquate for the identification and study of the lower order sloshing modes which would excite primarily the outer surface.

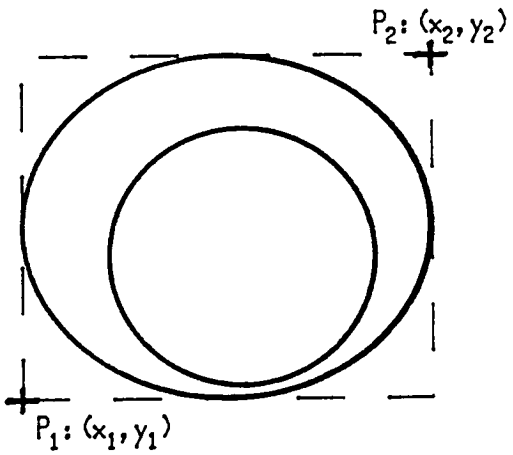

The two points required to define the minimal rectangle with vertical sides which contained the entire image of the shell and the time were recorded for each frame studied. The four graphs of Figure 1 illustrate the data obtained by combining the coordinates of the two points in various ways for the time immediately after deployment.

The relative amplitude of the oscillations for the first fraction of a second are 5% of the resting radius, a, for the response in the vertical direction, i.e. $V = (y_2-y_1)/2a$. For comparison, the amplitude of the displacement used to generate the shapes in Figure 2 of the theoretical section (Section 4.2) was 20%. By studying the envelope of the oscillations as their amplitude decreased an estimate of the damping was made. Using the first second of the Vertical data, a rate of decay, $\beta_V = 0.58$ sec^{-1} was obtained for an oscillation of roughly 6 Hz. Using the Difference data, $\beta_D = 0.74$ sec^{-1} for oscillations which were at 6.6Hz for at least the first 0.5 second after deployment.

The inviscid compound drop theory has predicted that the motions of the two surfaces for a shell of this size will be uncoupled. Assuming that they are uncoupled one can use the behavior of simple drops to estimate the damping coefficient for the low order sloshing sub-modes of the compound drop: $\beta_{2-} \sim 0.028$ sec^{-1}, $\beta_{3-} \sim 0.078$ sec^{-1}, and $\beta_{4-} \sim 0.151$ sec^{-1}. The damping coefficients predicted for the bubble sub-modes are $b_{2+} \sim 0.149$ sec^{-1} and $b_{3+} \sim 0.278$ sec^{-1}. The observed values are greater than any of the theoretical damping coefficients.

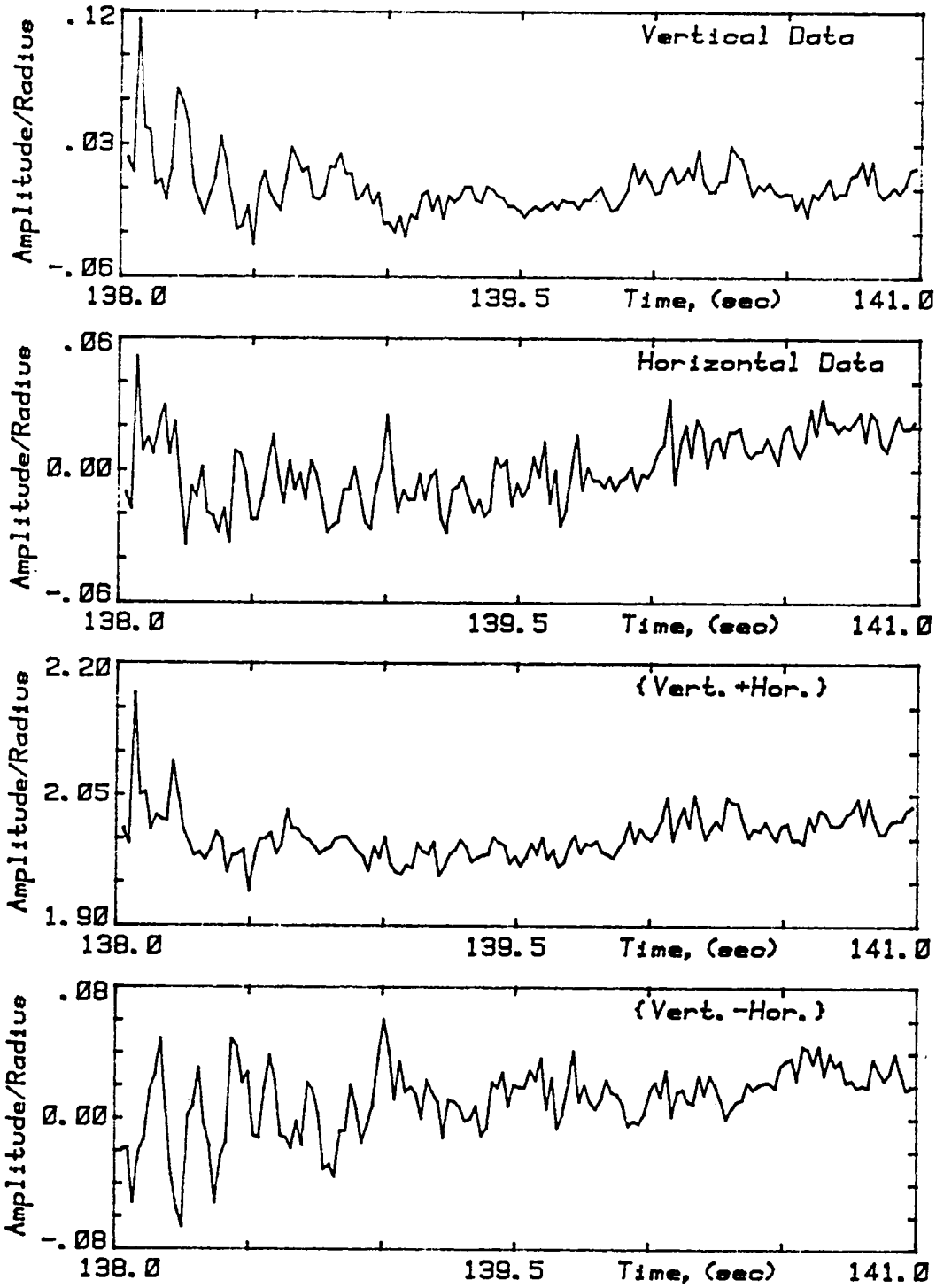

Figure 1. Four combinations of the BOX data describing the outer surface used to study the natural oscillations and damping after deployment of the shell.

To obtain more accurate values for the frequencies of these oscillations and to identify any signals which were not apparent in Figure 1, the BOX data was Fourier-transformed. Figure 2 contains the resulting frequency spectra (actually the square root of the power spectra) for the four combinations shown in Figure 1. The frequencies for each of the sub-modes were calculated from the theoretical model for a concentric water shell with the programmed volumes and are indicated on each graph by vertical lines. The resolution is limited by the length of time available to study the free oscillations after deployment - only three seconds. This gives rise to a limit upon the resolution of .3 Hz. The largest frequency which can be detected depends on the density of the time data: taking data from each frame available as was done here, at 48 frames/second, the imposed limit was $f_{max} \sim 24$Hz.

The peaks near 1.9Hz in all four graphs of Figure 2 are identified with the expected lowest order sloshing mode, f_{2-}, predicted to have a value of 1.80Hz. It is visible in the data of Figure 1 in the undulations of the envelope of the Difference data. The frequency peak for this combination has a width of 0.50 sec^{-1} at 0.707 times the maximum value. In the Vertical and Horizontal data the peaks are approximately 0.30 sec^{-1} wide. The widths of the peaks indicates the magnitude of the damping coefficient. However in this case the widths are the result of broadening due to the limited number of data points, so the values of β_v and β_h are actually less than 0.30 sec^{-1}. The value from the analysis of the time data, $\beta_D \sim 0.78$ sec^{-1}, is much greater.

The peaks near 3.7Hz in three of the four spectra are close to the predicted value of 3.9Hz for the n=3- oscillation frequency. If this particular mode is sensitive to either the shell's non-concentricity or the presence of the three small bubbles, the predictions of the concentric model may not be appropriate. If this mode were present its response would be due to the non-symmetrical stimulation of the shell at retraction. It is not possible to obtain damping information from the time data for this peak. The width of the frequency peaks, ~ 0.33 sec^{-1}, is due to the limited number of data, so $\beta_{3-} \lesssim$ 0.1 sec^{-1}. The value predicted by the model is 0.078 sec^{-1}.

There is a collection of peaks in the Vertical data near the expected frequencies of the n=2+ and n=4- oscillations, 6.32 and 6.51Hz, in which the central peak is at 6.67Hz and there are eight side peaks at 6.7 ± 0.4, $6.8 \pm$ 0.9Hz, 6.8 ± 1.4Hz, and 6.7 ± 1.9Hz. The regular spacing of 0.5Hz between the peaks and their number suggests that a degeneracy may have been broken in the 4- sub-mode. Another possible explanation is that the oscillation of both 2+ and 4- modes at frequencies which were almost the same causes an interaction between them which produces such a family of peaks. More likely is that the family of peaks is due to the Fourier-transformation of two decaying signals with a frequency separation of 0.8 Hz for a short period of time. Similar features in this frequency range were not seen in the spectra of the other combinations: the Horizontal and Sum data show no symmetry about 6.7Hz and the Difference data has a peak at 7.0Hz and two side peaks at 7.0 ± 0.7Hz. The widths of the Sum and Difference data are 0.30 and 0.54 sec^{-1}, respectively. The overall width of the family of peaks in the Vertical data is 1.4 sec^{-1}.

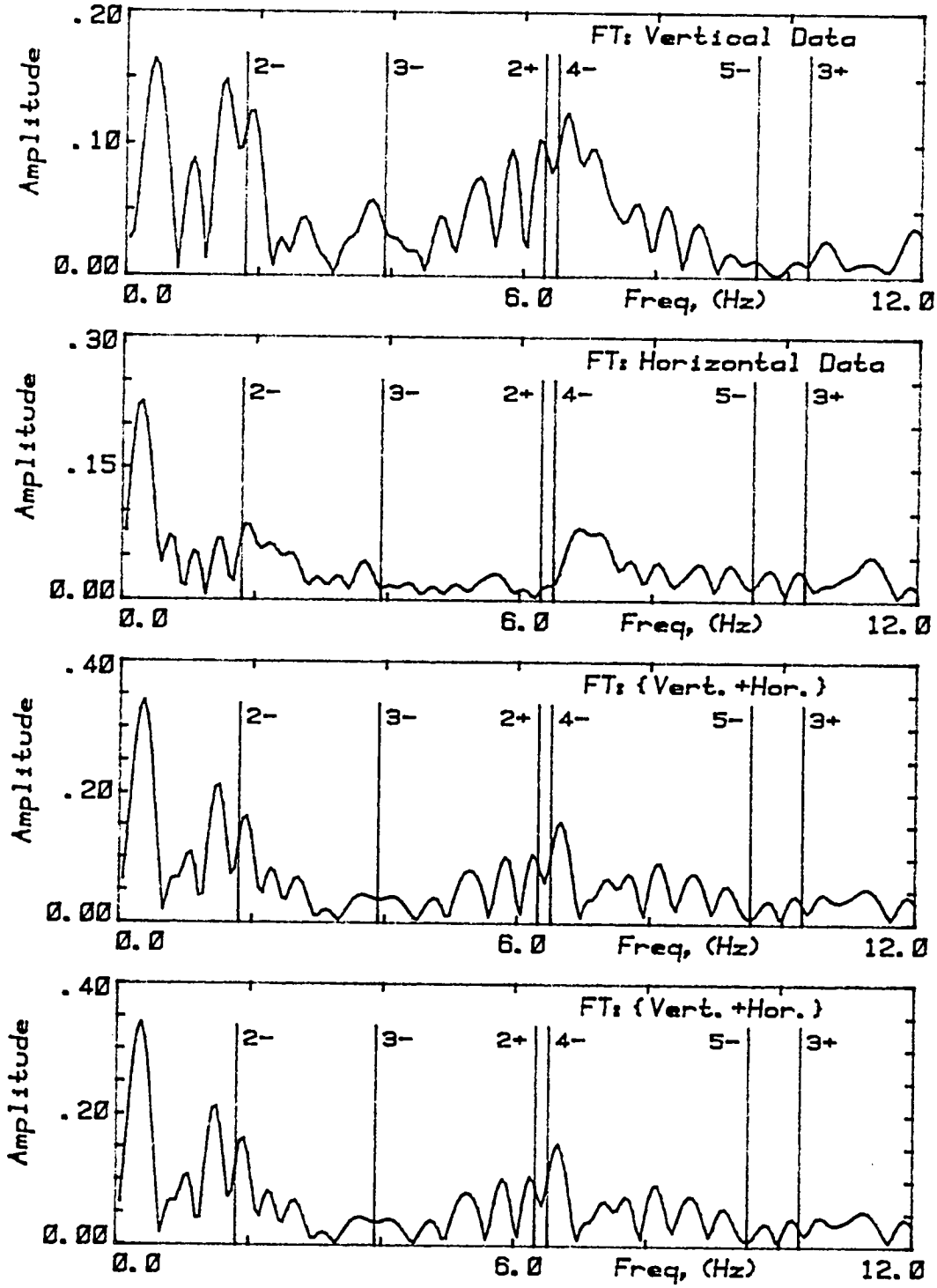

Figure 2. Fourier spectra obtained from the temporal data of Figure 1. The vertical lines indicate the predicted frequencies of the oscillations.

No signals in this data were identified with the n=5- and n=3+ oscillations expected at 9.5 and 10.3Hz.

Table A. Summary of Information from Outer Boundary after Deployment

mode	source	Frequency (obs.)	Frequency (th.)	Damping Coef. (obs.)	Damping Coef. (th.)
2+,4-?	V[t]	~6 Hz	6.3,6.5?	$1.73 s^{-1}$	$0.15 s^{-1}$
2+,4-?	D[t]	6.6	6.3,6.5?	1.35	0.15
2-	V,H,S[F]	1.89	1.80Hz.	1.60	0.028
3-	V,H,D[F]	3.68	3.90	0.30	0.078
2+,4-?	V[F]	6.67*	6.3,6.5?	0.40	~0.15
2-	D[F]	1.84	1.80	0.50	0.028
2+,4-?	D[F]	7.01	6.3,6.5?	0.50	0.150

* - family of peaks

B. Inner boundary - after deployment. The compound drop theory predicts that the amplitude of the displacement of the inner boundary would be much larger than that of the outer surface for bubble mode oscillations. Figure 3 shows BOX data for the bubble between retraction and the application of torque. The data were normalized by the resting radius of the outer boundary. No attempt has been made to remove the distortion due to viewing the bubble boundary through a curved surface which itself may be oscillating. While this extra signal may hide some of the bubble's behavior, it would be a complex matter to unfold its effect from the data and it provided another source to confirm observations and conclusions from the outer boundary analysis.

The amplitude of the Horizontal signal just after retraction was 9% of the resting radius. Also from this data a value of the damping coefficient was determined for an oscillation arround 7 Hz: $b_H \sim 0.58 \pm .15$ sec^{-1}. This was greater than the damping coefficient predicted for the lowest mode of oscillation for a 4.21cm^3 bubble in an infinite host: $b_{2+} \sim 0.149 \text{sec}^{-1}$. The oscillation frequency for the n=2, bubble submode was 6.3Hz. There were brief sequences of periodic behavior in the Sum and Difference data in which the data appeared to be the result of the beating of two signals seperated roughly by 0.6 Hz.

The Fourier transforms of the temporal data for the bubble dimensions are shown in Figure 4. The spectra of the Vertical data contains peaks at 6.3 Hz (2+ or 4-?), 2.0 Hz (2-), and 10.4 Hz (3+), while in the spectra for the Horizontal data there is a small 6.3 Hz signal and a large 7.1 Hz one. This indicates that the oscillations of the bubble differ in frequency between the two directions - meaning that the BOX method was sensitive to different oscillations when viewed along a given axes. Signals from the n=4- oscillations for which the shapes have a four-fold symmetry, should be amplified by the Sum and minimized by the Difference combinations. Similarly because the n=2+ will be unsymmetric, its Difference signal will be larger than that of

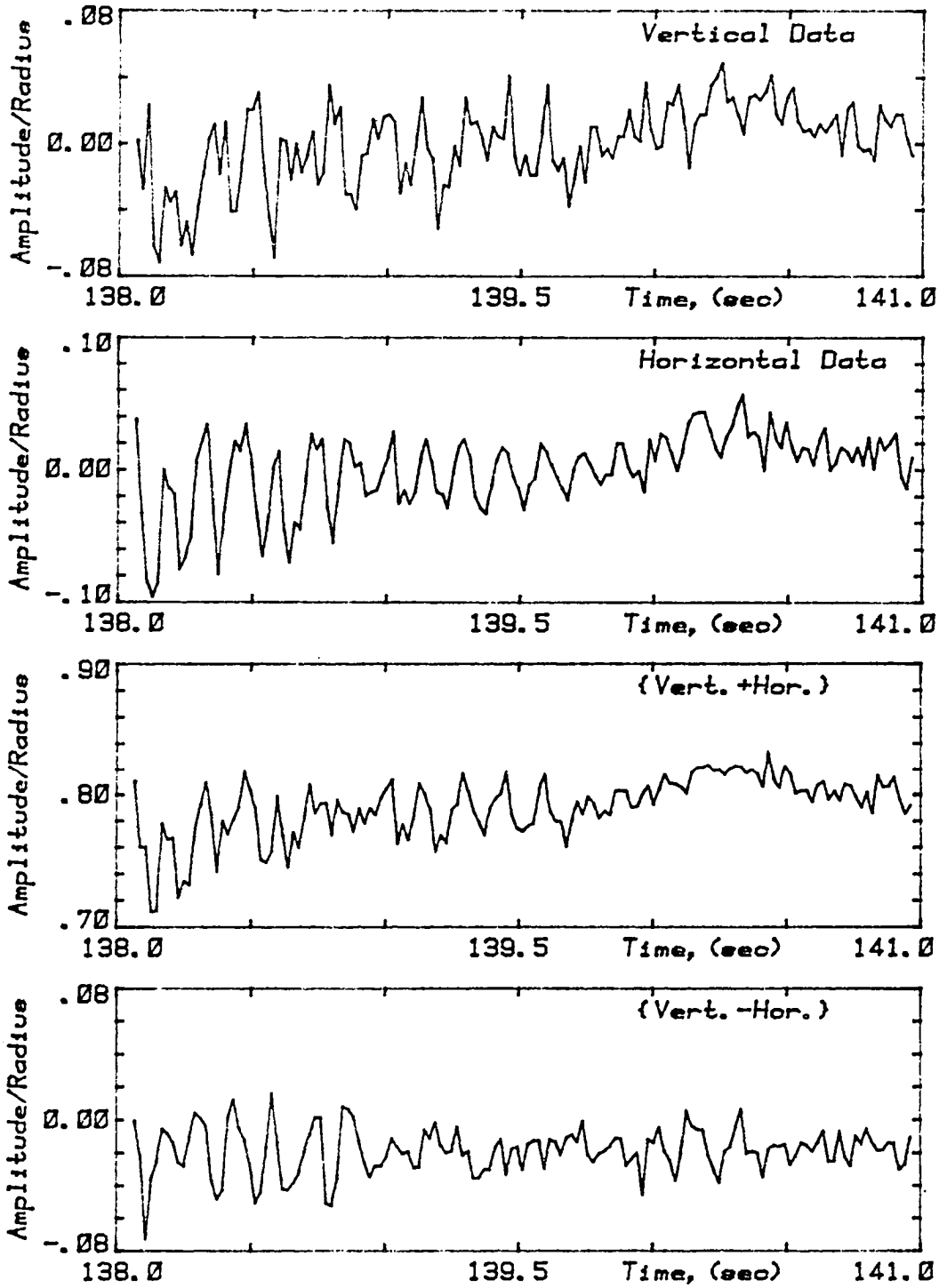

Figure 3. Box data using the inner surface for the three seconds after deployment and before the rotation sequence.

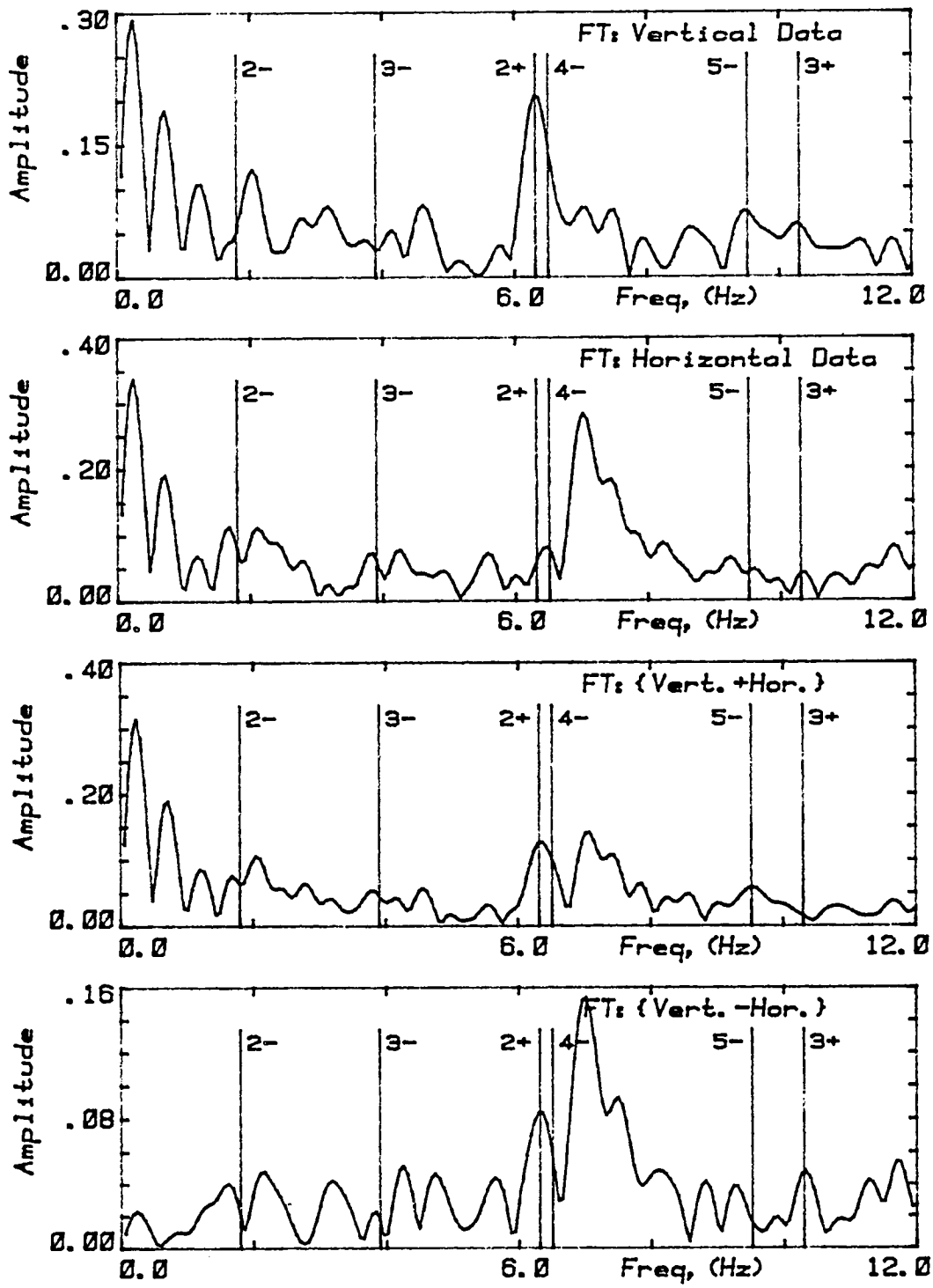

Figure 4. Fourier spectra of the Box data from the inner surface. The predicted frequencies of the normal mode oscillations are given by the vertical lines.

the Sum. The relative amplitude of the peak at 6.3 Hz in the Difference data is roughly a third less than its value in the Sum data while the magnitude of the 7.1 Hz peak does not change. This evidence indicates that the 6.3 Hz signal could be the n = 4, sloshing, mode which was predicted to occur at 6.5 Hz.

There were peaks in the spectra of the Horizontal, Vertical and Difference data near the anticipated n=3+ oscillation frequency at 10.4 Hz. The facts that it is at the predicted frequency, appears in three of the four data combinations, and that the shell was stimulated assymmetrically all lend support to identifying this signal as the n=3+ mode oscillation. No damping information could be isolated for this mode.

The peaks at 2.0Hz in the Vertical and Sum data in Figure 4 were identified with the n=2 sloshing sub-mode. They were probably the result of viewing the inner surface through the oscillating outer surface or possibly the result of motion in the inner boundary on a greater scale than the theory had predicted, i.e. $\delta R_i(n=2-) \sim (1/597)\delta R_o(n=2-)$.

Table B. Summary of Information from the Inner Boundary after Deployment

mode	source	Frequency		Damping Coef.	
		(obs.)	(th.)	(obs.)	(th.)
2+,4-?	H[t]	~7Hz	6.3,6.5	$0.58s^{-1}$	$0.15s^{-1}$
2+?	H,S,D[F]	7.0	6.3Hz.	0.39	0.15
2-	V,S[F]	2.0	1.80	0.36	0.03
3+	V,H,D[F]	10.4	10.3	0.30	0.28
4-?	H,S,D[F]	6.3	6.5	0.39	0.15

C. Combined Data: inner and outer boundaries - after deployment. Because the above data did not clearly identify the modes to which the 6.3 and 7.0 signals corresponded, the data from both surfaces were combined. Information about the oscillation modes should be provided as well as about bubble centering by this data. If the motion of the two surfaces were coupled, the presence of the bubble modes would be harder to detect, and the stronger the coupling, the more prominent the sloshing modes should be.

Figures 5 and 6 contain the time and frequency descriptions of the thickness of the shell as seen in the main view. The data indicate that the bubble moved to the left and slightly towards the top during the first three seconds. The data were checked to determine if they were the result of surface oscillations or of center of mass motions. Study of the appropriate combinations of data during this period indicated that this centering was not due to relative bubble motion as the shell moved in the potential well. The amplitude of the left side time data decreased with a decay constant of $\beta \sim 0.83\ sec^{-1}$ while oscillating near 7 Hz. The Bottom data shows a strong signal at 6.3 Hz, as well as lesser peaks at 1.9 and 10.3 Hz. It also is the region with the greatest thickness.

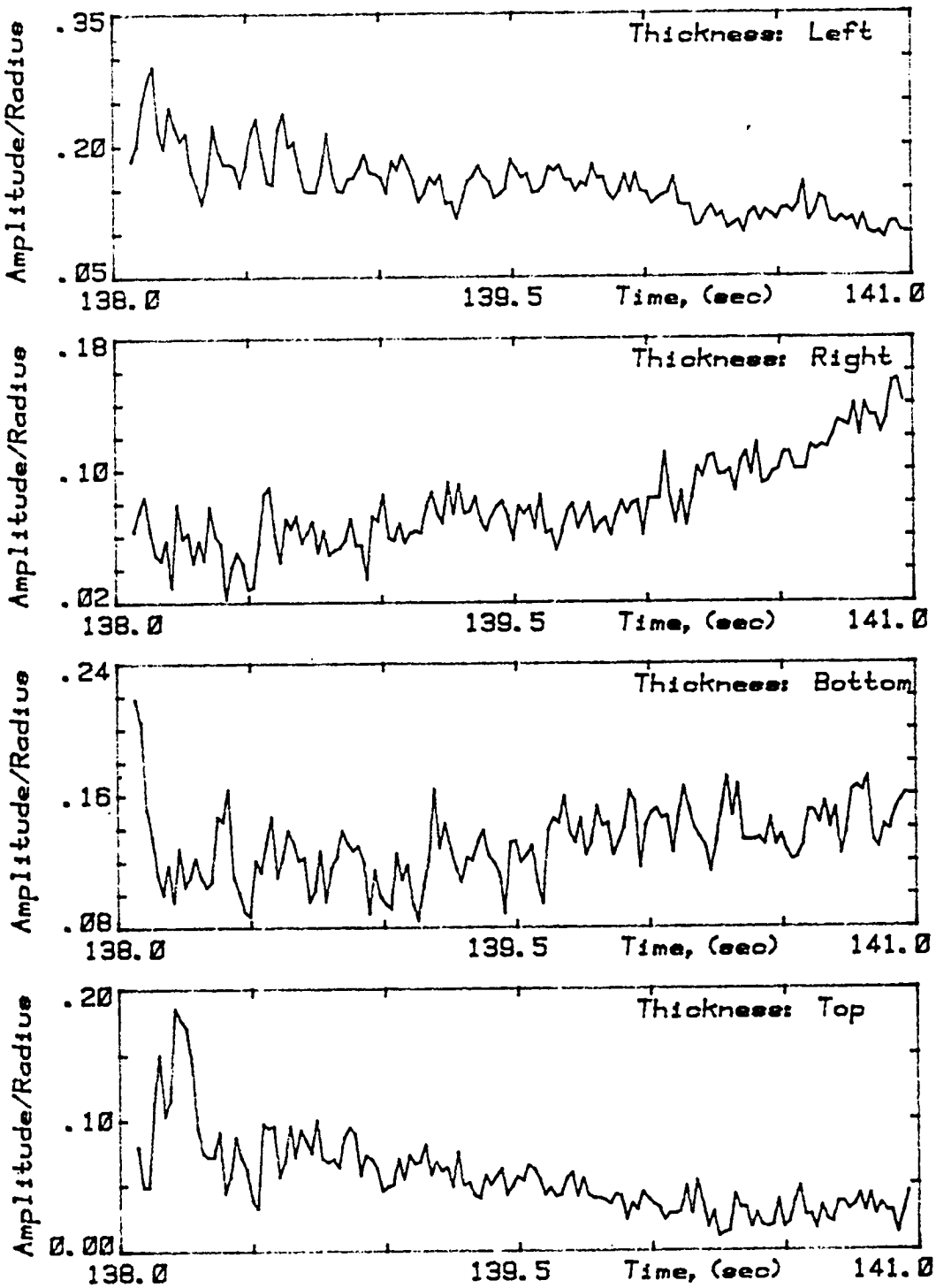

Figure 5. Data combining the Box information from both surfaces for the period between deployment and the applied torque.

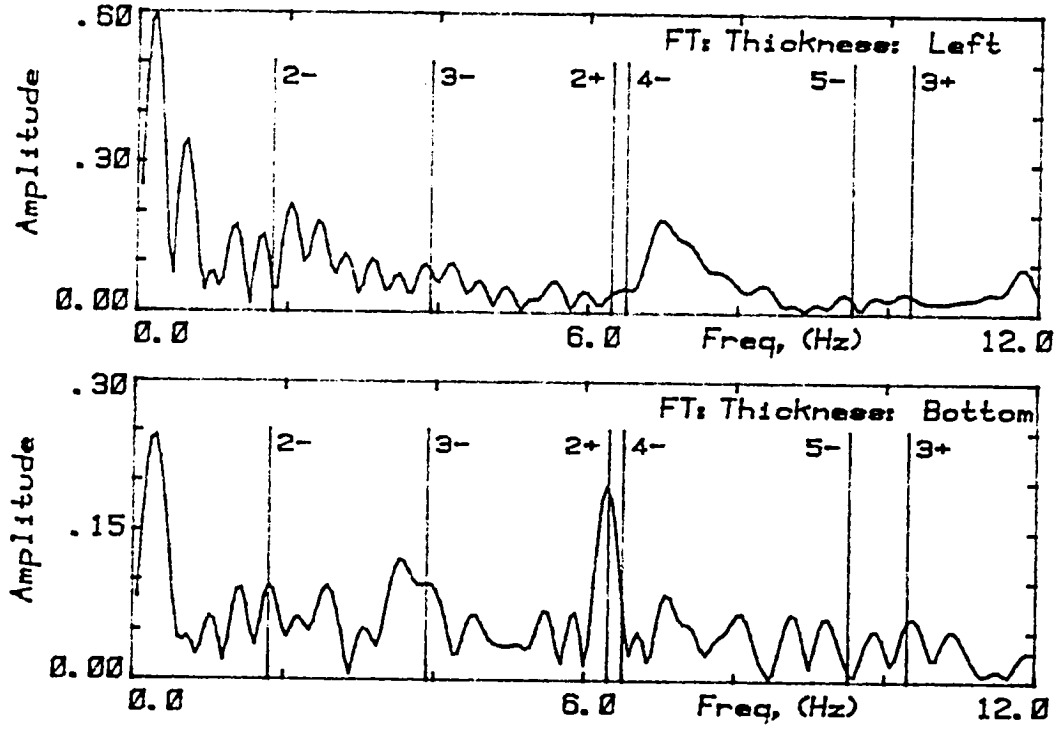

Figure 6. Fourier spectra from the thickness of the shell on the left and the bottom.

It is surprising that a strong signal for the n=2- oscillation is not present in any of the combined data for it was the lowest energy mode and was present in the data for both the inner and outer surfaces.

Table C. Summary of Information from the Combined Data after Deployment

mode	source	Frequency (obs.)	Frequency (th.)	Damping Coef. (obs.)	Damping Coef. (th.)
2+,4-?	L[t]	~7 Hz	6.3,6.5?	$0.83s^{-1}$	$0.15s^{-1}$
2+,4-?	B[F]	6.3	6.3,6.5	0.27	0.15
2-	B[F]	1.9	1.8		
2+,4-?	L[F]	7.0	6.3,6.5?		

D. Spot Study - after deployment. In an effort to verify and clarify the above observations another look at the oscillations after retraction was made using the positions of two bright spots, reflected images of the same photolight visible in the main view from the two surfaces. The four numbers were put through the same analysis described above. Some of the time and frequency results are shown in Figure 7.

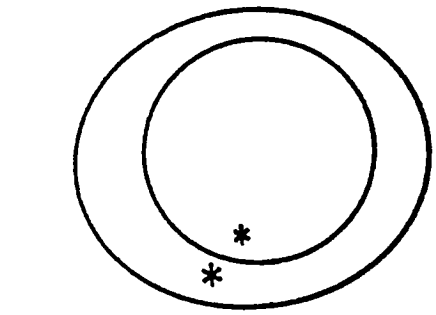

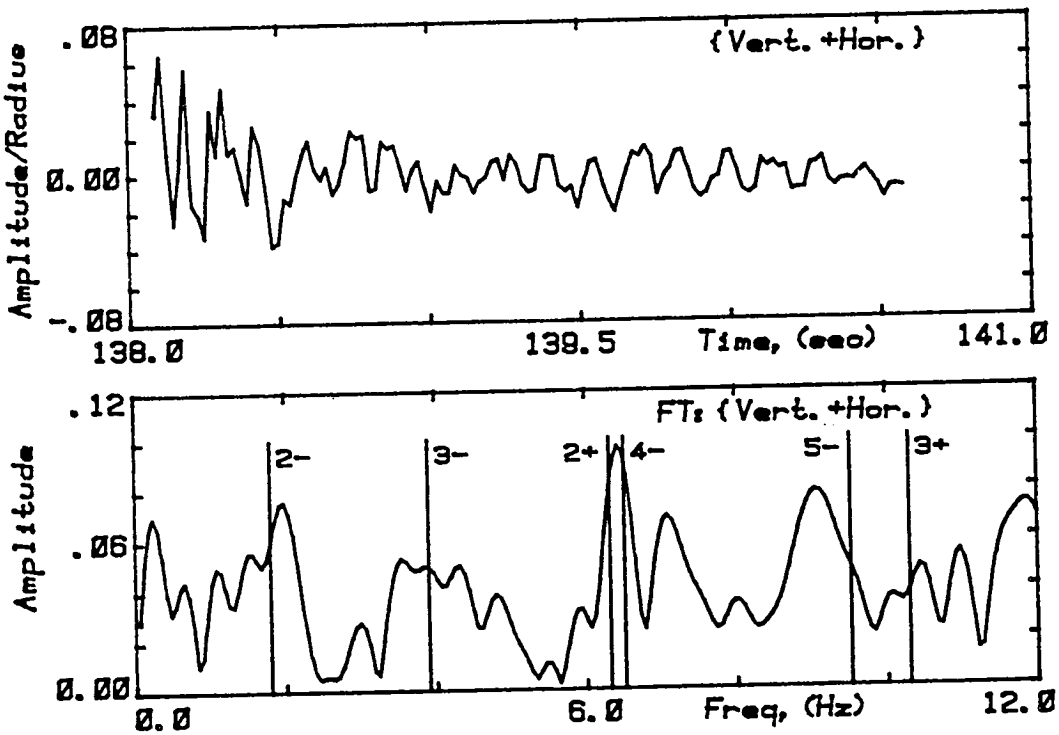

Figure 7. The reflections of a photo-lamp from the two surfaces were used to study the frequencies and damping of the natural oscillations after deployment.

Information on the damping coefficients was obtained from the Horizontal and Sum data: $\beta \sim 0.22\,sec^{-1}$ and $\beta \sim 0.33\,sec^{-1}$ at indeterminate frequencies. The center of mass motion dominated the other signals because the relative positions of the reflections were highly sensitive to the location of the shell in the chamber. The effects of the bulk motion of the drop seemed to cancel each other out for the Sum data. The resulting frequency spectra shows peaks at 1.96, 6.43, 7.08 and 9.07Hz. The first peak corresponds well with the previous identifications of the f_{2-} mode (at least within the limits imposed by the finite time available - .4Hz). The peaks at 6.4 and 7.1 Hz were also seen in other data and have been identified with the n=4- and n=2+

modes - although which is which is not clear - but the spot data adds no new information. The broad peak at 9.1 Hz was not seen in other spectra.

Table D. Summary of Information from the Two Spots after Deployment

mode	source	Frequency (obs.)	Frequency (th.)	Damping Coef. (obs.)	Damping Coef. (th.)
?	H[t]			$1.74s^{-1}$	
?	S[t]			0.33	
2-	S[F]	1.96Hz	1.8Hz	0.42	0.03Hz
2+,4-?	H,S[F]	6.43	6.3,6.5?	0.35	0.15
2+,4-?	H,S[F]	7.08	6.3,6.5?	0.45	0.15
?	S[F]	9.07			

E. Outer boundary - after the acoustic torque was removed. When the acoustic torque was turned off at 173 seconds ALO the shell 'popped' back to roughly spherical shape after having been flattened by an imbalance between the x- and y-axis acoustic forces (see Section 5B for more information about the imbalance). This flattening was along an axis perpendicular to the axis of rotation. Figure 8 shows the data obtained from this period. The time data includes the normalized amplitude for the last half second of the applied

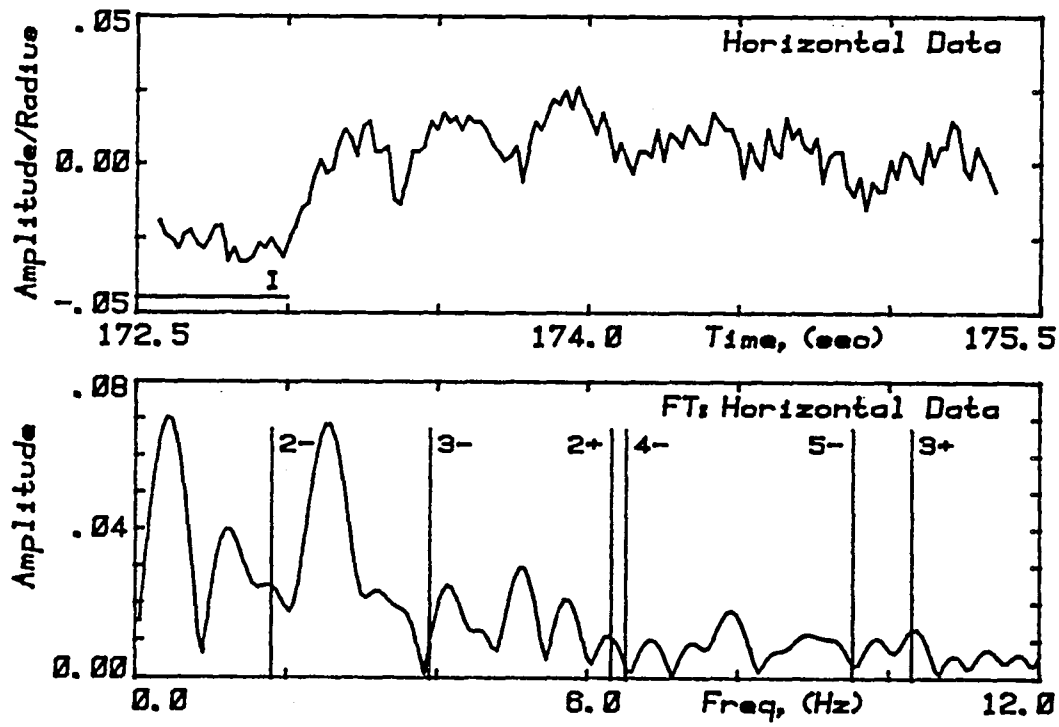

Figure 8. This data showing the effects of rotation and free oscillation when the torque was removed.

torque sequence while only the data after 173.15 seconds were Fourier transformed. During this time the shell was rotating at roughly 3.1 radians per second at the poles about an axis perpendicular to the images studied. This rotation would produce a frequency peak near 3.1 rps (or 1.0Hz) for a deformed shell and split any oscillation peaks by the same amount. The n=2- mode was expected to dominate as the outer boundary relaxed, peaks were expected at 1.9 $\pm$ 1.0 Hz.

The peaks in the Horizontal frequency data at 1.2 and 2.55 Hz indicate a rate of rotation of 4.2 radians/sec at the equator. It is probable that at this time the equator was moving at a faster rate than the poles because the trace bubbles at the top were rotating faster after the torque was removed. The effects due to oscillation are small because of the rotation of the shell. Changes in the acoustic centering forces require times on the order of $Q/f_x \sim 0.05$ sec and the expected time characteristic of the damping, roughly 36 seconds. The change from distorted to circular profile took approximately 0.2 seconds which would indicate that the restored balanced force pushed the drop into symmetry rather than allowing it to relax naturally.

Table E. Summary of Information from Data Taken as Torque Was Removed

mode	source	Frequency (obs.)	Frequency (th.)	Damping Coef. (obs.)	Damping Coef. (th.)
2-	H[F]	1.89 Hz	1.80 Hz		$0.03 s^{-1}$
Rotation Rate	H[F]	$\pm$0.67			

F. Both boundaries - after stimulated oscillations. At the end of each of the three stimulated oscillation sequences, the amplitude modulation of the z axis centering signal was turned off. As the force was removed the shell responded with natural oscillations which decreased in a time characteristc of the excited mode's damping coefficient. Because the deformation was greatest along the direction of propagation of the amplitude-modulated sound, a side view which showed the image in the x=0 plane was used. The outer boundary was described by a box and a spot of light reflected off the top of the inner boundary was used as an indicator of the bubble's response. Even though the shell was rotating during these sequences, Ω(216sec) ~ 3.6rps, Ω(246sec) ~ 3.5rps, and Ω(276) ~ 3.0rps, its effects were minimized by using data in the direction of the axis of rotation.

1) After the 5.0 to 7.0 Hz modulation. From analysis of the oscillations of the shell's size after the modulated centering force had been removed, $\beta_V \sim 0.59\ s^{-1}$. Fourier analysis of the data after 216 seconds showed that the dominant frequency was 7.23 Hz with smaller peaks at 6.5 and 8.0 Hz (see Figure 8). The smaller peaks represent a rotation rate of 4.7 rps which is 25% greater than the rate indicated by the small bubbles at the pole (see scetion 5D). Close study of the shell's behavior on the film did not help to distinguish whether the oscillations observed corresponded to the n=2 bubble sub-mode or to the n=4 sloshing mode.

2) After the 1.0 to 2.4Hz sequence. The data shown in Figure 9 give $\beta_T \sim 0.86$ sec^{-1} which is lower than that obtained from the data after deployment but still quite a bit larger than the predicted value.

3) After the 2.5 to 4.0 Hz modulation. The already small signal decreased at a rate of 1.95 sec^{-1}. It should not be possible to stimulate odd mode oscillations with a symmetric acoustic field. The dominant feature in the transformed Thickness data is the n=2- peak.

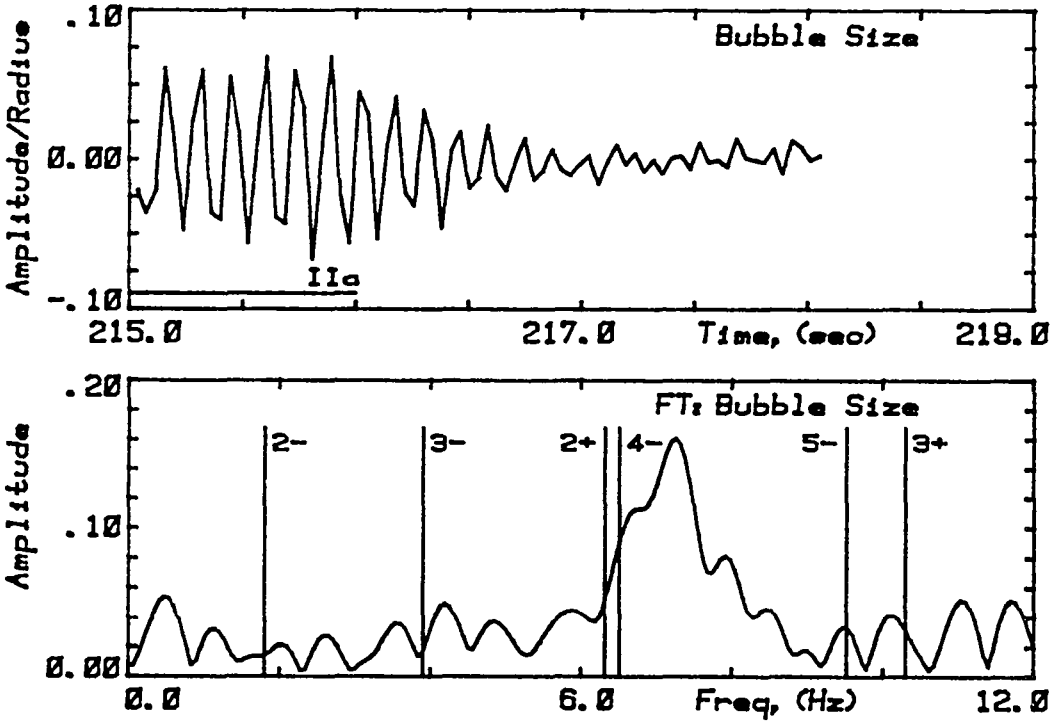

Figure 9. Free decay of the oscillations stimulated by the amplitude modulation of the z axis (swept from 5.0 to 7.0Hz).

Table F. Summary of Information from Data Taken after Modulation

mode	source	Frequency (obs.)	Frequency (th.)	Damping Coef. (obs.)	Damping Coef. (th.)
2+,4-?	1:V,B[F]	7.24Hz	6.3,6.5?		
Rotation rate (4.7rps)		±.75Hz			
2+,4-?	V[F]	6.5	6.3,6.5		
2+,4-?	V[t]			$0.59s^{-1}$	$0.15s^{-1}$
2+,4-?	B[t]			0.55	0.15
2-	2: T[t]	2.01	1.80	0.86	0.03
2-	D[F]	1.85	1.80	0.59	0.03
2-	T,H[F]	2.01	1.80	0.60	0.03
3-	3: B[t]			1.95	0.08
3-	T[F]	3.90	3.90		
2-	T[F]	1.81	1.80	0.81	0.03

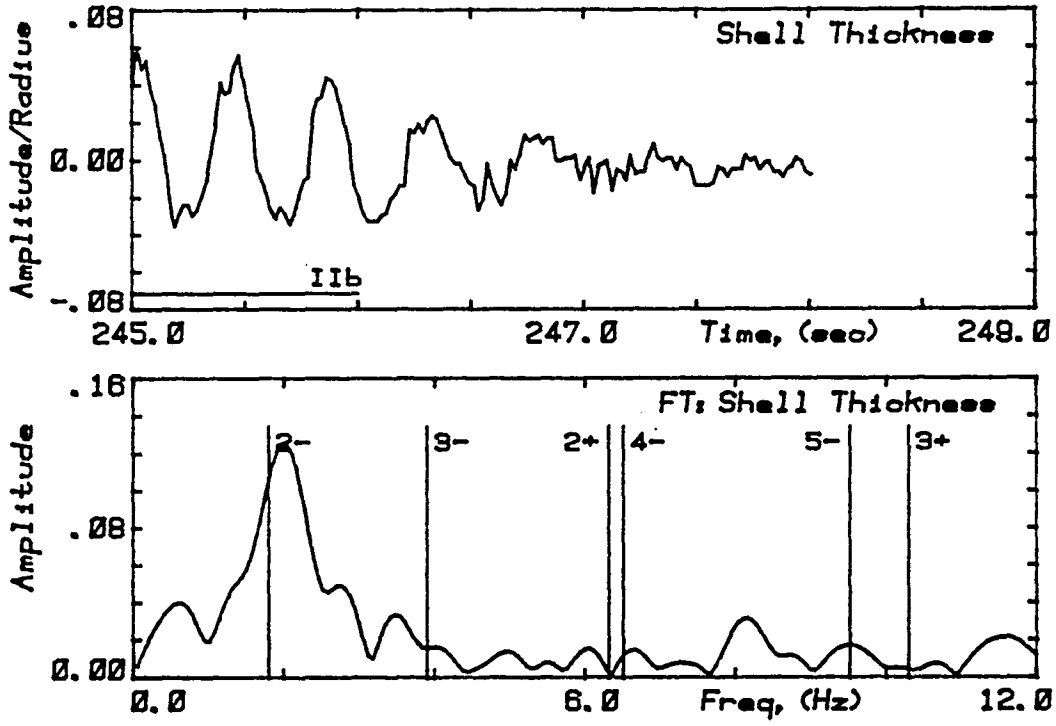

Figure 10. Free decay of the oscillations stimulated by the amplitude modulation of the z axis (swept from 1.0 to 2.4 Hz).

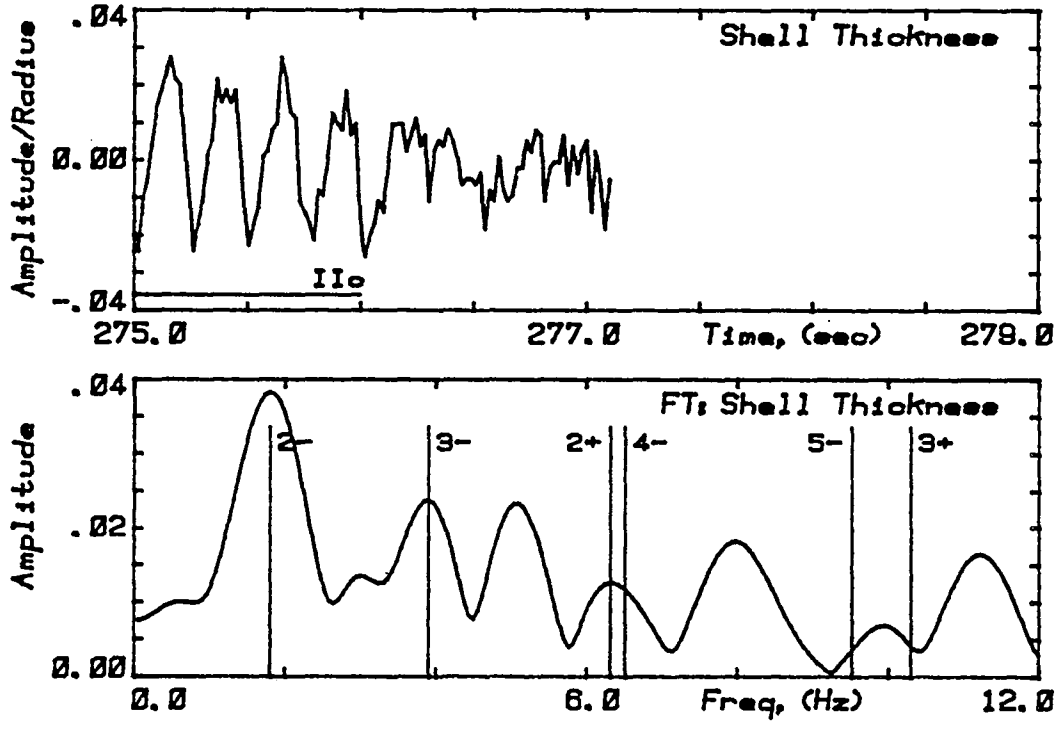

Figure 11. Free decay of the oscillations stimulated by the amplitude modulation of the z axis (swept from 2.5 to 4.0 Hz).

D. Acoustically Induced Rotation

The purpose of the rotation sequence was to observe the centering of a nonconcentric bubble when an acoustic torque was applied to the liquid shell. The rotation will cause a large centripetal force toward the axis of rotation and secondary flows may cause centering along the axis. This sequence also provided an opportunity to study the spin-up characteristics of a shell responding to an acoustic torque under controlled conditions.

At 141 seconds ALO - three seconds after the shell was deployed - the complementary modulation was switched off and both the x and y drivers were operated at constant amplitudes and with a constant phase difference of 90° between their acoustic signals. This produced an acoustic torque upon the shell about the z axis which caused it to rotate. The torque was removed at 173 seconds and there was a 25 second relaxation period before the forced oscillation sequence began.

Centering of the Bubble. The two graphs in Figure 1 show the location of the bubble's center relative to that of the outer boundary as functions of time. The data were taken from the main view of the chamber, so the image is that of the equatorial plane. The degree of centeredness is quantified by the parameter Δ,

$$\Delta_{LR} \equiv \delta_L - \delta_R$$

$$\Delta_{BT} \equiv \delta_B - \delta_T$$

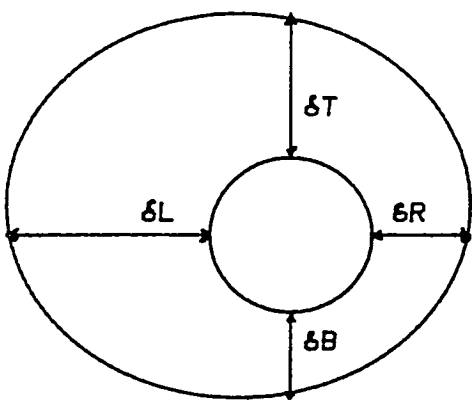

If the bubble's center is to the upper right of the shell's, then both Δ's will be greater than zero, and when the surfaces are concentric both will be zero. The position of the shell in the chamber along each direction is included.

The bubble began on the left side and remained on that side. Along the other direction the bubble center oscillated about the shell's center with decreasing amplitude. The relation between the motion of the shell in the chamber (the solid lines) and the bubble within the shell (the points) is not clear from the first twenty seconds of this data when the amplitude of the bubble's oscillation was decreasing. Thereafter the rotation was sufficient to overwhelm it. The scatter in the data is a reflection of the difficulty of determining the edge of the inner boundary. The non-zero mean value is due to the camera's viewing the bubble at a slight angle to the z axis and because the bubble did not center along the axis of rotation.

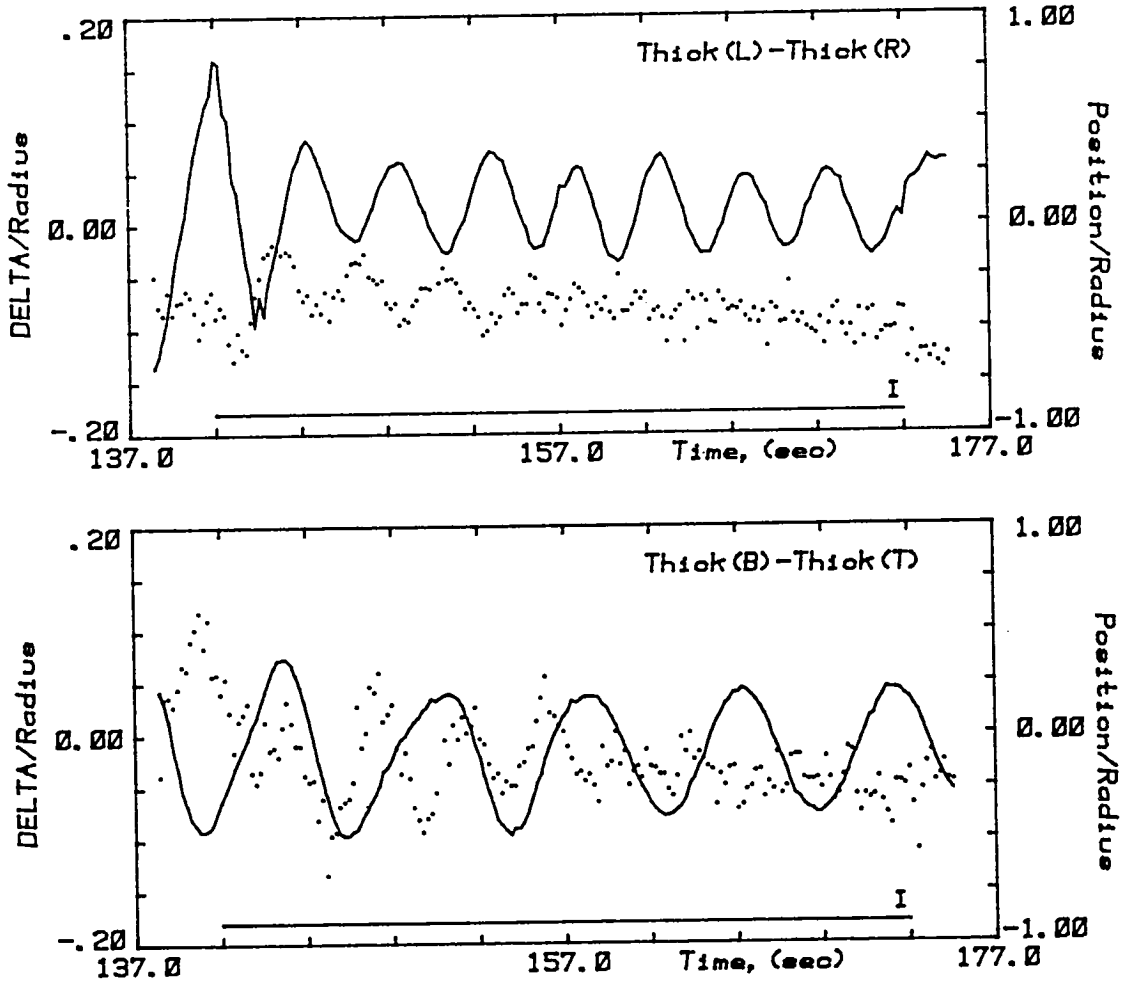

Figure 1. Centering of the bubble in the equatorial plane as the shell begins to rotate. The data points (and the left scale), show the concentricity of the two surfaces. The solid curves (and the right scale) give the position of the shell in the chamber relative to the center.

No forces along the axis of rotation were expected after the shell had achieved solid body rotation however it was considered that the differential rotation during spin-up might cause secondary forces upon the bubble in that direction. The fact that the bubble did not appear to move more to the center of the shell along the z axis confirms that these forces if they exist are very small.

In addition to the desired bubble, there were three small bubbles whose diameters were about 10% of that of the shell. As the shell began to rotate they migrated to the axis of rotation where they formed a stable triad at 150 seconds which remained at the pole until two of them burst during the expansion sequence.

These bubbles appeared small enough to allow the large bubble to move along the axis of rotation - but it did not move. That there was no room to move along the axis of rotation was supported by the observation that the bubbles remained in a plane perpendicular to that axis despite the centripetal forces to which which they were subjected.

Study of the Shell's Rotation. Without trace particles the only way of establishing the existence of rotation of a drop or shell from a film record is to observe the flattening of its poles and/or the bulging at the equator. To obtain the magnitude of the rate of rotation the change of shape must be used within a theoretical framework that relates the degree of oblateness to the angular velocity in a well-defined manner. The pertinent theory has been developed for simple drops in solid-body rotation by Chandrasekhar, Ross and Brown but no development exists to describe the spin-up of a viscous drop in which the angular velocity is not constant throughout the liquid.[25,26,27] Figure 2 in the theoretical section (sec. 4C) shows the relation between size and the rotation rate for a simple drop in solid-body rotation.

Using the BOX data read from the Vanguard Motion Analyser, the increase in the size of the shell in the equatorial plane (i.e. the image in the main view) and its slow decrease after the torque was removed were visible. Figure 2 shows the sum of the vertical and horizontal dimensions of the outer boundary of the shell as seen in the main view. When normalized by the resting radius the result is an average radius for the shell in the equatorial plane. The dashed line is a no-torque baseline taken from the data during the first three seconds when the shell was not being manipulated. The spin-down data, 173 to 215 seconds ALO (after lift-off), were fit to the function

$$F(t) = \frac{F(t_o)}{\{1+(\delta/2)\ F(t_o)(t-t_o)\}^2} \qquad (1)$$

which has the same form as the angular velocity when the only external force is the resistance of the air (Equation 16, in Section 4C). Because the size did not begin to decrease until five seconds after the torque had been removed, t_o was chosen to be 178 instead of 173sec. The solid line in Figure 2 shows the fit obtained using $\delta = 0.00011\ sec^{-1}$ and $F(t_o=177.4) = 1.016R_o$.

The equatorial size generally increased during the time the torque was applied and decreased when it was removed, however there were two unexpected features: the size decreased for the first five seconds after the torque had been applied and then did not stop increasing until 5 seconds after it was scheduled to turn off.

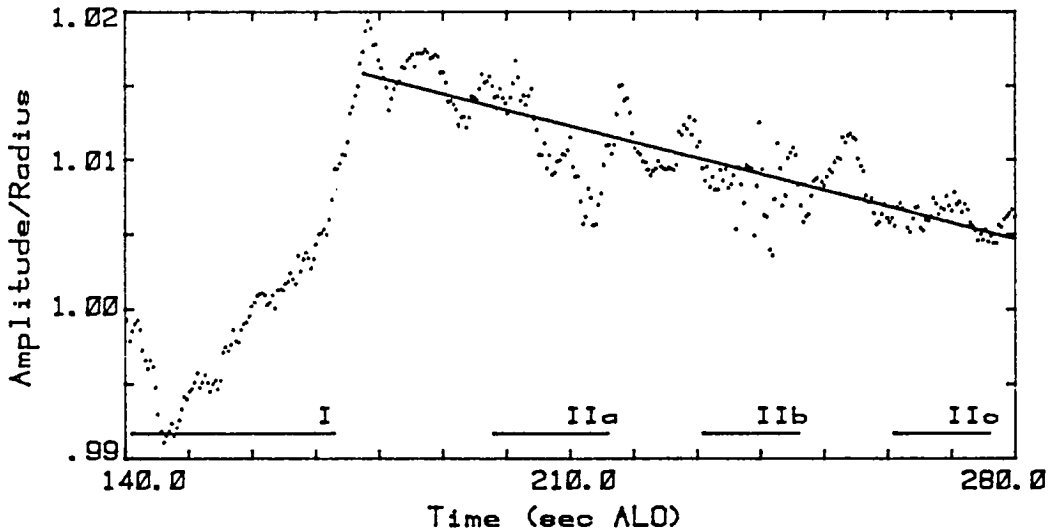

Figure 2. Average radius in the equatorial plane, normalized by the radius of the shell at rest from the early part of the experiment. The acoustic torque was applied between 141 and 173 seconds ALO.

To confirm that the torque was applied between the programmed times of 141 and 173 seconds ALO and not between 147 and 179 seconds – as it appears to be in Figure 2, the microphone levels for the x and y axes recorded in the telemetry data were checked to determine when those signals were switched from the complementary modulation to the constant phase shift used during rotation. The telemetry data indicated that there was a 1 second offset between the programmed times and the times recorded with the telemetry data and on the film record, but not 5 seconds. (The microphone outputs are shown in Figure 6 of Section 5B.)

Inspection of this graph revealed an error in the experiment program sequence: the intensity of the acoustic levels were to be reduced by a factor of 0.87 during the application of the torque, however the microphone voltage, and hence the acoustic pressure, for the x axis increased by roughly that amount. This meant that the acoustic centering force in the x direction was almost three times as large as that in the y direction (with the axis of rotation along the z axis). The effect of this imbalance was to distort the shape of the shell – flattening it in the x direction despite both surface tension and rotational forces trying to make it circular. By combining the data used in Figure 2 in a different manner, the imbalance is highlighted: Figure 8 in Section 5B shows the difference in size between the dimensions of the shell in the vertical and horizontal (or x and y) directions. Under normal circumstances the average difference will be zero for a rotating liquid, however during this rotation sequence the horizontal size was significantly greater.

Because the flattening due to the change in levels happened before the

oblation due to rotation began, the average equatorial size decreased until the rotation had built up to a sufficient level to cancel the effect (roughly 5 seconds). Similarly when the torque and the distorting force were removed at 173 seconds, the size of the shell increased as it once again became circular - this also took 5 seconds. Because the shell was not symmetric about the z axis while the torque was applied, it could not have achieved solid body rotation. The energy required to keep the liquid flowing in elliptical paths about the z axis acted as a brake and kept the rate from building up. Other ramifications of the imbalance in the acoustic forces are discussed in the section concerned with the acoustic positioning of the shell (sec. 5B).

A simple analysis parallelling that valid for a simple rotating drop was initiated: the polar and equatorial dimensions were compared with the values predicted by the theory developed for solid-body rotation. Using the dimensions of the shell taken from the film record, the size of the equatorial plane from the main view data (normalized by the non-rotating radius) and the ratio of the polar to equatorial thickness from the data of a side view, Figure 3 was constructed. The solid line represents the theoretical relation of the parameters for a simple drop in solid-body rotation.

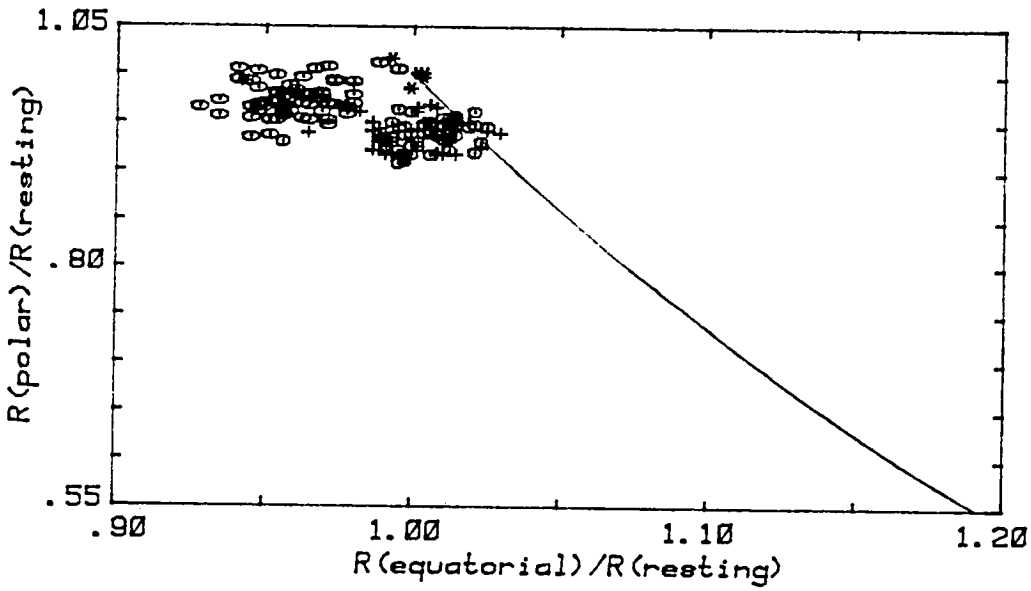

Figure 3. Comparison of the polar and equatorial dimensions of the shell. The solid line is from theoretical data for a simple water drop in air which is in solid-body rotation.[27] The symbols correspond to different time periods: * (138-141), ⊖ (141-173), o (173-198), + (198-220).

Because of the imbalance in the centering force during the time when the torque was applied to the shell, the data for that period (indicated by the ellipses) should not be compared to the theory. However the sizes for the three seconds before torque was applied (when the shell was not rotating -

indicated by *) and the 175 seconds after the torque was removed (and the rotation was often solid-body) can be compared to the simple drop theory. The data from the 25 seconds after the torque were removed are represented by little o's and that from after 198 seconds ALO by +'s. The data from the various sequences cluster well, however the scatter is too great to identify a qualitative relation between the equatorial size and the ratio of radii from this plot.

Fortunately (for the rotation analysis) there were three unexpected bubbles ($r \sim 0.10R_0$) in addition to the large programmed bubble ($r \sim 0.79R_0$). They provided convenient trace particles to show the shell's rotation. Before the torque was applied to the shell, they were located in a random pattern in the liquid. As the shell began to rotate the small bubbles, responding to the centripetal forces, moved to the pole of the shell and formed a triangular cluster. By observing and recording the time at which each side of the triangle formed by the centers of the small bubbles was vertical or horizontal, twelve times were obtained for each complete revolution. These data provided a direct view of both the buildup of the shell's rotation and its slow decrease which are independent of any theory. To minimize the effects of errors inherent in the data-gathering process, a smoothed rate of rotation was calculated

$$\Omega(j) = \frac{2\pi/3}{\mathrm{TIME}(j+2)+\mathrm{TIME}(j-2)}. \qquad (2)$$

The data for the first half of the experiment are shown in Figure 4.

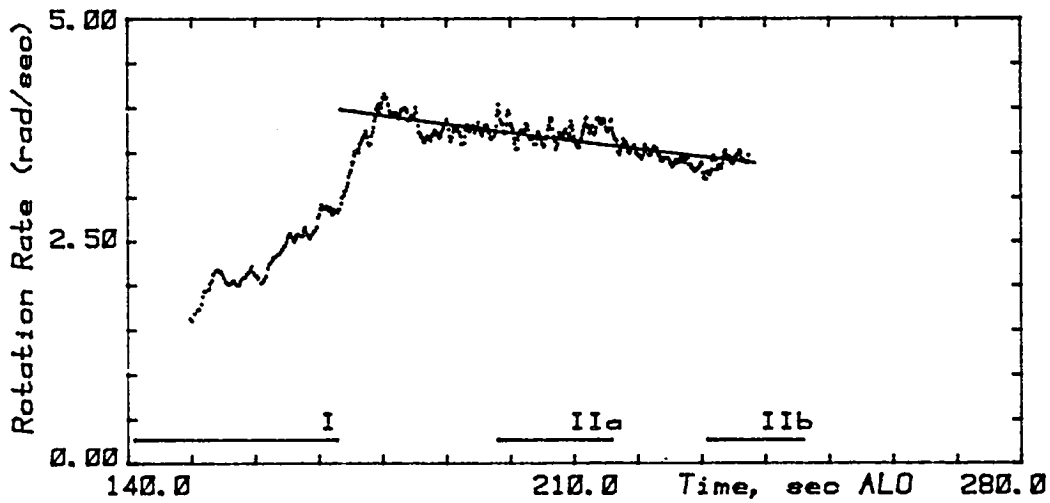

Figure 4. Rotation rate of the shell versus time from data obtained by using three small bubbles as tracers. The solid line is the best fit to the spin-down equation with $\delta = 0.0013$ $\mathrm{sec}^{-1/2}$ and $\Omega(t_o=177) = 3.94\mathrm{sec}^{-1}$.

Using the data between 180 and 230 seconds, a value for the drag coefficient was determined using a least squares fit to the function $F(t) \equiv \Omega(t)$, the rotation rate in radians/sec, in Equation 1. The solid line is the fit obtained for a rotation rate at the onset of spin-down of $\Omega_o = \Omega(t_o=177) = 3.94$ rad/sec and a drag coefficient of 0.0013 $sec^{-1/2}$. Because it was difficult to determine the rotation rate until the small bubbles were close to the pole where they were clearly visible, there are no data points for the earliest part of the rotation sequence (141 to 150 sec).

The data shown in Figures 2 and 4 are similar on a large scale rising to peaks at 180 sec ALO and then slowly decreasing but on closer inspection the small bumps and valleys do not correlate with each other. This is the result of scatter in both sets of data rather than to a fundemental process.

Using the theoretical equation for the acoustic torque (Eq. 14 in section 4E) with $p_x = 4.4 \times 10^3$ dynes/cm^2 and $p_y = 2.6 \times 10^3$ dynes/cm^2 from the center of mass analysis, a surface area of 22.4 cm^2 and a viscous layer thickness, $L_v \equiv \nu/\omega$, of 0.015cm, the torque is 2.57 dyne-cm. At this point it has been assumed that the imbalance in the amplitudes of the acoustic pressure has not affected the torque through its change of the shell's shape. If the shell were rigid and concentric, its moment of inertia would have been 5.42 g-cm^2 - giving a value of the ratio, τ/I, of 0.47 sec^{-2}. The data from the small bubbles between 149 and 154 seconds indicate a value of 0.17 sec^{-2}.

Using values from the fit to the spin-down data for the rotation rate at 173 seconds and the drag coefficient, the solid spin-up curve in Figure 5 was generated by requiring a value of the ratio of the torque to moment of inertia of 0.13 sec^{-2}. Using $\tau/I = 0.17$ sec^2, the two dashed lines determined: the upper with $\Omega(173) = 3.94$ sec^{-1} and $\delta = 0.012$ $sec^{1/2}$ and with $\Omega(173) = 2.82$ sec^{-1} and $\delta = 0.030$ $sec^{1/2}$ for the lower. The remaining curve (composed of dots and dashes) uses $\tau/I = 0.47$ sec^{-2} and in order to pass through both Ω(141 sec ALO) = 0.0 and $\Omega(173) = 3.94$ sec^{-1}, the drag coefficient was set to 0.058 $sec^{1/2}$. Although it is probable that the ratio of τ/I was less than 0.47 sec^1, the data seem to indicate that while the torquue was on the 'effective resistance' was close to 0.03 $sec^{1/2}$. This value is the result of the normal braking due to air resistance on a sphere plus a component due to the braking action resulting from the imbalance between the x and y centering forces.

There were several effects which might combine to cause the rotation of the small bubbles to not mirror the rotation rate of the entire shell. Because the torque at a point on the surface was greater the further that point was from the center of the chamber, it was maximum at the shell's equator and the fluid there was subject to a greater force and spun up more quickly than the liquid at the poles. Because the small bubbles which were being used as tracers were located at the pole where the magnitude of the torque was least, the rate of rotation of the small bubbles was always less than or equal to the rate at any other part of the shell. An additional factor which would tend to increase the speed at the equator relative to that at the poles was that when the torque was first applied the effective moment of inertia was less than that of a rigid shell. Since stress was transmitted into the interior by viscous forces, initially only a thin shell at the outer surface was affected by the torque and began to rotate. This 'affected shell'

grew inward with time. Because energy had built up in the equatorial region, the trace bubbles located at the pole continued to increase their rate of rotation for another five seconds after the torque was removed at which point solid-body rotation was achieved.

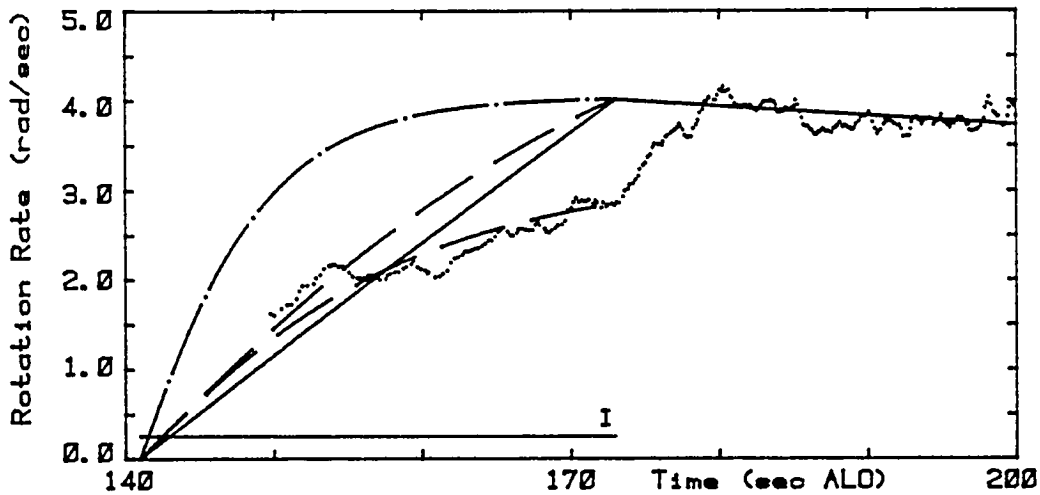

Figure 5. The rotation rate curves during spin-up were constructed for various values of the damping coefficient and the ratio, τ/I. The points are the rates determined from observing the small bubbles at the pole.

Both the polar to equatorial ratio and the equatorial size can be related to the drop's angular velocity (see Figure 2 in the theoretical section). Using the dimensions of the shell's outer surface and the rotation rate at the pole from the trace bubbles, the relationship between the angular velocity and the size of the shell can be illustrated. Figure 6a compares the polar/equatorial ratio to $S \equiv \{\Omega/\omega(n=2,-)\}^2$, which has the same form as , the dimensionless rotation parameter used for simple drop analysis. The normalized equatorial radius is plotted versus S in Figure 6b. The theoretical curves for a simple drop in solid-body rotation are included for comparison.

The shell continued to rotate throughout most of the experiment. The last observation of rotation was at 339 seconds ALO when the second small bubble popped leaving only one large and one small bubble. Figure 7 shows the rotation rates obtained from the small bubbles for the 185 seconds the shell was observed to rotate. Extrapolating from this data, the shell stopped rotating arround 350 seconds or 175 seconds after the torque was removed. It is clear that the modulated acoustic signals intended to stimulate the shell's normal mode oscillations also affected the rotation rate: the rate increased during the second half of the first two forced oscillation sequences.

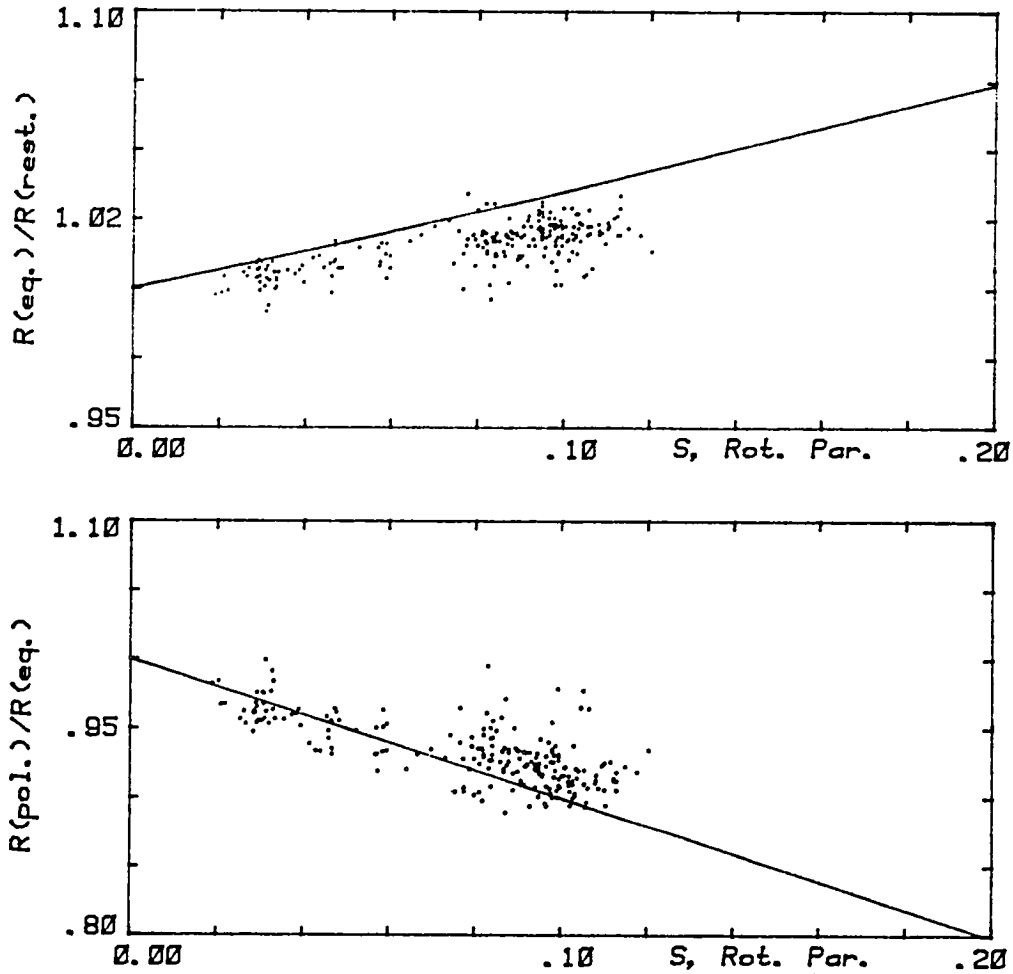

Figure 6. Comparison of the shape data, R(eq)/R(rest) and R(pol)/R(eq), and the dimensionless parameter S, a function of the rotation rates obtained from the tracer bubbles. The solid lines are the theoretical relations for simple drops.[27]

One of the features which was unresolvable from the cine film was the shape of the bubble during the rotation of the shell. The same forces that tend to flatten a simple drop - or the outer surface of a shell - which is rotating would also tend to elongate a rotating bubble. The distortion through the outer surface and the uncenteredness of the bubble along the axis of rotation did not permit the measurement of the deformation of the inner boundary. That the three small bubbles were not able to line up along the axis indicated that the large bubble was constraining them in some way and, in turn, may have been prevented from elongating by them.

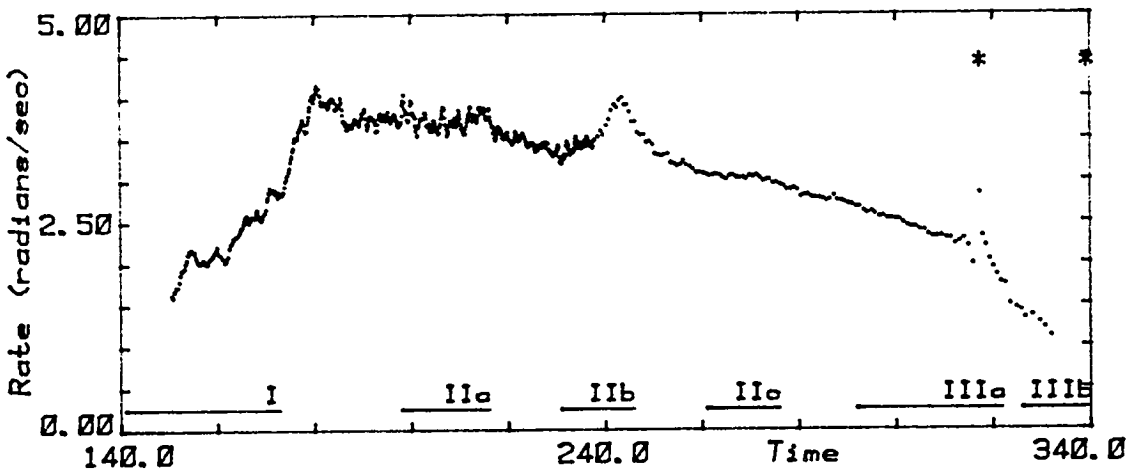

Figure 7. Rotation rate of the shell determined from the three unexpected small bubbles at the pole. The asterisks indicate when the two small bubbles popped.

E. Forced Oscillation

A modulated acoustic force was applied to the drop over three different frequency ranges in an effort to identify the frequencies of the normal mode shape oscillations, to study the relative motion of the two boundaries and to observe and quantify any centering forces generated by this type of external stimulation.

In the first sequence which lasted 18 seconds (198 to 216 seconds ALO - after liftoff) the amplitude of the centering force along the z axis was modulated while the frequency of that modulation was swept from 5.0 to 7.0 Hz. For the programmed volumes of water and air the expected frequencies of oscillation in this range were 6.32 Hz (n=2, bubble submode) and 6.51 Hz (n=4, sloshing submode). After a 15 second relaxation period the z axis acoustic signal was again amplitude-modulated for 15 seconds with the frequency going between 1.0 to 2.4 Hz, a range which contained the expected n=2, sloshing submode, resonance at 1.80 Hz. The final 15 second modulation sequence (after an equal resting period) spanned 2.5 to 4.0 Hz with the frequency of the n=3, sloshing submode, oscillation at 3.90 Hz: a resonant response was not expected because the symmetric acoustic forces should not be able to stimulate odd modes of oscillation whose shapes are not symmetric about the z=0 plane.

Several bright spots due to multiple reflections of the photo lamps between the two boundaries of the shell were visible in the main view and were observed to be sensitive indicators of oscillation. Their behavior clearly showed that there was some response in each of the three sequences. In the side views the oscillation of the outer surface in the z direction was clearly visible.

Even though the image in the main view was the largest and sharpest of the three, a side view was picked to study the forced response because the stimulation was along the z axis, its response was more pronounced in that direction and if there were any centering along the z axis, it would be observable only in a side view. In addition the contrast between the motion parallel and perpendicular to the forcing axis would aid the analysis and interpretation.

The major purpose of these sequences was to center the bubble along the z axis. Because of the the three small bubbles the large bubble was not able to move closer to the center of the shell along that direction. As was mentioned in the rotation section (5D), that the small bubbles were stuck between the inner and outer surfaces was demonstrated by their remaining in a plane perpendicular to the axis of rotation despite centripetal forces. Even if the index of the amplitude modulation had been larger, the bubbles would still have prevented motion of the big bubble toward the center.

The bubble was discentered to such a degree that the bottom portion of

its boundary was not visible in either side view making it impossible to to study the relative boundary responses at the top, bottom, left and right as hoped. The bubble boundary in the other three directions was not sharp because of the smaller image size and slight disfocus of the side view. For these reasons a response the reflection of one of the photo lamps which was near the thick part of the shell was used as an indicator of the bubble's response. The reflected spot of light which was used was not at the top of the bubble. Although these points were not usable in the study of the bulk motion, they did provide information about the response of the inner and outer surfaces of the shell. Distortions due to viewing the spot through the curved outer boundary were not corrected.

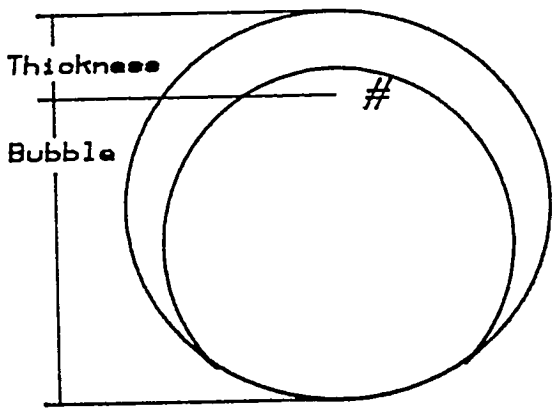

5.0 to 7.0 Hz Amplitude Modulation

This sequence began 25 seconds after the torque on the shell had been removed. Because there was no mechanism except air resistance to slow it down, the shell was still rotating at a rate of 3.7 radians/sec (or 0.6 rev/sec) about the z axis when the amplitude modulation of the centering force - also in the z direction - began. Because of the torque the bubble had centered about the axis of rotation however along that axis it remained uncentered.

The contrasting character of the surface motion was anticipated to have been sufficient to indicate the presence of one or the other of the two modes: in the bubble submode the two surfaces should move in phase (through a progression of prolate/oblate oscillations) and the amplitude of the displacement of the inner boundary should be significantly greater than that of the outer one, while for the sloshing submode the surfaces would be moving out of phase but with the inner surface moving much less (with the the outer surface a series of square/diamond shapes). Even though it was clear that the shell was responding, it was difficult to identify whether the surfaces were moving in or out of phase but the bubble was oscillating more than the outer surface. The shell's response was indicated not by identifiable shape oscillations but only by regular motions of the reflections of the lights and slight motions of the boundary. From inspection of the film alone a tentative identification of the bubble sub-mode (n=2,+) oscillation was made for the second half of the sequence.

Figure 1 shows the results of the analysis of data from a side view using the size of the outer boundary in the vertical (z) direction and the position of the reflection of a photo lamp off the inner boundary. The times corresponding to the resonant frequencies of free oscillation, 6.32Hz for

n=2(+) and 6.51Hz for n=4(−), are roughly 210.0 and 211.6 seconds. Any resonant response corresponding to these modes should have been apparent by these times. The graphs of the shell's response in Figure 1 show no such behavior before 211 seconds ALO. There is a very gradual increase in amplitude of the bubble and shell sizes between 198 and 216 seconds but there was no decrease until the modulated force was removed.

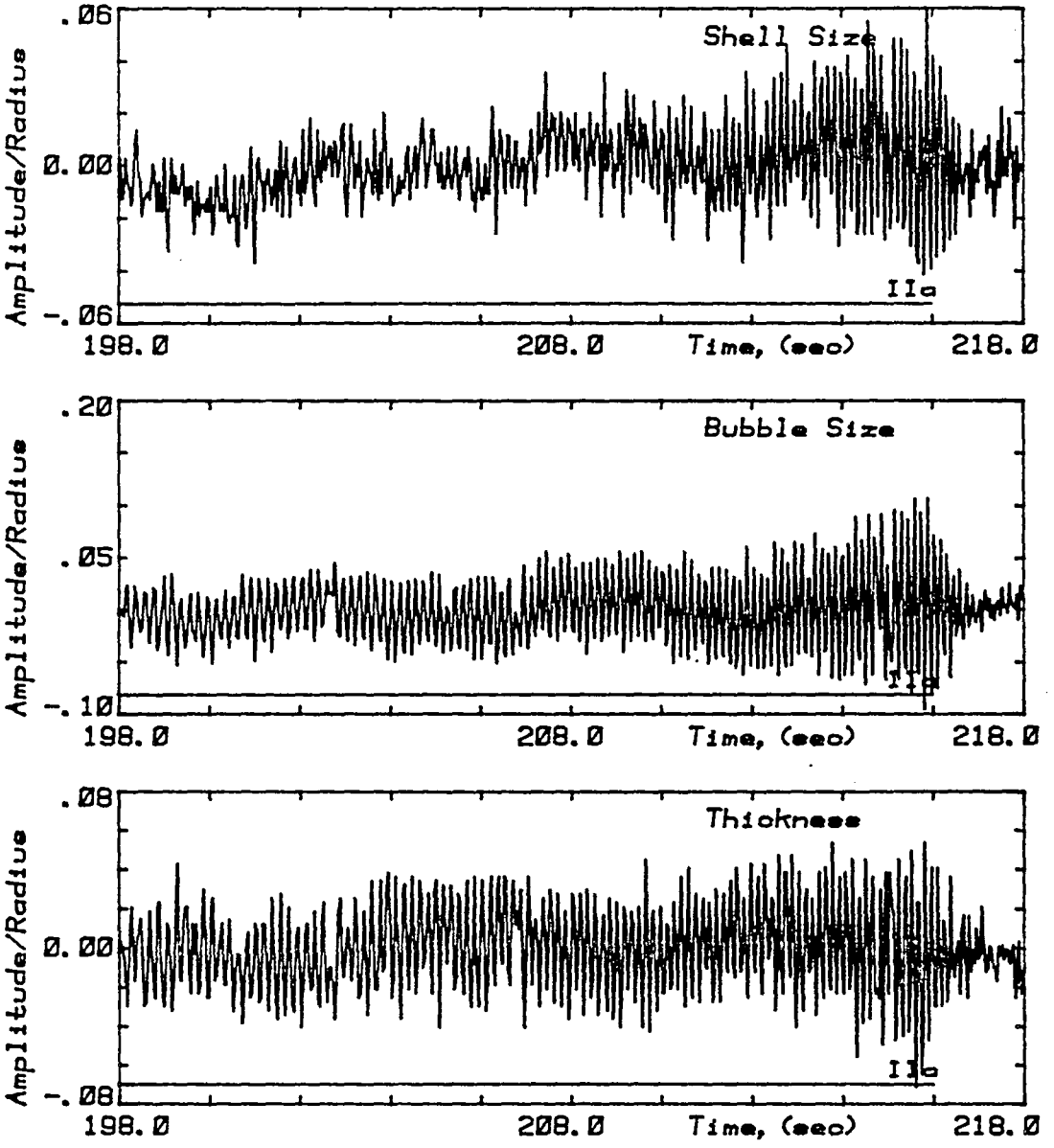

Figure 1. Data from the first stimulated oscillation sequence in which the force was amplitude-modulated at a frequency which was swept from 5.0 to 7.0 Hz between 198 and 216 seconds after liftoff.

The Fourier transform of the bubble size data - shown in Figure 2 - has its greatest amplitude near 6.8 Hz which corresponds to the increase in amplitude observed in the time data near the end of the stimulation. The individual peaks between 5 and 5.5 Hz are not significant only the increase in their maxima is. Because the seperation between the frequencies of the two modes is so small, the two modes may have interacted with each other in such a way to inhibit the growth of any single-mode oscillations. This may explain the lack of a peak and between 6.0 and 6.8 Hz. The frequency information does not corroborate the tentative identification of the bubble mode nor provide any other explanantion of the shell's response.

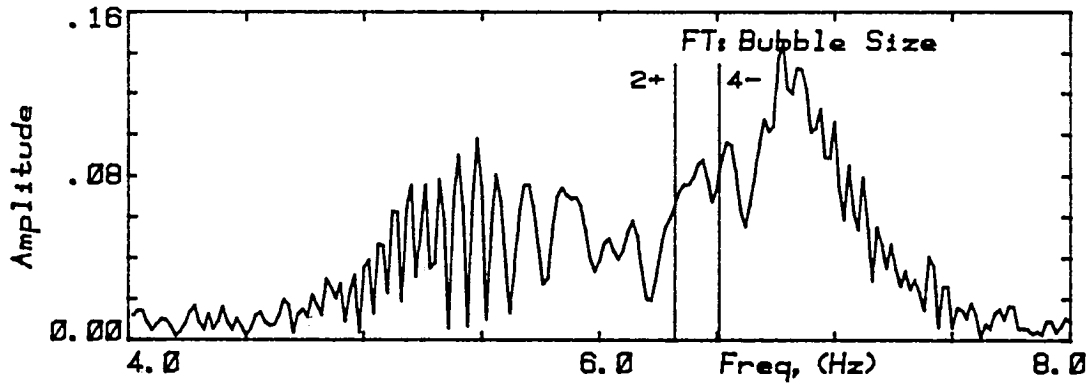

Figure 2. The Fourier spectra obtained from the bubble size data of Figure 1. The frequencies of the n=2+ and n=4- natural oscillation modes are indicated for reference.

Study of the free decay after 216 seconds (section 5C) showed that the frequency of the decreasing oscillation was 7.2 Hz which would indicate that the amplitude of the time signals had not yet reached its maximum value when the modulation was turned off which is not inconsistent with the data shown in Figure 1. Possibly the n=2, bubble mode oscillation frequency is higher than predicted. The effects which the three small bubbles located along the z axis and between the two surfaces would have upon the shell's response can not be estimated from the present understanding of compound drop behavior.

1.0 to 2.4 Hz

The second sequence began at 231 seconds ALO with the acoustic force in the z direction amplitude-modulated at 1.0Hz and this frequency was increased to 2.4Hz at 246 seconds - a rate of 0.93Hz/sec. The frequency of free oscillation of the n=2 (sloshing) mode was predicted to be present within this range at 1.80 Hz and the frequency of the forced response at a slightly lower value.

Figure 3 shows three combinations of data taken from the film record: the size of the shell, the size of the bubble, and their difference - the distance between the two surfaces. The growth of the oscillation in the outer

boundary ia very slight. The bubble does not appear to respond until 239 seconds ALO when its amplitude increases. The thickness of the shell shows a definite increase and decrease in the amplitude of its oscillations with a maximum arround 241 seconds (at which time the force was amplitude-modulated at 1.94 Hz). That most of the oscillation occurred in the outer surface was reflected in the greater amplitude of the thickness oscillations compared to those of the bubble size data.

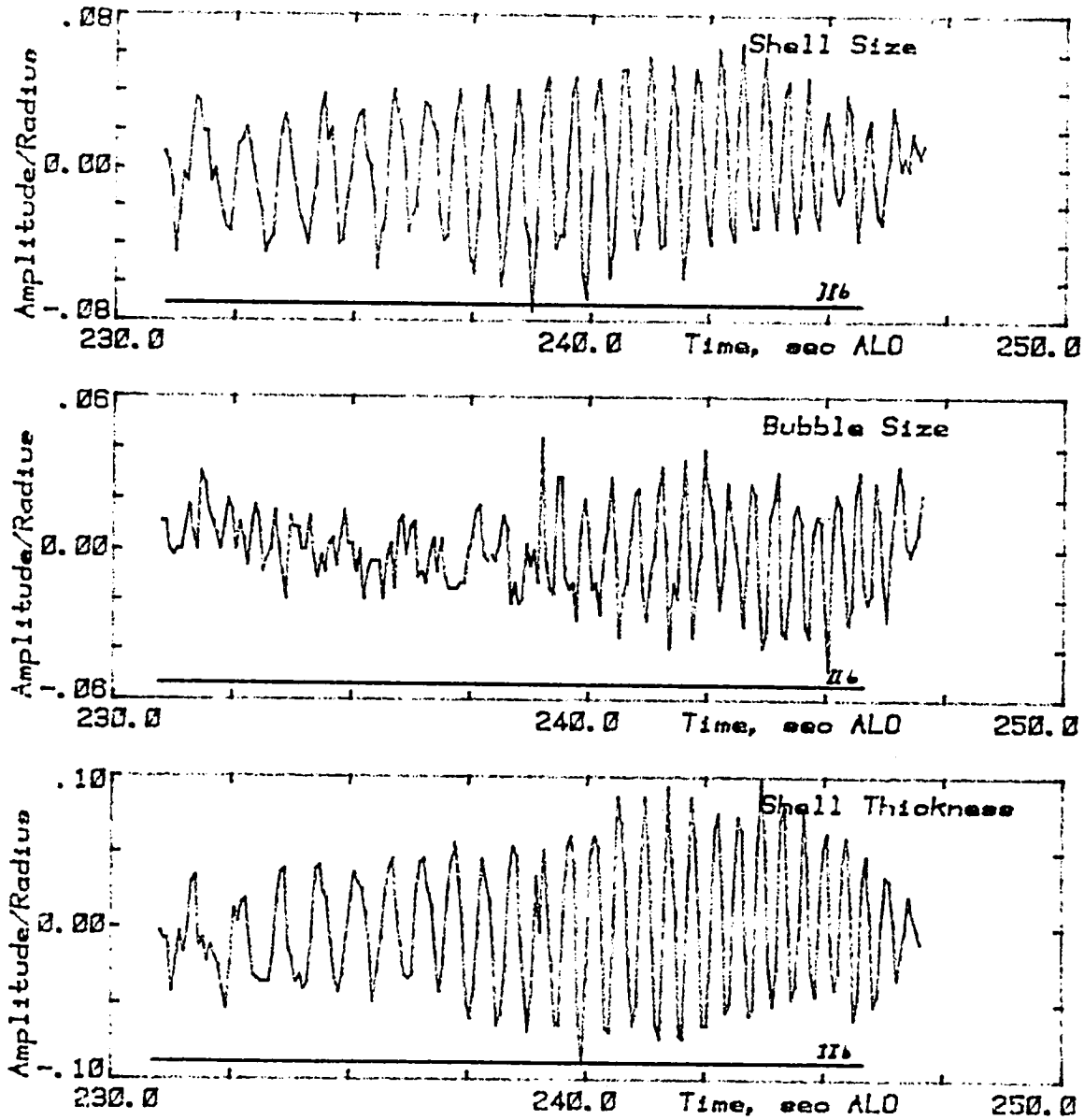

Figure 3. Dimensions of the shell and bubble and their difference for the second stimulated oscillation sequence. Between 231 and 246 seconds ALO the frequency of the modulation was swept from 1.0 to 2.4Hz.

The Fourier transform of the shell thickness data is shown in Figure 4. The peak at 2.0 Hz is not symmetric - reflecting the slow buildup and quick decrease of the amplitude shown in Figure 3. It illustrates the typical resonance response anticipated for this experiments with its start at a low amplitude at 1.0 Hz and its increase to a maximum near 2.0 and its subsequent decrease. The quick decrease in amplitude in both time and frequency data are due to the interference of the forced oscillations with the dampened natural oscillations stimulated shortly before.

The frequency of the decaying oscillations (after 236 seconds) was also 2.0 Hz. That this frequency is greater than the 1.9 Hz observed after deployment is due to the shell's rotation and/or the presence of the three small bubbles and their distorting effect upon the shell's concentricity.

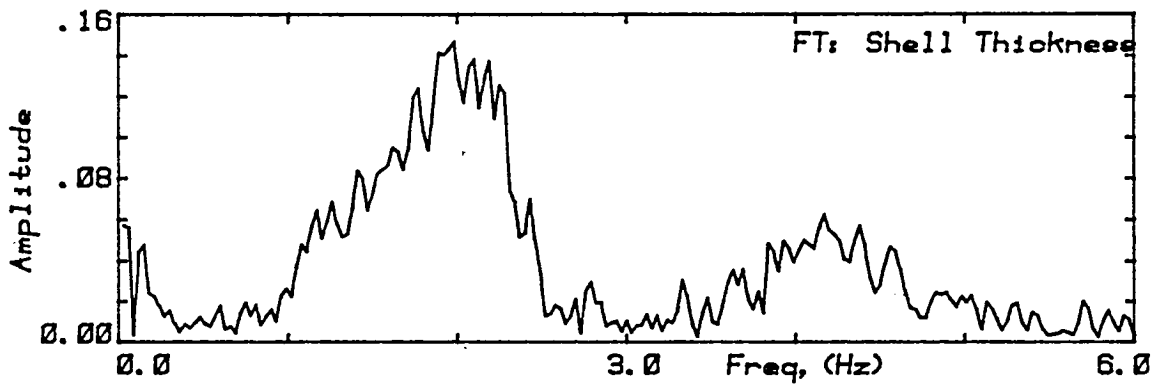

Figure 4. Fourier-transformed thickness data for the 1.0 to 2.4 Hz stimulated oscillation sequence.

2.5 to 4.0 Hz

Between 261 and 276 seconds ALO the amplitude of the acoustic centering force in the z direction was modulated while the frequency of the modulation was swept from 2.5 to 4.0 Hz. The n=3, sloshing submode of the shape oscillation was predicted to occur at 3.9 Hz. It was not expected that this mode could be stimulated acoustically because the driving force was symmetric and the shape oscillations were not. The BOX technique which was used in this analysis is poorly designed to study shapes with threefold symmetry, for it relies upon the Vanguard Motion Analyser which has two perpendicular cross hairs.

Study of the boundaries indicated that the shell did respond to the acoustic force (see Figure 5) with most of the oscillation occurring in the inner boundary. The amplitude of the oscillations was less than half that of

the other two sequences. The frequency spectrum of the shell thickness data (Figure 6) has both resonant and non-resonant features. The amplitude of the response is too weak to draw any definitve conclusions.

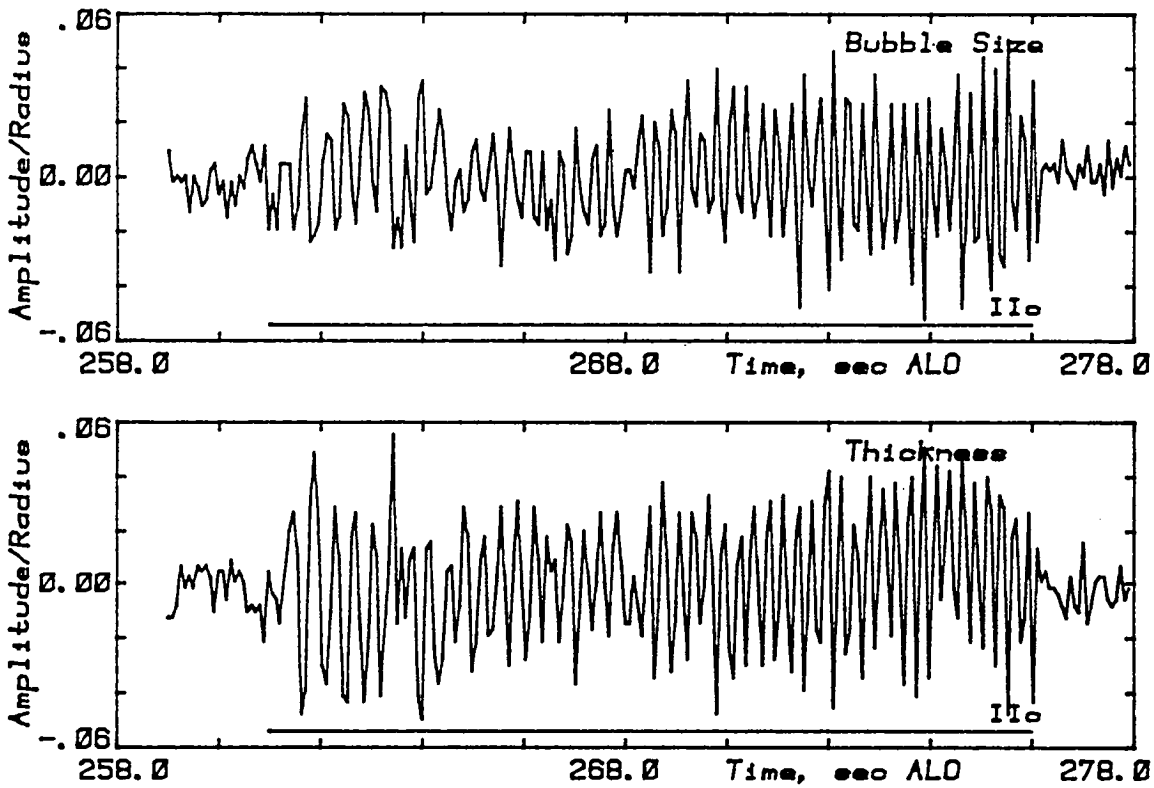

Figure 5. Stimulated oscillation data from the third sequence: f_{mod} was swept from 2.5 to 4.0 Hz.

The rate at which the modulation frequency is swept has been shown in the laboratory to be important: sufficient time is required for the amplitude of the oscillations to build up. In this experiment the rates were 111, 93 and 100 mHz/sec for the three sequences. Trinh reported that in his laboratory experiments, sweep rates of 10mHz/sec were used to prevent inaccurate resonance curves. The sweep rates in the SPAR VI and SPAR VII stimulated oscillation sequences were 5mHz/sec and 8.3mHz/sec. The response of the drop and shell to the low-frequency acoustic force was large in both cases. Because the frequency changed so quickly in this experiment, the resonance

behavior could not build up in this experiment.

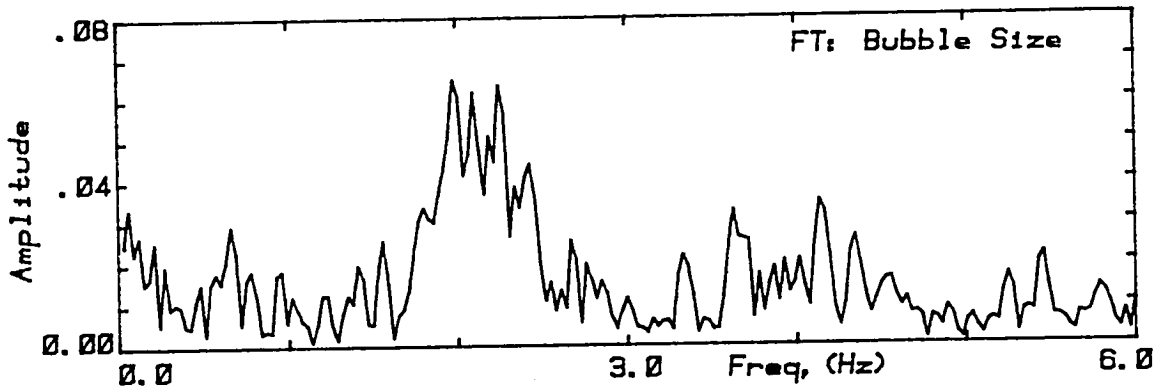

Figure 6. Frequency spectra of the Bubble Size data during the 2.5 to 4.0 Hz stimulated oscillation sequence.

Another feature of these sequences was the coupling between the oscillation and rotation. Figure 7 shows the rotation rate determined from the three small bubbles during this time. At 243 seconds the amplitude of the oscillation response and the rotation rate were both at their maximum values. Similarly in the first sequence both the rate and the oscillation increased between 212 and 216 seconds.

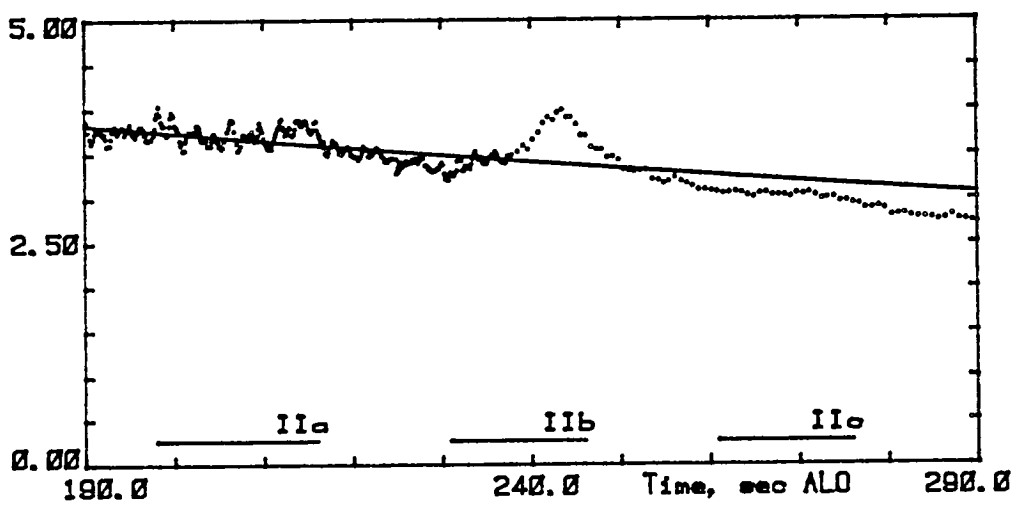

Figure 7. Rotation rates during the stimulated oscillation sequences showing the effects on rotation of the coupling between the two types of behavior.

F. Adiabatic Expansion

The purposes of this sequence were to study the slow expansion of the shell and the centering of the bubble and to observe any manifestions of instability. The expansion was accomplished using a two step decompression of the acoustic chamber: at 293 seconds ALO (after liftoff) a valve which connected the chamber to an overboard vent was opened and at 323 seconds it was closed. A second valve was kept open between 327 and 366 seconds.

The relative volume of the bubble increased from 42% to 77% in 70 seconds. The three small bubbles which had been injected during the early part of the bubble deployment were still present at the beginning of the expansion sequence. Two of them popped out of the liquid during the expansion. The other small bubble was still present when the shell hit the wall at 420 seconds.

Figure 1 shows the output from a pressure transducer connected to the interior of the acoustic chamber. The change in the ambient pressure when the valves were open is clear. The horizontal bars (IIIa and IIIb) indicate the periods when the valves were open. A time constant to describe the decompression was determined by finding the best fit to the pressure data while the valves were open. Using an exponential function, $P = P_0 \exp(-t/\tau)$, $\tau \sim 39.5$ sec. The telemetry data of Figure 1 indicate that the ambient pressure dropped from roughly 14.1 psi to 9.4 psi during the time that the first valve was open. By the time that the second valve closed the pressure had dropped to approximately 6.8 psi.

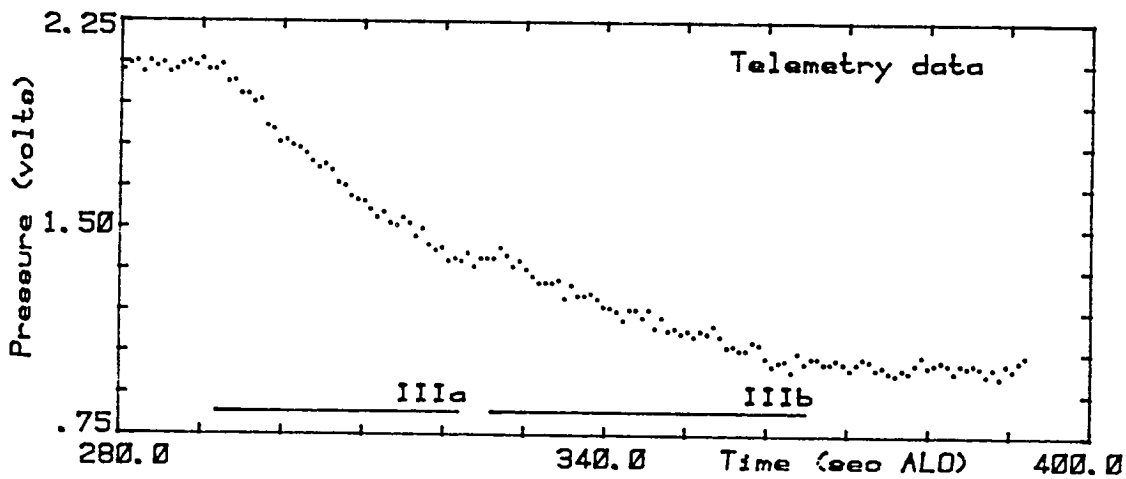

Figure 1. The static pressure in the acoustic chamber (from the telemetry record of the experiment).

Figure 2 shows the response of the shell to the drop in pressure: its average size as seen in the main view and normalized by the size at 280 seconds after liftoff. The size increased while the valves were open. The relative radius increased from 1.0 to 1.1 during the first sequence and from 1.1 to 1.35 in the 36 seconds of the second stage of the decompression. The shell's volume increased 33% while the the first valve was open and 250% while the second remained open. The volume of the bubble increased by a factor of 4.46, and its relative size (radius) increased from .421 (.750) to 0.765 (.915) at 365 seconds.

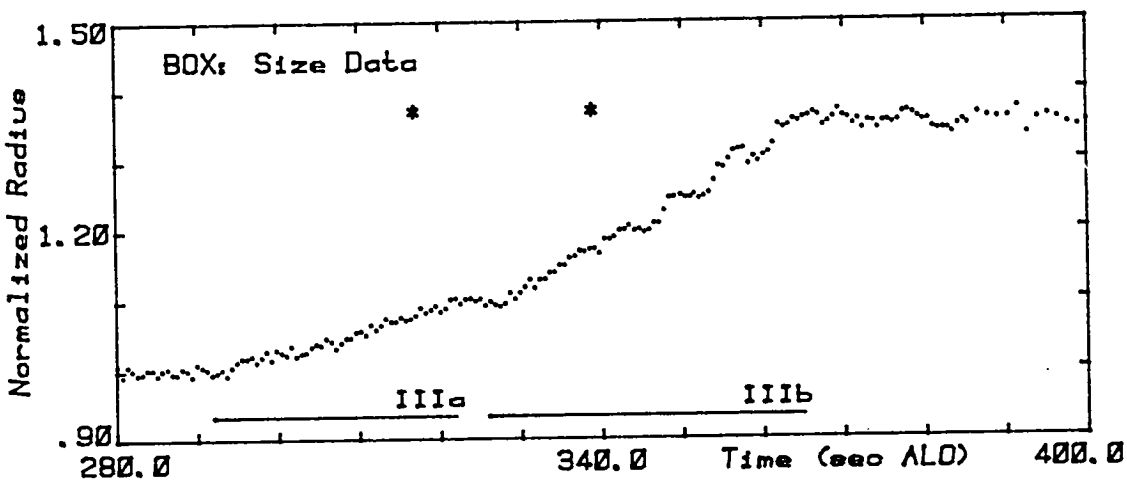

Figure 2. The average size of the shell as seen in the main view while the pressure in the chamber decreased. The asterisks indicate when two of the three small bubbles popped.

The times at which the two small bubbles popped out are indicated by the asterisks. The oscillation that begins arround 345 seconds ALO reflects the distortion caused by the remaining small bubble when the shell began to rock in the acoustic well as the rotation stopped. That small bubble had grown so that its diameter was roughly 20% of the shell's. It was greatly deformed by the two surfaces as the bubbles grew and in turn deformed the shell greatly by causing most of the mass of the fluid to move to the area where the large and small bubble touched.

Figure 3 illustrates the adiabatic quality of the bubble's expansion: using the data shown in the first two figures to construct the function K which will be constant in time for an adiabatic process. versus time where

$$K(t) \equiv P_{bub} \{V_{tot} - V_{liq}\}^{\gamma} \qquad (1)$$

V_{bub} is the volume of the bubble and P_{bub} is its pressure which is the external pressure plus a small correction due to the pressure jumps over the

two interfaces (Eq.5 in section 4E). The data was normalized so that $K(t_o=280) = 1.0$. In the data shown γ, the ratio of the specific heats of the gas, is 1.4 and V_{liq}, the volume of the liquid part of the shell, is $0.58V_{tot}(t_o)$.

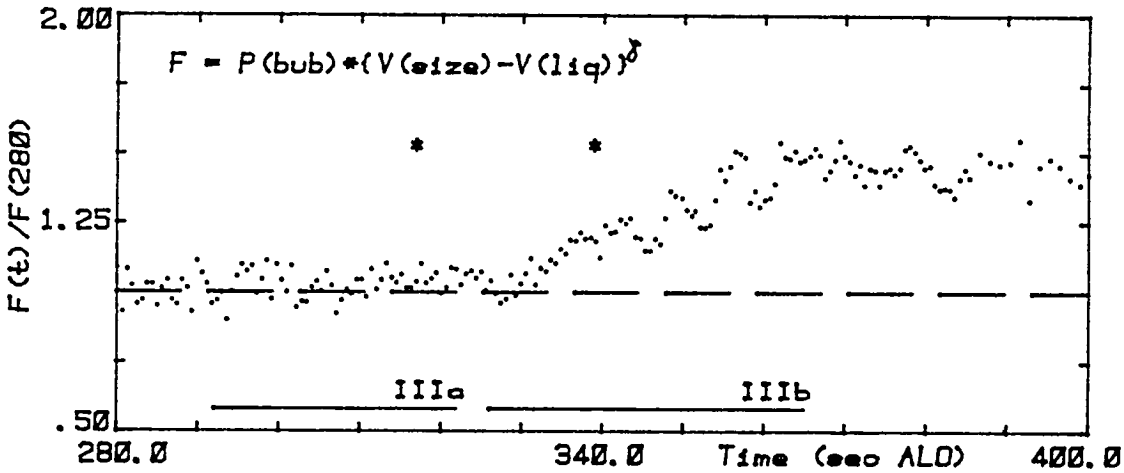

Figure 3. A check using data from both the telemetry (the pressure) and the film (the shell size) records to determine the quality of the bubble's adiabatic expansion. For an adiabatic process K(t) = 1.

An indication of the temperature of the air inside the chamber was provided by the telemetry data for the frequency of the z-axis acoustic positioning signal (see Figure 4). As the temperature of the air decreased - due to the drop in the pressure the frequency also dropped and at a rate proportional to the square root of the change in the absolute temperature. But because the walls of the chamber had a much greater heat capacity and did not cool as much during the depressurization, the frequency increased between 322 and 326 when both valves were shut as the air was warmed slightly. The decrease in the frequency from its value before expansion to the one after it is due to the cooling of the entire payload.

The liquid of the shell provided some isolation for the bubble from these temperature fluctuations. Because of the presence of the small bubble one half of the shell became very thin after 345 seconds which removed the isolation of the bubble.

The large bubble did not become centered during the early part of this sequence because the small bubbles also grew and pushed against both the inner and outer surfaces as they all expanded. The pressure on the small bubbles exerted by the larger surfaces caused two of the small bubbles to pop out of the shell at 316.6 and 338.6 seconds. When they burst they caused some very short-lived surface oscillations but no other discernible effects. The

third bubble never popped and as a result the large bubble was prevented from being centered for the rest of the experiment.

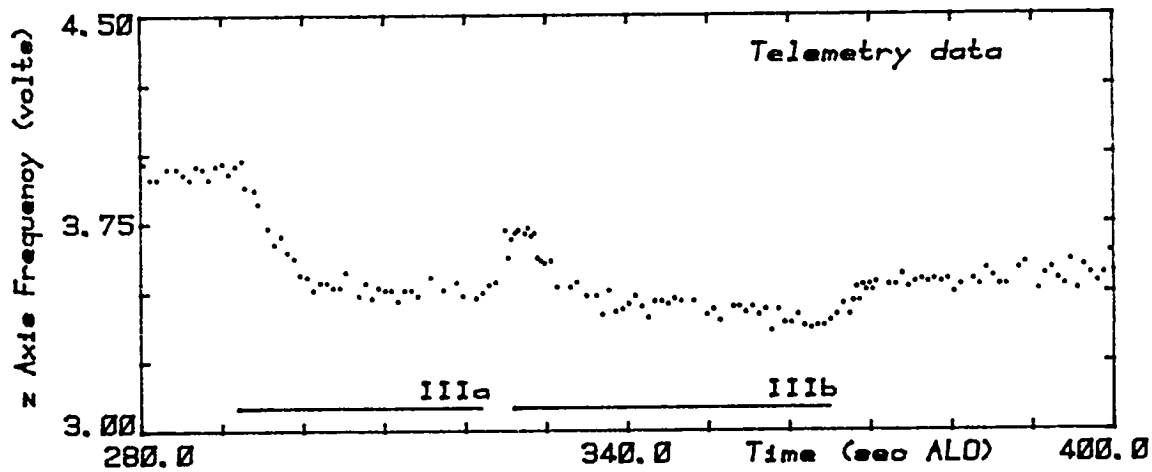

Figure 4. The frequency of the acoustic signal used for positioning along the z axis. It is proportional to the square root of the absolute temperature of the air in the chamber.

Conservation of angular momentum required that as the shell expanded its rate of rotation decrease - slowing it down much faster than air resistance alone could have. The rotation of the shell increased its stability and after the rotation rate had decreased below a critical level the precession which led to the oscillations after 345 seconds in Figure 2 began. The rotation persisted past 339 seconds when the second small bubble popped.

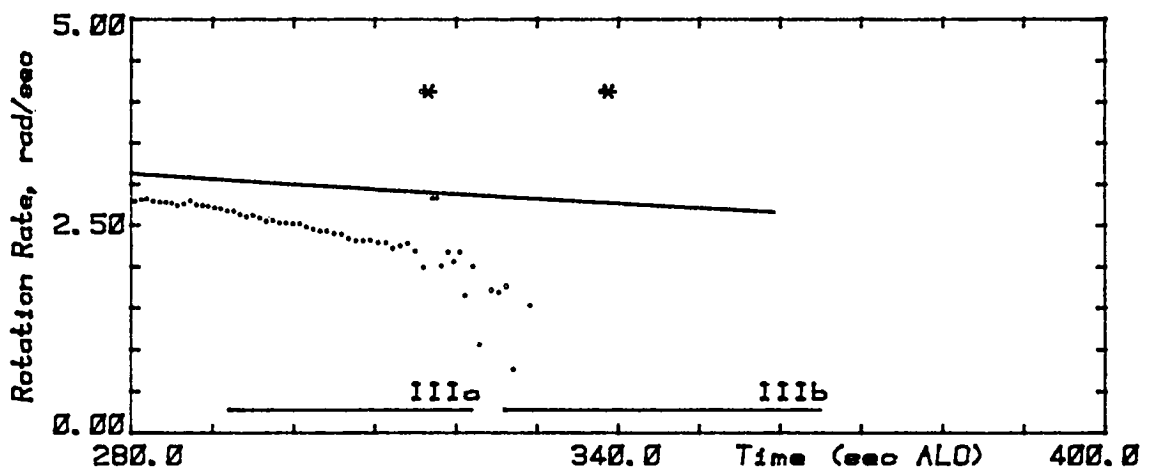

Figure 5. Rotation rate of the shell as determined by observing the relative positions of the three (or two) small bubbles.

No evidence of instablity was present nor were any flows visible as the bubble expanded slowly. Unlike the expansion sequence of Experiment 77-18/1 flown on SPAR VII, no very small bubbles were observed as the chamber was depressurized. This was a result of the more thorough degassing procedure used to treat the water. As a result the only flows visible were due to either the rotation of the shell, as evidenced by the motion of the three small bubbles, or after the two had popped the flow of fluid from arround the large bubble to the area where it and the small bubble touched. No evidence of any other flows was found.

The shell was stable enough to remain integral as the two small bubbles burst and while it was stimulated into oscillation by the 30 Hz switching frequency of the complementary modulation. It was not clear whether it was the entire shell or one of the two bubbles which responded. The oscillations were observed at several times between 350 and the end of the experiment. There was some correlation between the position and orientation of the shell and the times that the surface oscillated. The frequencies of both the surface oscillations as the bubbles popped and of the stimulated shape oscillations were too high, and their amplitude to small to analyze them quantitatively.

G. Concluding Remarks

The principal objective of this experiment was to study the dynamics of a liquid shell in a micro-g environment: its sphericity, the concentricity of the bubble within it and its behavior during adiabatic expansion.

The camera, lighting and deployment systems worked as desired. The shell, composed of 5.8cc of water and 4.2cc of air was successfully deployed.

The surface oscillations generated by the retraction of the injectors permitted the study of the natural oscillations of an air-water-air compound drop. Several modes were seen at the frequencies predicted by the theory: the n=2/sloshing submode (1.9 Hz), the n=3/sloshing submode (3.7 Hz), the n=2/bubble submode (7.0 Hz) and the n=4/sloshing submode (6.3 Hz) were identified.

The motion of the shell's center of mass was studied for the entirety of the experiment. From the oscillations in the x and y directions the drag on the shell as it moved through the air was determined. The large amplitude behavior at the end of the experiment was due to the precession of the expanding shell as its rotation rate became smaller - an effect which highlighted the stabiblizing influence of the rotation. The few small spikes in the rocket's acceleration did not cause any significant changes in the bulk motion of the shell.

In general the rotation of a liquid can be determined by studying the behavior of trace particles within it or, if they are not available, by observing changes in the relative dimensions of the drop. In this experiment both means were provided allowing the comparison of the shell's dimensions with its actual rate of rotation. Three small bubbles were used to determine the rotation rate at the pole. There presence was crucial because the necessary theoretical framework relating shell dimensions to rotation rates does not exist. The acoustic torque caused the shell to spin up to a rate of 4.1 rps. An imbalance in the acoustic forces distorted the shell and restricted the analysis to a qualitative comparision with the theory of acoustic torques. The shell rotated sufficiently to center the bubble and continued to rotate for 175 seconds after the torque had been removed. From this experiment, a very precise value of the drag on a shell due to air resistance was determined ($0.0012\ sec^{-1}$). Furthermore, this experiment for the first time provided an opportunity to observe the interplay between rotation and stimulated oscillation and between rotation and the expansion of the shell.

The shell responded to the modulated acoustic force during each of the three stimulated oscillation sequences. When the modulation was swept through the frequency of the n=2/sloshing submode the shell's response was weakly resonant; when the shell was stimulated at the n=3/sloshing frequency its oscillations were very small and nonresonant - as expected. As the frequency of the modulation was swept through a region containing both the n=2/bubble and n=4/sloshing mode free oscillation frequencies, the shell responded to the bubble submode at a resonant frequency near 7.0 Hz but showed no response near the expected frequency of the other mode. The larger response of the

n=2/bubble mode was due to the fact that the modulating acoustic force can stimulate oblate/prolate oscillations much more easily than the symmetric boundary motions of the higher modes. The amplitude of the response in all sequences was not very large nor were the shell's oscillations able to center the bubble along the z axis. We believe this can be attributed to the presence of three small bubbles at the pole. The rapid rate at which the frequency of the amplitude modulation was swept also inhibitted the buildup of a large-amplitude response.

The bubble expanded as the pressure in the chamber was decreased - its volume increased by a factor of 4.5. Two of the small bubbles popped during the first half of the expansion, but the third did not. Its presence prevented centering due to the expansion of the shell.

From this flight several suggestions for improving this type of experiment were obtained. The slow separation of the injector probes as the bubble grows would allow it to remain closer to the center of the chamber and thus minimize the amplitude of its oscillations in the potential well. A programmed variation of the acoustic force levels, distorting the field (and the shell) and then releasing it, would permit the study of a drop or shell's free decay for varying initial distortions as well as provide more data on the static shape distortion due to acoustic force imbalances. The use of a larger bubble would separate the resonant frequencies of the n=2+ and n=4- modes. Theoretical and laboratory investigations into the damping characteristics of compound drops should be initiated. A data gathering system intermediate in sophistication between the manual digitization used with the Vanguard Motion Analyzer and fully automated digitization provided by established image processing facilities should be developed. The former is slow and tiring for the operator while the latter does not have the speed and flexibility required to study data in different ways as the analysis proceeds.

The specific objectives of this experiment were met:

1) to study the sphericity of a liquid shell - during the periods when the shell was not being manipulated the sphericity of the shell was measured to be better than 1%.

2) to use acoustic techniques to center a large bubble - rotation generated by the acoustic torque centered the bubble in the x and y directions, but the stimulated oscillations were prevented from centering it along the z axis by the presence of the small bubbles.

3) to study perturbations in centering as a result of motion of the shell in the acoustic potential well due to g-jitter - rotation of the shell prevented the effects of the large-amplitude oscillation in the chamber from affecting the bubble position within the drop along the x and y axes. In the z direction the shell's bulk motion was very small and the large bubble was not free to respond as it was pinned between the small bubbles and the outer surface.

4) to study the resonant frequency and damping mechanism of bubble oscillation - the frequency data were consistent with the existing theory for the two lowest frequency submodes and complex behavior was observed in the region predicted for the next two modes. The damping information obtained from the lowest modes will allow comparison with values generated by any theoretical studies of compound drops which incorporate viscosity.

5) to expand a bubble adiabatically - the chamber depressurization scheme worked causing the bubble to expand significantly. No new information was provided on the feasibility of using bubble expansion as a centering technique.

CHAPTER III

SECTION 6

REFERENCES

1. T. G. Wang, D. D. Elleman, M. M. Saffren, 'Drop Dynamics in Space,' Proceedings of the International Colloquium on Drops and Bubbles, Pasadena, CA, 266, (1974).

2. T. G. Wang, D. D. Elleman, M. M. Saffren, 'Acoustic Chamber for Weightless Positioning,' AIAA paper 74-155, (1974).

3. T. G. Wang, D. D. Elleman, M. M. Saffren, 'Drop Dynamics in Space,' Progress in Astronautics and Aeronautics, vol. 52, AIAA, (1977).

4. T. G. Wang, D. D. Elleman, M. M. Saffren, 'Dynamics of Rotating and Oscillating Free Drops: Investigations and Technical Plan,' JPL Document 701-238, 1978.

5. T. G. Wang, D. D. Elleman, N. Jacobi, R. P. Tagg, 'Containerless Processing Technology Report, SPAR IV Experiment 76-20 Flight 1,' JPL Document 750-133, 1978.

6. N. Jacobi, R. P. Tagg, J. M. Kendall, D. D. Elleman, T. G. Wang, 'Free Oscillations of a Large Drop in Space,' AIAA Paper 79-0225, (1979).

7. T. G. Wang, D. D. Elleman, 'Results of Containerless Science Study from SPAR VI Flight,' 31st Congress of Int. Astronautical Fed., (1980).

8. T. G. Wang, D. D. Elleman, N. Jacobi, A. P. Croonquist, 'Containerless Processing Technology Report, SPAR VI Experiment 76-20, Flight 2,' JPL Document, 1981.

9. N. Jacobi, A. P. Croonquist, D. D. Elleman, T. G. Wang, 'Acoustically Induced Oscillation and Rotation of a Large Drop in Space,' Proceedings of Second International Colloquium on Drops and Bubbles, Monterey, CA, 31, (1981).

10. A. P. Croonquist, T. G. Wang, D. D. Elleman, P. H. Rayermann, 'Report on the Containerless Processing Technology Experiment, Dynamics of Liquid Drops, SPAR VII Experiment 76-20, Flight 3,' JPL Document, 1981.

11. D. D. Elleman, A. P. Croonquist, N. Jacobi, T. G. Wang, 'Report on Containerless Processing Technology Experiment, Dynamics of Liquid Bubbles, SPAR VII Experiment 77-18, Flight 1,' JPL Document, 1981.

12. L. D. Landau, E. M. Lifshitz, Fluid Mechanics, Pergamon Press, 1959.

13. L. V. King, 'On the Acoustic Radiation Pressure on a Sphere,' Proc. Roy. Soc., 147, 212, (1934).

14. N. Jacobi, M. Barmatz, 'Equilibrium Shapes of Acoustically Levitated Liquid Drops,' Proc. IEEE Ultrasonics Symposium, ed. by deKlerk and McAvoy, 476, (1979).

15. E. Leung, N. Jacobi, T. G. Wang, 'Acoustic Radiation Force on a Rigid Sphere in a Resonance Chamber,' J. Acoust. Soc. Am., 70, 1762, (1981).

16. J. Stoneburner, M. Barmatz, N. Jacobi, 'Equilibrium Positions of Acoustically Levitated Spheres,' J. Acoust. Soc. Am., 68, S45, (1980).

17. M. M. Saffren, D. D. Elleman, W. K. Rhim, 'Dynamics of Liquid Shells,' Technical Digest of the Topical Meeting of Inertial Confinement Fusion (Optical Society of America), 60, (1980).

18. M. M. Saffren, D. D. Elleman, W. K. Rhim, 'Normal Modes of a Compound Drop,' Proc. of Second International Colloquium on Drops and Bubbles, Monterey, CA, 7, (1981).

19. H. Lamb, Hydrodynamics, 6th. edition, Dover, New York, 1932.

20. A. Prosperetti, 'On the Oscillations of Drops and Bubbles in Viscous Liquids,' Proc. of International Colloquium on Drops and Bubbles, Pasadena, CA, 357, (1974).

21. Lord Rayleigh, The Theory of Sound, 2nd Ed., art.364, Macmillan, (1894). Dover reprint (1945).

22. T. G. Wang, H. Kanber, 'Nonlinear Acoustic Torque in an Intense Sound Field,' J. Acoust. Soc. Am., 64, S14, (1977).

23. T. G. Wang, H. Kanber, I. Rudnick, 'First Order Acoustic Torques and Spin Velocities of Solid Bodies in Intense Sound Fields,' Phys. Rev. Let., 38, 128, (1977).

24. F. H. Busse, T. G. Wang, 'Torque Generated by Orthogonal Acoustic Waves - Theory,' J. Acoust. Soc. Am., 69, 1634, (1981).

25. S. Chandrasekhar, 'The Stability of a Rotating Liquid Drop,' Proc. Roy. Soc. (London),286, 1, (1965). (and Proc. Roy. Soc. 286A, 25,(1965).)

26. D. K. Ross, 'The Shape and Energy of a Revolving Liquid Mass Held Together by Surface Tension,' Aust. J. Phys., 21, 823, (1968).

27. R. Brown, 'The Shape and Stability of Three-Dimensional Interfaces,' PhD. thesis, University of Minnesota, (Minneapolis, MN, 1979).

28. R. P. Tagg, L. S. Cammack, A. P. Croonquist, T. G. Wang, 'Rotating Liquid Drops: Plateau's Experiment Revisited,' JPL Publication 80-66, (1980).

29. T. G. Wang, R. P. Tagg, L. S. Cammack, A. P. Croonquist, 'Non-axisymmetric Shapes of a Rotating Drop in an Immiscible System,' Proc. Second International Colloquium on Drops and Bubbles, Monterey, CA, 203,(1981).

30. E. H. Trinh, T. G. Wang, 'A Quantitative Study of Some Non-linear Aspects of Drop Shape Oscillations,' J. Acoust. Soc. Am., 68, S45, (1980).

31. E. H. Trinh, A. Zwern, T. G. Wang, 'An Experimental Study of Small-Amplitude Drop Oscillations in Immiscible Liquid Systems,' J. Fluid Mech., 115, 453, (1982).

32. E. H. Trinh, T. G. Wang, 'Large Amplitude Drop Shape Oscillations,' Proc. Second International Colloquium on Drops and Bubbles, Monterey, CA, 143, (1981).

33. M. C. Lee, I. Feng, D. D. Elleman, T. G. Wang, A. T. Young, 'Generation of a Strong Core-centering Force in a Submillimeter Compound Droplet System,' Proc. Second International Colloquium on Drops and Bubbles, Monterey, CA, 107, (1981).

34. I.M. Ryshik, I.S. Gradstein, Tables of Series, Products, and Integrals, VEB Deutscher Verlag der Wissenshaften, Berlin, (1963). (eq. 2.1457)

35. L.E. Kinsler, A.R. Frey, Fundamentals of Acoustics, 2nd. ed., John Wiley and Sons, New York, 1962.

36. L. Rosenhead (ed.), Laminar Boundary Layers, Oxford Press, 1963. (p. 463).

CHAPTER III

APPENDIX

The BOX Method

This technique of collecting and analyzing data was developed to make the data-gathering process using a Vanguard Motion Analyzer as quick and simple as possible while providing adaquate information for studying the SPAR experiments. The Analyzer allows the frame by frame viewing of 16mm cine film and the characterization of any point in the frame by x and y coordinates determined by the intersection of two manually controlled cross hairs. The cross hairs are parallel to the edges of the viewing screen and to obtain a different orientation of the perpendicular cross hairs, the projection head of the Analyzer can be rotated.

The analysis - whether simple plotting of the time data or the study of the Fourier spectra for that data - uses the dimensions and the positions of boxes from each frame digitized to characterize the behavior of the drop and its acoustic environment. This system has the flexibility of allowing the operators to take or retake data on any part of the film whenever needed, but the price which must be paid is sitting in front of the Motion Analyzer for often long periods of time. The main virtue of the system is its simplicity. However this simplicity limits the kinds of shapes that can be studied with confidence to to those that are themselves simple: the less elliptical the boundary, the less meaningful the data. This problem is particularly acute when studying the shell's behavior when it is distorted, e.g. just after deployment.

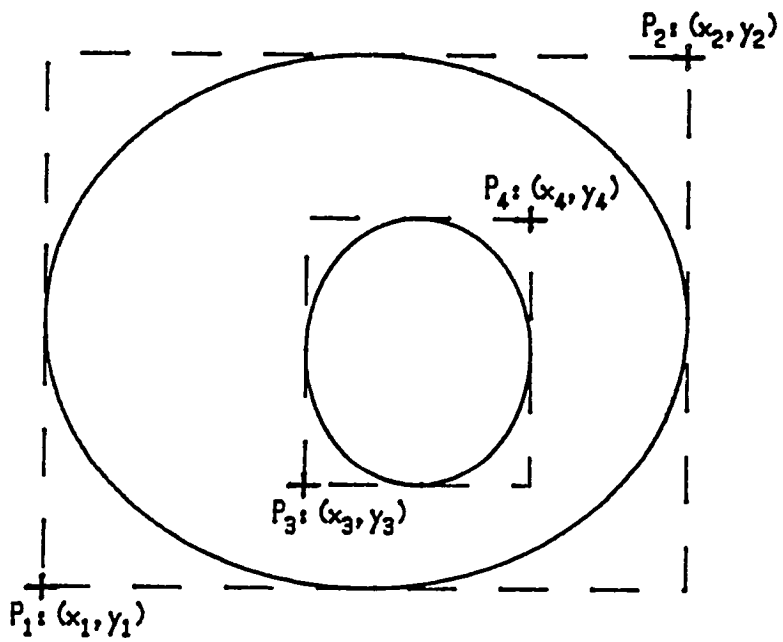

Figure 1. Schematic of a shell image and the locations of the four points used to characterize that shell in the BOX analysis.

For a simple drop the data-gathering procedure would be to determine the experiment time (in seconds after liftoff) from the edge of the film (which was partially visible on the Analyzer) and then adjust the cross hairs to just touch the bottom and left edge of the image, record the coordinates and move the cross-hairs to the right and top edge and take the coordinates for that position. This gives five numbers per frame: t, x_1, y_1, x_2 and y_2. When studying a shell an inner box is constructed producing four more coordinates: x_3, y_3, x_4 and y_4 (see Figure 1).

Two broad classes of information are sought from this kind of analysis: motion of the entire shell in the chamber or the bubble within the shell and motions of the surfaces as they oscillate. The former are obtained from combinations of sums of the four points:

$$x_s = \frac{x_1+x_2}{2a}, \quad x_b = \frac{x_3+x_4}{2a}, \quad x_{bs} = \frac{(x_3+x_4)-(x_1+x_2)}{2a}, \text{ etc.,} \tag{1}$$

$$\text{where } a \equiv \frac{1}{4}\sum_n \{(x_2-x_1)+(y_2-y_1)\} \tag{2}$$

is the average radius for that view determined by summing the vertical and horizontal dimensions of the shell over n frames in the time period of interest. The first quantity, x_s, approximates the position of the shell's center of mass on the film image. Actually it is the center of the image - if the image is symmetric. x_b and x_{bs} are the positions of the bubble in the chamber and relative to the shell's center. To correct x_s, x_b, and other center-of-mass-type points so that they are relative to the chamber's center for that view, the coordinate of the center, x_c, must be subtracted before normalizing. These combinations are used to generate date to study motion of the shell in the acoustic potential well, eg. see Figure 2a in section 5B. x_{bs} and y_{bs} can also be used to study the centeredness of the bubble within the shell (see Figure 1 in section 5D).

When a shell contains a large bubble which is free to move through the liquid as the shell oscillates in the potential well, a better approximation to the true center of mass than (x_s,y_s) will be (x_s^*,y_s^*).

$$\begin{aligned} x_s^* &= \frac{x_1+x_2}{2a} + \Delta\rho\left\{\frac{x_1+x_2}{2a} - \frac{x_3+x_4}{2a}\right\} \\ &= \frac{x_1+x_2}{2a}\left\{1 + \Delta\rho\left(1 - \frac{x_3+x_4}{x_1+x_2}\right)\right\} \end{aligned} \tag{3}$$

where $\Delta\rho$ is the difference in density between the air and the liquid.

To study oscillations of the surfaces, differences between the four points can be combined in many ways:

$$s_x = \frac{x_2-x_1}{2a}, \quad b_x = \frac{x_4-x_3}{2a}, \quad t_{top} = \frac{x_2-x_4}{2a}, \text{ etc.,} \tag{4a}$$

$$D = \frac{(x_2+x_1)-(y_2+y_1)}{2a}, \qquad S = \frac{(x_2-x_1)+(y_2-y_1)}{2a}, \tag{4b}$$

$$\delta_s = \frac{(x_2-x_1)-(x_4-x_3)}{2a}, \qquad \delta_b = \frac{(x_2-x_1)+(x_4-x_3)}{2a}. \tag{4c}$$

The oscillation of the outer surface along the x axis will show up in the shell size, s_x, but also to a varying degree in the difference and sum data, D and S. δ_s will highlight out of phase oscillations in the x direction while δ_b will do the same for oscillations in which the two surfaces move in phase. The four thicknesses, t_{top}, t_{right}, t_{bot}, and t_{left}, provide useful frequency information when the bubble is not concentric with the outer surface. Examples of the various combinations are contained in the section concerned with natural oscillations, section 5C. These combinations are also used to generate data on the relative dimensions of the shell parallel and perpendicular to the axis of rotation (Figure 2, section 5D). The relative dimensions obtained indicate the how well balanced the acoustic forces are (Table 2, section 5B).

SSD 81 0165

SPAR VIII EXPERIMENT REPORT
CONTAINERLESS PROCESSING OF GLASS
EXPERIMENT 74-42

SEPTEMBER 24, 1981

Contract NAS8-32023

R. A. Happe, Principal Investigator

and

K. S. Kim

TABLE OF CONTENTS

ILLUSTRATIONS

TABLES

CHAPTER IV

SUMMARY

The second containerless glass melting experiment, NASA experiment 74-42, was flown on the SPAR VIII sounding rocket on November 18, 198(.

This report includes descriptions of the flight sample and the flight events for the SPAR VIII experiment and a summary of the SPAR VI experiment which formed a basis for determining the objectives of the SPAR VIII experiment.

The flight experiment was designed to produce a single 0.64cm (¼ inch) diameter silica-modified gallia-calcia glass (39.3 Ga_2O_3: 35.7 CaO: 25.0 SiO_2 in mol percent, i.e. the same composition as the SPAR VI sample) containerless melted and cooled in a single-axis acoustic levitator built under contract to NASA by Intersonics, Inc.

In the first experiment (SPAR VI) (Ref. 1) the performance of the flight experiment hardware was in most regards satisfactory with one exception, that being the acoustic levitator, which suspended the sample for only 27 seconds of the desired 240 seconds. Therefore, one of the principal objectives of the SPAR VIII experiment was to increase the sonic positioning time to encompass the entire processing cycle.

The payload parachute for the SPAR VIII experiment opened prematurely at higher-than-planned altitude resulting in knotting of the central portion of the parachute and tearing of the fabric. As a result of the parachute malfunction, the payload impacted the ground at a speed of approximately 300ft/sec (∿200MPH) and the experiment package suffered severe damage.

The flight experiment sample has not been recovered to date. The flight motion picture film, however, was recovered and successfully developed. The analysis of the motion picture showed that the experiment hardware functioned in most regards as planned, except the acoustic levitator, which suspended the sample for only 82 seconds of the desired 240 seconds.

INTRODUCTION

If the promise of containerless melting and cooling, made possible by space processing, is realized fully in the years that lie ahead, an important new area of optical glasses will become a reality. In part, this new area may be visualized by referring to the schematic of Figure 1. The ordinate is the index of refraction, and the abscissa, the Abbe number (ν), an inverse measure of dispersion. The higher Abbe numbers, to the left, of the diagram indicate a low dispersion (i.e., a flatter slope of the index versus wavelength curve). The lower Abbe numbers, to the right, have a high dispersion (steep index versus wavelength curve). A century ago flint glasses were developed. This permitted construction of the first achromatic, or color-corrected, multi-element lenses. Responding to the demands for better quality lenses, the optical glass industry developed more glasses with properties between those of the crown and flint glasses. More recently glasses have been developed to fill out the vertically hatched commercial glass area. The trend has been to push the area up and to the left with glasses of complex compositions.

If glasses beyond the reach of current terrestrial technology could be prepared from the more reluctant glass forming oxides, the area of useful

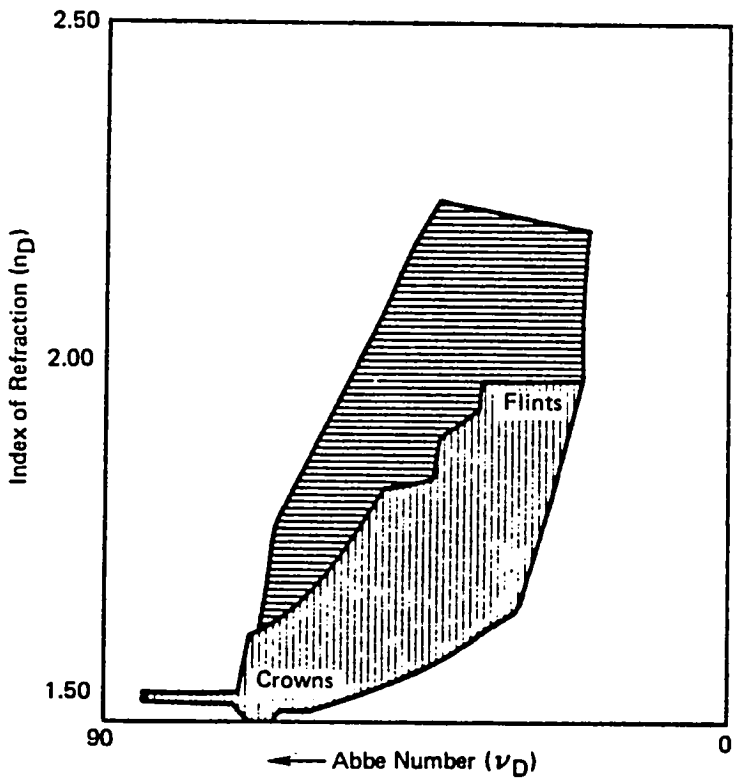

Figure 1. n-ν Diagram for Optical Glasses

properties could be expanded significantly. The expansion would occur by the addition of space-prepared glasses (horizontally hatched area of Figure 1) to the terrestrial base.

THE RATIONALE FOR SPACE PROCESSING

For most of the past decade, the Principal Investigator has been investigating possibilities for producing new optical glasses by containerless melting and cooling utilizing the near-zero-gravity environment available in earth orbit. The paragraphs that follow cover the technical thinking behind the concept of containerless processing in space, a summary of experience to date, and reasons for the interest in space processing of optical glasses.

When a molten oxide is cooled slowly enough to approach equilibrium conditions, it crystallizes near its crystalline melting point. In the case of the conventional glasses, usually based on oxides such as SiO_2, P_2O_5, B_2O_3, or GeO_2, the viscosity of the molten glass is very high. With this high viscosity, the molecular mobility is very low. Thus, when such substances are cooled from the molten state, it is difficult for the molecules to rearrange themselves into the orderly state of the crystalline lattice. Because of this sluggishness, the movement of the molecules into the crystalline lattice positions is incomplete on cooling with normal cooling rates. In these cases, the semi-random molecular arrangement of the liquid state is essentially preserved on cooling, and the substance remains amorphous, the resulting product being called a glass.

The crystallization phenomenon may be considered to occur in two stages: (1) nucleation and (2) crystal growth. In conventional glasses the sluggishness effectively inhibits both of these processes, especially the latter. Therefore, even if the substance manages to nucleate on cooling from the melt, the crystal growth rate is so slow that the nucleii remain, for practical purposes, undetectable in the glass. There are, however, only a few oxides that have sufficiently high viscosities to permit glass formation under normal circumstances.

For the past two decades, glasses have been made terrestrially in the laboratory from some of the less viscous oxides. Invariably, the technique used for preparing them involves extremely high cooling rates from the liquid state. The familiar splat-cooling technique (Reference 2) is a case in point. While such techniques yield valuable research information about the nature of the glasses so prepared, their application for commercial purposes is extremely limited. By the nature of the technique, only very thin films can be prepared. With this technique the liquid, as a very thin layer, is cooled in contact with a chill plate, usually of copper. While the copper provides numerous nucleation sites, the very rapid cooling effectively suppresses crystal growth.

Containerless melting in space offers the first practical opportunity to prepare glasses in massive form from the large number of oxides whose liquid viscosity* is not high. If nucleation can be prevented on cooling, then crystal growth obviously cannot occur, and a glass should result.

It is generally recognized that there are two kinds of nucleation: (1) heterogeneous and (2) homogeneous. Heterogeneous nucleation results from contact of the cooling liquid with crystalline material. Such a material may be entirely different in chemical composition from the melt. Common container wall materials are cases in point. Of course, it can also be of the same or similar composition, for example, unmelted portions of the bath or cool seed crystals of similar composition deliberately introduced into the cooling melt. In practice it is very difficult, or virtually impossible, to eliminate heterogeneous nucleation sites with conventional, terrestrial practice. Normally, a crystalline container must be used both for melting and for cooling. Further, the impingement of cool dust particles on the cooling melt may be enough to cause heterogeneous nucleation, and if the viscosity remains low enough in the supercooled liquid, crystal growth rates will be high and the glassy state will not be obtained.**

Homogeneous nucleation is another matter. Theoretical studies (Reference 3) have shown that homogeneous nucleation rates for oxide glasses are much slower than for heterogeneous nucleation. Experimentally, it is difficult to determine whether nucleation is truly homogeneous. There are those who believe that it may never truly have been observed in an oxide glass. Since only a few molecules of a heterogeneous nucleator need to be present, the detection of such a small amount is a formidable technical problem. Thus, the assumption, *a priori*, that nucleation which occurs, for example, throughout the mass of a cooling substance is homogeneous may be erroneous. One can always argue that an undetectably small amount of a crystalline substance was present at the nucleation sites. At any rate, if heterogeneous nucleation can be effectively prevented, it is probable that homogeneous nucleation, if it can occur, will not occur unless the cooling rate is quite slow.

Over the past several years, the principal investigator has successfully prepared numerous approximately 6-mm-diameter (about 3/4 gram) glass boules

---

*It is recognized that the slope of the viscosity versus temperature curve below the crystalline melting point (i.e., in the supercooled region) is very important to the glass formation process. However no such data exist for the oxides proposed here. It is probable that the general tendencies of viscosity change in the supercooled region can be inferred from future terrestrial and space studies.

**The presence of insoluble crystalline material in the melt could also cause heterogeneous nucleation. Fortunately oxides are very good solvents. It therefore follows that with enough melting time this problem should be held to a minimum.

of roughly spherical shape from several oxide compositions that have low viscosity in the molten state. That work is covered in detail in References 4 and 5. Among the compositions prepared are the gallia-calcia eutectic at approximately 19 weight percent calcia, an alumina-calcia composition with 30 weight percent calcia, and a ternary, 40 weight percent lanthana-40 weight percent alumina--20 weight percent calcia composition. The alumina-calcia composition is well outside the reported glass-forming region based on 20 mg melts (Reference 6). The gallia-calcia composition had been reported to be a glass former in the laboratory, but in sizes less than 40 mg (Reference 7). Furtheremore, water quenching was required to achieve the glassy condition. Thus the preparation of crack-free boules with 50 times the mass of those of the earlier work represents a significant technical achievement. A glass of the ternary composition, to the principal investigator's knowledge has never been reported in the literature.

The method for preparing the 6-mm boules is described in detail in Reference 4. Briefly, the samples in contact with a silica (glass) sting are suspended in a vertical air column. The energy for melting comes from a CO_2 laser beam aimed at one side of the boule. The silica sting was found necessary to stabilize the motion of the melt and is a definite convenience for getting the process started. The oxide is transferred to the sting from a laser melted area of well-mixed powders of the desired composition. While the technique developed by the principal investigator is excellent for demonstrating that new glasses can indeed be prepared with containerless melting and cooling techniques, it does suffer from several limitations, as follows:

1. Because of the relationship among viscosity, surface tension, and mass, 6 mm is very near the maximum sized boule that can be prepared in this fashion.

2. The silica sting material continuously dissolves into the sample during melting and holding at superheat temperature. Simultaneously, the sample constituents as well as silica are boiled out of the "hot spot" where the laser beam impinges. The end result is a net increase in the silica content. In order to keep the silica content as low as possible it is necessary to keep the melting time as short as possible (on the order of 30 seconds). As a consequence then, good mixing is not obtained.

3. It is very difficult to eliminate dust in the air from the wind tunnel. Thus the molten sample can be considered to be continually bombarded by dust particles while it is cooling. For this reason the technique may be unnecessarily restrictive compared with the more favorable conditions expected to accrue from space melting.

Space melting promises to eliminate or significantly reduce all three of the shortcomings inherent in the air suspension/laser melting equipment. Very large boules should ultimately be possible if enough power for melting can be made available. The silica sting will not be required with the acoustic

positioning technique being developed by NASA. Since space melting can be accomplished in a furnace with nearly isothermal conditions, the localized heating of the specimen intrinsic in the terrestrial laser melting technique will not be experienced. Space melting can be accomplished in an essentially static atmosphere, significantly reducing the possibilities for dust-caused nucleation. It is entirely possible that some of the compositions that failed to form glass in our terrestrial experiments may prove to be glass formers under space melting and cooling conditions.

THE SOUNDING ROCKET PROGRAM

The Space Processing Applications Rocket (SPAR) program is considered a precursor to the Shuttle and later manned orbital programs. While conditions are not ideal for glass melting aboard a sounding rocket, largely because of the rather short melting time (less than five minutes) available, the program does afford a good opportunity to gain early experience with glass melting within the limitations and, more importantly, with space glass melting equipment development.

The gallia-calcia composition mentioned in the previous section of this report was originally chosen as a suitable composition for two sounding rocket experiments and for early Shuttle experiments using the NASA-provided Materials Experiment Assembly (MEA). The composition is a eutectic between the compounds $CaO:Ga_2O_3$ and $CaO:2Ga_2O_3$ and its composition, under equilibrium conditions, is approximately 19 wt. % CaO, balance Ga_2O_3 (approximately 56 mol % CaO). The phase diagram for the binary gallia-calcia system is shown in Figure 2.

This particular composition was chosen for the following reasons:

1. It has the lowest melting temperature of any of the new optical glass compositions studied by the principal investigator prior to the initiation of the SPAR program.

2. It is a relatively good glass former in the 1/4-inch (approximately 0.6-cm) (about 0.8 gm.) size under terrestrial containerless melting conditions.

3. It potentially has optical properties of interest to the optics industry.

4. Prior to our terrestrial melting work, it had not been prepared in a size exceeding 50 mg (0.050 gm).

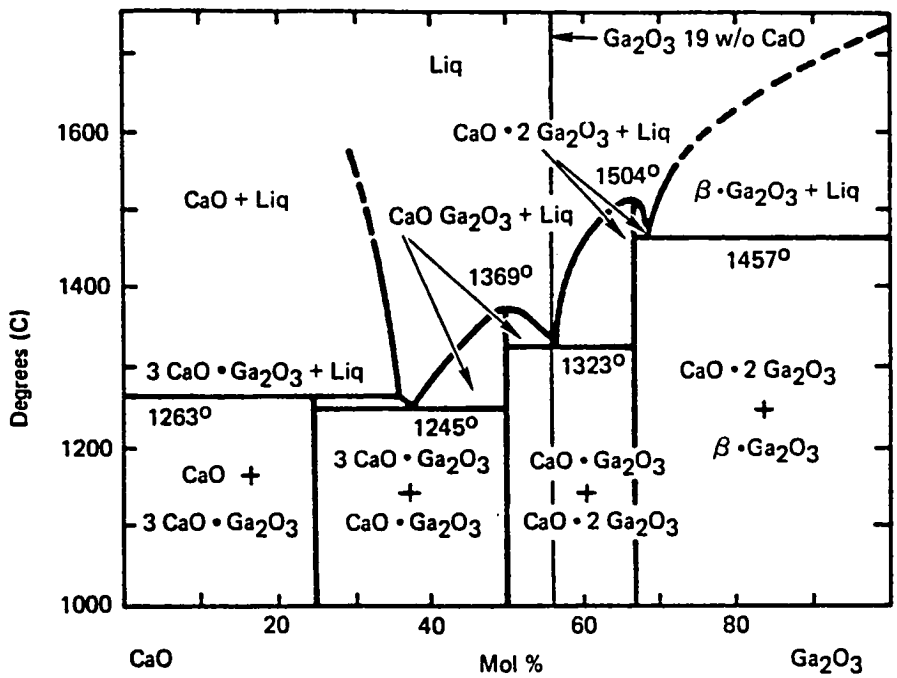

Figure 2. The CaO - Ga_2O_3 Phase Diagram (From Reference 8)

SUMMARY OF THE SPAR VI EXPERIMENT

The first containerless glass melting experiment, NASA experiment 74-42 was flown on the SPAR VI sounding rocket on October 17, 1979. A detailed reporting of that experiment is give in Reference 1.

During the flight experiment, a single 1/4-inch diameter (6.4 mm.) sample of a silica-modified gallia-calcia glass of composition 39.3 Ga_2O_3 : 35.7 CaO : 25.0 SiO_2 in mol percent was containerless melted and cooled in a single-axis acoustic positioning apparatus built under contract to NASA by Intersonics, Inc. Since this was the first containerless glass flight, the principal objective of the experiment was to determine the functioning of the flight experiment hardware under actual flight conditions. The flight hardware included a silicon carbide element furnace equipped with a single-axis positioning device designed to prevent contact of the molten sample with other than the gaseous (approximately one-ground-level air) atmosphere during the 4 minutes of low-gravity flight. At the completion of the melting and soaking portion of the processing cycle, which was performed at a nominal temperature of 1575 C, a massive copper cooling shroud was introduced into the hot zone of the furnace to radiation-cool the sample. An injection cage fashioned from platinum and 30-percent rhodium alloy was used to inject the sample into the sonic well, and a single motion-picture camera was provided to observe the flight sample during the entire processing cycle. The hardware package included necessary electronics, timers, temperature control equipment, and mechanical devices, the last for operation of the injection mechanism, furnace wall gates, and cooling shroud.

The sample was completely melted during the flight and was cooled to a clear glass. Injection into the furnace hot zone was accomplished. After it touched the cage four times in the first 9 seconds, the sample remained in suspension 27 seconds, at which time it drifted to the injection cage and attached itself to one of the platinum alloy wires making up the cage. It remained attached and centered on the cage wire during the remainder of the processing cycle.

During the post-flight evaluation, the sample was found to be free of unmelted, crystalline, material. It contained three small bubbles near the platinum wire. The shape of the sample was spherical except for projections caused by wetting the wire by the glass at either pole where the platinum wire emerged from the sample. Unexpectedly, the surface of the sample was found to contain numerous small crystal rosettes not large enough to be seen by the unaided eye. Analysis of the crystal rosettes with a scanning electron microscope showed them to be of approximately the same composition as the glass. Platinum (with some rhodium present) was found to be the probable cause of crystal nucleation. The principal constituent of the rosettes was found by indirect methods to be $Ca_2Ga_2SiO_7$. The most probable causes of the platinum contamination of the surface are thought to be either (1) mechanical transfer from the loose-fitting injection cage during lift-off

of the rocket or (2) surface diffusion from the platinum-rhodium wire which was in contact with the glass sample during most of the flight experiment cycle.

OBJECTIVES AND RATIONALE OF THE SPAR VIII EXPERIMENT

The principal objectives of the 74-42 SPAR VIII experiment were: (1) To increase the sonic positioning time to encompass the entire heating and cooling cycle, and (2) To eliminate the platinum contamination experienced with the SPAR VI experiment.

In order to accomplish the first objective, Intersonics, Inc. replaced the compact-design sonic driver used on SPAR VI with a less compact driver which had been flight tested aboard several KC-135 flights. Intersonics' analysis of the flight data showed that the sonic power had dropped significantly during the SPAR VI experiment and it was strongly suspected that the compact driver was at fault.

The second objective was addressed by covering the platinum injection cage wires in the area where the sample was gripped prior to injection with alumina (Al_2O_3) beads. It was felt that the alumina would prevent the platinum alloy from mechanically transferring to the specimen during the lift-off, high vibration, portion of the flight. Any alumina that might mechanically transfer to the sample would be quickly dissolved by the molten flight sample. The second possibility for platinum contamination mentioned in the previous section, i.e. surface diffusion from the Pt-Rh wire, would be eliminated if the sonic positioning mechanism operated throughout the experiment as planned.

DESCRIPTION OF THE FLIGHT SAMPLES

It was decided to use the same, silica-modified, composition used on the SPAR VI experiment for the SPAR VIII experiment. Samples No. 1, 2, 4, and 5 shown in the table on page 14 of Reference 1 were diamond re-ground at a local lapidary shop to reduce their sizes to more nearly match that of the SPAR VI flight sample. Data on the six flight samples, which were all cut from the same gallia-calcia-silica loaf casting are given in Table 1.

TABLE 1. WEIGHTS AND DISPOSITION OF SIX FLIGHT SAMPLES

Sample No.	Weight gm.		Disposition
	Original	Reground	
1	1.2578	0.5948	SPAR VIII flight sample
2	--- (*)	0.5721	SPAR VIII all systems test (**)
3	0.8972	------	SPAR VI all systems test (**)
4	0.8975	0.5804	Not used to date
5	0.9865	0.6014	Not used to date
6	0.5778	------	SPAR VI flight sample

Details of the selection of the silica-modified composition and the preparation of the flight samples shown above are given on pages 9 through 17 of Reference 1.

(*) Sample No. 2 had been contaminated with porcelain on the surface and therefore was not considered for use in the SPAR VI experiment. It was felt that the regrinding would effectively remove the contamination and therefore this sample was deemed satisfactory for all systems test purposes.
(**) A ground test performed by MSFC prior to flight during which the sample was melted in a platinum crucible in the flight experiment hardware.

FLIGHT EVENTS

EVENTS AT WHITE SANDS MISSILE RANGE

SPAR VIII, with flight sample No. 1 loaded in the injection cage, was launched at 5:40 pm, MST - White Sands Missile Range, New Mexico, November 18, 1980. Flight telemetry data appeared normal during 74-42 experiment operation and all functions appeared to occur as planned.

The payload parachute opened prematurely at higher-than-planned altitude resulting in knotting of the central portion of the parachute and tearing of the fabric. As a result of the parachute malfunction the payload impacted the desert floor at a velocity of approximately 300 ft./sec. (~ 200 MPH). Since the 74-42 package was located at the lower end of the payload stack (opposite end from the parachute), it suffered severe damage from the impact, its length being reduced from about three feet to less than one foot. Two views of the returned experiment hardware are shown in Figure 3.

On the morning of November 19, 1980 the remains of the experiment apparatus were loaded onto the bed of an Army truck and hauled approximately 45 miles to the Vehicle Assembly Building (VAB). During the trip, debris from the crushed package spilled out over the truck bed.

After the crushed 74-42 package was removed from the truck and placed in the VAB, the bed of the truck was swept, the debris was collected and placed in the VAB. During the afternoon of November 19 the crushed payload was pulled and cut apart. No trace of the flight motion picture film was found, although the crushed remains of the Photosonics camera was identified. The debris from the truck bed and from the crushed experiment package was screened. The screening yielded several glass fragments but nothing that appeared to be from the experiment gallia-calcia-silica sample. The crushed platinum alloy injection cage was identified, but a portion of the outer cage could not be located.

On the morning of November 20, 1980 the impact site was visited. Personnel included Charles Rey and Tom Danley of Intersonics and the principal investigator. The flight motion picture film, still entrapped in the twisted remains of the film magazine was found under the crushed remains of an access door in the bottom of the crater. Both were covered by 6 to 8 inches of loose dirt. The crater was quickly covered with black plastic to keep exposure to sunlight to a minimum; the film, canister and some of the dirt were double-wrapped in heavy, black, opaque plastic; and the package was thoroughly taped.

Much of the dirt in the impact crater was screened at the site, but no trace of the missing platinum cage wires or any glass fragments that appeared to be from the flight sample was found.

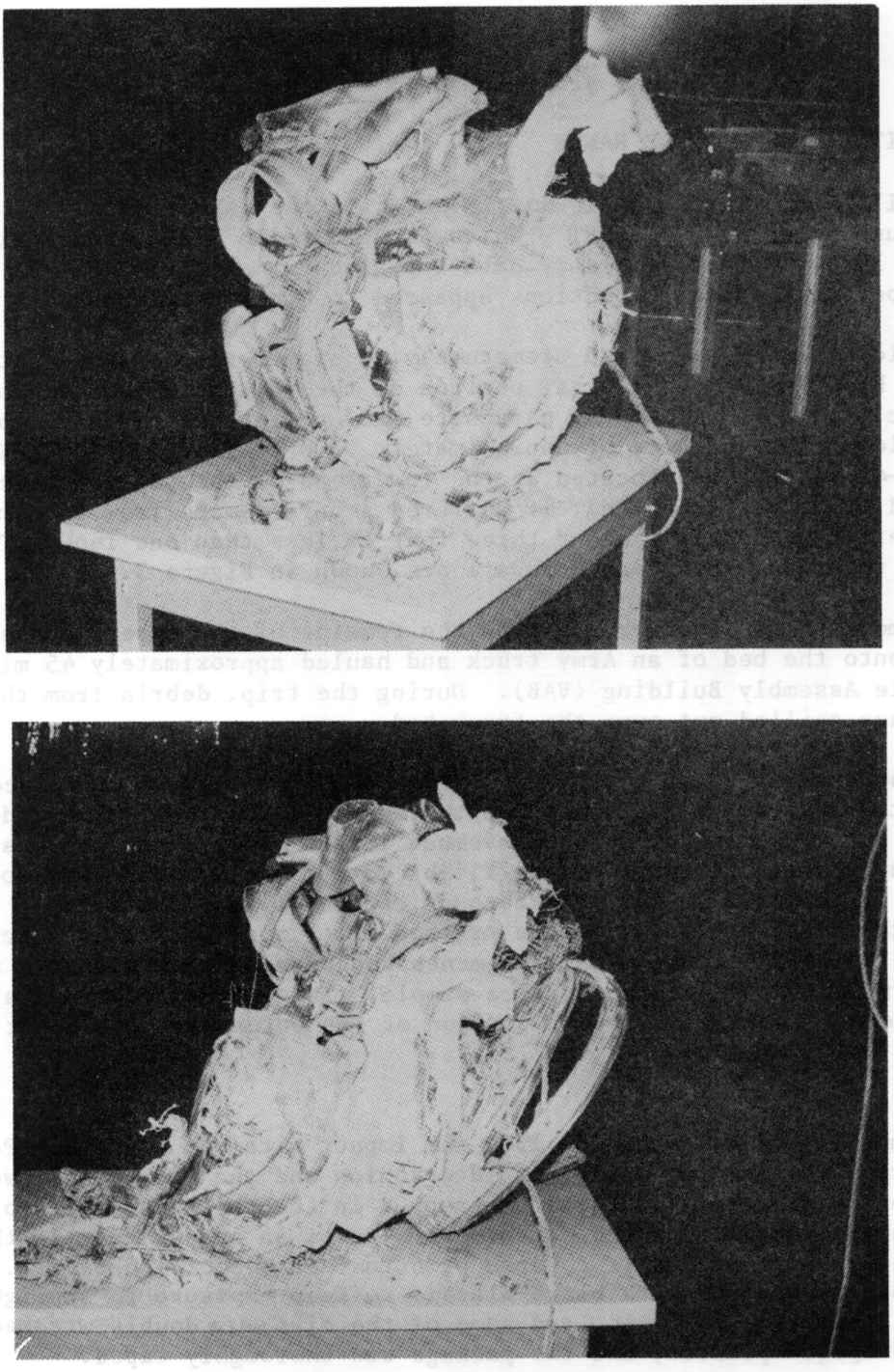

Figure 3. Two Views of the Returned Experiment Hardware

An area around the impact crater within a radius of about 15 feet was also searched. Much of this area was covered by tall grass as was the immediate impact site, which made searching difficult. One fragment of the experiment package shell was found about 33 yards south (toward the launch site) of the impact crater. After about an hour the search by 5 or 6 people was abandoned and all personnel flew back to the VAB.

After returning to the VAB, the package containing the film was opened in a dark room at LC 35. The film was separated from the remains of the magazine, cleaned of loose dirt, and re-wrapped thoroughly in heavy, black plastic and re-taped. Both the take-up and feeder spools of film appeared to be intact. The film was hand carried to Los Angeles (without x-ray inspection) by the P.I.

On January 9, 1981, the impact site was again visited by Rodger Chassay of MSFC, two U.S. Navy people assigned to the Missile Range and the P.I. The entire day was spent searching the impact crater and the area around it. Screening of the dirt yielded several glass fragments - none of which appeared to be from the flight sample. None of the missing Pt-alloy cage wires was found.

During the latter part of the week of January 12, 1981, Rodger Chassay and the two Navy people again visited the impact site. The grass around the impact site was burned off and much of the surface dirt was again screened. Three more glass fragments were found. A larger piece with a portion of an approximately spherical surface was also found embedded in a piece of hard dirt which had been compacted by the payload impact.

ANALYSIS OF GLASS FRAGMENTS

After the Principal Investigator received the larger piece of glass and the three small fragments found at the site the week of January 12, a chip was removed from the fracture face of the larger piece and it, along with the smaller fragments, were spectrographically analyzed. The results follow:

1) Larger fragment (with portion of approximately spherical surface)
   - Silicon - major (10 to 100%)
   - Magnesium - trace (0.01 to 0.5%)
   - Calcium - trace
   - Aluminum - trace
   - Zinc - slight trace (0.01%)
   - Iron - slight trace

2) Three smaller fragments
   - Silicon - major
   - Sodium - major
   - Magnesium - minor (0.5 to 10%)
   - Calcium - trace
   - Copper - slight trace

Since none of the above contained the major gallium and calcium expected with the flight sample, it must be concluded that none of them came from the flight sample.

Additionally, fifty-five fragments of glass from the wreckage and/or the vicinity of the impact site have been received by the P.I. Thirty three of these were ruled out as being from the flight sample either because they were too large or showed evidence of mirrored surfaces. The remaining twenty two fragments were spectrographically analyzed even though none of them showed the characteristic yellowish cast of the flight sample material. None of them showed major or even traces of gallium content. Therefore it must be concluded that as of the date of this writing, no trace of the flight sample has been found. The possibility that the flight sample may still be intact cannot be ruled out at this time.

It is the Principal Investigator's understanding that MSFC plans to continue the search for the missing flight sample in the future. If it is ever located, the writer plans to examine it in detail and prepare a supplement to this report giving the results of that examination.

FLIGHT MOTION PICTURES

On December 1, 1980, the film was hand carried to Hollywood Film Enterprises (HFE). About two feet of film from the larger (take-up) spool was removed because of excessive damage. After inspecting and re-spooling, the remainder of the film was developed as a negative without further incident. There was some edge damage and much wrinkling of the film. Because it was an Estar base film, which is very tough, no further tearing occurred during development.

It was obvious from cursory inspection of the processed flight film negative that there was too much damage to permit positive motion picture prints to be made using conventional printing techniques.

A frame-by-frame inspection of the film showed that it did indeed contain the complete flight record beginning with the first appearance of the platinum alloy wire injection cage and ending after the sample and cage had cooled sufficiently that they could no longer be seen against the relatively cool background of the cooling shroud.

Key events are summarized in the table which follows. All time calculations are based on the assumption that the flight camera was running accurately at 24 frames per second.

TABLE 2. KEY EVENTS OF FURNACE/LEVITATOR OPERATION

Frame	Event	Seconds Time	Seconds Δt
1	Injection gate beginning to open		
41	Injection cage first appears	1.7	
67	Injection fully open, sample in contact with inner cage (Al_2O_3 covered Pt)	2.8	
161	Sample begins to drift free of cage	6.7	
2080	Sample begins final excursion toward Pt cage	86.7	83.3
2160	Sample contacts cage wires	90.0	∿0.8 sec.
2180	Sample centered on cage wire	90.8	
3880	Cooling shroud gate begins to open	161.7	
3898	Cooling shroud gate fully open	162.4	
∿4000	Cooling underway	166.7	∿43
∿5040	Sample approx. same temperature as background	210	∿72
∿5720	Pt. cage approx. same temperature as background	238	
6009	End of film (cut at HFE)	251	

It is obvious from the film records that the sonic suspension system was not entirely successful, the sample drifting to a platinum alloy cage wire and attaching itself before the completion of the entire processing cycle. The sample did remain suspended for 82 seconds as compared with 27 seconds for the SPAR VI flight.

It was noted during detailed examination of the suspension portion of the film that this portion is in somewhat better condition than the terminal end, which contains the balance of the soaking portion of the cycle and the entire cooling portion. After the suspension portion was repaired to eliminate torn and/or frayed sprocket holes, an attempt was made by Hollywood Film Enterprises to make a print out of the film. The attempt proved to be a success and the resulting print was used as a master for making additional prints for distribution.

Prints of selected frames are shown in Figure 4. In frame 136 the sample is still at the base (top in the pricture) of the sample cage. Frames 165 through 920 show the motion of the sample. The two streaks shown in frame 920 are an evidence of the film damage sustained from the crash landing. Frames 1630 and 2120 indicate through poor contrast that the sample and the cage approach closely the furnace wall temperature. In frame 3898 the sample is shown impaled by the cage wire. The clarity of the sample and the cage indicates the relative coolness of the furnace wall. Frames subsequent to 3898 show the sample remains embedded in the same location on the cage wire.

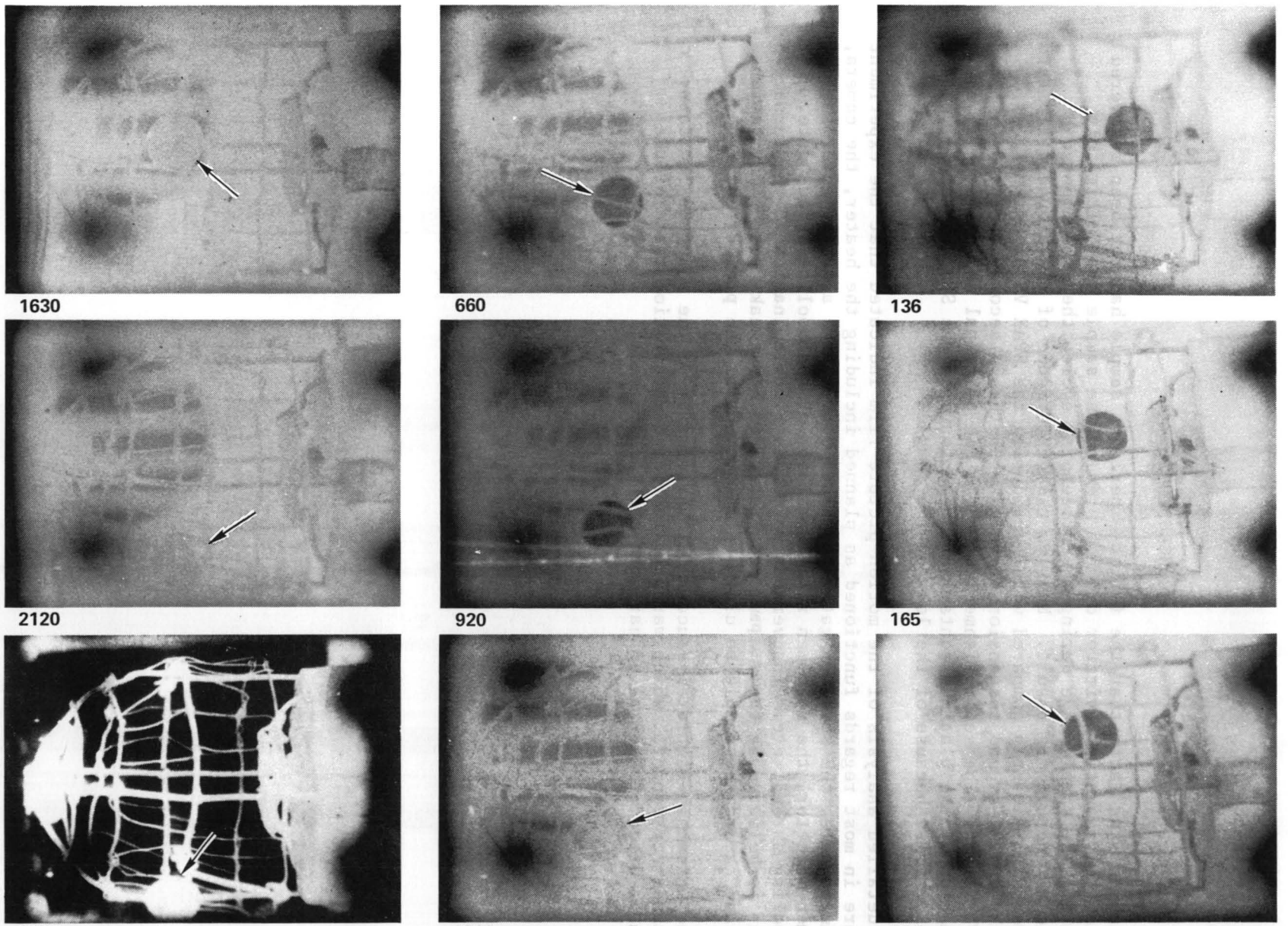

Figure 4. Prints of Selected Frames

CONCLUSIONS

Despite the facts that the flight experiment sample has not been recovered and that the acoustic levitator did not prevent the sample from ultimately contacting the sample cage during the processing cycle, the experiment did produce an encouraging result. Namely, the performance of the acoustic levitator improved significantly compared with that during the SPAR VI experiment, as shown by the 82-second suspension compared with the 27 second suspension of the SPAR VI flight. The accomplishment of the other principal objective, i.e. the elimination of the platinum contamination as found in the SPAR VI sample, could not be verified because of the loss of the sample.

A detailed analysis of the motion picture film indicated that the experiment hardware in most regards functioned as planned including the heater, the camera, the camera gate, the specimen gate, the sound source, the acoustic gate, the specimen injector, the specimen release mechanism, the cooling shroud gate, the cooling shroud, etc. Inadvertent water vapor contamination of the furnace chamber is believed by the equipment contractor to have weakened the levitation force and caused the sample to ultimately move out of the pressure well.

The less-than-completely-successful performance of the acoustic levitator is a cause for concern, which warrants further demonstration tests of the levitator after procedural or hardware changes are made.

ACKNOWLEDGEMENTS

The writers wish to express their gratitude to A. R. Sale of Rockwell Space Transportation System Group for printing selected frames of the flight motion picture film and assisting in the analysis and interpretation of the motion pictures. They also wish to express their gratitude to Drs. R. Whymark and C. Rey of Intersonics for valuable information given to them through many conversations.

REFERENCES

1. Happe, R. A. "SPAR VI Experiment Report - Containerless Processing of Glass, Experiment 74-42., Rockwell International, Space Operations and Satellite Systems Division, SSD80-0045 March, 1980.

2. Duwez, E. D. "Structure and Properties of Alloys Rapidly Quenched from the Liquid State." Trans. of the ASM 60 (1967) 606.

3. Neilson, G. F., and M. C. Weinberg. Development of Improved Amorphous Materials for Laser Systems - Final Report, Task Order RD-151, Contract 953846 under Contract NAS7-100, Owens Illinois, Inc. (November 1974).

4. Happe, R. A. Manufacturing Unique Glasses in Space - First Interim Report, Rockwell International Corporation, Space Division, SD 74-SA-0174 (November 1974).

5. Happe, R. A. Manufacturing Unique Glasses in Space - Second Interim Report, Rockwell International Corporation, Space Division, SD 76-SA-0029 (March 1976).

6. Rawson, H., Inorganic Glass-Forming Systems, Academic Press (1967).

7. Baynton, P.L., H. Rawson, and J. E. Stanworth, "Gallium Oxide Glasses," Nature (February 23, 1957).

8. Jeevaratnam, J. and F. P. Glasser. "The System CaO-Ga_2O_3," Journal of American Ceramics Society. 44 (1961) 564.

Space Systems Group
12214 Lakewood Boulevard
Downey, California 90241

Rockwell International

January 7, 1981

In Reply Refer to 80MA6302

National Aeronautics and Space Administration
George C. Marshall Space Flight Center
Marshall Space Flight Center, Alabama 35812

Attention: Robert Fallon, LA11

Subject: Experiment 74-42, Principal Investigator's "Quick Look" Report - SPAR VIII - NAS8-32023

Events at White Sands Missile Range

SPAR VIII was launched at 5:40 pm, MST - White Sands Missile Range, New Mexico, November 18, 1980. Flight telemetry data appeared normal during 74-42 experiment operation and all functions appeared to occur as planned.

The payload parachute opened prematurely at higher-than-planned altitude resulting in knotting of the central portion of the parachute and tearing of the fabric. As a result of the parachute malfunction the payload impacted the desert floor at a velocity of approximately 300 ft./sec. (~200 MPH). Since the 74-42 package was located at the lower end of the payload stack (opposite end from the parachute), it suffered severe damage from the impact, its length being reduced from about three feet to less than one foot.

On the morning of November 19, the remains of the experiment apparatus were loaded onto the bed of an Army truck and hauled approximately 45 miles to the Vehicle Assembly Building (VAB). During the trip, debris from the crushed package spilled out over the truck bed.

After the crushed 74-42 package was removed from the truck and placed in the VAB, the bed of the truck was swept, the debris was collected and placed in the VAB. During the afternoon of November 19 the crushed payload was pulled and cut apart. No trace of the flight motion picture film was found, although the crushed remains of the Photosonics camera was identified. The debris from the truck bed and from the crushed experiment package was screened. The screening yielded several glass fragments but nothing that appeared to be from the experiment gallia-calcia-silica sample. The glass fragments have been saved and will be checked for index of refraction along with additional glass fragments to be received by the P.I. from MSFC and Intersonics. It should be noted at this point that a portion of the platinum outer cage appeared to be missing.

On the morning of November 20, the impact site was visited. Personnel included Charles Rey and Tom Danley of Intersonics and the writer. The flight motion picture film, still entrapped in the twisted remains of the film magazine was found under the crushed remains of an access door in the bottom of the crater. Both were covered by 6 to 8 inches of loose dirt. The crater was quickly covered with black plastic to keep exposure to sunlight to a minimum and the film, cannister and some of the dirt was doubled-wrapped in heavy, black, opaque plastic, and the package was thoroughly taped.

Much of the dirt in the hole was screened at the site, but no trace of the missing platinum cage wires or any glass fragments that appeared to be from the flight sample was found.

An area around the impact crater within a radius of about 15 feet was also searched. Much of this area was covered by tall grass as was the immediate impact site, which made searching difficult. One fragment of the experiment package shell was found about 33 yards south (toward the launch site) of the impact crater. After about an hour the search by 5 or 6 people was abandoned and all personnel flew back to the VAB.

After returning to the VAB, the package containing the film was opened in a dark room at LC 35. The film was separated from the remains of the magazine, cleaned of loose dirt, and re-wrapped thoroughly in heavy, black plastic and re-taped. Both the take-up and feeder spools of film appeared to be intact. The film was hand carried to Los Angeles without x-ray inspection by the P.I.

Preliminary Post-Flight Analysis

On December 1, 1980, the film was hand carried to Hollywood Film Enterprises. About two feet of film from the larger (take-up) spool was removed because of excessive damage. After inspecting and re-spooling, the remainder of the film was developed as a negative without further incident. There was some edge damage and much wrinkling of the film. Because it was an Estar base film, which is very tough, no further tearing occurred during development.

It was obvious from cursory inspection of the processed flight film negative that there was too much damage to permit positive motion picture prints to be made using conventional printing techniques.

A frame-by-frame inspection of the film showed that it did indeed contain the complete flight record beginning with the first appearance of the platinum alloy wire injection cage and ending after the sample and cage had cooled sufficiently that they could no longer be seen against the relatively cool background of the cooling shroud. Sheets dated 12-3-80

and 12-5-80 are attached as enclosures 1 and 2 giving a detailed summary of key events depicted on the film and containing a sketch every twenty frames (5/6 second) of the sample position during the suspension portion of the cycle have been mailed to Intersonics, MSFC, and NASA Headquarters.

Key events are summarized in the table which follows. All time calculations are based on the assumption that the flight camera was running accurately at 24 frames per second.

Frame No.	Event	Seconds Time	Seconds Δt
1	Injection gate beginning to open		
41	Injection cage first appears	1.7	
67	Injection fully open, sample in contact with inner cage (Al_2O_3 covered Pt)	2.8	
161	Sample begins to drift free of cage	6.7	
2080	Sample begins final excursion toward Pt cage	86.7	83.3
2160	Sample contacts cage wires	90.0	≈0.8 sec.
2180	Sample centered on cage wire	90.8	
3880	Cooling shroud gate begins to open	161.7	
3898	Cooling shroud gate fully open	162.4	
≈ 4000	Cooling underway	166.7	≈43
≈ 5040	Sample approx. same temperature as background	≈ 210	≈72
≈ 5720	Pt cage approx. same temperature as background	≈ 238	
6009	End of film (cut at HFE)	251	

It is obvious from the film records that the sonic suspension system was not entirely successful, the sample drifting to a platinum alloy cage wire and attaching itself before the completion of the entire processing

cycle. The sample did remain suspended for 83 seconds as compared with 27 seconds for the SPAR VI flight.

Attempts to determine when sample melting occurred have been deferred until it can be determined whether motion picture prints can be made of the suspension portion of the film (see Future Work section). Based on the SPAR VI film data, the knowledge that furnace temperatures were probably somewhat higher in SPAR VIII than in SPAR VI, and that the samples during the two flights were of almost identical size and composition, it is expected that melting should have occurred in the 22 to 35 seconds time span (frames 530 to 840) or earlier. Examination of the sketches every 24 frames referred to earlier show that motions during this portion were quite small and the sample remained reasonably well centered in the energy well.

Future Work

It was noted during detailed examination of the suspension portion of the film that this portion is in somewhat better condition than the tail end, which contains the balance of the soaking portion of the cycle and the entire cooling portion. The suspension portion has been repaired to eliminate torn and/or frayed sprocket holes. A discussion was held with Hollywood Film Enterprises, who examined the repaired portion of the film. After we do more clean-up on the repairs, HFE feels that there will be a 50/50 chance of successfully making one print. The writer gave his authorization to proceed. If this print can be made it will be used as a master for making 10 or 12 additional prints for distribution to interested parties.

If prints can be made and loaded into a projector, it may be possible to detect sample melting. Such prints will also permit more detailed analysis of sample motions during the suspension portion of the cycle. Selected individual frame still prints will be made during the latter part of the soaking portion of the cycle and during the cooling portion.

Glass fragments from the experiment package will be examined to determine whether any of them are of the flight sample (gallia-calcia-silica) composition. If a portion of the outer surface of the flight sample can be recovered, it may be possible to determine whether elimination of contact with the platinum cage during launch was successful in handling the Pt-Rh contamination problem encountered with SPAR VI.

Recommendations

It seems appropriate at this time to offer comments for improvements in recovery operations at the White Sands Missile Range for future SPAR flights. Even though the writer and the Intersonics people were on hand well in advance of the arrival and departure of the helicopter on the morning of November 19, no one who had a direct knowledge of the 72-42 experiment was included as a passenger on that flight.

It is the writer's belief that had at least one of the Intersonics people been included on the roster of the first helicopter flight, more care would have been exercised in moving and transporting the remains and the chances of finding the missing flight sample enhanced.

It is therefore strongly urged that in all future SPAR flights the first recovery vehicle roster should include a minimum of one person who is intimately familiar with the experiment package contents and the objectives of the experiment. These three or four people should have top priority on the roster of the first vehicle.

ROCKWELL INTERNATIONAL CORPORATION
Space Operations & Satellite Systems Division

R. A. Happe
Principal Investigator
Contract NAS8-32023

gd

Encl:

Distribution for "Quick Look" Report

NASA

Code	No. of Copies
D. Schaefer, LA11	8 + Reproducible
AP29-F	1
AS21D	3
Mr. G. A. Abbott, NASA/MSFC, Downey	1
EH34/R. Nichols	1
EH23/L. H. Berge	1
AT01	1
ES74/J. Johnson	1

Distribution for "Quick Look" Report (Continued)

NASA

Code	No. of Copies
Dr. John Carruthors Code EM-7 NASA Headquarters Washington, D.C 20546	1
Dr. William Oran Code EM-7 NASA Headquarters Washington, D.C 20546	1

EXTERNAL

Dr. Charles Rey Intersonic, Incorporated 425 Huehl Rd - Unit 11A Northbrook, Illinois 60062	1
Dr. Delbert E. Day University of Missouri at Rolla Dept. of Ceramic Engineering Rolla, Missouri 65401	1
Dr. Norbert J. Kreidl 1433 Canyon Rd. Santa Fe, New Mexico 87501	1
Dr. Guy E. Rindone Ceramic Science Section 201 Mineral Industries Building Pennsylvania State University University Park, Penn. 16802	1
Dr. Elias Snitzer Manager, Technical Planning United Technologies Research Center East Hartford, Conn. 06108	1
Dr. Donald R. Uhlmann Dept. of Metallurgy & Mineral Science Mass. Institute of Technology Cambridge, Mass. 02139	1

MOTION PICTURE PRELIMINARY SUMMARY
FINDINGS – SPAR VIII, EXP'T 74-42
P.A. Hogge 12/2/80

ENCLOSURE 1

Frame No.	Seconds	Event	Elapsed ET Time sec.	Frame #
1	1/64 (.042)	1st identifiable frame, injection gate beginning to open		878+19
23	23/24 (.96)	Gate appears fully open		877+17
41	1.7	Tip of inj. cage 1st visible		
53	2.2	Inner cage begins to retract		
60	2.5	Cage all the way in		
67	2.8	Inner cage fully retracted	4.5	
161 (117)	6.7	(Sample in contact with inner cage) Sample begins to leave inner cage		870+19
161 to 2153±13 (2082)	6.7 to 84.7	Sample in suspension	83.	870+19 to 771+1
1640	68.3	Sample near axis (at hdwr wire 2*)		797
1660	69.2	" starts drift to rt*	2½	796
~1720	71.7	Max. excursion to rt. (~½ radius)		793
~1760	73.3	Moving to left.	1¾	791
~1800	75.0	Nr. axis		789
~1820	75.8	Moving to rt.	5	788
1940	80.8	Max. excursion to rt. (~½ radius)		782
1960	81.7	Moving to left	1¾	781
1980	82.5	On axis (at h.w. 2)		780
2000	83.3	" " (" " ")		779
2020	84.2	Slightly to left of axis		778
2040	85.0	On axis		777
2060	85.8	" "		776
2080	86.7	Moving to rt. (start of final kick)	3	775
2153±13	89.7 ± .54	Appears to have contacted Pt wire		771+7
~2167	~90.3	Appears to be impaled on Pt cage wires ??? (very low contrast)		

* See notes on page 2

Frame No.	Seconds	Event	Elapsed Time, sec.	EK Frame #
~2180 to 3888	~90.8 to 162.0	Sample cannot be seen	71	~770 to 689+12
~3880	~161.7	Cooling shroud gate begins to open	0.8	~690
3888	162.0	1st view of sample impaled on cage wire**		689+12
3898	162.4	Cooling shroud gate fully open		689+2
~4000	~166.7	Cooling under way	~43	684
~5040	~210	Sample merged with background (Can see cage wires only)		632
5720	238.3	Cage merged with background	~72	588
6009	250.4	End of film		583+11

Notes

* Orientation (Definitions)

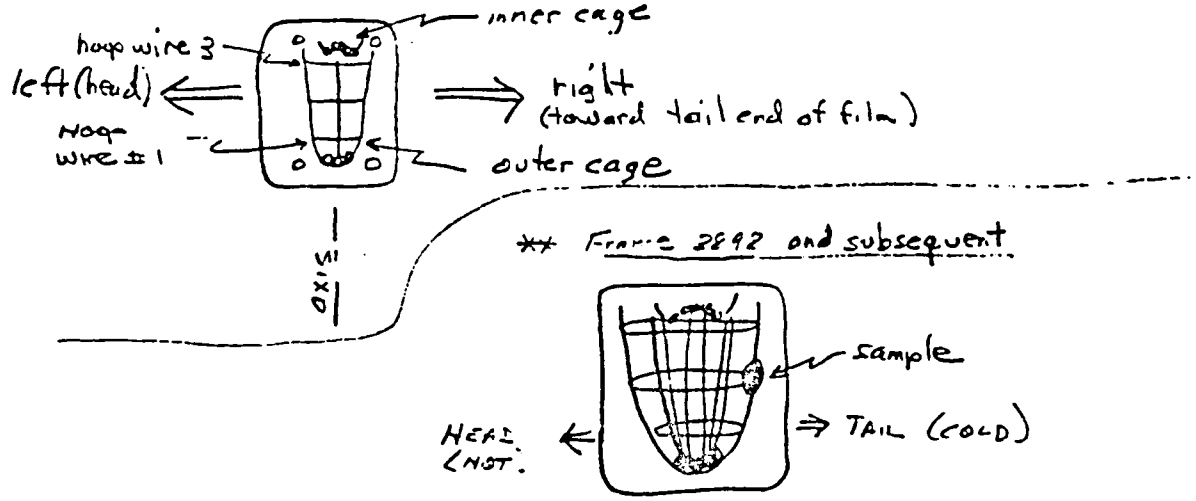

EK Film numbering (example)

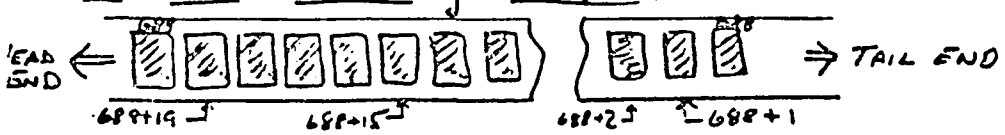

(1) 12/5/80 SHEET 1 OF 7

ENCLOSURE 2

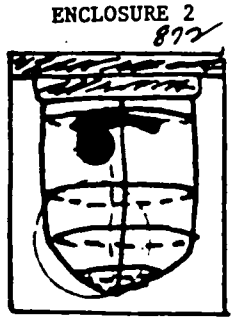

FR 140 5.8 sec

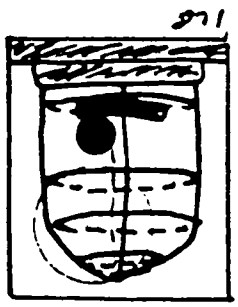

FR 160 6.7 sec

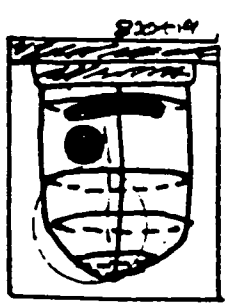

FR 161 6.7 sec

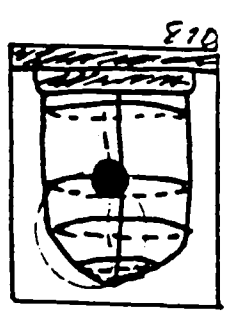

FR 180 2[illegible] sec.

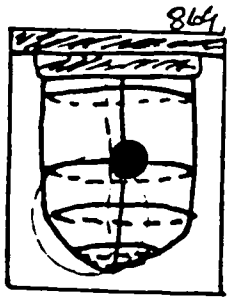

FR 200 8.3 sec

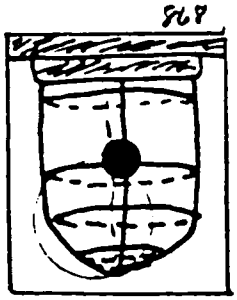

FR 220 9.[illegible] sec

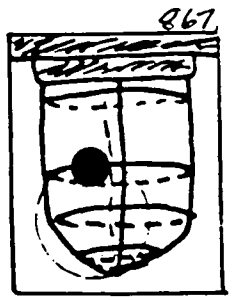

FR 240 10. sec.

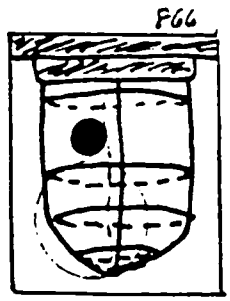

FR 260 10.8 sec

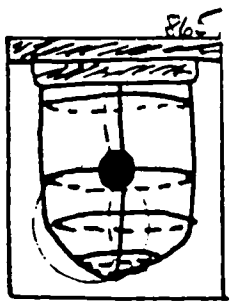

FR 280 11.7 sec

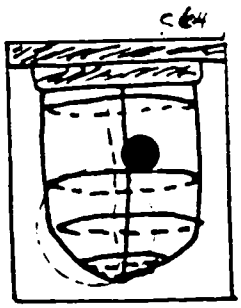

FR 300 12.5 sec.

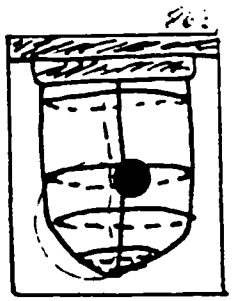

FR 320 [illegible]

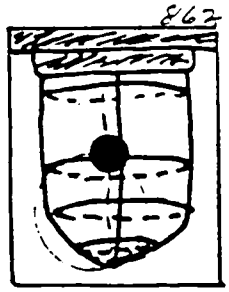

FR [illegible] [illegible]

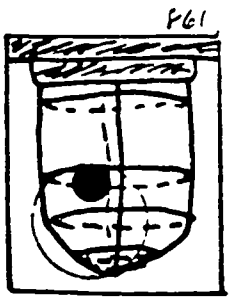

FR 360 15. sec

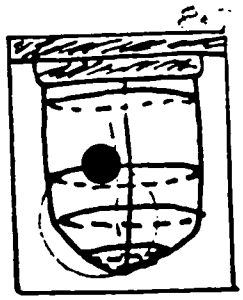

FR 380 15.8 sec

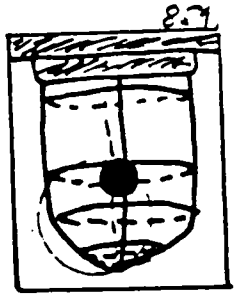

FR 400 16.7 sec

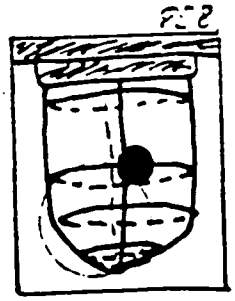

FR 420 17.5 sec.

(2)

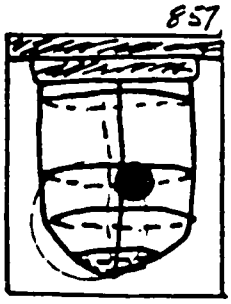

Fr 440 18.3 sec.

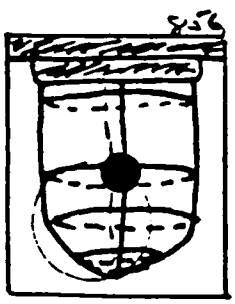

Fr 460 19.2 sec

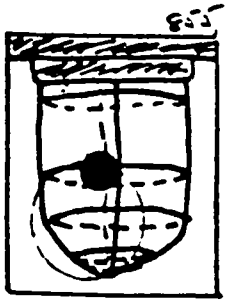

Fr 480 20. sec

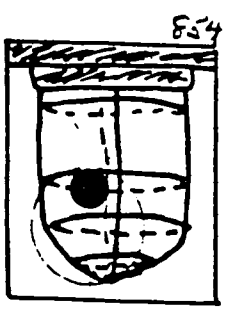

Fr 500 20.8 sec.

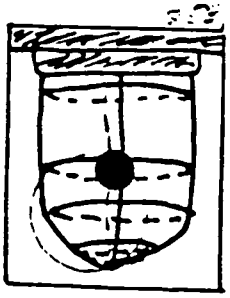

Fr 520 21.7 sec

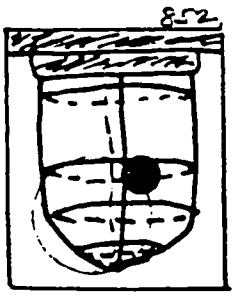

Fr 540 22.5 sec

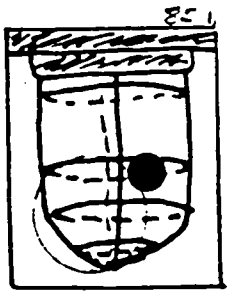

Fr 560 23.3 sec

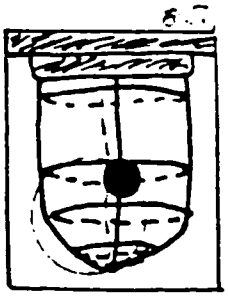

Fr 580 24.2 sec.

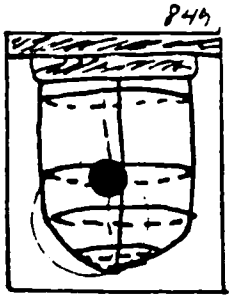

Fr 600 25. sec

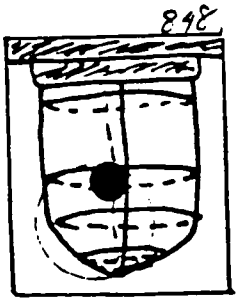

Fr 620 25.8 sec

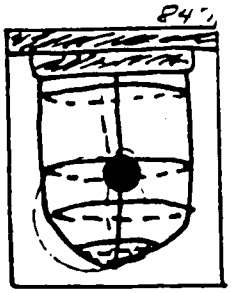

Fr 640 26.7 sec

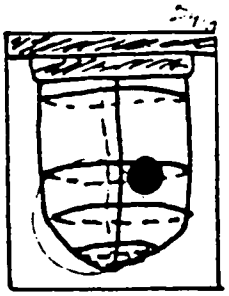

Fr 660 27.5 sec

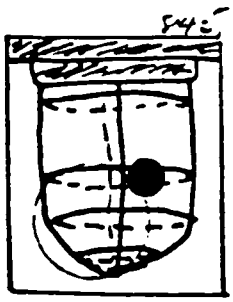

Fr 680 28.3 sec

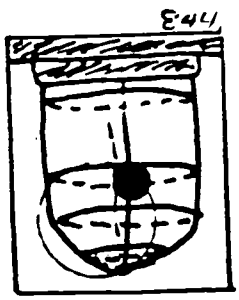

Fr 700 29.2 sec

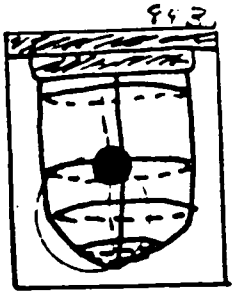

Fr 720 30. sec

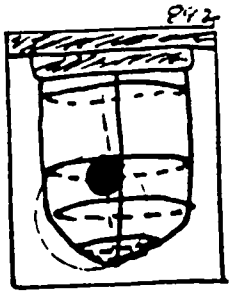

Fr 740 30.8 sec.

③

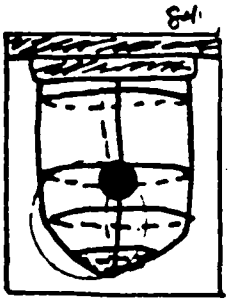

Fr 760 31.7 sec.

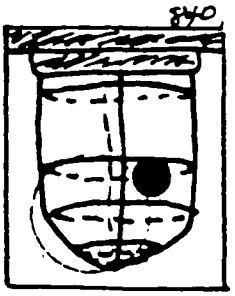

Fr 780 32.5 sec

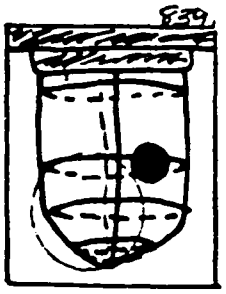

Fr 800 33.3 sec

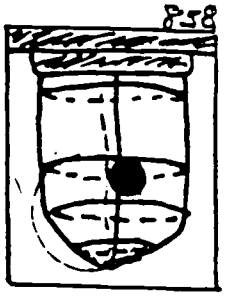

Fr. 820 34.2 sec.

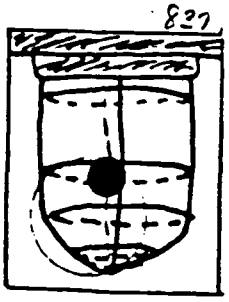

Fr 840 35. sec

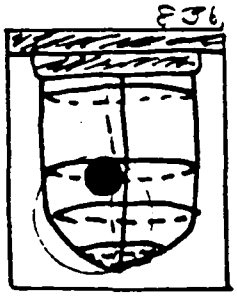

Fr 860 35.8 sec

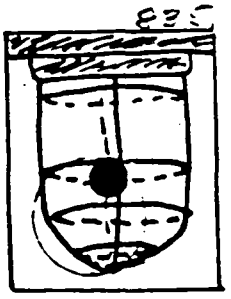

Fr 880 36.7 sec.

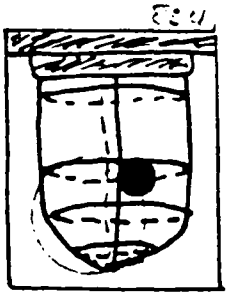

Fr 900 37.5 sec.

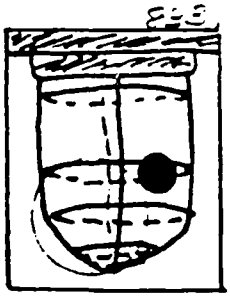

Fr 920 38.3 sec

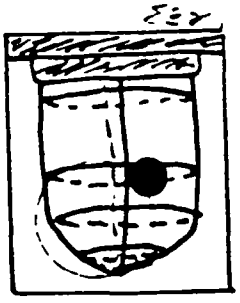

Fr 940 39.2 sec

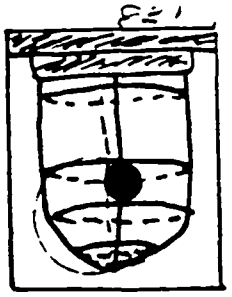

Fr. 960 40. sec

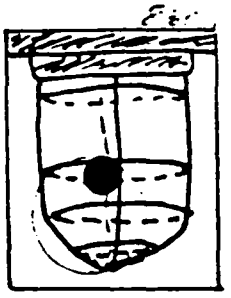

Fr 980 40.8 sec.

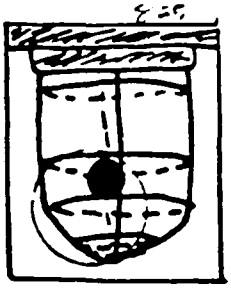

Fr. 1000 41.7 sec

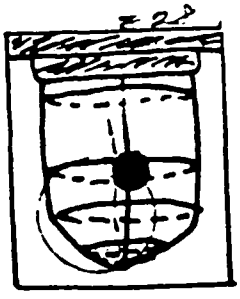

Fr 1020 42.5 sec

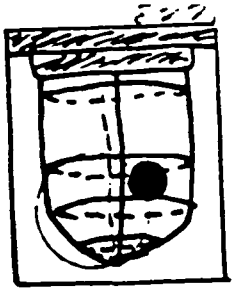

Fr Large 43.8 sec

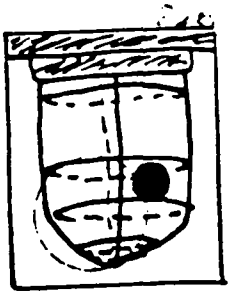

Fr 1060 44.2 sec.

④

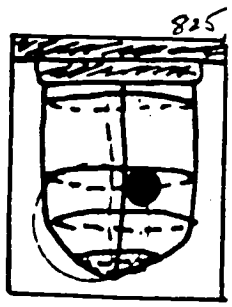

Fr 1080 41. sec

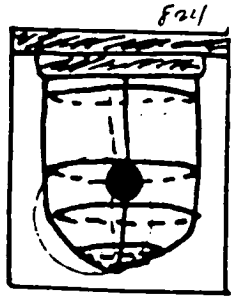

Fr 1100 45.8 sec

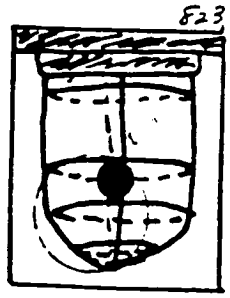

Fr 1120 46.7 sec

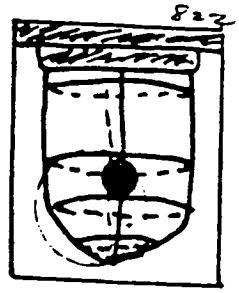

Fr 1140 42.5 sec

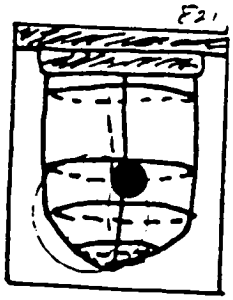

Fr 1160 48.3 sec

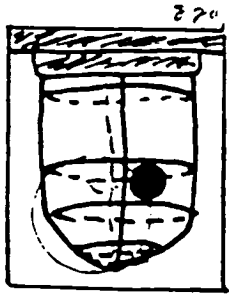

Fr 1180 49.2 sec

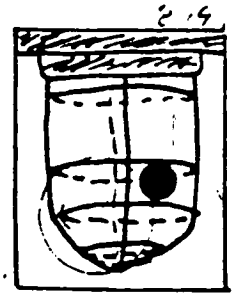

Fr 1200 50. sec

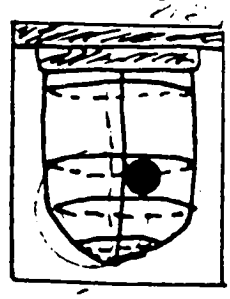

Fr 1220 50.8 sec

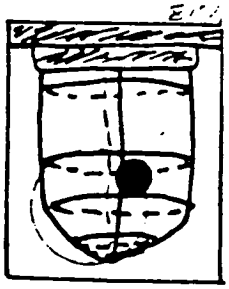

Fr 1240 51.7 sec

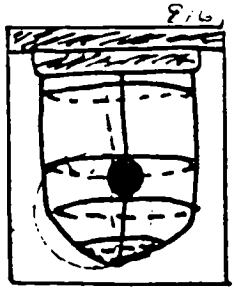

Fr 1260 52.5 sec

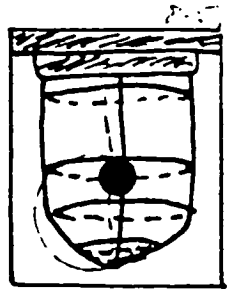

Fr 1280 53.3 sec

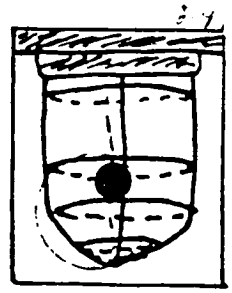

Fr 1300 54.2 sec

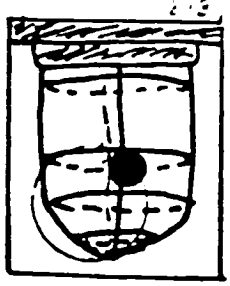

Fr 1320 55. sec

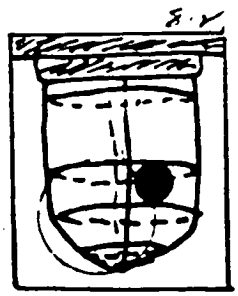

Fr 1340 55.8 sec

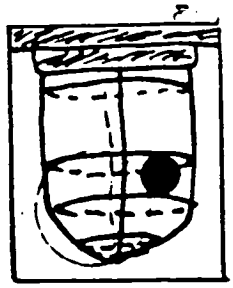

Fr 1360 56.7 sec

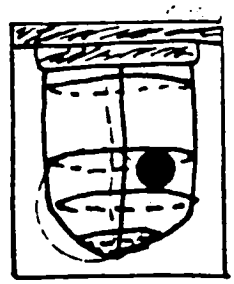

Fr 1380 57.5 sec

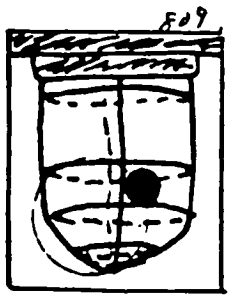

Fr 1400 58.3 sec.

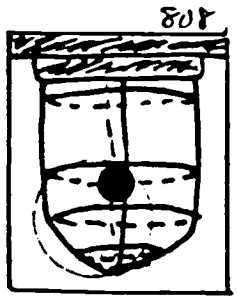

Fr 1420 59.2 sec

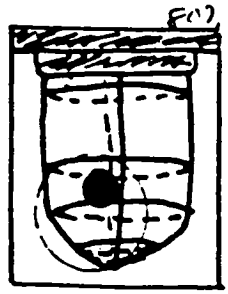

Fr 1440 60. sec

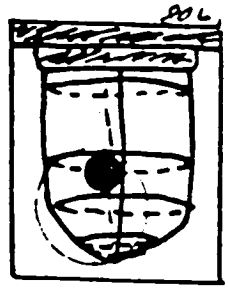

Fr. 1460 60.8 sec.

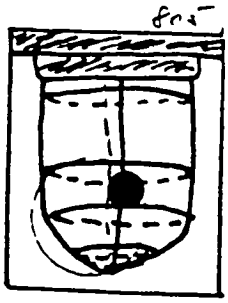

Fr 1480 61.6 sec

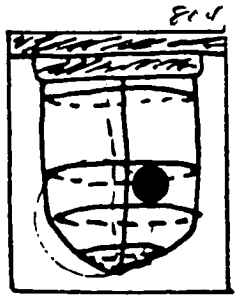

Fr 1500 62.4 sec

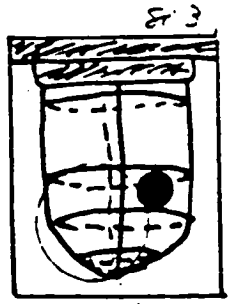

Fr 1520 63.2 sec:

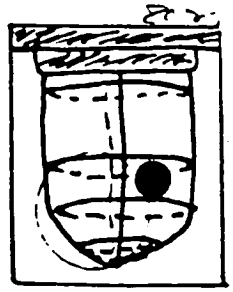

Fr 1540 64.2 sec

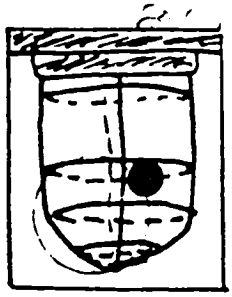

Fr 1560 65. sec

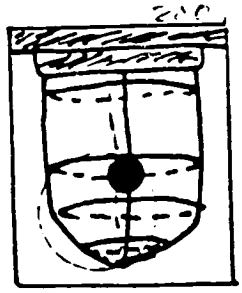

Fr 1580 65.8 sec

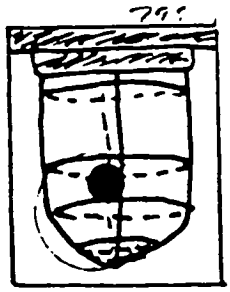

Fr. 1600 66.7 sec

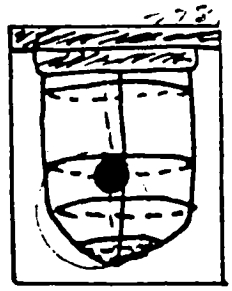

Fr 1620 67.5 sec.

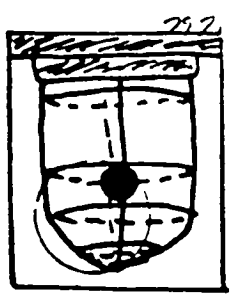

Fr 1640 68.3 sec

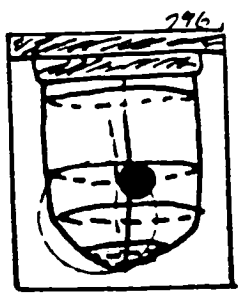

Fr 1660 69.2 sec

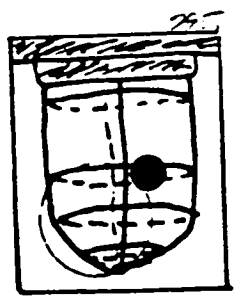

Fr 1680 70. sec

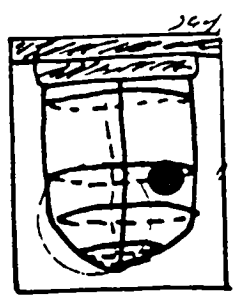

Fr 1700 70.8 sec

(6)

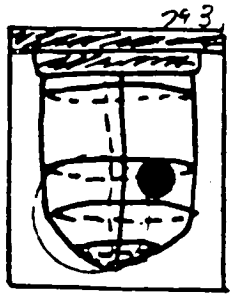

Fr 1720 21.7 sec

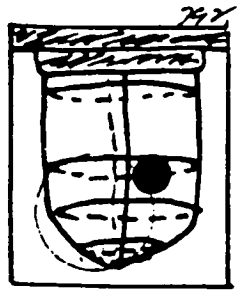

Fr 1740 22.5 sec

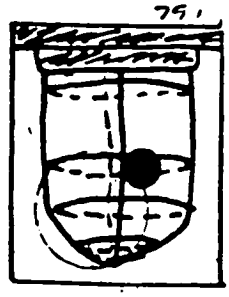

Fr 1760 23.3 sec

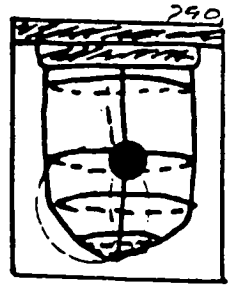

Fr 1780 24.2 sec

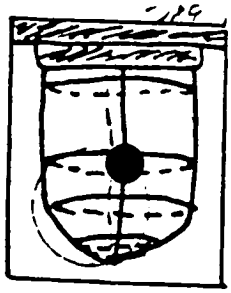

Fr 1800 25. sec

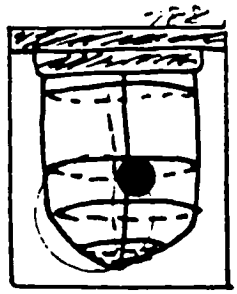

Fr 1820 25.8 sec

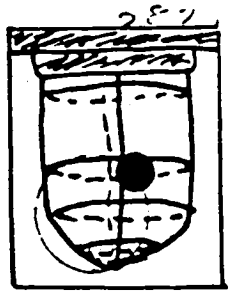

Fr 1840 26.7 sec

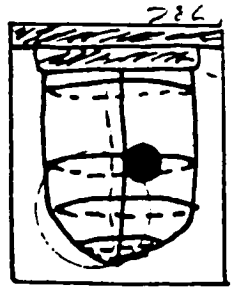

Fr 1860 27.5 sec

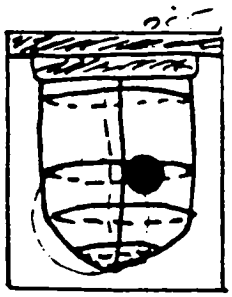

Fr 1880 28.3 sec

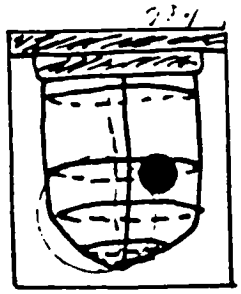

Fr 1900 29.2 sec

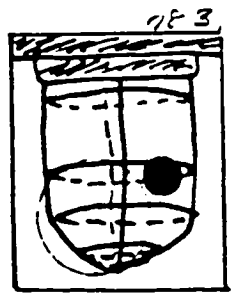

Fr 1920 30. sec

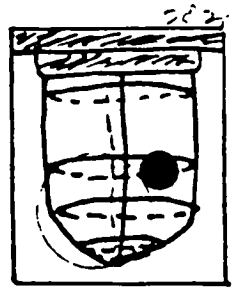

Fr 1940 30.8 sec

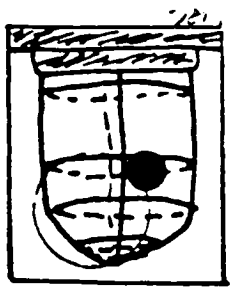

Fr 1960 31.7 sec

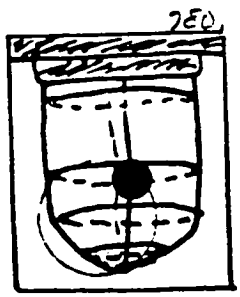

Fr 1980 32.5 sec

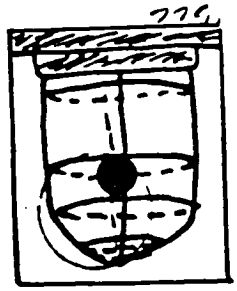

Fr 2000 33.3 sec

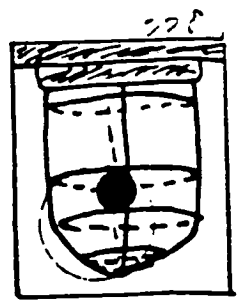

Fr 2020 34.2 sec

(7)

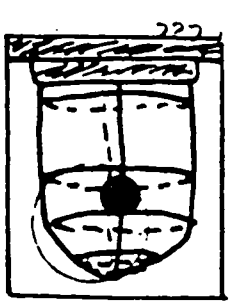

FR 2040 85. sec

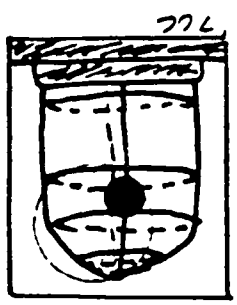

FR 2060 85.8 sec

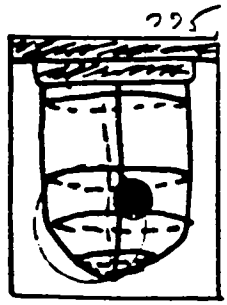

FR 2080 86.7 sec

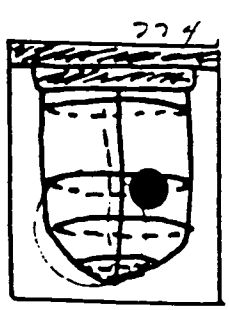

FR 2100 87.5 sec.

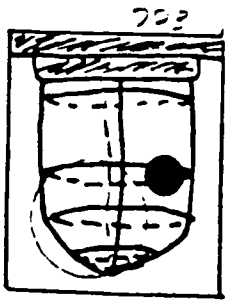

FR 2120 88.3 sec

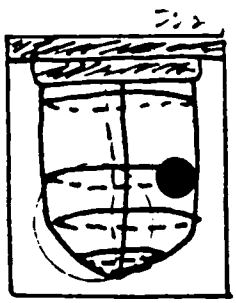

FR 2140 89.2 sec

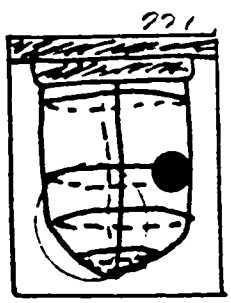

FR 2160 90. sec.

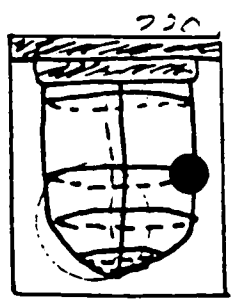

FR 2180 90.8 sec.

NOTE-

BY VIEWING THE LATER FRAMES WITH AN OLYMPUS 85mm - f/2 ICAS (WITH U.V. FILTER) IT WAS POSSIBLE TO RESOLVE THE SPECIMEN IN THE POSITION SHOWN IN FRAME 2180. THE NEXT 5 OR 10 FRAMES SHOW THE SAME THING.

10/15/80

NOTE ALSO: FRAME REEL (0) IS ONE FR. BEFORE THE 1ST IDENTIFIABLE FRAME ON THE FILM. SEE SHEETS DATED 12/9/80.

A PRELIMINARY ANALYSIS OF THE DATA FROM EXPERIMENT 77-13 AND FINAL REPORT ON GLASS FINING EXPERIMENT IN LOW GRAVITY

W. R. Wilcox
Principal Investigator

R. S. Subramanian, M. Meyyappan
Co-Investigators
Clarkson College, Potsdam, NY

H. D. Smith, D. M. Mattox, D. P. Partlow
Co-Investigators
(W) R&D Center
Pittsburgh, PA 15235

Final Report
Contract No. NAS8-33017

George C. Marshall Space Flight Center
Marshall Space Flight Center, Alabama 35812

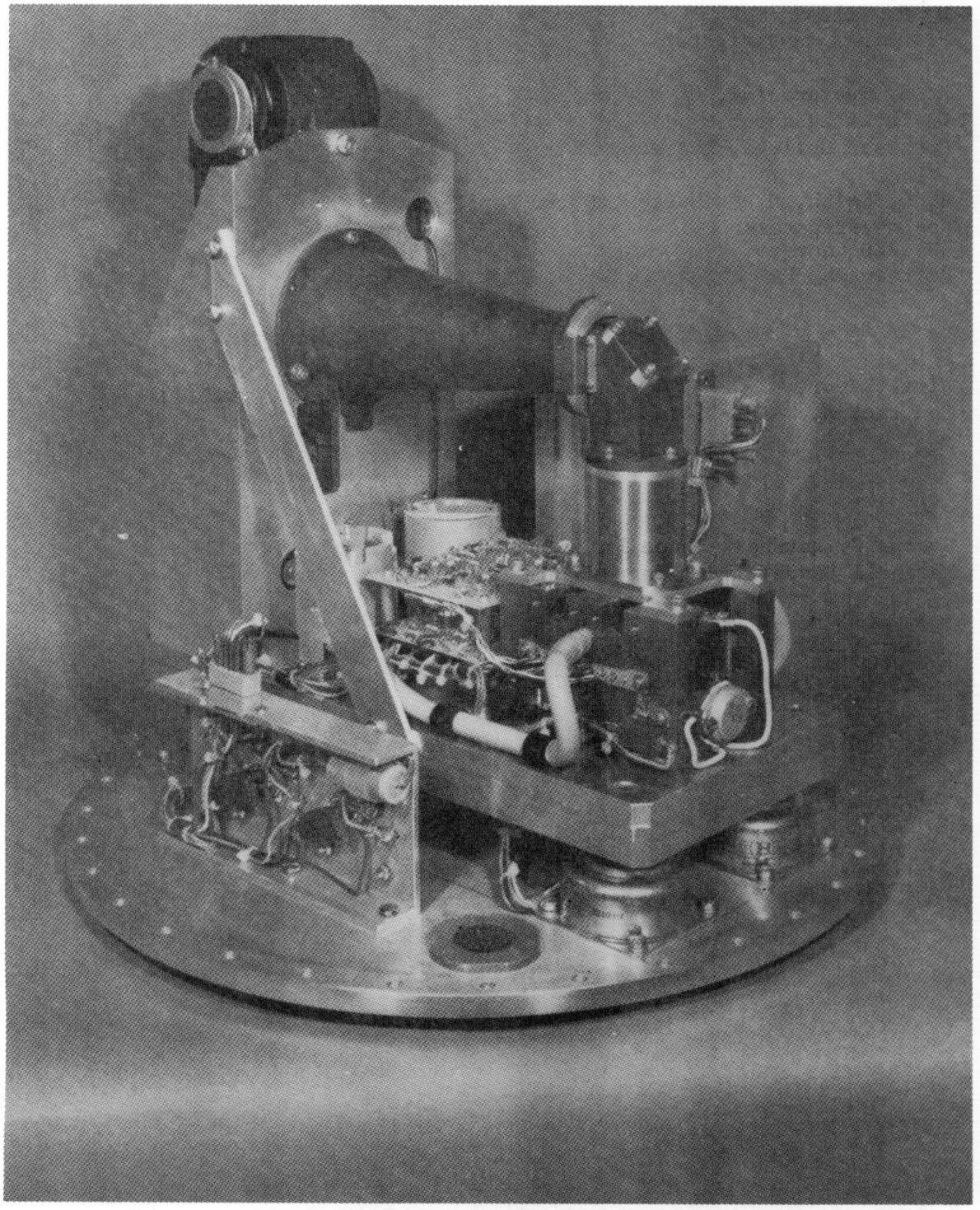

SPAR VIII EXPERIMENT 77-13 FLIGHT APPARATUS

TABLE OF CONTENTS

TABLE OF CONTENTS (Cont'd)

LIST OF FIGURES

LIST OF FIGURES (Cont'd)

SUMMARY

Bubbles are always formed during glass manufacture. They arise from batch reactions, entrained voids contained in the original batch, etc., and are commonly removed in earth based manufactured glasses by a combination of buoyant and chemical fining procedures. Buoyant fining requires the presence of gravity, and chemical fining requires the addition of a chemical dopant to the glass—neither of which is applicable to containerless melting of ultrapure or special glass systems in space. Thermal fining, i.e. thermal migration of bubbles, on the other hand requires only the imposition of a temperature gradient in the molten glass and does not require physical contact with the sample or the presence of a gravitational field. Theoretical models and ground based experiments both predict the thermal migration of bubbles under reduced gravity conditions.

The objectives of the present study were to demonstrate the thermal migration of bubbles under reduced gravity conditions and if possible provide quantitative data with which to verify current theoretical models. An automatic system was designed to perform an experiment aboard a SPAR rocket payload during the 5-6 minutes of zero gravity available. Experimental data (bubble location and temperatures as a function of time) were recorded on film or telemetered back to earth. The experimental sample was a sodium borate glass (29.9% Na_2O) for which a negative temperature coefficient of surface tension was measured (.0756 dynes/cm°C). The sample was contained in a cell which consisted of fused silica and a tapered platinum rhodium (20%) heater strip.

The photographic record of the experiment indicated that bubbles moved in response to the temperature gradient imposed on the molten glass sample. The motion was both in the plane of the heater strip and perpendicular to it in a way consistent with the temperature gradients measured by thermocouples in the sample. It is not yet known if the data will be quantitative enough to confirm the results of theoretical calculations.

Further work is indicated to modify the experimental apparatus to accept multiple samples and to refine the cell design to orient the thermal gradient parallel to the cell axis. Future experiments should include glasses with positive temperature coefficients, different melting temperatures, and/or borax the glass studied in this experiment over a different temperature range. The effect of impurities, e.g. water, needs to be studied in these systems.

CHAPTER V

1. INTRODUCTION

1.1 Fining

There is one feature common to all aspects of glass melting. At one stage or another, raw materials are melted together. This liberates gases which were chemically combined or adsorbed on the raw material, leading to bubble entrapment. To render the glass transparent and to provide useable strength levels, these bubbles are eliminated in a process known as "fining". While this particular terminology is limited to bulk glasses, the requirement for eliminating bubbles is a dominant feature of the processing of most glass-containing systems. Ceramic-to-metal seals (high pressure sodium lamps) and glass-to-glass or glass-to-ceramic seals (cathode ray tubes) are formed with powdered glass (solder) seals. Hermeticity and acceptable strength directly correlate with the elimination of the void structure. Predictability and reliability in integrated circuits are commonly ensured by the use of passivating glass coatings. These are applied by elaborate techniques using powdered glass in liquid slurries to assure thin continuous coatings. The typical low expansion semiconducting materials require glasses which barely fuse at temperatures close to the stability limits of some of the components. The necessity of eliminating the entrapped bubbles dictates the times required at these elevated temperatures.

Another example of glass processing which is regulated by bubble behavior is conventional porcelain enameling. In this process, bubbles must be eliminated to the point of leaving a smooth glass surface, but in this particular application a rather well defined subsurface bubble structure imparts desirable performance benefits. In fact, certain additives, such as clay, are introduced to generate a bubble structure. The prevention of the defect called "fishscale" in sheet iron is one such benefit.

1.1.1 Buoyant Fining

In spite of the great wealth of experience possessed by glass manufacturers, little is understood about the process of fining and even less is understood about bubble elimination in sealing glasses or enamels. The traditional viewpoint[1-2] of glass fining is based on the effect of additives, called "fining agents." These decompose rapidly, to form new bubbles, or the gases diffuse into existing bubbles, causing them to grow, whereupon they rise quickly out of the melt under the action of buoyant forces. The velocity at which bubbles rise in the molten glass may be approximated by the following equation:

$$V = \frac{D^2 g \rho}{12 \eta} \qquad (1)$$

where D = bubble diameter
g = gravitational constant
ρ = density of the melt
η = viscosity of the glass.

Simple calculation shows that beneath a particular size bubble, buoyant fining does not occur fast enough to eliminate bubbles in the times used in conventional processing. For example, a bubble 0.1 mm in diameter in a lime glass with a viscosity of 100 p will rise about 17 cm/day - too slow for commercial processing. An additional mechanism is necessary to explain the fining of commercial glasses.

1.1.2 "Chemical Fining"

Another important mechanism of fining of commercial glasses is due to small amounts of chemical agents added to the batch. Traditionally, arsenic and antimony oxides as well as sodium sulfate have been employed for this purpose in concentrations less than 1 weight percent of the batch. The role played by chemical agents is not quite clear at this time. Two schools of thought prevail, both supported by incomplete experimental evidence. The experiments of Greene and Gaffney[4] as well as others (Cable et al.[5]) suggest that bubbles dissolve more rapidly

the presence of fining agents than in their absence. This may be attributed to chemical reactions of the diffusing gas with the fining agents. However, Nemec[6] has recently observed that bubbles, in fact, grow more rapidly in the presence of fining agents than in their absence. Since the buoyant rise velocity is proportional to the square of the bubble diameter, his argument is that fining agents promote the growth and therefore rapid rise of small bubbles from the melt. The reason for this confusion in the literature and the two opposite schools is simply that the experiments were not performed under sufficiently controlled conditions. The initial gas concentrations in the melt which are crucial in determining whether the melt is undersaturated or supersaturated with respect to a given gaseous species were not controlled in the different experiments to a sufficient degree. Furthermore, the melts typically contained several dissolved gaseous species. Therefore, even if a single-component bubble is injected, soon, it would become a multicomponent bubble with some species possibly diffusing in while the others are diffusing out, and complex reactions would be simultaneously occurring in the melt. Thus, while chemical fining is effective as an industrial practice, much remains to be done in elucidating the actual mechanisms by which it occurs.

1.1.3 "Thermal" Fining

"Thermal" fining, to coin a parallel phrase, is a mechanism that has been largely overlooked and little understood.[7] A temperature gradient, with its effect on surface tension, produces a displacive force on bubbles. Thermal fining may be the principal mechanism of bubble elimination in sealing, soldering, and enamelling operations. It is commonly observed that bubbles quickly come to the surface of glass enamel, regardless of the orientation of the enamel. Since seals, solders, and enamels are typically heated externally, it is presumed that a driving force toward the external surface is established on the bubbles in the fluid glass.

While significant evidence has been reported[8-12] which confirms that gas bubbles can move in a temperature gradient, no evidence has been reported for this phenomenon in glass systems, in spite of its obvious importance in glass sealing and enamelling. The effect of this mechanism has possibly been observed in experiences with direct electric melting of bulk glasses. Contrary to fuel fired furnaces, electric melters are hottest at the bottom of the tank. This gradient would oppose buoyant fining, and indeed, electrically melted glasses require more time to fine, although there are other factors which contribute to this.

While the mechanism of thermal fining is obviously of great commercial significance in many high technology applications, it represents an even more important mechanism in the space processing of glasses. There has been considerable interest in producing glasses in a zero gravity environment, particularly because the materials could be cooled in a containerless fashion avoiding heterogeneous nucleation as well as contamination by the container walls. It has been proposed that certain difficult glass formers be produced in free fall for this reason (M. C. Weinberg, "Glass Processing in Space", Glass Industry, p. 22, March 1978, G. F. Nielson and M. C. Weinberg, "Outer Space Formation of a Laser Host Glass", J. Non-Crystalline Solids, 23, 43, 1977). One of us (RSS) is currently involved in planning space shuttle experiments on the use of thermal gradients for fining bubbles from levitated molten glass drops (see R. S. Subramanian and R. Cole, "Experiment Requirements and Implementation Plan (ERIP) for Physical Phenomena in Containerless Glass Processing", Marshall Space Flight Center Document 77FR010, August 1979).

1.2 Thermal Fining in Molten Borax: Ground Based Laboratory Results From Demonstration Study

As reported earlier[13], ground based experiments were run to demonstrate bubble movement and the feasibility of the techniques to be employed for a SPAR experiment. Thermal migration of bubbles in

molten borax was observed in both a quartz capillary tube and in an inverted silica channel. The temperature gradient was generated by passing electrical current through a tapered platinum strip under the capillary tube or channel. The best observations were made with the inverted channel because its shallow depth (500 μm) allowed all bubbles to be seen at once and because there was good thermal contact of the melt with the heating strip.

This demonstration experiment was run by melting a piece of glass cane containing bubbles into an inverted channel in a fused silica cover using the platinum heater strip. A simple schematic of this cell is shown in Figure 1.2-1. During the first minute or so the molten glass flowed into the channel and formed a thin film between the silica cover and the platinum heater strip. Once the channel was full and the thin film occupied the rest of the areas between the silica cover and platinum strip, the physical flow of the melt ceased. This was clear from the fact that the physical boundaries did not change position and bubble groups no longer moved *en masse*. During that initial melt down period many of the bubbles moved toward the hot spot and coalesced into few larger bubbles. However, bubbles further away from the hot spot did not have time to move far during that time and they continued to move individually toward the hot spot after the glass itself ceased flowing. At this point several photographic sequences were taken with time intervals of 5 or 10 seconds in the sections with rapidly moving bubbles, and 20 seconds in the outer region with slower moving bubbles.

The bubble migration observed is illustrated by Figure 1.2-2. Here bubbles next to the channel wall (dark band just above two larger bubbles) are shown migrating toward a region of higher temperature. Two features to look for in this series of pictures are: (1) bubbles accelerate as they move to higher temperature, and (2) larger bubbles move faster than smaller ones. The difference in velocity due to size is illustrated by the second largest bubble overtaking the smaller one just ahead (to the right) of it by the 20-second frame. Most interesting was an apparent attraction of bubbles to one another, enhancing coalescence. This phenomena had not been reported before, and stimulated enthusiasm for a flight experiment.

Dwg. 7745A27

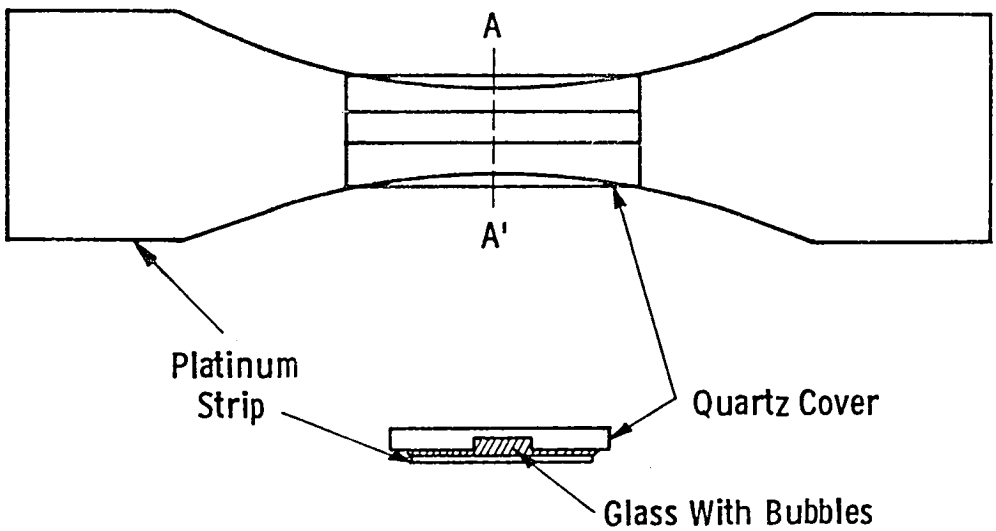

Fig. 1.2-1—Quartz cover with inverted channel in place on platinum heater strip

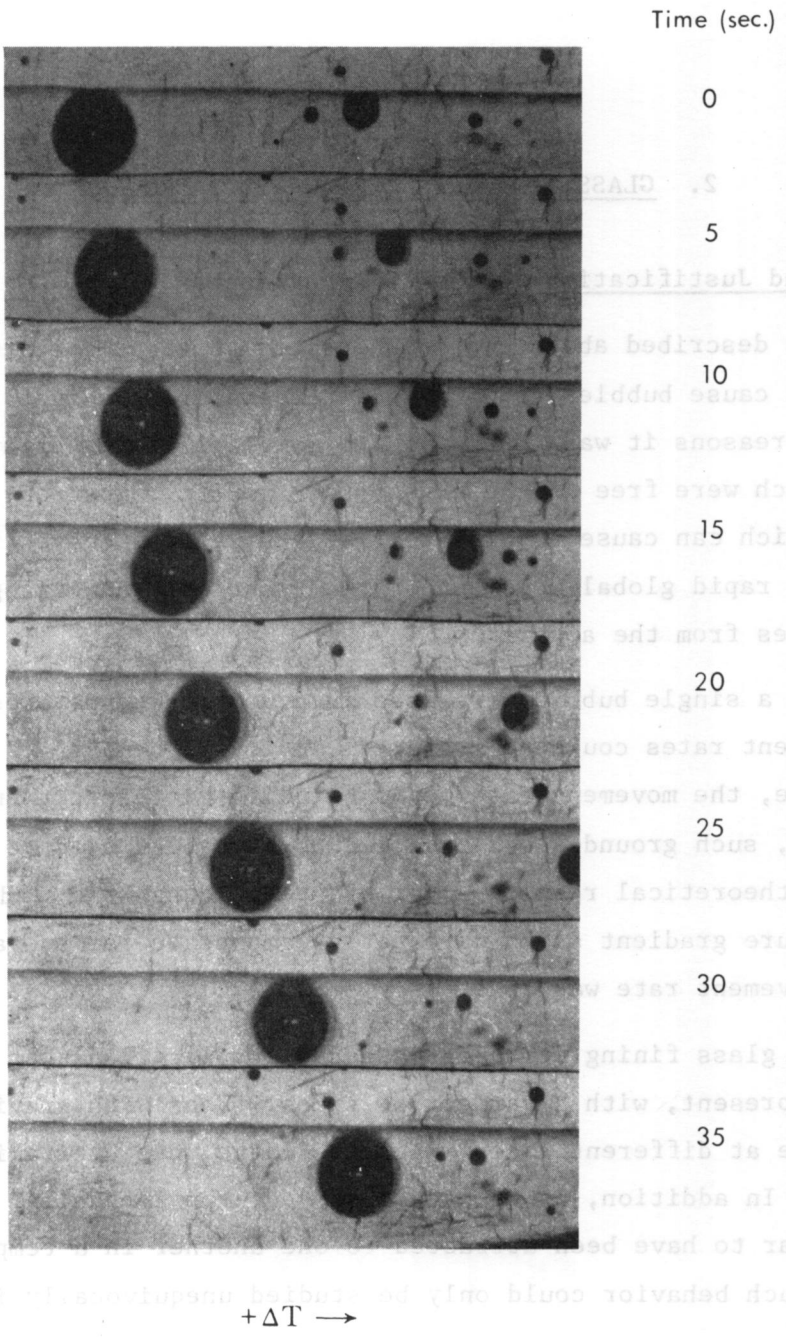

Figure 1.2-2 - Bubble migration in molten borax. Large bubble is 260 μm in diameter. Wall of channel in which bubble moves just above large bubble. Small bubbles at top of each frame are trapped between platinum heater strip and silica cover and do not move. (Ground based demonstration experiment.)

2. GLASS FINING IN ZERO GRAVITY PROGRAM

2.1 Need and Justification for Low-G Experiments

As described above, we demonstrated that a temperature gradient can cause bubbles to move in a temperature gradient. However, for several reasons it was impossible to do glass fining experiments on earth which were free of the effects of gravity. Most obvious is buoyancy, which can cause bubbles to rise, and natural convection, leading to a rapid global movement of the glass melt and irregular thermal losses from the apparatus.

If a single bubble were used in a vertical apparatus, then bubble movement rates could be measured. However, because of buoyancy of the bubble, the movement rate would be quite different than in space. Nevertheless, such ground-based experiments have been used to test approximate theoretical results. For example, Young et al. adjusted the temperature gradient so as to exactly compensate for buoyancy, i.e., the movement rate was zero.

In glass fining we have the added complication that many bubbles are present, with a variety of sizes. Thus with gravity they will all rise at different rates, with the large ones overtaking the small ones. In addition, as we have observed experimentally, the bubbles appear to have been attracted to one another in a temperature gradient. Such behavior could only be studied unequivocally in space.

2.2 Objectives

Ground based studies have shown that bubbles in molten sodium borate (borax) do move in response to an imposed temperature gradient. It was the primary objective of the experimental part of this study to demonstrate that this observed movement was not due in some way to

gravitational influences. The minimum success requirements to meet this objective were designated as follows:

1. A good photographic record of the motion of bubbles in molten sodium borate covering a period of at least 60 seconds at zero gravity.
2. A hot spot temperature of about 900°C.
3. A temperature gradient of several hundred degrees per centimeter in the molten glass region photographed.

It was also hoped that the thermal region of the hot stage would be known well enough so that the experimentally measured motion could be compared meaningfully with theory also to be generated as part of this program. The photographs should also have provided valuable information about bubble-bubble interactions and bubble-wall interactions.

Parallel with the experimental work, there was the need to advance the quality of the current theoretical models for bubble motion due to the presence of a temperature gradient. This modeling was to more accurately solve the hydrodynamic equations that govern bubble motion, and to extend the theory to bubble-bubble and bubble-wall interactions.

To make the comparison between theory and experiment as meaningful as possible, the important physical parameters, viscosity and surface tension, needed to be known as accurately as possible. Therefore, measurements of the surface tension were made as a function of temperature on a melt of known composition. Suitable viscosity data were identified in the literature, so it was not necessary to perform these measurements in the laboratory.

2.3 Program Task Definition

This program was organized into four tasks:

2.3.1 Task I

Develop, assemble, and qualify a piece of experimental hardware that could perform the experiment automatically and record photographically and telemetrically all of the critical experimental results. This included the manufacture of the experimental sample for the flight. The Westinghouse R&D Center carried out this task.

2.3.2 Task II

Make very accurate measurements of the surface tension of dry, molten sodium borate under a dry N_2 atmosphere as a function of temperature. The temperatures included the total range to occur in the experiment. The Westinghouse R&D Center carried out this task and published the results in the Journal of Physics and Chemistry of Glasses, Vol. 21, No. 6, Dec. 1980, pp. 221-223.

2.3.3 Task III

Develop mathematical models for bubble motion and interaction. This included the development of computer programs which could make the necessary calculations. These studies were made by Clarkson College of Technology. Two articles based on this work have been accepted for publication and will shortly appear in the Journal of Colloid and Interface Science and the AIChE Journal (21,22). A third article is currently under preparation.

2.3.4 Task IV

Evaluate bubble behavior from photographic record of SPAR experiment, using motion analyzer at Clarkson College of Technology. Compare with theoretical predictions. An article based on this work is currently under preparation.

3. EXPERIMENT APPARATUS FOR THE SPAR VIII FLIGHT

The entire experiment was designed to be packaged in a 17" x 24" sealed cylindrical canister. The AFT plate of the canister was blind tapped formounting 4 shock pads which supported the critical sections of the experiment. These sections were: 1) the camera, 2) microscope tube, 3) experiment hot stage, 4) stage support heat sink, 5) the electronic circuit boards for heater power control and thermocouple amplifiers.

A printed circuit card cage and some other sundry electrical components were hard mounted directly on the AFT plate. In the following sections, more detail is provided on the Photographic System, which consisted of the camera and microscope tube with objective lens, Experimental Hot Stage and the Electrical System.

3.1 Photographic System

The layout of the photographic system is shown in Figure 3.1-1. The system consisted of an objective lens, phototube with front surface mirror to deflect the optical path 90°, camera without lens and two light pipes that acted as edge illuminators. One light pipe was actually used with the other serving as a backup.

The camera was a Nikon F-2 equipped with a 250 frame magazine back and a Nikon MD-2 motor drive. The camera was actuated by an external timing circuit. The current drawn by the camera motor-drive was monitored by telemetry and served as a record of the actual photographing rate.

The objective lens was a 1.2X Nikon microscope objective which provided $\sim$6X magnification. This lens had the necessary depth of focus and included enough surrounding detail to make orientation and scaling

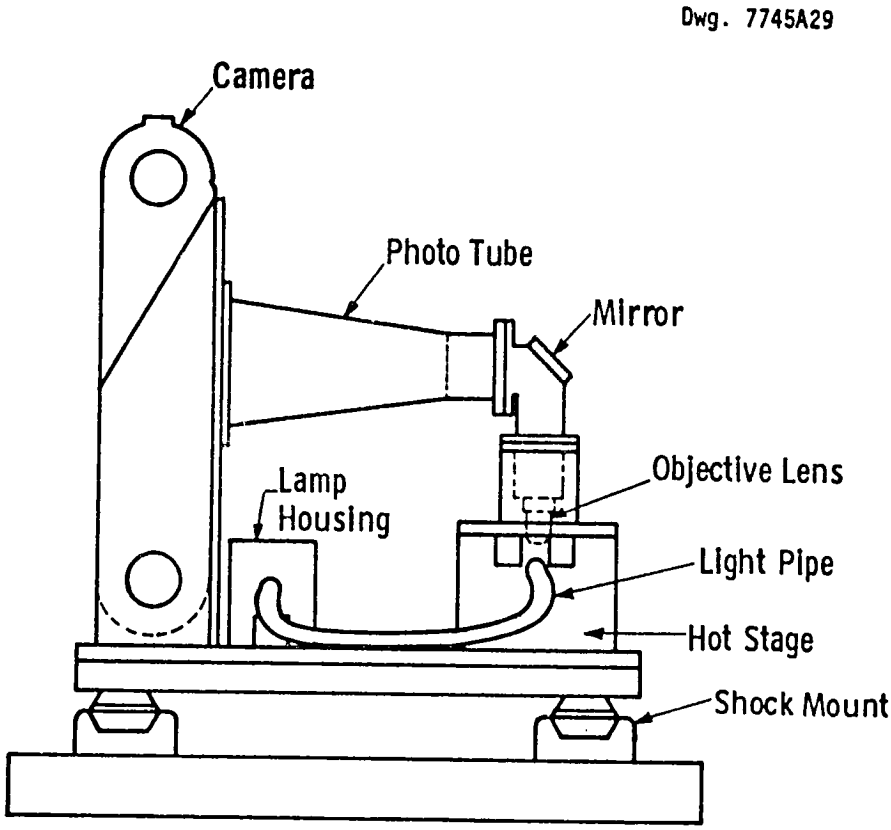

Fig. 3.1-1—Major components of the photographic system

of the photographic record relatively straightforward with little chance of serious error. The magnification was still good enough to track ~10 μm bubbles.

3.2 Experiment Hot Stage

An exploded view of the hot stage and of the sample plate-heat shield assembly is shown in Figures 3.2.1 and 3.2.2. The hot stage was designed to perform the following functions:

- To hold the sample plate-heater strip with accompanying heat shields in alignment with the objective lens so that the cell could be properly photographed.
- To allow power to be applied to the heater strip to establish the experimental conditions and light to be ducted to the glass sample to properly illuminate it.
- To act as a sink for the heat generated by the heater-strip.

The heat shields and sample plate were fused silica. The heat shields were gold flashed on the side away from the sample plate only, to reduce the chance of shorting the thermocouple leads. The spacers or shims isolating the plate and shields were made from either Kapton tape or silicone rubber. The entire stack is shown in more detail in Figure 3.2-2. This stack was pre-assembled so that with minimal alignment it could be automatically located on the optic axis and in the focal plane of the photographic system. The thermocouple leads were arranged to coincide with the correct terminal on the side of the hot stage. These leads were captured by laminating them between pieces of Kapton tape which also insulated them from the hot stage and thermocouple clamp.

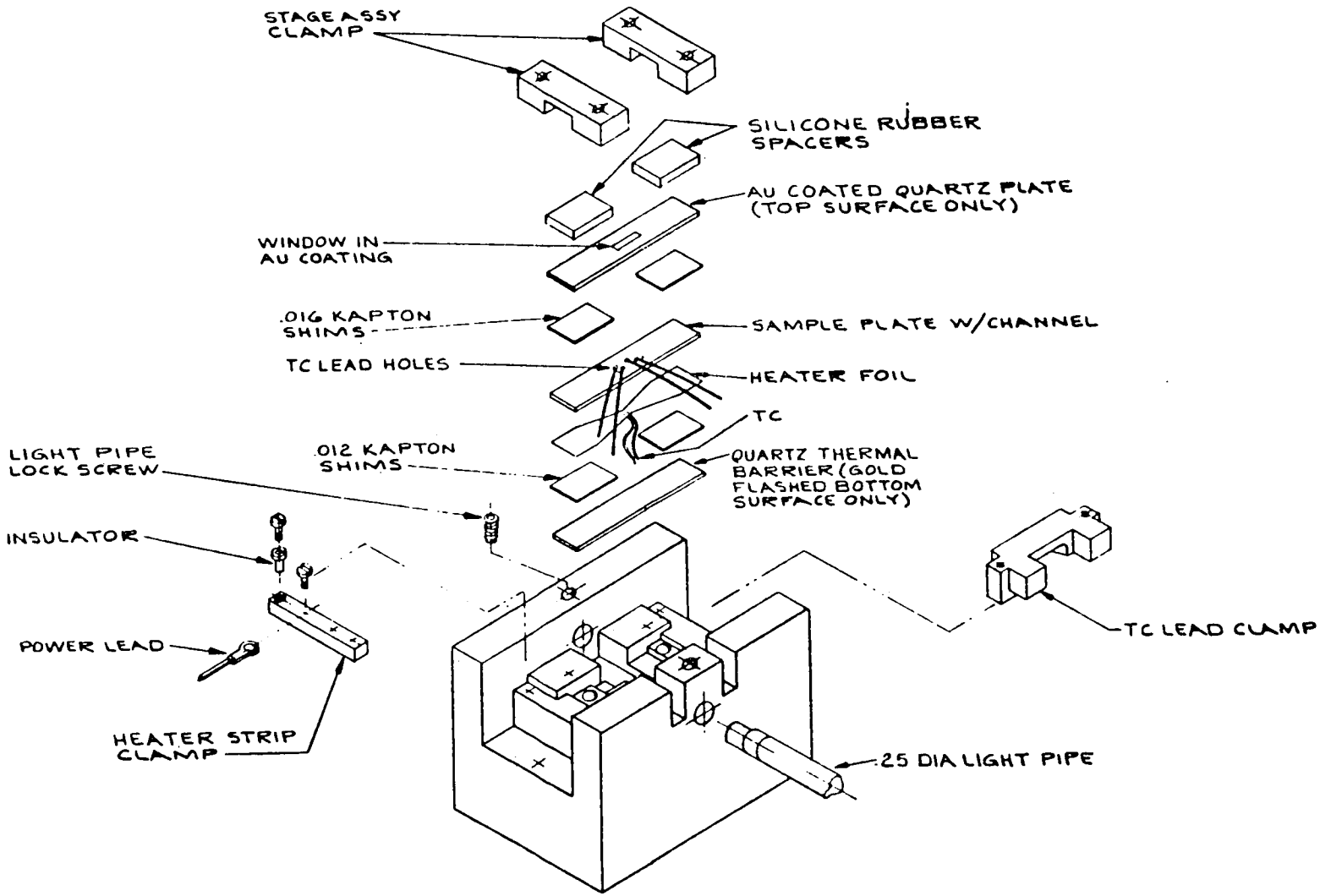

Figure 3.2-1 - Experiment hot stage composite assembly.

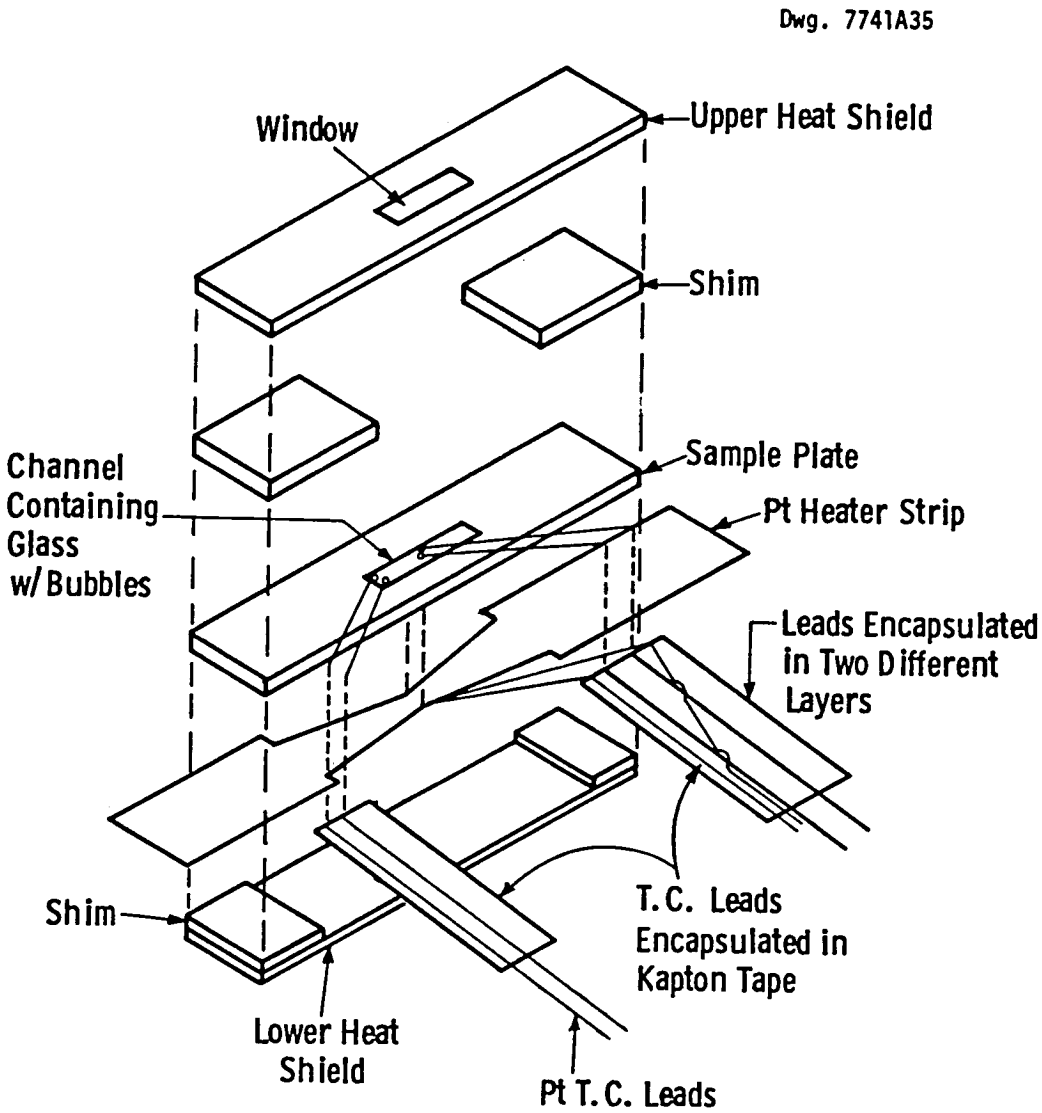

Fig. 3.2.2—Expanded schematic of sample cell assembly

Two thermocouples were implanted in the glass with the leads exiting from the top of the sample plate through .015" holes. The other thermocouple was spot welded to the bottom of the platinum-rhodium heating strip at the hot spot. This latter thermocouple was used to control the strip temperature while the first two monitored the temperature and the temperature gradient in the molten glass.

3.3 Electrical Control System

The electrical control system for this experiment consisted of the five primary functional blocks shown in the block diagram of Figure 3.3-1. These functional blocks are: (1) isolating power supply, (2) logic circuitry, (3) power conditioning circuitry, (4) signal conditioning circuitry, and (5) the experiment itself. The relative relationships of these functions are indicated in the block diagram. Primary power to the system was derived from the 28V dc bus. Power for the isolating power supply, logic circuitry, and power conditioning circuitry was derived directly from this bus. The signal conditioning circuitry for amplifying the thermocouple signals and generating telemetry signals was isolated ohmically from the 28V dc bus. This isolation was maintained by transformer isolation of power signals and light-coupled (LED) isolation of control signals.

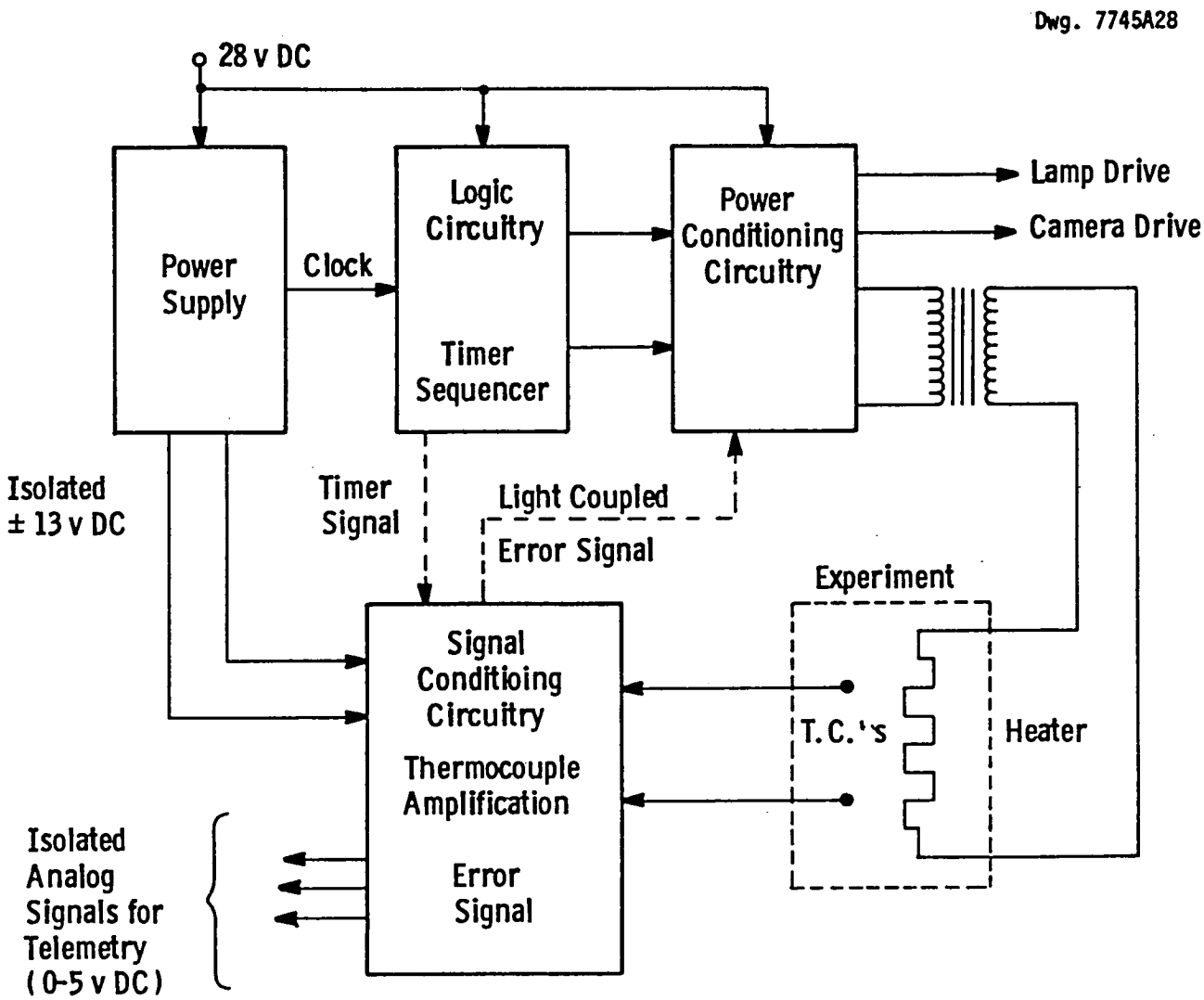

Fig. 3.3-1—Block diagram of the control system

3.4 Temperature vs. Position and Time in Typical Flight Samples

The first objective of the experimental apparatus was to develop a stable temperature gradient in the sample of glass containing bubbles. The gradient was generated by the tapered platinum rhodium (20%) heater strip. The gradient was oriented along the axis of the strip pointing horizontally toward the narrow spot where the hot spot occurred and vertically into the strip (because a large vertical gradient also existed).

3.4.1 Temperature vs. Position

The platinum (rhodium 20%) heater strip shown in Figure 3.2.2 was cut from .001" x .4" (10 mm) strip with a rubber die. The tapered section of the strip decreased in width from 6 mm at the ends to 2.5 mm at the center. This took place over a distance of 10 mm.

The temperature profile of several heating strip-sample assemblies was determined using an IRCON model #300 T5C optical pyrometer. This model read the radiation in the interval 2.0 - 2.6 μm. The spot size read was 2 mm in diameter.

The following procedure was used to determine the temperature profile. The central hot spot was read with the IRCON and the emittance control adjusted until the pyrometer read the same as the thermocouple on the heater strip. The stage was then moved in .625 mm increments and a temperature measurement made for each increment. The pyrometer was kept stationary. Representative results are shown in Fig. 3.4.1-1.

The results are summarized as follows:

- The temperature gradient measured in this way was linear over the region to be photographed.
- The gradient shape was quite reproducible from strip to strip.
- The gradient increased with temperature from ∿300°C/cm when the hot spot read 700°C to ∿550°C/cm when the hot spot read 1035°C.

Curve 728466-A

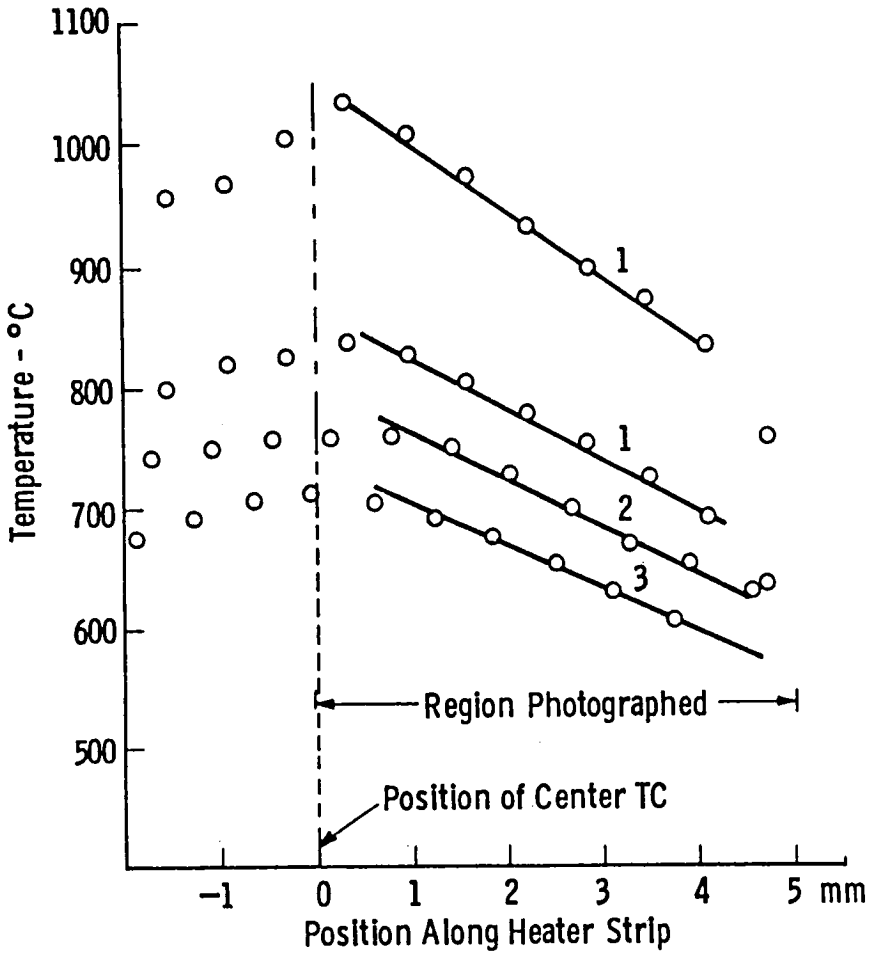

Fig. 3.4.1-1—Some typical temperature profiles measured on the hot strip heater with the IRCON. The readings were made on a complete hot stage assembly without the upper heat shield. Results from three separate strips are shown. The lines are a visual fit to the points

Temperatures measured by the control thermocouple on the bottom of the platinum heater strip and by another thermocouple at the top of the channel directly above it in the glass indicated a strong vertical gradient in all of the sample plate assemblies. The addition of the gold-flashed heat shields decreased its magnitude about 20%. With a shield, gradients of between 26°C and 50°C were measured. A best estimate would be 30-40°C because the presence of large bubbles in some cases appeared to raise the measured gradient.

3.4.2 Temperature vs. Time

The time-temperature characteristics of several sample plate assemblies were recorded during test runs while the electronic control system was adjusted. Figure 3.4.2-1 shows a typical set of traces from the thermocouples in the glass. A final horizontal gradient of 310°C/cm was generated in the case shown. It was very important to accurately locate the vertical position of the thermocouples after the flight experiment because of the vertical gradient.

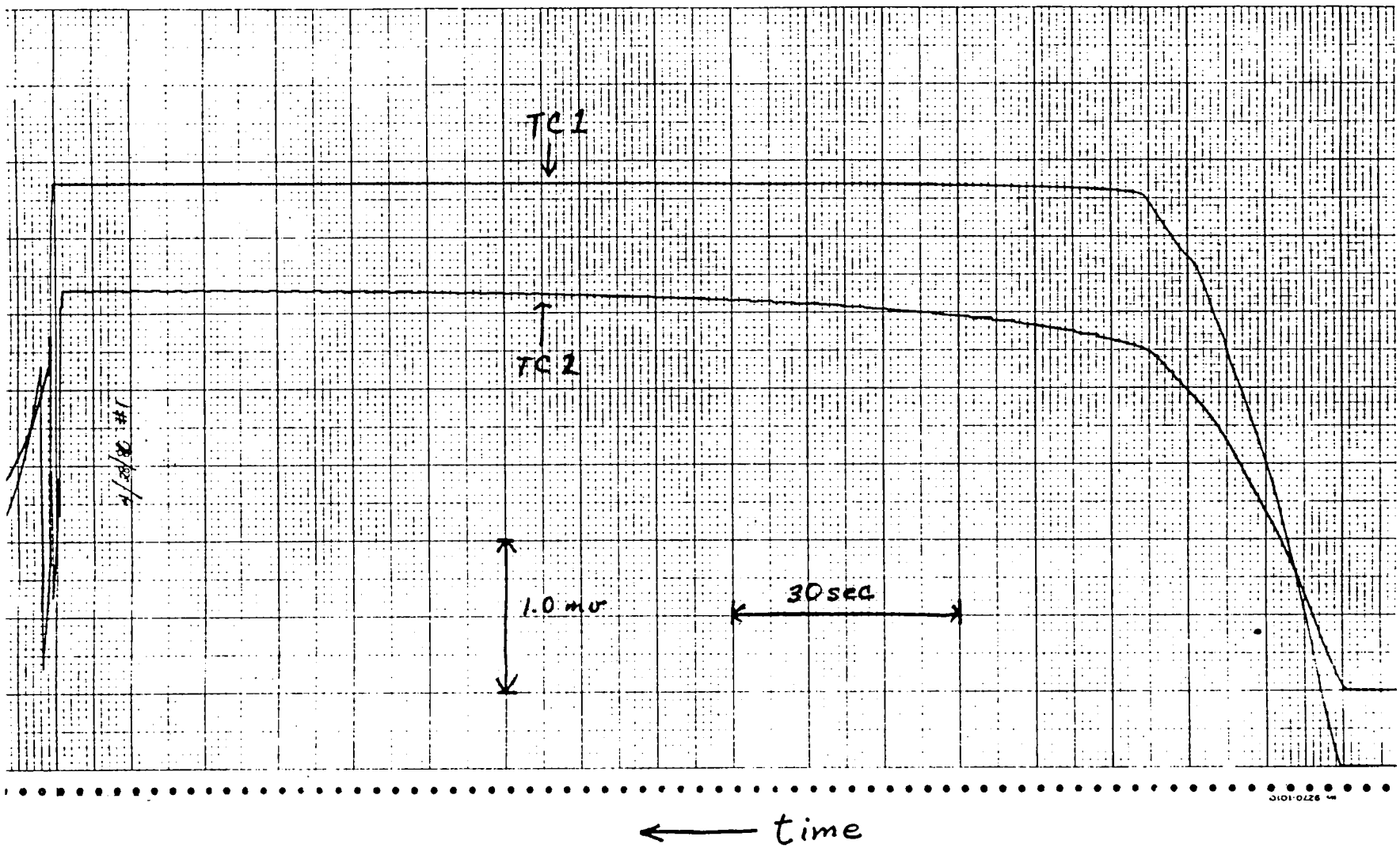

Figure 3.4.2-1 - Time-temperature profile for a sample plate assembly in place in the hot stage. TC1 indicated a maximum temperature of 887°C and TC2 a maximum temperature of 732°C.

4. SODIUM BORATE GLASS PREPARATION AND FABRICATION OF THE FLIGHT EXPERIMENT CELL

4.1 Sodium Borate Glass Preparation

The glass was prepared by melting Fisher certified $Na_2B_4O_7 \cdot 10H_2O$ in a platinum crucible at 800°C. The water content was reduced to a measured (βOH) value of .0234% by bubbling the melt with very dry nitrogen (liquid N_2 boil-off) for 17 hrs. Samples were taken from the crucible melt for chemical analysis before and after surface tension measurements were made. Na_2O was found to be about 1% higher after the measurements. Since Na_2O was expected to preferentially volatilize, the before and after values were averaged giving 29.9 wt % Na_2O. At this point one millimeter glass cane (rod) was drawn from the crucible melt and stored under dry N_2 in sealed glass vials in anticipation of constructing flight experiment samples.

4.2 Surface Tension and Viscosity of the Sodium Borate Glass

The surface tension of the sodium borate glass was carefully determined using a maximum pull-on cylinder technique over the temperature range 725°C - 925°C. The data over that range are well reproduced by the equation σ(dynes/cm) = 261 - .0756 T(°C), where the temperature coefficient-.0756 has the units dynes/cm-°C. A full report of this study is given in the report by Partlow et al. (1980)[14].

Several studies of the viscosity of sodium borate have been reported in the literature. However the study by Matusita et al. (1980)[15] specifically measured the viscosity of very low water sodium borate melts. They state that the water content of a 29.6 wt % Na_2O melt was .03 mole %, which is close to the value found for our glass. The following values were taken from a graph in their report:

700°C - 681 poise

800°C - 40 poise

900°C - 5.0 poise

The other studies, by Shartsis et al. (1953)[16] and Kaiura and Toguri (1976)[17], were performed on glass melts that probably contained more water, although their results do not differ greatly from the above values.

4.3 Fabrication of the Flight Experiment Cell

The flight sample was encapsulated by a fused silica plate 1 x 12 x 48 millimeters in dimensions. The sample cavity itself had the dimensions .5 x 1 x 10 millimeters (see Figure 4.3-1). The sixth surface of the sample was enclosed by the platinum heater strip. The elimination of all free surfaces was necessary to prevent thermocapillary convection from occurring and generating bulk flow in the melt. The fused silica slide was also an excellent optical medium to photograph through. The only drawback of this construction was the generation of small cracks in the fused silica wall bounding the sodium borate glass. However, as seen below this was an unavoidable condition.

The flight experiment sample was generated in two steps. First the leads of two platinum-rhodium thermocouples were threaded through the ports in the top of the sample chamber and then a suitable piece of glass cane ($\sim$1 cm long) was laid in the channel on top of the thermocouple beads. The system was placed in a furnace at $\sim$1000°C for $\sim$45 seconds. The furnace was constantly flushed with dry N_2 and the cooling sample was flushed with N_2 also. Figure 4.3-1 a b shows the sample plate before and after the first firing. In the second step, the platinum rhodium 20% heating strip was attached to the sample plate by fusing the sodium borate glass through passage of current through the heater strip itself. When fused by the platinum strip, the glass flowed into an equilibrium mechanical configuration under the influence

of capillary and gravitational forces. By including this step, an experimental cell was produced in which the glass had completely filled the inverted channel and also filled the thin space between the silica cover and the heater strip. This physical distribution of glass was similar to that observed previously in the demonstration study. Hence, it was expected that very little bulk flow would occur during the initial phase of the flight experiment because most if not all of the bulk flow occurred during the fabrication step. Incidentally, during this step any bubbles present were observed to migrate toward the hot spot. Figure 4.3-1 illustrates the effect of this second firing. Again a stream of dry N_2 was directed over the sample during this procedure. The sample was stored under dry N_2 until incorporated in the sample cell assembly described previously.

The cracks in the sample glass caused by the expansion mismatch between the sodium borate and the fused silica plate acted as bubble generators for the experiment. Bubbles put into the glass prior to the final firing were almost always completely removed by subsequent processing due to thermocapillary movement. The cracks produced microvolumes which were filled with the dry N_2 atmosphere in which the sample was stored. These voids rounded off into spherical bubbles during the melt down of the glass at the beginning of the experiment. By forming many bubbles, their distribution throughout the glass assured that several would be in a position to provide useful data.

A complete sample cell assembly is shown in Figure 4.3-2. This assembly was constructed so that the glass sample was in the focal plane of the photographic system as installed and so that the thermocouple leads were captured for much of their length, preventing any chance of shorting.

One final comment about the fabrication of the flight experiment cell. Though the fabrication steps seemed straight forward, there were several processes occurring that were difficult to control. These included the wetting of the silica and platinum surfaces and flow of

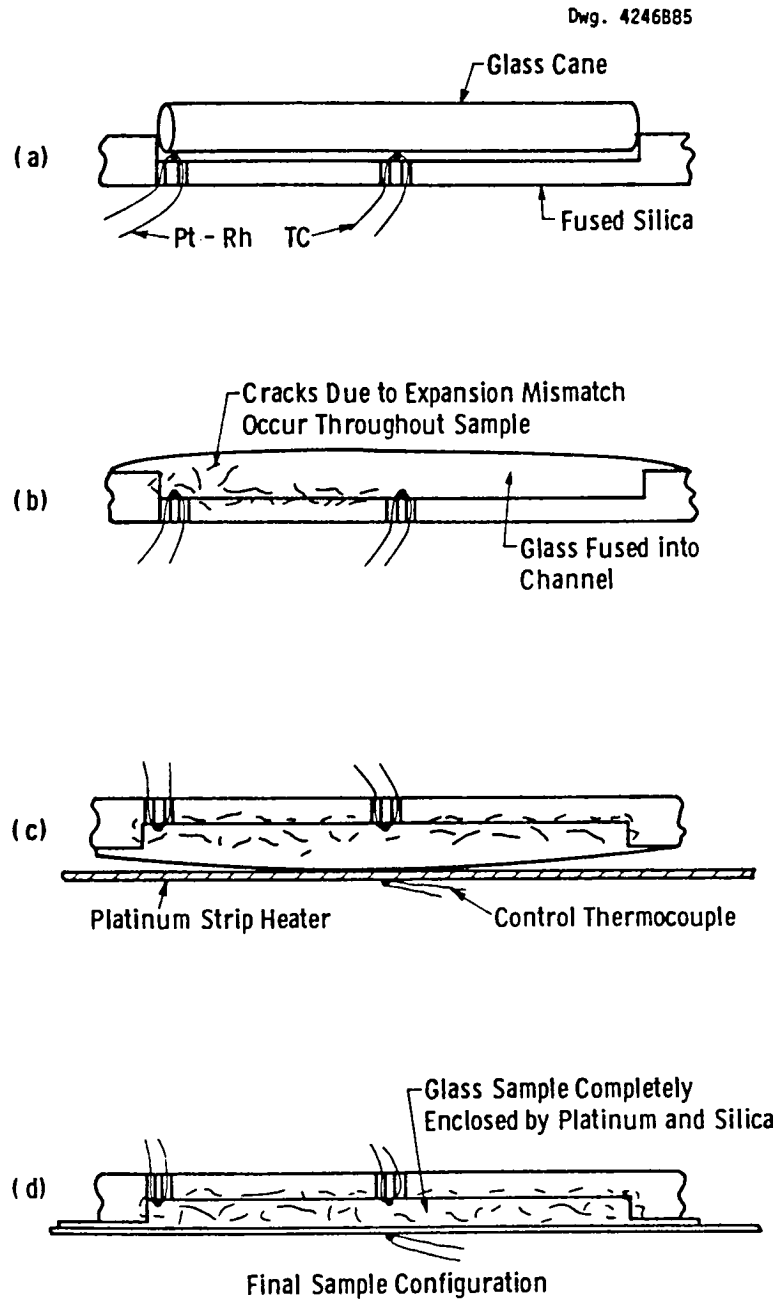

Fig. 4.3-1—a) and b) First step in assembling the flight sample. The glass (Na borate) was fused filling the channel and encapsulating the thermocouples. Second step c) and d). The platinum heater strip was used to fuse the sample glass which flowed to bring the system into mechanical equilibrium. Crazing (formation of small cracks) occurred throughout the glass and in the surrounding silica plate. The channel was 0.5 mm deep.

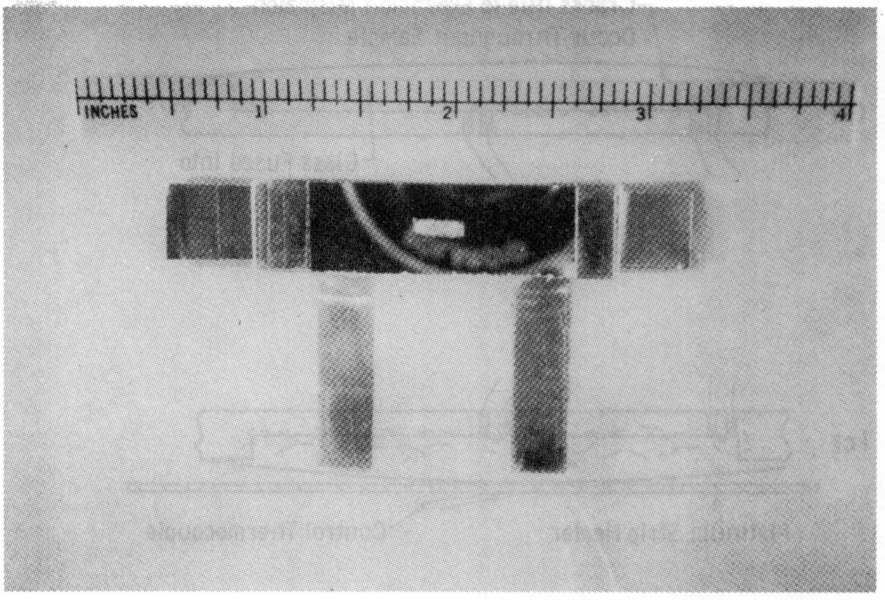

Figure 4.3-2. Top view of complete sample cell assembly ready for installation. Figure 3.2-2 shows the expanded schematic of the assembly.

the melted glass, the formation and migration of bubbles during the second melting step, and the cracking process that degraded the photo-optics but generated bubbles for the experiment. As a result of these factors, the yield of good cells varied from 10 to 50 percent.

5. THEORY

Young, Goldstein and Block[8] (YGB) were the first to consider bubble motion in a surface tension gradient. They assumed a spherical bubble and neglected convective momentum and heat transfer. That is, they solved the creeping flow hydrodynamic equations and the conductive heat transfer equations. In the absence of gravity they predicted a bubble movement velocity V of

$$V = \frac{\partial T}{\partial x} \frac{\partial \sigma}{\partial T} \frac{a}{2\eta} \qquad (1)$$

where T is temperature far from the bubble, x is distance along the temperature gradient, σ is surface tension, a is bubble radius, and η is viscosity. The results of YGB have been verified experimentally for low viscosity fluids in relatively low temperature gradients[8,18-20].

Molten glasses have high viscosities, and some processing requirements may call for moderately high temperature gradients. Under such conditions the movement rate may be sufficiently low that the creeping flow approximation is still valid, but appreciable convective heat transfer may occur. Convective heat transfer would lower the temperature gradient along the bubble surface, and thereby lower the movement rate V.

5.1 Single Bubble in Large Melt

We first attempted to develop a general finite difference numerical scheme for the single bubble problem, using an M.S. student, Vincent Milito, who was not actually paid from this contract. Several cases at low Marangoni number* were solved. Better agreement with the experiments of Hardy[18] was obtained than provided by YGB's results. In attempts to develop a general new equation, we

*Marangoni number, $Ma = \frac{\partial T}{\partial x} \frac{\partial \sigma}{\partial T} \frac{a^2}{\eta \alpha}$, where $\alpha = k/\rho C_p$ is the thermal diffusivity.

decided to make a few more computer runs for different conditions. Unfortunately Milito's computer program would no longer produce sensible results. Milito has left Clarkson (without the M.S.) and consequently we now have little confidence in his results.

Fortunately Professor Subramanian was able to reach an analytical solution of this problem using a matched asymptotic expansion.[21] The final result is

$$V = \frac{\partial T}{\partial x}\frac{\partial \sigma}{\partial T}\frac{a}{\eta}\left[\frac{1}{2} - \frac{301}{14{,}400}\,Ma^2 + O(Ma^4) - \quad \cdots \cdot\right] \qquad (2)$$

which is probably valid roughly up to Marangoni number Ma ~ 1. Note that the first term (1/2) is YGB's result and that only even powered terms in Ma appear. While this result should be sufficient for nearly all glass processing experiments, there are some fascinating mathematical questions in going to high Ma that should be considered in the work.

5.2 Single Bubble Near Surface

In real glass fining (bubble removal) isolated bubbles do not occur in unbounded melts under static conditions. Bubbles interact with one another and with walls. This was certainly true in our SPAR experiment. Thus we have devoted considerable attention to interaction phenomena.

We have solved the problem of a bubble moving near a surface with a temperature gradient normal to the surface.[22] It was found that the bubble slows down from the YGB velocity as it approaches a surface. The retardation begins when the bubble surface is about one diameter from the surface, with the retardation greater for a solid surface than for a free surface (liquid-gas). This may be compared with the larger retardations experienced out to 5 diameters by a bubble rising due solely to buoyancy (gravity).

5.3 Two Bubbles in Large Melt

Meyyappan and Subramanian have also solved the double-bubble problem, using an analytical technique with bispherical coordinates. Since they are still

interpreting these results, a manuscript has not yet been written. They considered two bubbles in line along the temperature gradient. The results are summarized in Figures 5.3-1 and 5.3-2. Note that a small bubble may be greatly accelerated by the presence of a large bubble, with the velocity increasing as the large bubble increases in size and as the distance between the bubbles decreases. The result is the same whether the large bubble is "in front" or the small bubble is in front. The large bubble is slowed down, but only slightly. Bubbles which are both of the same size move at their YGB velocity, i.e. they have no net influence on the movement of one another.

It appears that the large bubble will catch a small bubble when the small bubble is in front, but not vice versa. We are not entirely certain about this, however, because our solution does not yield results when the bubbles are near one another.

5.4 Theoretical Work Remaining

Not all theoretical problems relevent to glass fining have been solved. Among those remaining are:

a. Single bubble at large Marangoni number.
b. Bubble near surface with temperature gradient at angle to surface.
c. Physical explanation for absence of net effect with two bubbles of same size.
d. Two bubbles near one another.
e. Coalescence of two bubbles.
f. Two bubbles not aligned with temperature gradient.
g. Multiple bubbles.

Some of these are probably amenable to analytical approaches, while the solution of others will require numerical modelling on the computer.

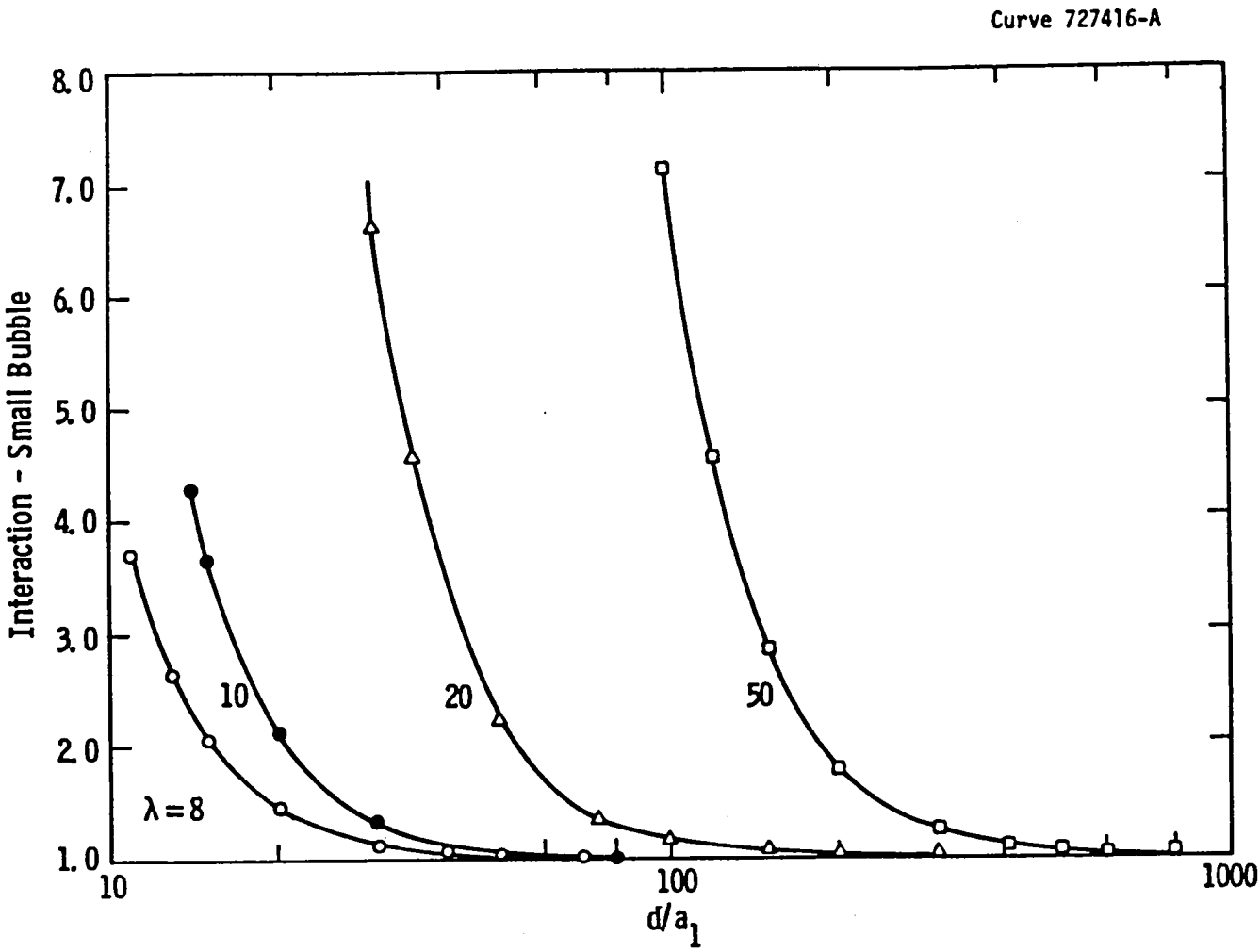

Fig. 5.3-1-Solution to double bubble problem. Here $\lambda = a_2/a_1$, a_2 is the radius of the large bubble, a_1 is the radius of the small bubble, d is the distance between the centers of the bubbles (they touch at $d = a_1 + a_2$), and "INTERACTION" is the ratio of the actual velocity of the small bubble to its YGB velocity

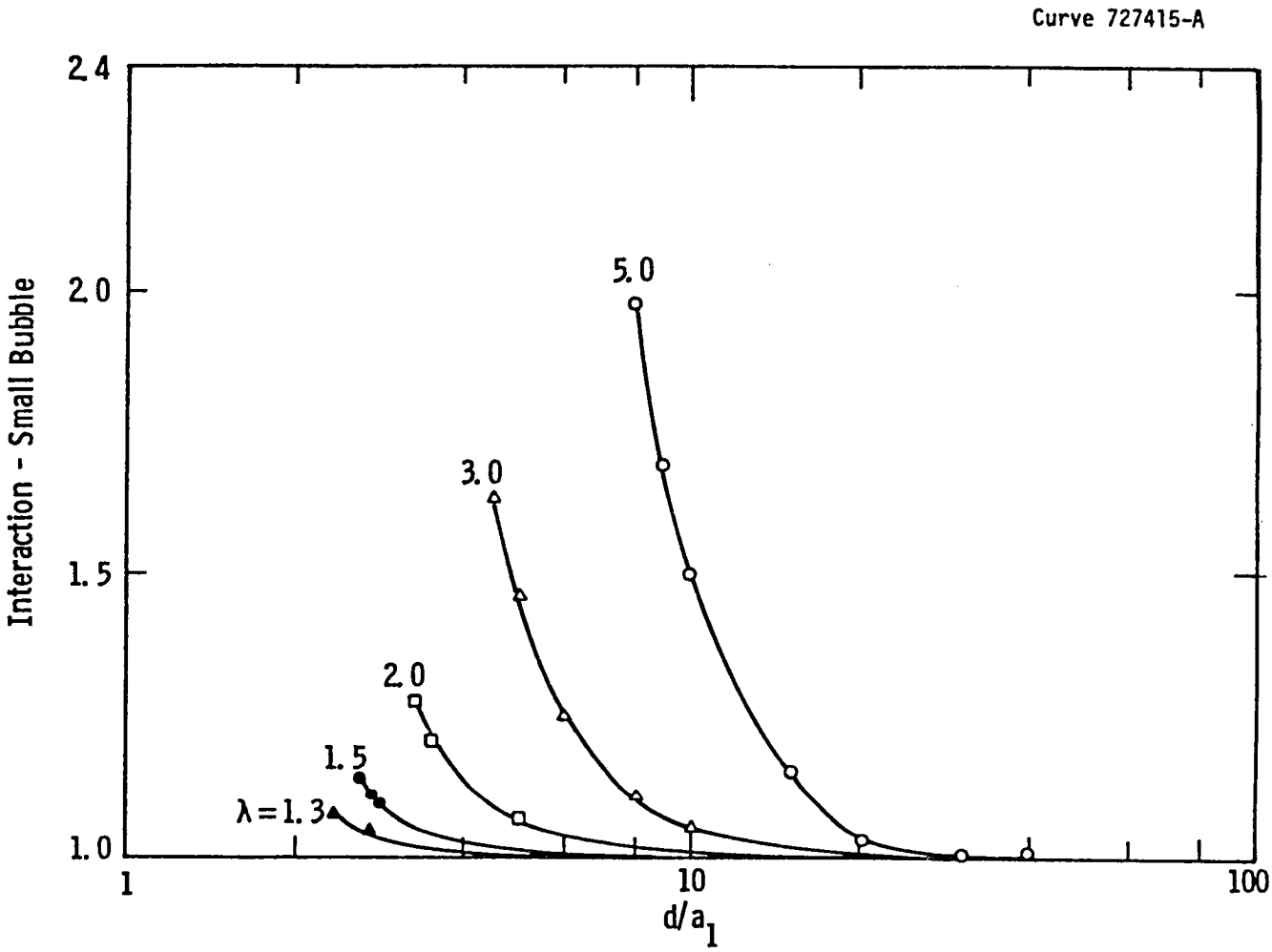

Fig. 5.3-2 —Continuation of figure 5.1 for smaller values of λ (radius ratio)

6. The SPAR VIII Experiment 77-13

Description and Interpretation

6.1 Introduction

On November 18, 1980, the SPAR VIII rocket carrying experiment 77-13 was launched. During the flight, the experimental apparatus operated flawlessly for more than 4 minutes under an average acceleration near zero. During that time, 246 photographs of the molten glass sample were taken at one second intervals. One of these photographs clearly showing abundant bubbles is reproduced in Figure 6.1-1. At the same time, temperature data from the three thermocouples embedded in the molten glass and welded to the heating strip were telemetered back to the ground. Telemetry of a signal proportional to the current drawn by the camera film advance motor provided a time indicator for the film sequence.

The flight film was recovered intact despite a hard landing by the payload. The developed film showed that the bubbles in the molten glass clearly moved toward the hotter areas in the sample. In the following sections we present an evaluation of the experiment performance and a preliminary analysis of the data and a comparison to the theory presented in the previous section.

6.2 Sample Description

The sample was constructed as illustrated in Figures 3.2-2, 4.3-2. Its appearance was changed little by the experiment. The sample without the upper heat shield is shown in Figure 6.2-1a, b, and c. The sample does not appear clear because of the large amount of crazing (cracking) that occurred due to expansion mismatch between the silica and the sodium borate glass when the glass froze. The large void coincident with one of the thermocouple wells at the center of the channel formed during manufacture of the flight sample. The side view shows that the platinum heating strip did not pull away from the

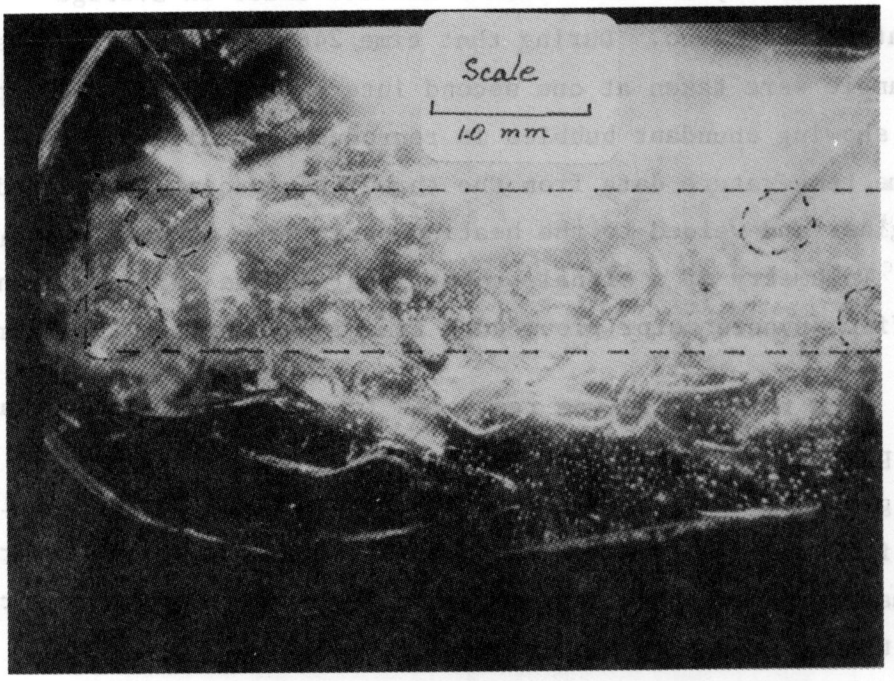

Figure 6.1-1 - Reproduction of one of the 70 mm photographs taken during the flight while the glass sample was molten. Unavoidable crazing (cracking) of the fused silica at the channel walls is visible. Dashed lines indicate the position of the walls and thermocouple lead wells.

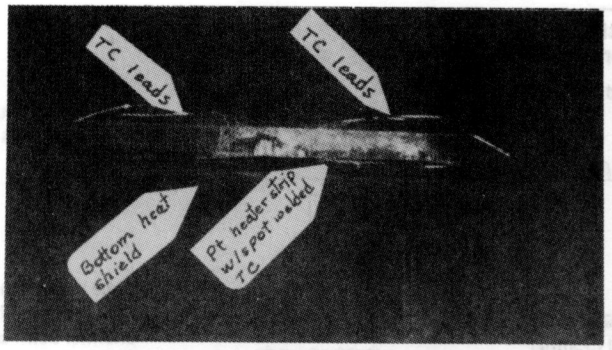

a) Side view of the flight sample (3.3X)

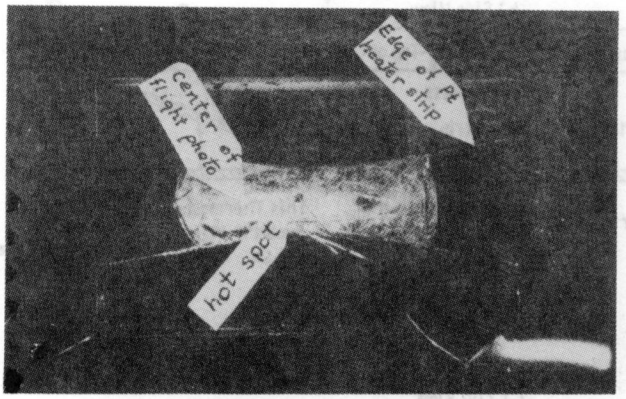

b) Top view of the flight sample (3.3X)

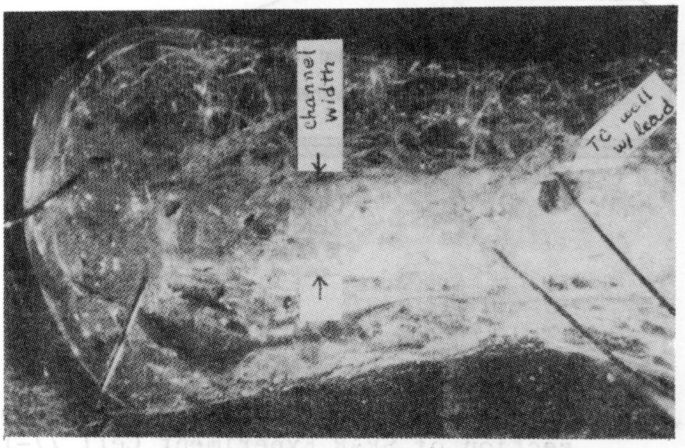

c) Close-up of the photographed area of the flight sample (13.5X)

Figure 6.2-1 - The flight sample with the upper heat shield removed

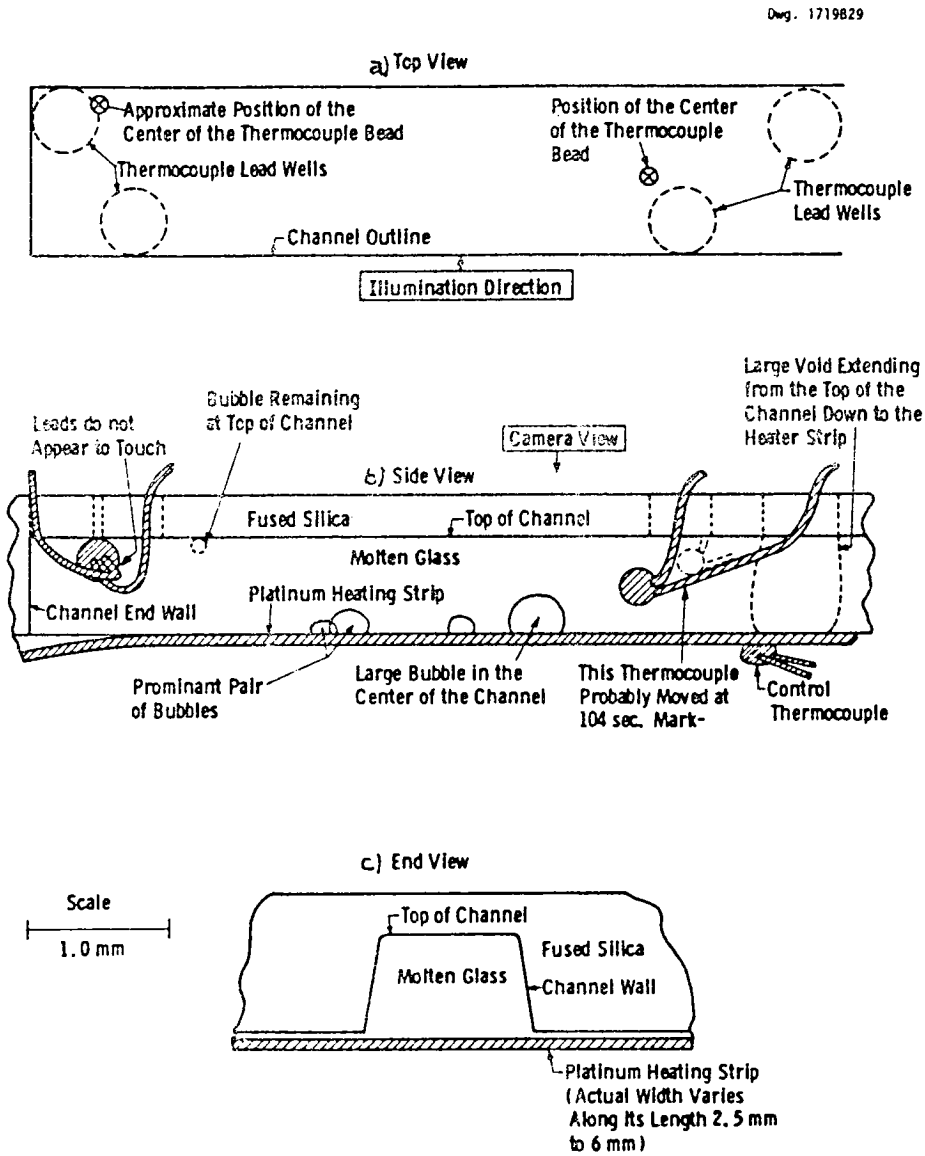

Figure 6.2-2a,b,c - Diagramatic reproduction of photographed section of SPAR Experiment Cell 77-13 and some bubbles. The prominant pair of bubbles is visible in figures 6.1,6.2-3,6.2-4.

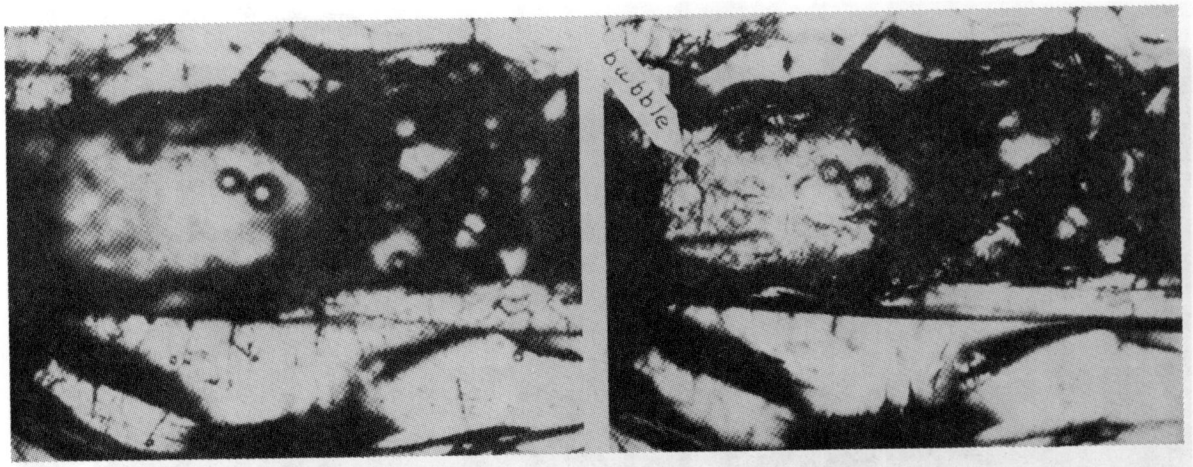

a) focused at the bottom of the channel

b) focused at the top of the channel

Figure 6.2-3 - Top views of the documented region of the flight sample. Bubbles were found to be either at the silica cover or at the platinum heater strip. Transmitted light, 27.5X.

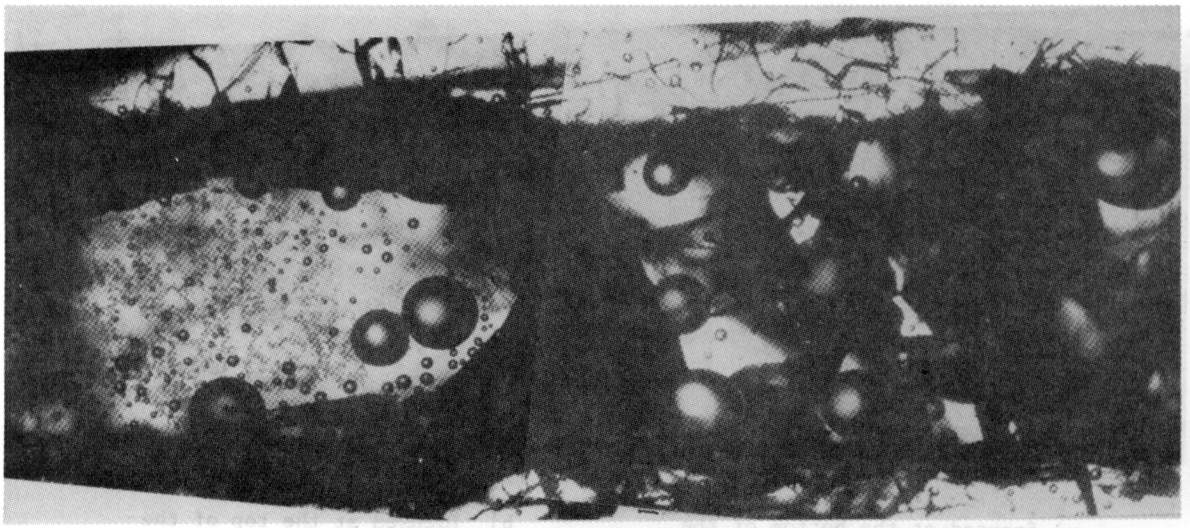

Figure 6.2-4 - Bottom view of documented area of the flight sample. Objective focused on the surface that was next to the heater strip. Almost all of the bubbles were found at this surface. Transmitted light, 44X. Dendritic pattern on the surface is believed to be due to reaction of moisture with the glass after the flight.

silica plate during the flight (Figure 6.2-1b). Figure 6.2-1c shows the area photographed during the experiment. The glass was much clearer during the experiment when it was molten, with the only cracks remaining being those in the silica.

Figure 6.2-2a, b, c is a diagramatic sketch of the flight cell shown in Figure 6.2-1c. The location of the thermocouples was determined by first sectioning the sample alongside each pair of wells and then viewing with the aid of an index oil from both the side and the bottom (after the heater strip was removed). The relative thickness of glass and fused silica as well as the shape of the channel cross section was determined from the sawed sample cross section.

In Figure 6.2-3a, b, the sample is viewed from the top after removing the bottom heat shield and the platinum heater strip. Bubbles were found to be either at the top of the channel (Fig. 6.2-3b) or at the bottom (Fig. 6.2-3a). The objective lens used to make these observations had a focal depth much less than the depth of the channel. By focusing up and down it was apparent that the intervening glass had at least no large bubbles $\gtrsim$30 μm remaining in it. By turning the sample over it was possible to focus directly on the bottom without interference as shown in Figure 6.2-4. The sharpness of all these bubble images indicates that they lay in the focal plane of the objective, and therefore were on the platinum strip. This again reinforces the opinion that all of the bubbles in the flight sample had moved to the platinum strip except for a few which adhered to the silica cover.

6.3 Time-Temperature Data

Temperatures were measured at three different positions in the experiment (see figure 6.2-2). Table I summarizes the available data for the temperatures read by each thermocouple at 10 second intervals. These data were originally taken from the strip chart recording of the telemetry signals made at the time of the flight. These have since been corrected slightly by comparing them to the digitized telemetry data provided by Marshall Space Flight Center. Corrections were 5°C or less.

Table 1 - Time-Temperature Telemetry Data

Time (from lift-off)	Control TC (on heater strip)	TC in Glass (hot spot)	TC in Glass (cooler and sample)
94 (sec.)	ambient	ambient	ambient
104	833°C	675°C	432°C
114	908	838	562
124	911	851	600
134	911	859	628
144	912	862	647
154	912	867	659
164	912	869	669
174	912	872	676
184	912	872	682
194	912	873	688
204	913	873	691
214	913	874	694
224	913	874	696
234	913	874	697
244	913	874	698
254	913	875	700
264	913	875	701
274	913	875	701
284	913	875	701
294	913	875	703
304	913	875	703
314	913	875	703
324	913	875	703
334	913	875	703

The temperatures approached steady state asymptotically. The farther a thermocouple was from the heating area the longer it took to come to equilibrium. This is one reason we made the system so small. It is clear that any bubble motion studies made roughly during the first 120 seconds will have to consider the changing temperature and temperature gradients. After about 120 seconds the temperature changes were small and so probably insignificant in comparison with the perturbing effects of bubble interactions and proximity to silica or platinum surfaces. Note that since velocity is proportional to ∇T, we need only to know the parallel gradient because we are measuring velocity in that direction.

Figure 6.3-1 is a diagram taken from Figure 6.2-2 with a preliminary estimate of the attitude of the isothermal surfaces in the flight sample. It is clear that the thermocapillary force was directed toward the hot spot on the platinum strip with components of the force both parallel and perpendicular to the strip. The attitude of the isotherm at the hot spot was estimated by assuming that the temperature gradient perpendicular to the heater strip was the same as the gradient between the control thermocouple on the strip and the thermocouple in the glass. This estimate is consistent with previous laboratory measurements of this gradient. The other isotherms are considered to be parallel to that one. The trajectories of the bubbles should be perpendicular to the isotherms, except when they are near other bubbles or near the platinum or silica surfaces.

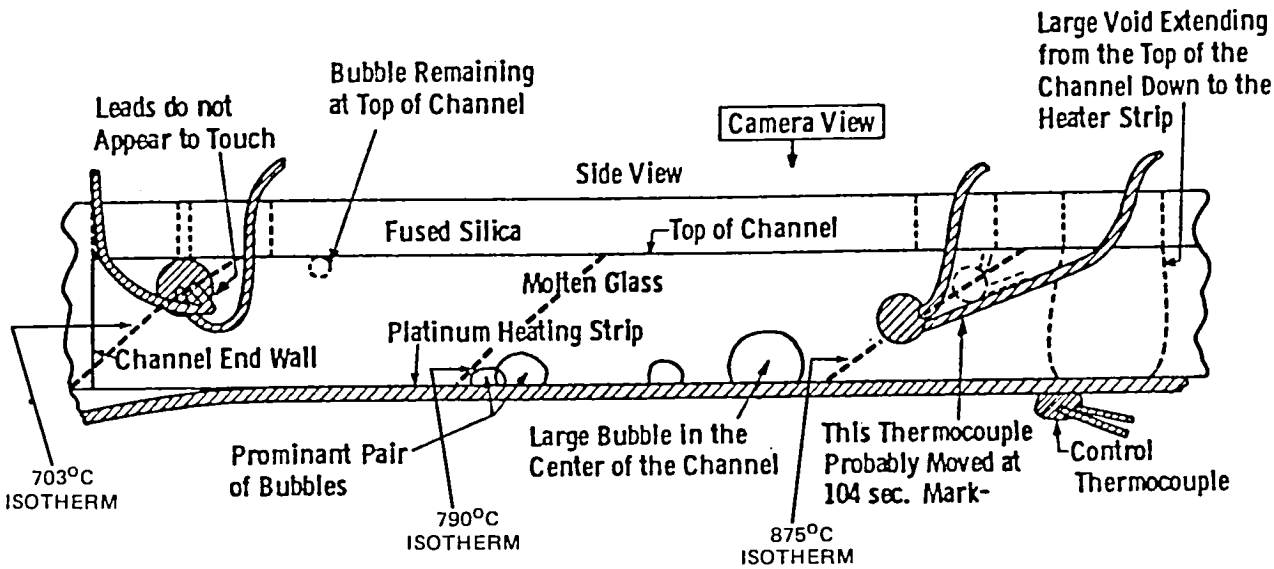

6.3-1 - Some postulated isotherms superimposed on Figure 6.2-2b.

6.4 A Preliminary Analysis of Bubble Motion in the Presence of a Temperature Gradient Under Zero Gravity Conditions

Since the flight film from experiment 77-13 was developed and subsequently made into a strip of 16 mm movie film, we have had the opportunity to observe the motion of the bubbles repeatedly. Based on these observations and the post flight evaluation of the flight sample, we have been able to qualitatively analyze the bubble motion that occurred during the SPAR VIII flight. Unfortunately it took much longer than anticipated to reproduce the same film strip on the stock that is appropriate for the Clarkson Vanguard Motion Analyzer, so Mr. Meyyappan of Clarkson has had a minimal amount of time to make quantitative measurements of bubble motion and even less time to make a careful comparison with the theory. This analysis is continuing and a thorough analysis of the film and comparison of the bubble motion with theory will be forthcoming.

We will restrict our analysis here to general observations and to a first order evaluation of the motion of the few bubbles that Mr. Meyyappan has been able to track with the motion analyzer.

6.4.1 Comments About the Film

The strip of movie film was made by copying the flight film frame for frame. The movie film differs from the flight film in that only the center half of the flight film was copied. This was done because the Nikon was set to take a double 35 mm frame (i.e. 70 mm) which gave excellent coverage of the experiment but could not be directly reproduced in full on the 16 mm frame. However the section reproduced was selected after studying the flight film. It appears to contain the most pertinent information.

6.4.2 Data Analysis Using Vanguard Motion Analyzer

The procedure involved the tracking of the center of a given bubble through the frames, i.e. as a function of time. Usually this was done by placing the vertical and horizontal cross wires of the analyzer tangential to the bubble at points 1, 2, 3, and 4 successively. The corresponding x and y coordinate values and frame number (and hence

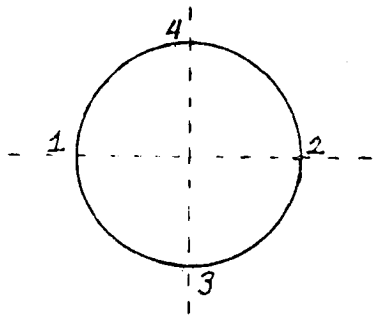

the time) may be fed directly to an IMSAI 8080 computer wherein these data are stored on disks. A basic program to manipulate this data to obtain the necessary parameters is available. Unfortunately the IMSAI was malfunctioning, and so all data taking and analysis were done manually because of the short time available.

In observing the SPAR film it was noted that the frames jumped around a bit. (This also occurred in the Papazian Grumman films). In order to ascertain the correct bubble motion it was therefore also necessary to measure the position of an immobile reference (fiducial) mark. A crack was selected which seemed to be stationary.

A few observations are worth mentioning.

1. The time duration of the experiment was 240 secs (and hence 240 frames). However the first 110 or 120 frames contain little useful data because during this period the temperature profile was being established. With melting in progress, some bulk melt movement may have occurred. After 120 seconds the temperature readings were steady.

2. This analysis has some level of uncertainty (i.e. in data measurement), which is yet to be determined. Repeat measurements at a later date will establish this.

3. The size of each bubble was also calculated from the measurements. This did change during the course of the experiment. Some fluctuations were probably the consequence of measurement errors, especially since the bubbles were not as clear in some frames as in others. Expansion of the bubbles due to changes in temperature and coalescence also occurred as they moved toward the hot end of the channel. Coalescence with a neighboring small bubble was observed with one bubble that was monitored.

6.4.3 General Observations

The experiment can be broken down into two general periods of activity. The first period is the melt-down of the glass. During this period the sample becomes much more transparent as the fractures disappear in the melting glass. As the clearing proceeds, many bubbles are observed moving toward the hot spot. However since this is a period of rapid temperature change and melting, it is impossible to know how much of the bubble motion is thermocapillary migration and how much is mechanical re-equilibration. Certainly there is some of both. The second period is perhaps twice as long as the first. It is characterized by the motion of one or two bubbles at a time while the others (there are many visible) seem to be stationary. Those that move seem to accelerate during their movement and then come to a sudden stop. Some bubble coalescence is observed.

Based on what is known about the orientation of the temperature gradients in the channel and what can be observed in the film, the following general explanation can be given for the observed motion. Many of the bubbles initially formed in the glass as it melts are rapidly swept out of the glass by the high temperature gradients that are present while the sample is heating up. Since there is also a strong vertical gradient these bubbles not only migrate along the channel but vertically to the platinum heater strip. Once they contact the strip they

become attached to it, and move only slowly at best. As the experiment progresses bubbles that were in cooler areas and/or at the top of the channel are slowly drawn toward the center of the channel. Bubbles touching the top of the channel may tend to stick there.

6.4.4 Measurement and Evaluation of the Motion of Three Bubbles

Two prominent bubbles in the center of the channel were observed to execute the motion shown in Figures 6.4-1 and 6.4-2. For convenience the bubble positions were plotted in cm as viewed on the motion analyzer vs. time. The magnification factor has since been determined to be 42.7 ± 1. (These bubbles are clearly visible in Figure 6.1-1 near the center. The larger of the pair is 212 μm in diameter; the smaller, 165 μm). Bubble 1 begins to move slowly, then accelerates and finally comes to a sudden stop. Bubble 2 appears to behave in a similar way, as again it appears to be accelerating when it suddenly comes to almost a complete stop. The early motion of bubble #2 was partially obscured by a small crack in the silica at the top of the channel. Therefore bubble #2 was not tracked in the earlier part of the motion, but its behavior appears to be similar to that of bubble #1.

The motion of these two bubbles appears to be consistent with the general picture outlined in the preceding section. These bubbles appear to have been in contact with the top of the channel, moving at first very slowly, perhaps retarded by interaction with the wall. Finally as they move away from the wall, the influence of the temperature gradient takes over and the bubble moves horizontally toward the hot spot on the heater strip and at the same time downward toward the strip because of the vertical temperature gradient. The bubble accelerates as its diameter increases and as the melt viscosity decreases with increasing temperature. Note that the temperature coefficient of surface tension is quite constant over the range of temperatures encountered. Therefore, the observed change in bubble velocity is most likely due to the above reasons. When the bubble strikes the heater strip it apparently sticks quite strongly judging from its lack of movement after that instant.

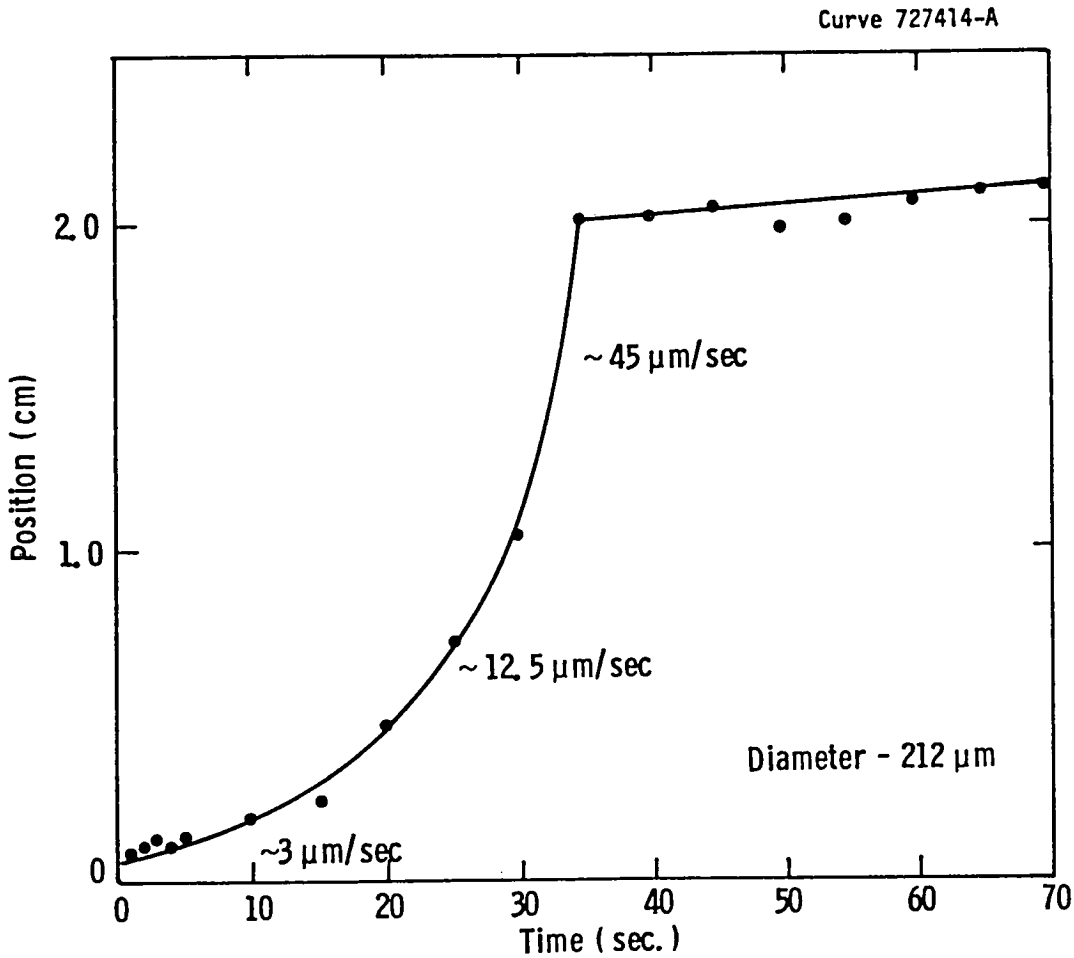

Fig. 6.4-1—Bubble #1

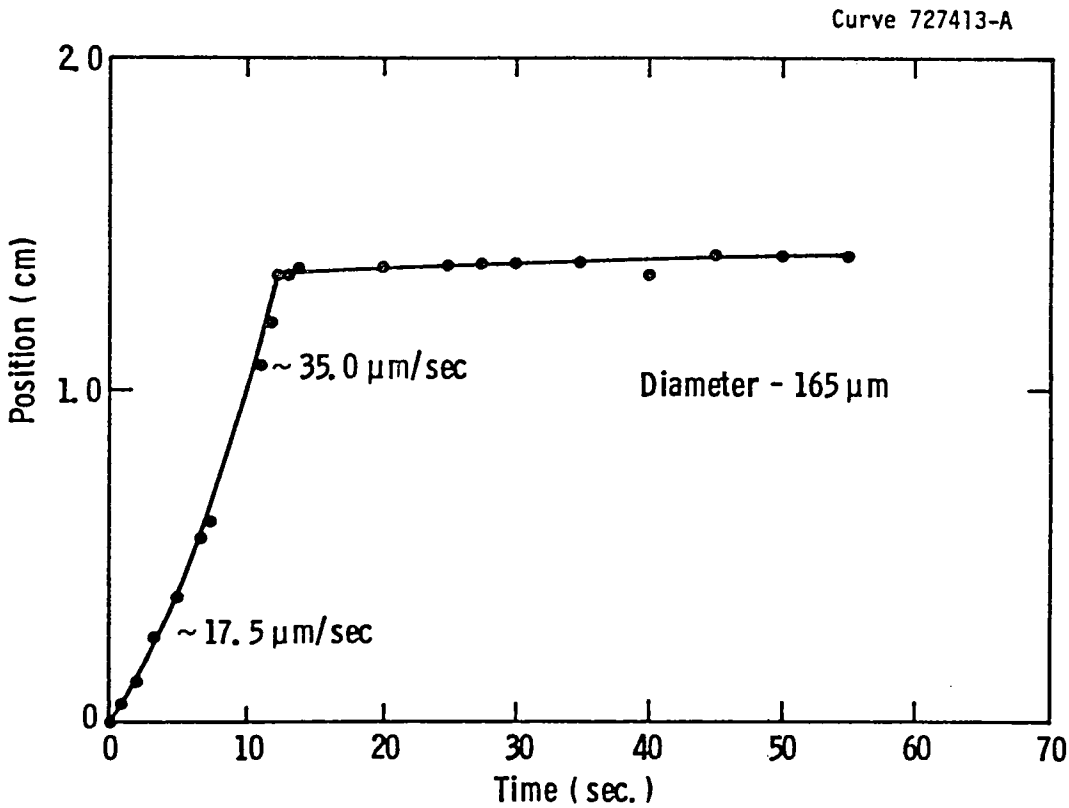

Fig. 6.4-2—Bubble #2

The velocities indicated on Figures 6.4-1 and 6.4-2 are the horizontal components of the actual bubble velocities, but they should be directly proportional to the actual velocities. Since the horizontal temperature gradient is measured during the experiment we can make a zero-order comparison with the modfied YGB theory from Chapter 5. According to the YGB theory, the velocity of the bubble v is

$$v = \left|\frac{\partial T}{\partial X}\right| \left|\frac{\partial \gamma}{\partial T}\right| \frac{a}{2\eta}$$

where $\frac{\partial T}{\partial X}$ = 438 °C/cm (from the temperature table)

$\frac{\partial \gamma}{\partial T}$ = .0756 dyne/cm °C[14]

η = the viscosity in poise

a = the bubble diameter, .0212 cm, .0165 cm

The horizontal YGB velocities are 35 μm/sec for bubble 1 and 27 μm/sec for bubble 2. These velocities are in the same ratio as those estimated in Figures 6.4-1 and 6.4-2 for the rapid period of motion (i.e. 45 and 35 μm/sec). This strongly indicates that the velocity of the bubble is linearly dependent on its diameter, as predicted by the theory. The YGB velocties were calculated assuming a viscosity of 100 poise which is a reasonable value in the estimated temperature range of 750°-800°C. Clarkson is currently conducting a more thorough analysis of the bubble motion and its relation to the thermal field. When this is complete, it will be possible to make a more precise comparison between the theory and experiment. Though a complete verification of the theory cannot be conducted, there are no serious discrepancies.

Bubble 3 is an example of a bubble "stuck" to the platinum heater strip. Figure 6.4-3 shows the measurements taken in Bubble 3. Bubble 3 maintained a fairly constant size of about 76 μm diameter. (on the screen). This corresponds to a YGB velocity of 4.9 μm/sec. In Figure 6.4-3 the data are extremely scattered and it appears that

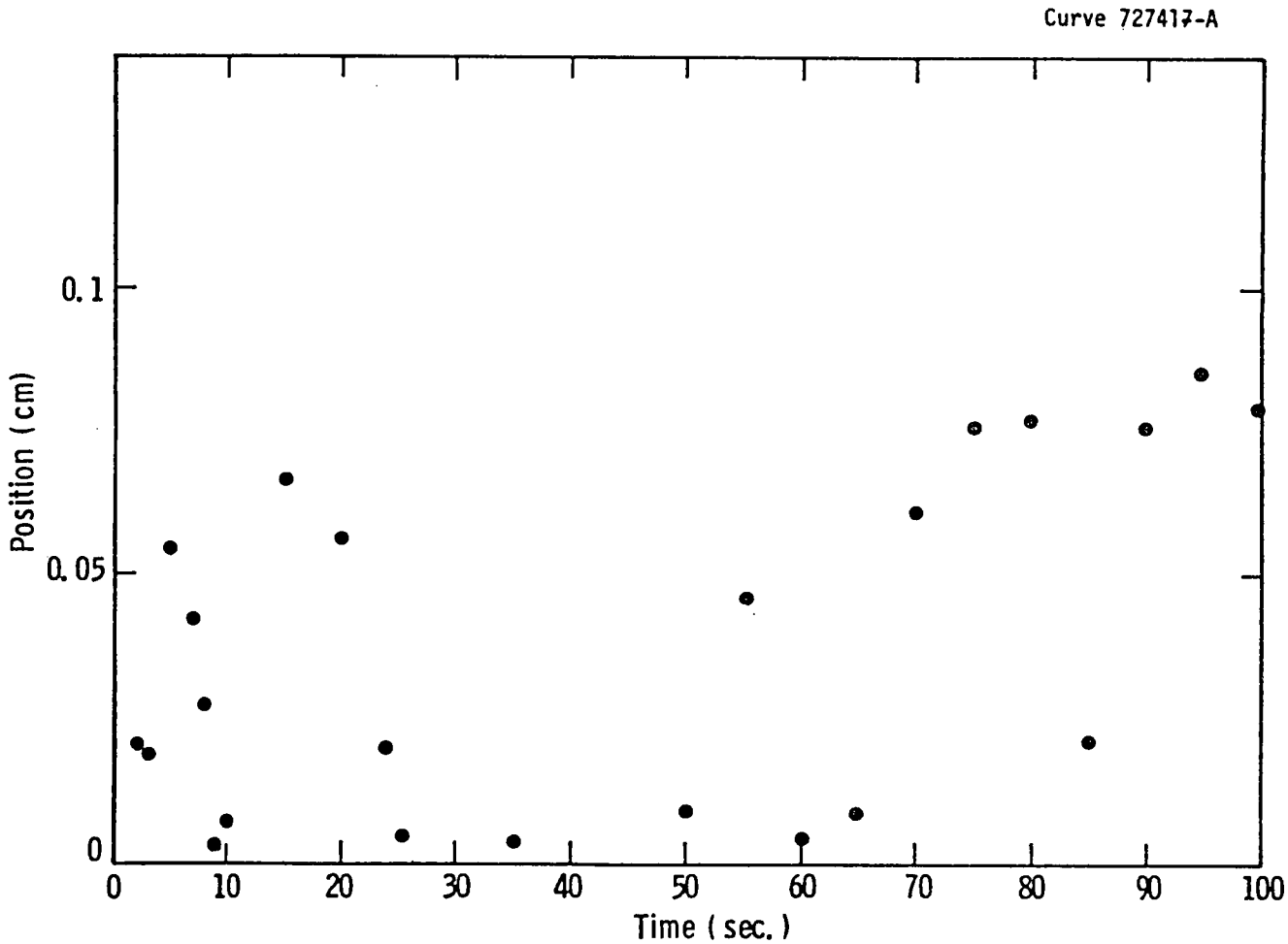

Fig. 6.4-3—Bubble #3

there was vibration or oscillation, but no appreciable net movement. In the neighborhood of Bubble 3, another bubble of roughly the same size was also analyzed. It exhibited a similar oscillatory behavior. We believe these bubbles were "pinned" to the platinum strip and exhibited oscillatory behavior either due to the movement of nearby "free" bubbles, or to an inherent oscillation of the thermocapillary plumes emitted by each. This is an interesting phenomenon not reported previously. In the months ahead we will quantify this behavior in more detail and attempt to determine a mechanism.

6.5 Concluding Comments

It is clear from our work to date that the motion of the bubbles is consistent with the Clarkson model of thermocapillary bubble migration. This conclusion is based on the observed direction and rates of bubble motion and the known orientation of isothermal surfaces in the flight experiment sample. The agreement is at present only semi-quantitative and it will take further careful analysis of the flight data to determine if they will provide a quantitative test for the theoretical model. This analysis is currently under way.

Other new information is also anticipated from further analysis of the data. Our preliminary observations have already shown that bubble coalescence, bubble-bubble interaction, and bubble-wall interaction all occurred during the flight experiment. If even semi-quantitative information can be extracted from the flight data it will indicate the validity of the theoretical models of these kinds of bubble intereactions. Hence we expect to obtain some equally exciting results from this further study of the flight data.

Further studies of the thermocapillary migration need to be carried out under low gravity conditions. The present experimental system could perform several kinds of additional experiments such as measuring

thermocapillary bubble migration glass systems with different surface tension temperature coefficients (e.g. positive) or melts containing a volatile component (e.g. water in a borate glass). These data, in addition to confirming our SPAR VIII results, will either confirm the general applicability of the Clarkson model or demonstrate its limitations and indicate suitable modifications.

The present system may prove to be too qualitative to provide a proper test for the Clarkson model. In that case, the experimental system should be redesigned probably to a larger size and the definitive experiments run on a shuttle flight. In any case an additional SPAR flight with the present apparatus design is in order, perhaps with borax at a lower temperature so that more bubble-bubble interactings can be observed.

REFERENCES

1. G. E. Rindone, Fining, Part I, Glass Industry, 38 (9) 1957 pg. 489-528.

2. G. E. Rindone, Fining, Part II, Glass Industry, 38 (10) 1957, pg. 561-577.

3. S. R. Scholes, Modern Glass Practice, Cahness Books, Boston, Mass., 1975, pg. 216.

4. C. H. Greene and R. F. Gaffney, Apparatus for Measuring the Rate of Absorption of a Bubble in Glass, J. Am. Ceram. Soc. 42(6) 1959, pg. 273.

5. M. Cable, A. R. Clarke, M. A. Haroon, Glass Tech. 9. (1968) p. 101; 10 (1969) p. 15.

6. L. Nemec, "Refining in the Glass Melting Process," J. Amer. Ceram. Soc., 60, No. 10 436-40 (1977).

7. C. H. Greene and A. Haynes, Jr., Effect of As_2O_3 and $NaNO_3$ on the Solution of O_2 in Soda-Lime Glass, J. Am. Ceram. Soc., 48 (10) 1965 p. 528.

8. N. O. Young, J. S. Goldstein, and M. J. Block, "The Motion of Bubbles in a Vertical Temperature Gradient," J. Fluid Mech. 6, 350 (1959).

9. E. Roedder, 1965 Meeting of the Geological Society of America (from U.S. Geological Survey).

10. W. R. Wilcox, "Anomalous Gas-Liquid Inclusion Movement," Ind. Eng. Chem. 61, 76 (March 1969).

11. T. R. Anthony and H. E. Cline, "The Thermomigration of Biphase Vapor-Liquid Droplets in Solids," Acta. Met. 20, 247 (1972).

12. S. R. Coriell, S. C. Hardy and M. R. Cordes, "Melt Shape in Weightless Crystal Growth," NBSIR 77-1208, Feb. 1977.

13. H. D. Smith, D. M. Mattox, W. R. Wilcox, and R. S. Subramanian, "Glass Fining Experiments in Zero Gravity," Final Rept. to George C. Marshall Space Flight Center, Contract No. NAS8-32351, June 30, 1977.

REFERENCES (Cont'd)

14. Partlow, D. P., H. D. Smith, and D. M. Mattox, "Variation in the Surface Tension of Molten Sodium Borate With Temperature," Phys. Chem. Glasses, Vol. 21, No. 6, 221-224, 1980.

15. Matusita, K., T. Watanabe, K. Kamiya, and S. Sakka, "Viscosities of Single and Mixed Alkali Borate Glasses," Phys. Chem. Glasses, Vol. 21, No. 2, 78-84, 1980.

16. Shartsis, L., W. Capps, and S. Spinner, "Viscosity and Electrical Resistivity of Molten Alkali Borates," Jour. of Am. Cer. Soc., Vol. 36, No. 10, 319-326, 1953.

17. Kaiura, G. H., and J. M. Toguri, "The Viscosity and Structure of Sodium Borate Melts," Phys. Chem. Glasses, Vol. 17, No. 3, 62-69, 1976.

18. S. C. Hardy, "The Motion of Bubbles in a Vertical Temperature Gradient," J. Colloid Interface Sci. 69, 157 (1979).

19. J. L. McGrew, T. L. Rehm and R. G. Griskey, "The Effect of Temperature - Indiced Surface Tension Gradients on Bubble Mechanics," Appl. Sci. Res. 29, 195 (1974).

20. R. L. Thompson, K. J. deWitt, and T. L. Labus, "Marangoni Bubble Motion Phenomenon in Zero Gravity," Chem. Eng. Commun. 5, 299 (1980).

21. Subramanian, R. Shankar, "The Slow Migration of a Gas Bubble in a Thermal Gradient." Accepted for publication, AIChE Journ. Sept. 1980.

22. Meyyappan, M., W. R. Wilcox, and R. Shankar Subramanian, "Thermocapillary Migration of a Bubble Normal to a Plane Surface." Accepted for publication, Journ. of Colloid and Interface Science, Jan. 1981.

ACKNOWLEDGMENTS

This report describes an experiment that was the outcome of a team effort of several of Westinghouse contributors. Their names follow:

R. G. Seidensticker - Hot stage - design and evaluation.

R. A. Johnson - Electronic systems - power supply, control, and telemetry interface.

N. A. Salemi - Flight experiment assembly - integration of hardware and electronic systems.

1. REPORT NO.	2. GOVERNMENT ACCESSION NO.	3. RECIPIENT'S CATALOG NO.
NASA TM- 82578		

4. TITLE AND SUBTITLE	5. REPORT DATE
SPACE PROCESSING APPLICATIONS ROCKET PROJECT SPAR VIII FINAL REPORT	June 1984
	6. PERFORMING ORGANIZATION CODE JA62
7. AUTHOR(S) CHASSAY, ROGER P., EDITOR	8. PERFORMING ORGANIZATION REPORT #
9. PERFORMING ORGANIZATION NAME AND ADDRESS GEORGE C. MARSHALL SPACE FLIGHT CENTER MARSHALL SPACE FLIGHT CENTER, AL 35812	10. WORK UNIT NO. M-452
	11. CONTRACT OR GRANT NO.
12. SPONSORING AGENCY NAME AND ADDRESS NATIONAL AERONAUTICS AND SPACE ADMINISTRATION WASHINGTON, D.C. 20546	13. TYPE OF REPORT & PERIOD COVERED TECHNICAL MEMORANDUM
	14. SPONSORING AGENCY CODE

15. SUPPLEMENTARY NOTES

16. ABSTRACT

The Space Processing Applications Rocket Project (SPAR) VIII Final Report contains the engineering report prepared at the Marshall Space Flight Center (MSFC) as well as the three reports from the principal investigators. These reports also describe pertinent portions of ground-based research leading to the ultimate selection of the flight sample composition, including design, fabrication, and testing, all of which are expected to contribute immeasurably to an improved comprehension of materials processing in space.

The SPAR project is coordinated and managed by MSFC as part of the Materials Processing in Space (MPS) program of the Office of Space and Terrestrial Applications (OSTA) of NASA Headquarters.

This technical memorandum is directed entirely to the payload manifest flown in the eighth of a series of SPAR flights conducted at the White Sands Missile Range (WSMR) and includes the experiments entitled" Glass Formation Experiment" SPAR 74-42/1R, "Glass Fining Experiment in Low-Gravity" SPAR 77-13/1, and "Dynamics of Liquid Bubbles" SPAR Experiment 77-18/2.

17. KEY WORDS	18. DISTRIBUTION STATEMENT
SPACE PROCESSING CONTAINERLESS PROCESSING ACOUSTIC LEVITATION SOLIDIFICATION	UNCLASSIFIED - UNLIMITED Subject Category: 15

19. SECURITY CLASSIF. (of this report)	20. SECURITY CLASSIF. (of this page)	21. NO. OF PAGES	22. PRICE
UNCLASSIFIED	UNCLASSIFIED	231	A10

For sale by National Technical Information Service, Springfield, Virginia 22161 NASA-Langley, 1984

National Aeronautics and
Space Administration

Washington, D.C.
20546

Official Business
Penalty for Private Use, $300

SPECIAL FOURTH CLASS MAIL
BOOK

Postage and Fees Paid
National Aeronautics and
Space Administration
NASA-451

NASA

POSTMASTER: If Undeliverable (Section 158
Postal Manual) Do Not Return